THE APPLICATION OF VORTEX TUBES TO GAS TURBINE FILM COOLING

DISSERTATION

Matthew N. Fuqua, Lieutenant Colonel, USAF

AFIT-ENY-21-S-093

DEPARTMENT OF THE AIR FORCE
AIR UNIVERSITY

AIR FORCE INSTITUTE OF TECHNOLOGY

Wright-Patterson Air Force Base, Ohio

AFIT-ENY-21-S-093

THE APPLICATION OF VORTEX TUBES TO GAS TURBINE FILM COOLING

DISSERTATION

Presented to the Faculty

Graduate School of Engineering and Management

Air Force Institute of Technology

Air University

Air Education and Training Command

in Partial Fulfillment of the Requirements for the

Degree of Doctor of Philosophy in Aeronautical Engineering

Matthew N. Fuqua, B.S.A.E, M.S.E.M., M.S.G.W.

Lieutenant Colonel, USAF

September 16, 2021

AFIT-ENY-21-S-093

THE APPLICATION OF VORTEX TUBES TO GAS TURBINE FILM COOLING

Matthew N. Fuqua, B.S.A.E, M.S.E.M., M.S.G.W.

Lieutenant Colonel, USAF

COMMITTEE MEMBERSHIP:

Lt Col James Rutledge, PhD
Chairman

Marc Polanka, PhD
Member

Andrew Lethander, PhD
Member

Lt Col Robert Tournay, PhD
Member

Adedeji B. Badiru, PhD
Dean, Graduate School of Engineering and Management

AFIT-ENY-21-S-093

Abstract

To improve thermal efficiency and reduce fuel consumption, gas turbine engines typically operate at increasingly higher turbine inlet temperatures—well in excess of turbine blade material limits—and film cooling schemes are normally employed to reduce metal temperatures within acceptable limits and prevent structural failure. Cooling requirements vary across a blade surface, but there currently exists no means by which coolant temperatures can be locally adjusted to facilitate optimized usage across a blade. Ranque-Hilsch vortex tubes were investigated as a means of adjusting coolant temperatures solely by fluidic means, induced by the phenomenon of temperature separation.

Analytical frameworks were developed to determine adiabatic and overall effectiveness in the presence of multiple coolant temperatures and validated via experiment. Through the integrated application of experimental, analytical, and computational investigations, the parameters which govern temperature separation were identified as well as the proper means of scaling temperature separation and the underlying physics behind the mechanism of temperature separation. Heat transfer characteristics of vortex tubes were determined and vortex tube performance near engine conditions was modeled. Findings were synthesized to estimate the net effect of multiple local coolant temperatures on turbine blades, including adiabatic wall temperatures and thermally conductive metal surface temperatures, and the effect was found under some circumstances to be operationally significant.

This page is intentionally left blank

Acknowledgments

I am deeply grateful that I have been surrounded by countless exceptional people during this research, and it surely could not have been completed without them. I would especially like to thank my advisor, Lieutenant Colonel James Rutledge, for his tireless advice and insight. Brian Crabtree and the entire crew of the machine shop fabricated the experimental test articles and every time I thought I had asked too much, they came through in spades. Andrew Lethander and Natalia Posada were ever the gracious hosts at the laboratory and always found a way to get to yes on all things big and small—without them, so much of this work could have been lost for the want of a nail. Our industrious research assistants—Mitchell, Marta, Daniel, and Kaylin—constructed much of the lab and their sweat and fingerprints are all over this work. Finally, and most of all, I want to thank my family: to my kids, whose curiosity is contagious and who keep me asking why; and to my wife, whose encouragement was vital to starting down this path and to seeing it through.

<div align="right">Matthew N. Fuqua</div>

This page is intentionally left blank

Table of Contents

This page is intentionally left blank

Nomenclature

A = cross sectional area, (m^2)

$A*$ = hypothetical nozzle area at which $M = 1$, (m^2)

ACR = advective capacity ratio, $\left(\frac{\rho_c C_{pc} U_c}{\rho_\infty C_{p\infty} U_\infty}\right)$

C_p = specific heat at constant pressure, (J/kg-K)

C_v = specific heat at constant volume, (J/kg-K)

D = cooling hole diameter, (m)

D_h = hydraulic diameter, (m)

DR = density ratio, $\left(\frac{\rho_c}{\rho_\infty}\right)$

e = specific internal energy, (J/kg)

F_i = acceleration due to body force, (m/s^2)

g = acceleration due to gravity, (m/s^2)

h = [heat transfer] heat transfer coefficient, (W/m^2-K)

h = [fluid property] specific enthalpy, (J/kg)

k = thermal conductivity, (W/m-K)

L = reference length, (m)

I = momentum flux ratio, $\left(\frac{\rho_c U_c^2}{\rho_\infty U_\infty^2}\right)$

$\dot{m}$ = mass flow rate, (kg/s)

M = [film cooling] mass flux (blowing) ratio, $\left(\frac{\rho_c U_c}{\rho_\infty U_\infty}\right)$

M = [flow property] Mach number

n_i = component of unit surface normal vector

P = pressure, (Pa)

Pe = Péclet number, $Re \times Pr$

Pr = Prandtl number, $C_p \mu / k$

q'' = heat flux, (W/m^2)

q_i = heat flux component in index notation, (W/m^2)

q = heat transfer, (W)

r	=	length, (m)
R	=	[nondimensionalization] length scale, (m)
R	=	[gas property] specific gas constant, (J/kg-K)
R^2	=	coefficient of correlation
Re	=	Reynolds number, $\left(\frac{\rho U L}{\mu}\right)$
t	=	time, (s)
T	=	temperature, (K)
T_{ij}	=	stress tensor, Pa
U	=	velocity, (m/s)
v	=	velocity, (m/s)
V	=	velocity, (m/s)
$V\!\!\!\!\!-$	=	volume, (m^3)
VR	=	velocity ratio, $\left(\frac{U_c}{U_\infty}\right)$
w_i	=	surface velocity component, (m/s)
w	=	work, (W)
x	=	first ordinate, (m)
y	=	second ordinate, (m)
y^+	=	dimensionless wall distance
Z	=	height above a reference plane, (m)
α	=	[gas property] isothermal compressibility coefficient, (Pa^{-1})
α	=	[vortex tubes] fraction of added heat retained in cold flow, $\left(\frac{q_{cold}}{q_{total}}\right)$
β	=	[gas property] isobaric thermal expansion coefficient, (K^{-1})
β	=	[statistics] linear regression coefficient
γ	=	ratio of specific heats, $\left(\frac{C_p}{C_v}\right)$
δ_{ij}	=	Kronecker delta
δT	=	slight change or perturbation in temperature, (K)
Δ	=	difference or change in a property or measurement
ε	=	measurement uncertainty

ζ	=	coolant temperature variation parameter, $\left(\frac{(1-\mu)\Delta T_{c,2}-\mu\Delta T_{c,1}}{T_\infty-T_{mean}}\right)$
η	=	adiabatic effectiveness, $\left(\frac{T_\infty-T_{aw}}{T_\infty-T_{c,exit}}\right)$
$\bar{\eta}$	=	laterally-averaged adiabatic effectiveness
$\bar{\bar{\eta}}$	=	area-averaged adiabatic effectiveness
$\hat{\eta}$	=	adiabatic effectiveness with multiple coolant temperatures, $\left(\frac{T_\infty-T_{aw}}{T_\infty-T_{ref}}\right)$
μ	=	[fluid property] dynamic viscosity, (Pa-s)
μ	=	[film cooling] coolant enthalpy weighting parameter, $\left(\frac{\dot{m}_{c,1}C_{p,c,1}}{\dot{m}_{c,1}C_{p,c,1}+\dot{m}_{c,2}C_{p,c,2}}\right)$
μ_C	=	vortex tube cold fraction, $\left(\frac{\dot{m}_{cold}}{\dot{m}_{inlet}}\right)$
μ_{JT}	=	Joule-Thomson coefficient, (K/bar)
ν_T	=	turbulent viscosity, (m^2/s)
ξ	=	[film cooling] coolant temperature ratio parameter, $\left(\frac{T_\infty-T_{c2}}{T_\infty-T_{c1}}\right)$
ξ	=	[vortex tubes] pressure loss coefficient, $\left(\frac{\Delta P}{\frac{1}{2}\rho V^2}\right)$
π_b	=	combustor pressure ratio, $\left(\frac{P_{t4}}{P_{t3}}\right)$
π_c	=	compressor pressure ratio, $\left(\frac{P_{t3}}{P_{t2}}\right)$
ρ	=	density, (kg/m^3)
τ_c	=	compressor temperature ratio, $\left(\frac{T_{t3}}{T_{t2}}\right)$
τ_{ij}	=	viscous stress tensor, (Pa)
ϕ	=	overall effectiveness, $\left(\frac{T_\infty-T_s}{T_\infty-T_{c,i}}\right)$
$\hat{\phi}$	=	overall effectiveness with two coolant temperatures, $\left(\frac{T_\infty-T_s}{T_\infty-T_{mean}}\right)$
Ω	=	angular velocity, (1/s)

Subscripts

adiabatic	=	without heat addition
aw	=	adiabatic wall
c	=	coolant property
cold	=	evaluated at the vortex tube cold exit
D	=	based on hole diameter
D_h	=	based on hydraulic diameter
exit	=	evaluated at the exit of the film cooling hole or vortex tube
eff	=	effective property, including turbulent and molecular contributions
f	=	in the presence of film cooling
hot	=	evaluated at the vortex tube hot exit
i	=	evaluated at internal cooling passages
inlet	=	evaluated at vortex tube inlet
mean	=	mean
measured	=	based on experimental measurement
nonadiabatic	=	with external heat addition
nozzle	=	evaluated at vortex tube nozzle
r	=	[film cooling] reduction
r	=	[cylindrical coordinates] radial component
ref	=	reference value
s	=	[film cooling] evaluated on a thermally conductive surface
s	=	[vortex tubes, historical] corresponding to isentropic expansion
s	=	[vortex tubes, CFD] corresponding to static pressure
static	=	static property
superposition	=	based on superposition estimate
t	=	total property
total	=	total property
w	=	wall (nonadiabatic)
z	=	axial component in cylindrical coordinate system
θ	=	circumferential component in cylindrical coordinate system
0	=	[film cooling] no surface cooling

0	=	[nondimensionalization] scale value
1	=	upstream row in a double-row configuration
1T	=	referring to a double-row configuration with one coolant temperature
2	=	downstream row in a double-row configuration
1T	=	referring to a double-row configuration with two coolant temperatures
∞	=	freestream property

Acronyms

AR	=	arbitrary region
CFD	=	computational fluid dynamics
HPC	=	high pressure compressor
HPT	=	high pressure turbine
IR	=	infrared
LES	=	large eddy simulation
RNG	=	renormalization group
RSM	=	Reynolds stress model
SLPM	=	standard liters per minute

This page is intentionally left blank

THE APPLICATION OF VORTEX TUBES TO GAS TURBINE FILM COOLING

1 Introduction

1.1 Motivation

Since the conception of the gas turbine engine, designers have continuously pushed the state of the art to operate at ever-higher turbine inlet temperatures to increase engine performance. The gas turbine engine is most closely modeled using the Brayton thermodynamic cycle, and it can be shown that thrust specific fuel consumption (TSFC) can be reduced by increasing the compressor pressure ratio, which—due to the nature of the Brayton cycle—also increases turbine inlet temperatures; similarly, engine specific thrust can be increased with higher turbine inlet temperatures [1].

As turbine inlet temperatures have progressively increased, a variety of turbine cooling schemes have evolved over several decades, enabling turbine blades to operate in freestream temperatures far greater than the temperature capability of their constituent materials. Maintaining this trend toward greater turbine inlet temperatures requires new options for the turbine designer: higher fidelity modeling techniques, greater efficiency of cooling methods, and more precise tailoring of cooling strategies to areas of concern.

The need for precisely tailored cooling strategies provides the greatest impetus for the present research. To cool the exterior surfaces of turbine blades, designers have employed film-cooling techniques with great effect for many years. Turbine blade exterior surfaces are designed to perform optimally in complex flow fields and are therefore quite complex as well. Cooling requirements vary considerably across the surface of turbine blades; some regions—such as the leading edge—are known to have

especially significant cooling needs, while other local hot spots may exist which require additional film cooling. Temperature gradients within the turbine blade material present an additional cooling challenge. Such gradients contribute to low-cycle thermal fatigue, which can degrade the structural integrity of the part and ultimately reduce its life [2].

A designer would presumably want as close a match as possible between the cooling requirement of a particular site and the cooling characteristics of the technique applied to that site. For example, the coldest coolant ideally would be applied to regions with the greatest cooling requirement while regions with lesser requirements may sufficiently benefit from slightly warmer coolant. Options to match coolant temperatures to cooling requirements are currently somewhat limited in practice. Although coolant temperatures may vary across the blade due, for example, to heat transfer in the internal cooling passages, deliberate adjustments to coolant temperatures cannot be applied locally across a blade. This represents a limiting factor in cooling strategies: if coolant temperatures could be adjusted or rebalanced, the new options could potentially permit operation at higher temperatures or increase the life of the turbine blade.

Indeed, several means do exist by which coolant temperatures might be adjusted, which fall into a category known as "temperature separation." Temperature separation is a phenomenon in which a fluid at an initially uniform temperature is induced solely by fluidic means to non-uniform temperatures, with some regions at lower temperatures than initial and other regions at greater temperatures than initial. This peculiar behavior has been observed in different contexts and is attributable to different underlying physics. Eckert observed temperature separation in the wake of a cylinder in crossflow [3] and found regions on the cylinder surface that were colder than the freestream temperature;

2

Eckert attributed this to pressure forces acting in an unsteady flow. In Rakowski's swirling annular cascade [4], a striking example of temperature separation accompanied by a deafening whistle was described by Kurosaka [5]; Kurosaka attributed this to "acoustic streaming." Seol and Goldstein acoustically excited temperature separation in a jet [6]. Temperature separation induced in binary gas mixtures is known as the DuFour effect, in which a concentration gradient produces a temperature gradient [7,8].

By far the most widely used and studied example of temperature separation is in the Ranque-Hilsch vortex tube, which will be referred to simply as a "vortex tube". High pressure gas is injected tangentially into the device to induce a strong swirling motion in the flow. The highest velocity fluid in the outer layers of the vortex achieves a high total temperature while conversely the slower inner core of the vortex is brought to a low total temperature. The conventional vortex tube design exploits this temperate gradient by exhausting the cooler vortex core through an orifice at one end while exhausting the hotter outer region through an annular opening at the opposite end. Using only compressed air at nominal room temperature, commercially available vortex tubes can produce cold-side temperatures as low as 228 K (-50°F) and hot-side temperatures as high as 400 K (260°F) [9]. The device has no moving parts and depends exclusively on the behavior of high velocity fluids with a vortical flow structure, although a precise explanation for this effect remains a matter of debate.

By carefully integrating vortex tubes into the cooling architecture of a gas turbine engine, it may be possible to leverage temperature separation and manipulate the temperature of many coolant streams. Exerting this control may allow, in turn, the skillful turbine designer to optimize cooling performance across the entire turbine section.

3

Neither vortex tubes nor other aspects of temperature separation have been deliberately exploited in film cooling or combustion environments and several unknowns must be resolved before such an application is possible.

1.2 Problem Statement

Explain how vortex tubes work and exploit that understanding to use vortex tubes to adjust turbine engine coolant temperatures.

1.3 Investigative Questions

In the pursuit of vortex tubes as a viable enhancement to gas turbine film cooling techniques, several investigative questions emerge:

- How do vortex tubes work? In other words, what are the underlying physics that permit temperature separation?

- How does vortex tube temperature separation scale? Can performance be nondimensionalized, and what are the governing parameters?

- To what extent can the physics of temperature separation be exploited in the extreme environment of a gas turbine engine?

- Would multiple local coolant temperatures be beneficial?

- To what extent can we inform turbine cooling design decisions with this understanding?

An improved understanding of the temperature separation phenomenon in vortex tubes is essential, particularly with respect to gas turbine environments, to facilitate design and prototyping. Next, because several temperature separation-based cooling architectures are possible, it is valuable to develop a means of characterizing film cooling

performance when multiple coolant temperatures are available; this will allow the designer to model the benefit of temperature separation in film cooling applications. Finally, it is desirable to demonstrate temperature separation under conditions that approach those downstream of the compressor in a gas turbine engine.

1.4 Research Objectives

Four principal research objectives will define the activities in this effort:

1. Model turbine blade cooling performance with more than one local coolant temperature

2. Characterize the phenomenon of temperature separation as observed in a vortex tube

3. Quantify the degree of temperature separation achievable at engine conditions

4. Apply vortex tube and film cooling findings to inform turbine engine design

1.5 Methodology

The present research is clearly multi-faceted, and thus will be approached from a multi-disciplinary perspective including analytical, experimental, and computational components. The film cooling work serves as a proof of concept to inform potential configurations and conduct a preliminary investigation of the manner in which vortex tubes could be applied to film cooling. The film cooling research will start with an analytical approach which will be borne out through experimentation.

With respect to vortex tube characterization, experimental research will serve as the bedrock and computational methods will be applied with the intent to match experimental data with the highest fidelity practical. The computational results will then be used to substantiate a viable explanation of the physics of temperature separation.

Analytical methods are essential in developing new film cooling frameworks, in determining the appropriate nondimensionalization of temperature separation, and in identifying any governing parameters. Experimental and computational methods will then serve as a means of assessing performance under increasingly extreme environments and informing potential design changes as the understanding of the trade space evolves.

2 Research Objective 1: Model turbine blade cooling performance with multiple coolant temperatures available

Because the fundamental aim of this research is to apply vortex tubes to gas turbine film cooling, it is first necessary to craft a basic framework in which vortex tube contributions may be analyzed. Models will be developed to assess adiabatic wall temperatures and thermally conductive metal surface temperatures in the presence of multiple local coolant temperatures. This will ultimately permit the synthesis of vortex tube performance characteristics and estimated coolant temperatures to predict film cooling performance when multiple local coolant temperatures are present.

2.1 Literature Review: Gas Turbine Engine Cooling

Modern aircraft gas turbine engines typically have turbine inlet total temperatures in the range of 2000 K (~1730°C) [1], which presents a considerable engineering challenge to the turbine blade designer. These extremely high temperatures are first addressed using materials-based solutions. Blades are manufactured from nickel-based superalloys and the most modern alloys used in first-stage high pressure turbine applications have melting points in the range of 1320°C – 1450°C [10]. However, a more appropriate metric is the "temperature capability" of a material, which accounts for its ability to withstand high stresses at high temperatures. With the use of clever metallurgy in the form of single-crystal blades, turbine manufacturers have been able to push the temperature capability of superalloys very close to their melting points such that modern first-stage superalloys have temperature capabilities in the range of 1100°C [10].

Turbine inlet temperatures exceed the temperature capability of modern turbine blades by several hundred degrees, so it is clear that additional measures are required to

operate in such extreme freestream temperatures. Consequently, a variety of sophisticated turbine cooling schemes have evolved over several decades. First, coolant is directed through elaborate internal passages, which function essentially as miniature heat exchangers in which convective heat transfer from the metal to the coolant is maximized to reduce the metal temperature. An example of internal cooling passages is shown in Figure 1.
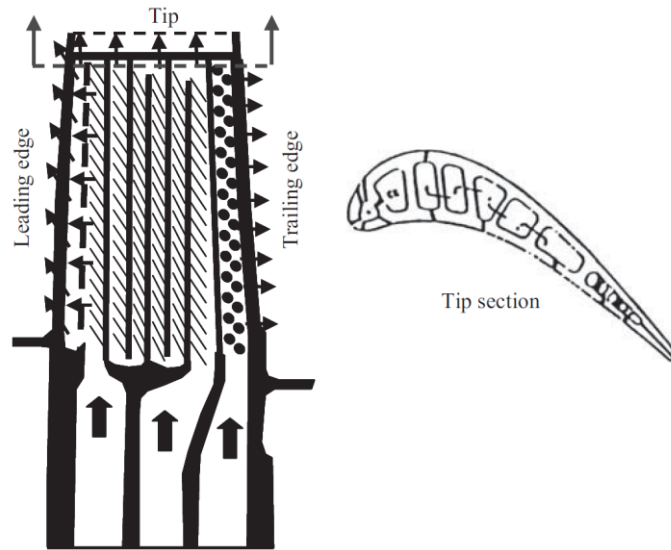
Figure 1. Turbine blade internal cooling passages [11]

Once the coolant passes through the internal cooling passages, it issues to the surface via cooling holes with a technique known as "film cooling". Intricate patterns of carefully shaped cooling holes are found on modern high-performance turbine blades. As can be seen in Figure 2, cooling holes are much more closely spaced in regions with greater cooling requirements, such as the leading edge near the stagnation line. While it is important to cool the hottest parts of the turbine blade, there is also a need to avoid inducing strong temperature gradients across the blade. Such gradients give rise to the

phenomenon known as low-cycle thermal fatigue [12], which induces stress in the blade [13] and reduces the life of the turbine blade [2].
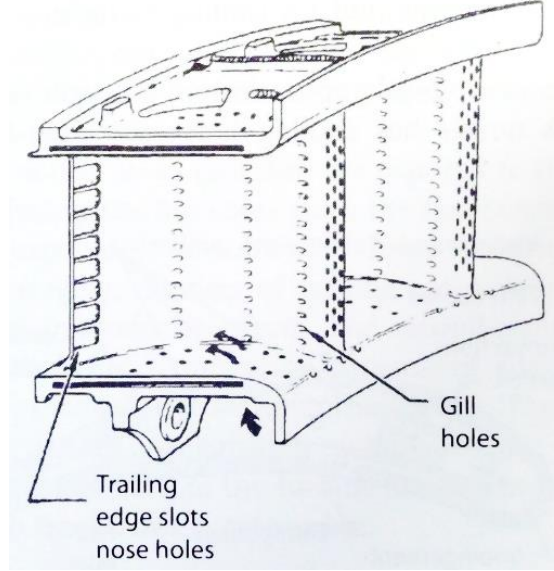
Figure 2. Turbine blade external film cooling [1]

The purpose of film cooling is to minimize convective heat transfer between the freestream and the blade surface, and many of the foundational equations for film cooling are summarized in Bogard and Thole [14]. The heat flux with film cooling present, q_f'', can be calculated using Eq (1), where T_{aw} is the adiabatic wall temperature, T_w is the actual wall temperature, and h_f is the heat transfer coefficient with film cooling present.

$$q_f'' = h_f(T_{aw} - T_w) \tag{1}$$

An array of options is available for the turbine designer to tailor the film cooling strategy to the cooling requirements. The shapes of the cooling holes are carefully designed and numerous varieties exist with various performance characteristics: a 2014 review [15] found 130 different hole shapes in the literature, and variations of the

9

laidback fan-shaped hole were most common. Three hole shapes are shown in Figure 3, which are essentially stages in hole design evolution. Because the present research is not concerned with improving hole design, only laidback fan-shaped holes were used in the film cooling studies here. Details will be provided later with experimental methods.
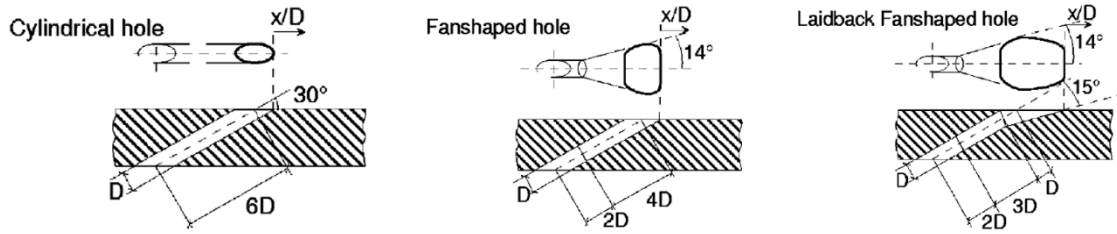
Figure 3. Common cooling hole shapes [16]

The coolant flow rate leaving the cooling holes is typically characterized in terms of a ratio with respect to freestream properties. Several such ratios used in the literature include the density ratio (*DR*), mass flux or blowing ratio (*M*), the momentum flux ratio (*I*), the velocity ratio (*VR*), and, as defined in Rutledge and Polanka [17], the advective capacity ratio (*ACR*). These ratios are important for documenting the performance of a cooling hole; for instance, it is well known that high values of the momentum ratio, I, may cause a coolant jet to separate from the surface and reduce its cooling performance. However, these ratios also represent scaling parameters. Testing cooling performance near engine operating conditions may be expensive, impractical, and in many cases impossible; therefore, it is normally necessary to test cooling performance at low-speed, low-temperature conditions while matching the desired ratio value(s). Implicit is the assumption that matching such a ratio value appropriately predicts cooling performance at engine conditions. Novel investigations on scaling parameters remain a rich field of

research but are out of scope of the present effort. The present effort will use *ACR* as the experimental ratio of choice.

$$DR = \frac{\rho_c}{\rho_\infty} \tag{2}$$

$$M = \frac{\rho_c U_c}{\rho_\infty U_\infty} \tag{3}$$

$$I = \frac{\rho_c U_c^2}{\rho_\infty U_\infty^2} \tag{4}$$

$$VR = \frac{U_c}{U_\infty} \tag{5}$$

$$ACR = \frac{\rho_c C_{pc} U_c}{\rho_\infty C_{p\infty} U_\infty} \tag{6}$$

Figure 4 presents a generalized engine station arrangement. The coolant injected into the high-pressure turbine (HPT) section is bled from the high-pressure compressor (HPC) and bypasses the combustor; it is the only stream of air in the engine at a higher pressure than the turbine section. The air in the HPC—and thus the coolant—is still quite hot; the temperature depends on the inlet air temperature and the compressor pressure ratio and a typical coolant temperature range is 800 K – 1000 K [1].
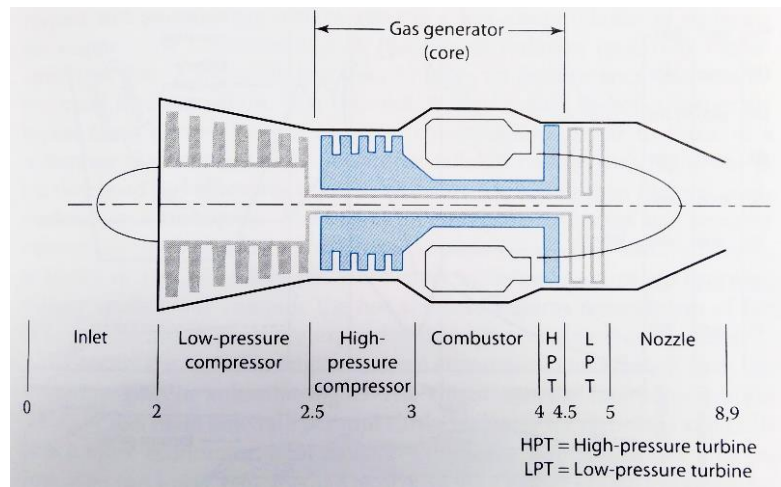
Figure 4. Aircraft engine station diagram [1]

11

To cool the turbine section in a modern military aircraft engine, between 20% and 30% of the compressor air is bled for coolant [11,18]. This is a substantial penalty, but one apparently worth the price for overall engine performance. However, the effectiveness of all cooling schemes is carefully evaluated with the aim of improving efficiency and effectiveness, since reducing the fraction of compressed air used as coolant also increases engine performance.

Multiple measures of cooling effectiveness exist derived by nondimensionalizing key terms in the heat flux equation, Eq (1). The most frequently employed measure of cooling effectiveness is adiabatic effectiveness, defined in Eq (7). Adiabatic effectiveness is essentially a nondimensionalization of adiabatic wall temperature, T_{aw}, in concert with the freestream temperature, T_∞, and the coolant temperature at the exit of the coolant hole, $T_{c,exit}$. The η distribution in a region is typically evaluated experimentally by measuring the surface temperature of a nearly adiabatic model—which is, by definition, nearly identical to T_{aw}—as well as T_∞ and $T_{c,exit}$. However, for early design investigations such as row spacings, experiments presumably require new models to be built for every conceivable configuration.

$$\eta = \frac{T_\infty - T_{aw}}{T_\infty - T_{c,exit}} \tag{7}$$

The theory of superposition with respect to film cooling was first proposed by Sellers [19] and demonstrated that a relatively simple method could be implemented to estimate a complex interaction: the combined effects of successive film cooling stations. By applying this analytical technique, it became possible to vastly reduce the demand for

experimental resources at the initial stages of design. Adopting Sellers' general approach, Muska et al. [20] developed further simplified equations which apply, for example, to a double row of cooling holes, which is a common cooling hole configuration.

The procedure for applying superposition will be demonstrated for the case of a double row, such as that shown with a side view in Figure 5. When a single row is issuing coolant, the adiabatic effectiveness at a downstream location is given by Eq (8), where η_1 is the adiabatic effectiveness due to only the upstream row issuing coolant. Similarly, η_2 is that due to only the downstream row as seen in Eq (9). For the case when both rows are operating, the *apparent* freestream temperature in Eq (9) is approximated as the adiabatic wall temperature that would result if only the upstream row were operating, expressed as Eq (10). The adiabatic wall temperature with both rows operating is isolated by rearranging Eq (9) and substituting in Eq (10) to yield Eq (11). By substituting the expression for $T_{aw,1}$ from Eq (8) into Eq (11) and then substituting the expression for T_{aw} in Eq (11) into Eq (7), one arrives at the familiar equation for superposition with a single coolant temperature [20].
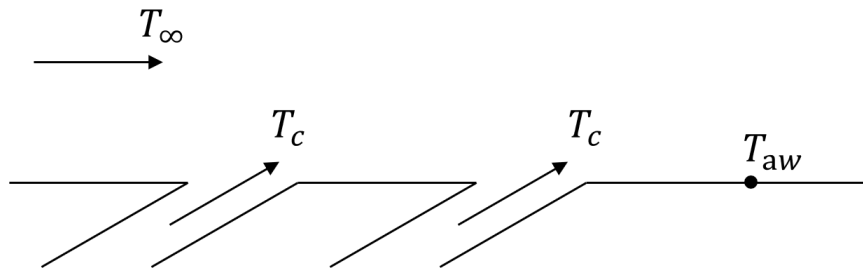
Figure 5. Double row cooling configuration with a single coolant temperature

$$\eta_1 = \frac{T_\infty - T_{aw,1}}{T_\infty - T_{c,exit}} \tag{8}$$

$$\eta_2 = \frac{T_\infty - T_{aw,2}}{T_\infty - T_{c,exit}} \tag{9}$$

$$T_\infty \approx T_{aw,1} \tag{10}$$

$$T_{aw} = T_{aw,1} - \eta_2\big(T_{aw,1} - T_c\big) \tag{11}$$

$$\eta = \eta_1 + \eta_2 - \eta_1\eta_2 \tag{12}$$

The accuracy of superposition ultimately hinges entirely on the validity of Eq (10), since it is the only assumption in the derivation, and Eq (10) is unlikely to hold when there are significant hydrodynamic interactions between rows. The method of superposition has been shown to accurately predict the effectiveness of a multiple rows of cylindrical cooling holes with blowing ratios of less than 0.50, as shown by Sasaki et al. [21]. Saumweber demonstrated successful prediction by superposition for a double row of fan-shaped holes, particularly if the blowing ratios for the row remain below 1.0 [22]. Metzger et al. found that superposition adequately predicted cooling performance for multiple slots, although the method underpredicted performance with very low downstream blowing ratios, e.g. $M_2 < 0.1$ [23]. Superposition has other known limitations, however, particularly with respect to complex hydrodynamic behavior. For example, Harrington et al. investigated the use of short normal injection holes and found

superposition estimates to be unsatisfactory for higher blowing ratios; the inaccuracy was attributed to jet separation and jet interaction [24].

Another common measure of cooling effectiveness is overall effectiveness, defined in Eq (11), which is a nondimensionalization of the surface temperature of the metal blade, T_s, using the freestream temperature and the coolant temperature prior to entering the cooling holes, $T_{c,i}$. Overall effectiveness is useful because it accounts for the contributions of both external film cooling and any cooling through internal passages.

$$\phi = \frac{T_\infty - T_s}{T_\infty - T_{c,i}} \tag{13}$$

Frequently, overall effectiveness is experimentally evaluated at temperatures much lower than engine conditions, but careful consideration must be given to experimental techniques if low temperature findings are to be extensible to engine conditions. Researchers such as Albert et al. [25] and Martiny et al. [26] have shown the sensitivity of overall effectiveness to Biot number; thus, the utility of scaled overall effectiveness research depends critically on matching the Biot number of the research model and conditions to those representative of an engine. This requirement dictates a careful selection of model materials, and prior studies have used alumina [25], Corian™ [27], and Titanium 6-4 [28]. Stewart and Dyson [29] demonstrated that the thermal conductivity of Inconel 718 also varies in such a manner to make it suitable for scaling low-temperature studies.

Overall effectiveness has been investigated by numerous workers in a variety of configurations. These include studies of a flat plate with backside impingement cooling [28] [29], the leading edge showerhead [25] [30] [31], and even fully cooled turbine

blades [32]. These previous investigations have focused on scenarios where it is reasonably assumed that there is one characteristic internal coolant temperature, $T_{c,i}$, either because the coolant is fed from a single plenum or multiple plenums are fed from the same source.

However, there may be scenarios in which multiple coolant temperatures are present. For example, coolant may be injected at a certain temperature from an upstream row or plenum and provide film cooling dozens of hole diameters downstream; meanwhile, other coolant from that same row or plenum may make several passes through internal channels before being exhausted from a separate row downstream at a greater temperature. An example of such a scenario can be seen in Figure 6, reflecting the current need for multiple temperature modeling. Additionally, engines may have multiple sources of coolant at various temperatures available for turbine designers to route the coldest coolant where it is required, whereas warmer coolant may be used in less demanding locations. In the present investigation, temperature separation induced by vortex tubes may also give rise to different coolant temperatures.
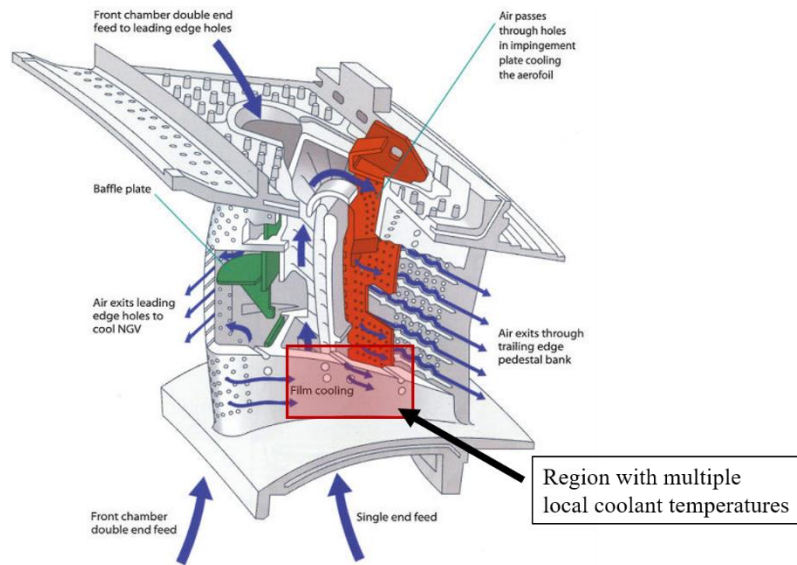
Figure 6. Cooling scenario with multiple local coolant temperatures

(image adapted from [33], emphasis added)

Very little research has been conducted on scenarios involving multiple coolant temperatures. Apart from the research contained herein, only a single known paper studied the topic, which was contemporary to the present effort: Alqefl et al. [34], whose work was contemporary with the present researched, investigated adiabatic effectiveness of a triple plenum cooling configuration on a turbine endwall and produced a superposition model. However, no studies have investigated the effect of multiple local coolant temperatures on overall effectiveness.

2.2   Adiabatic Effectiveness with Multiple Local Coolant Temperatures

In the study of film cooling effectiveness, adiabatic effectiveness is a conventional starting point, and it is here that the research on the effect of two coolant temperatures begins, using a simple configuration of a double row in a flat plate. The framework of superposition was thought to be an especially suitable starting point for the construction of a multiple-temperature cooling model involving adiabatic effectiveness. By developing such a model, it will eventually become possible—for a given cooling scenario—to determine the influence of multiple coolant temperatures on adiabatic wall temperature compared to a single coolant temperature.

2.2.1   *Development of Multiple Temperature Film Cooling Superposition Theory*

Attention now turns to the fact that coolant issuing from different rows of cooling holes necessarily travels through different internal cooling paths prior to reaching the coolant holes. An extreme case could be the coolant that travels to the leading edge showerhead by way of serpentine internal leading edge coolant channels complete with impingement cooling compared to different paths taken by the coolant traveling to downstream rows on the suction or pressure surfaces of the blade. While such temperature differences have generally been ignored in past studies, it is recognized that greater fidelity in turbine thermal behavior is critical as temperatures rise and material distress becomes more sensitive to errors in thermal predictions.

A double row of cooling holes, in which coolant is injected at different temperatures, is shown in Figure 7. To analyze such a scenario, it is necessary to modify Eq (12) and develop a new equation for adiabatic effectiveness using a new reference temperature, T_{ref}, in place of $T_{c,exit}$ since there is no longer a single value for $T_{c,exit}$. The

18

new representation is Eq (14); the symbol $\hat{\eta}$ is used to distinguish from adiabatic

effectiveness computed with a single coolant temperature.
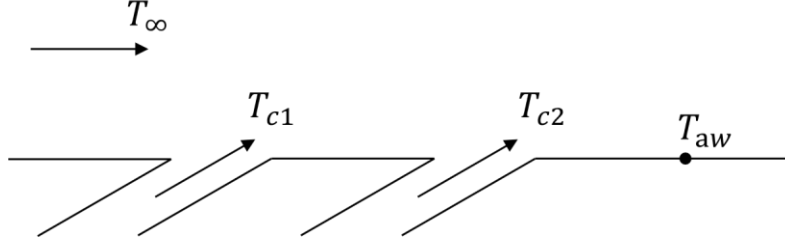
Figure 7. Double row cooling configuration with two coolant temperatures

$$\hat{\eta} = \frac{T_\infty - T_{aw}}{T_\infty - T_{ref}} \qquad (14)$$

The proposed approach is to express $\hat{\eta}$ as a piecewise function wherein the

reference temperature, T_{ref}, is the colder of the two coolant temperatures; if the

temperature of the coolant issuing from downstream row, T_{c2}, is lower than that of the

upstream row—i.e. $T_{c2} < T_{c1}$—then $T_{ref} = T_{c2}$ and vice versa. This choice of reference

temperature, despite precipitating a piecewise function, provides some convenient

mathematical features. First, selecting the coldest temperature as the reference bounds the

values of $\hat{\eta}$ by $0 < \hat{\eta} < 1$ and simplifies its interpretation. Next, as will be demonstrated

later in this particular study, it becomes more straightforward to predict a surprising

situation in which the coolant issuing from the second row can *reduce* cooling

performance.

Other choices of reference temperature are also possible, such as a mass-average

of the two coolant temperatures; indeed, this was the author's initial preference. Although

it avoids a piecewise function, it introduces a new difficulty in that such a reference

19

temperature is necessarily warmer than the colder coolant and therefore $\hat{\eta}$ is no longer bounded by $0 < \hat{\eta} < 1$. The maximum value of $\hat{\eta}$ increases unboundedly as the difference in temperatures increases and this "moving scale" complicates interpretation. Furthermore, this choice requires the explicit use of weighting parameters, such as the relative mass-fractions of coolant from each row. Obviously, one would need to employ scaling parameters—such as ACR or momentum flux ratio—in determining η_1 and η_2 no matter the choice of reference temperature, but the scaling parameters are independently selected in the coldest-reference approach with no need for separate weighting parameters. As will be demonstrated, this ultimately allows for a simple generalization to an arbitrary number of rows and coolant temperatures.

With a modified equation for adiabatic effectiveness in the case of two coolant temperatures, it is now possible to elaborate on a theory of superposition. With only a single row blowing, the adiabatic effectiveness in a particular location is given by Eqs (15) or (16), where T_{c1} is the exit temperature of coolant from the upstream row and T_{c2} is that of the downstream row.

$$\eta_1 = \frac{T_\infty - T_{aw,1}}{T_\infty - T_{c1}} \tag{15}$$

$$\eta_2 = \frac{T_\infty - T_{aw,2}}{T_\infty - T_{c2}} \tag{16}$$

Just as with classical superposition conceived by Sellers [19], the freestream temperature at a site affected by two rows of holes is replaced by the adiabatic wall temperature that would result with only the upstream row issuing, as in Eq (17). Applying a similar process of substitution as shown before, the adiabatic effectiveness is given by

the more complex Eq (18). Two different expressions for $\hat{\eta}$ are possible, owing to the piecewise nature of the calculation. A nondimensional parameter, ξ, may be defined as the ratio of the differences between the freestream temperature and those of the respective coolants as shown in Eq (19).

$$T_{aw} = T_{aw,1} - \eta_2\left(T_{aw,1} - T_{c2}\right) \tag{17}$$

$$\hat{\eta} = \frac{\eta_1(T_\infty - T_{c1}) + \eta_2(T_\infty - T_{c2}) - \eta_1\eta_2(T_\infty - T_{c1})}{T_\infty - T_{ref}} \tag{18}$$

$$\xi \equiv \frac{T_\infty - T_{c2}}{T_\infty - T_{c1}} \tag{19}$$

In the case where $T_{c2} < T_{c1}$, $\xi > 1$ and $T_{ref} = T_{c2}$. In the opposite case, $T_{c1} < T_{c2}$, $\xi < 1$ and $T_{ref} = T_{c1}$. Equations of superposition for a double row with two coolant temperatures then reduce to Eqs (20) and (21) for $\xi > 1$ and $\xi < 1$, respectively. It can be verified that when the two coolant temperatures are identical, i.e. $T_{c1} = T_{c2}$, then $\xi = 1$ and Eqs (20) and (21) both reduce to Eq (12). It is the aim of this particular study to examine the extent to which adiabatic effectiveness is a function of the coolant temperature difference ratio, ξ, and the degree to which Eqs (20) and (21) accurately predict adiabatic effectiveness.

$$\hat{\eta} = \frac{1}{\xi}(\eta_1 + \xi\eta_2 - \eta_1\eta_2) \tag{20}$$

$$\hat{\eta} = \eta_1 + \xi\eta_2 - \eta_1\eta_2 \tag{21}$$

2.2.2 Experimental Methodology

A new test apparatus was constructed to support these experiments. A flat plate test insert manufactured from low thermal conductivity foam ($k = 0.03$ W/m-K) was installed in a fashion similar to Fischer [35] in the afterbody of the 8.89 cm diameter leading edge model of Wiese [36], as shown in Figure 8. Two rows of coolant injection consisted of a slot upstream of a row of holes. This geometry was selected to increase the likelihood that the superposition method would be valid since the slot was not expected to have complex hydrodynamic interactions with the row of holes. As noted by Bogard and Thole [18], the practical use of slots may be limited by structural concerns, but their use in establishing experimental baselines is ideal due to a high degree of flow uniformity.
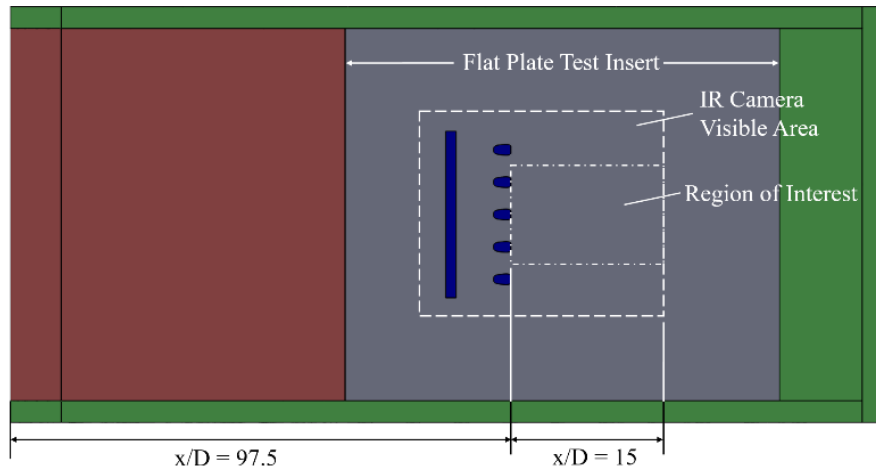
Figure 8. Test rig side view

The slot had a metering width of 4.5 mm, a 30° injection angle, and a vertical extent of $y/D = \pm16.2$. The downstream row consisted of five laid-back, fan-shaped holes of the 7-7-7 design proposed by Schroeder and Thole [15]. The 7-7-7 hole expands 7° laterally and in the forward direction, and has a 7° laid-back angle; it was chosen because

its baseline performance has been rigorously documented and its non-proprietary design is representative of current best practices.

The holes had a metering diameter of 4.5 mm and were spaced with a pitch of $y/D = 6.3$; the upstream edges of the holes were located 9 diameters downstream of the trailing edge of the slot; the exact configuration is detailed in Figure 9. The two rows were supplied via two different plenums so the coolant temperatures of the rows could be independently varied. This permitted control over the coolant temperature ratio parameter, ξ. Thermocouples were placed in the entrance of the slot and holes to measure coolant temperatures. An infrared (IR) camera was positioned to view the surface from just upstream of the slot to 15 hole diameters downstream of the row of holes. A smaller region of interest was selected to avoid nonuniform areas of flow near the edges of the slot. The region of interest lies downstream of the middle three holes from $0 < x/D < 15$ and $9.5 < y/D < -9.5$.

The flat plate was installed in an open-loop, temperature-regulated wind tunnel, in a configuration identical to that of Fischer et al. [35]; a schematic is shown in Figure 10. The freestream temperature was monitored with a thermocouple and the freestream velocity was measured with a pitot-static system so that the tunnel Reynolds number, Re_D, was monitored. Using a control circuit, Re_D was adjusted to stay within 2% of 3000 with a turbulence intensity of 0.67%.
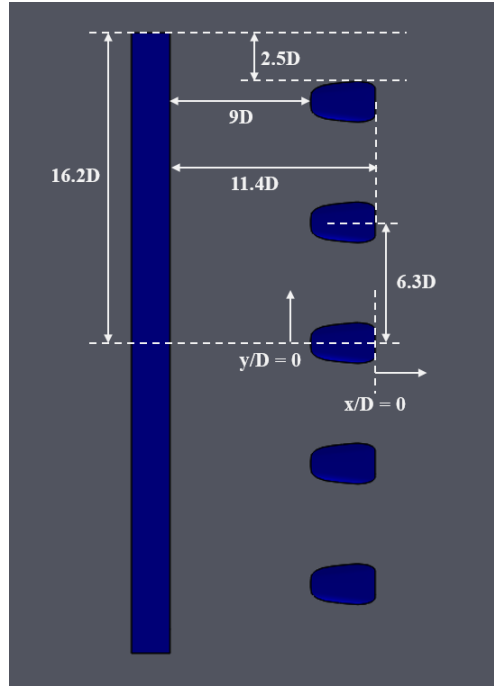
Figure 9. Diagram of test surface and origin
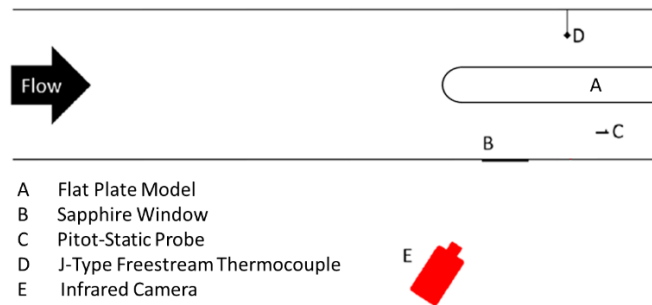
Figure 10. Wind tunnel schematic [35]

Coolant was injected from the slot at a constant *ACR* of 0.50 and from the row of

holes at a constant *ACR* of 0.75; these baseline *ACR* values were maintained for all runs.

The coolant flow rates are characterized in terms of *ACR* since Fischer et al. [35] showed

that *ACR* characterized the adiabatic effectiveness for a 7-7-7 shaped hole far better than

either blowing ratio or momentum flux ratio, provided that the momentum flux ratio was less than about 0.6, which is the case presently. The baseline ACR values were selected to ensure that neither row dominates the results and thus effects attributable to both rows are visible. The values were also selected to ensure that the coolant remained attached to the surface, thereby minimizing row interactions that interfere with superposition predictions. The coolant gas was air. Cases were run with freestream temperatures of 310K and 320K. While holding the tunnel freestream at the desired temperature and Reynolds number and baseline ACR values, the coolant temperatures of the rows were independently controlled. By varying T_{c1} between 282 K and 310 K and T_{c2} between 289 K and 305 K, the coolant temperature ratio parameter ranged an order of magnitude: from $0.40 < \xi < 4.0$.

Three thermocouples were also mounted on the surface of the model directly downstream of the slot at $y/D \approx -14$, a location which permitted variation of surface temperature via the slot but which was not directly upstream of the region of interest. Surface temperature measurements were correlated with infrared counts recorded by the camera to establish a calibration curve for the IR imagery.

When experimentation was complete, the imagery data and thermal calibration curve were used to derive surface temperature across the region of interest. This was used in turn with the coolant exit temperature thermocouples and Eq (7) to compute values for the apparent η, and with Eqs (20) and (21) to compute the apparent $\hat{\eta}$. A one-dimensional conduction correction was then applied to the apparent values in a manner similar to that applied by Williams et al. [27]; based on an examination of the cooling scene, a correction value of $\eta_0 = 0.06$ was found to be suitable. The uncertainties of η and $\hat{\eta}$ (when $\xi \neq 1$) within the region of interest, ε_η and $\varepsilon_{\hat{\eta}}$, were computed using the method of

Kline and McClintock [37]. It was found that ε_η and $\varepsilon_{\hat{\eta}}$ are most strongly functions of the

quantity $T_\infty - T_{ref}$ where small values of $T_\infty - T_{ref}$ yield the greatest ε values; the

largest values of ε_η and $\varepsilon_{\hat{\eta}}$ were found to be 0.037 and corresponded to cases where

$T_\infty - T_{ref} = 15$ K.

2.2.3   Results and Discussion

2.2.3.1   Confirmation of Legacy Superposition

The results begin with the single temperature case, in which $T_c = T_{c1} = T_{c2}$ and

for which $\xi = 1$. Verification cases were run with $T_\infty = 320$ K, $T_c = 289$ K, 295 K, and

305 K as well as $T_\infty = 310$ K, $T_c = 290$ K and 295 K to establish that the experimental

methods appropriately yield adiabatic effectiveness that is independent of coolant

temperature. A selection of results is shown in Figure 11, which reveals extremely similar

η profiles. Figure 12 indicates little variation in centerline adiabatic effectiveness

between the five cases for the hole centered at $y/D = 0$. The η values between the five

cases are within ± 0.025.
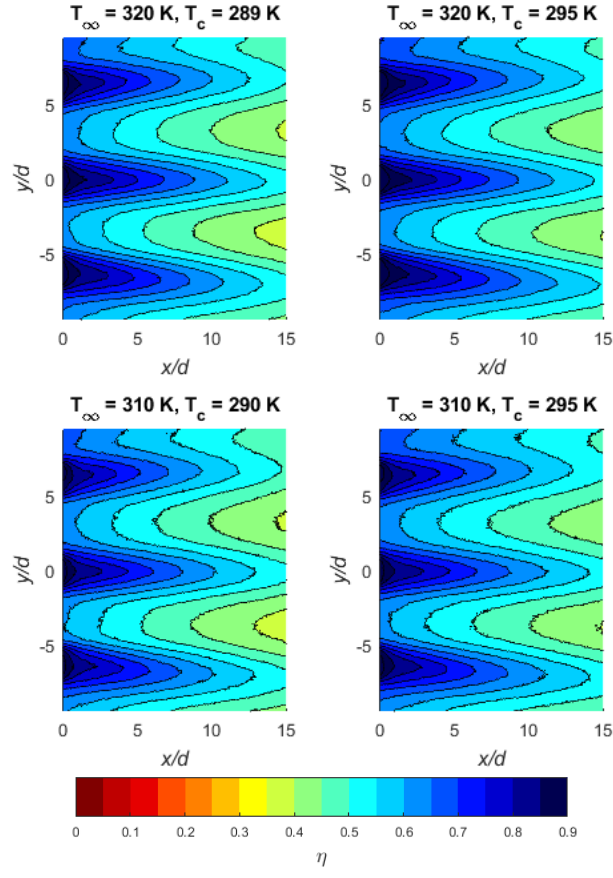
Figure 11. η for various T_∞ and T_c
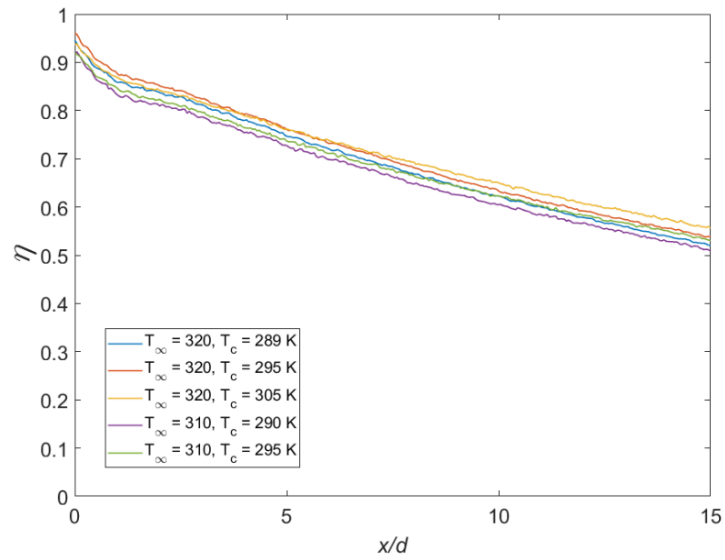
Figure 12. Centerline adiabatic effectiveness for cases of $T_{c1} = T_{c2}$

27

Measurements were also acquired with each row operating separately at their respective baseline *ACR* values. This also afforded an opportunity to examine flow uniformity. Figure 13 depicts contours of adiabatic effectiveness which represent η_1 and η_2 plots; the three coolant holes in the region of interest have uniform performance. The presence of those holes, however, generates a small hydrodynamic effect on the upstream coolant flow causing that flow to be nonuniform in the *y* direction in Figure 13 (left).
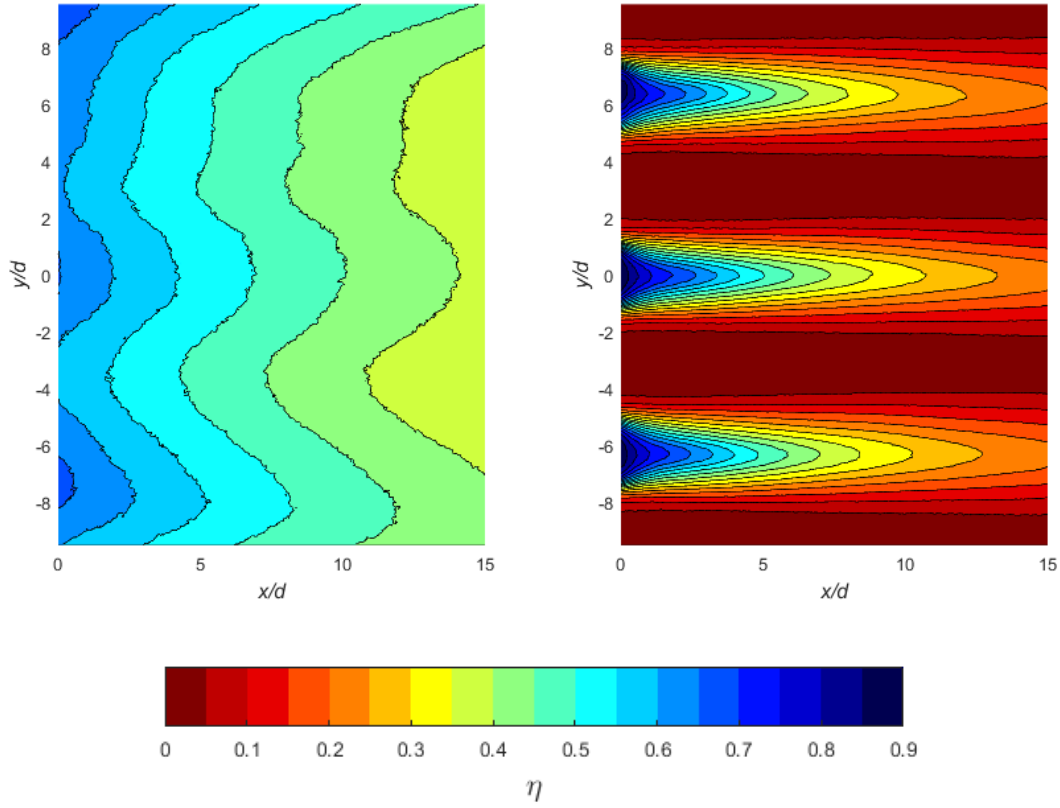
Figure 13. η_1 (left), η_2 (right)

By applying Eq (9) to the datasets plotted in Figure 13, η was estimated using standard superposition for both rows blowing and plotted in Figure 14. By visual

inspection, the estimated η profile under superposition agrees well with the experimental findings shown in Figure 11. To more quantitatively evaluate the efficacy of superposition, the difference between the superposition prediction and the measured values of η is defined according to Eq (22).

$$\Delta\eta = \eta_{superposition} - \eta_{measured} \tag{22}$$

Contours of $\Delta\eta$ were constructed to more precisely reveal regions of relative accuracy and are shown in Figure 15. Positive values indicate that superposition has over-predicted η and negative values indicate the superposition underestimates effectiveness. The areas of least accuracy are within five hole diameters immediately downstream of the cooling holes, where superposition overpredicts effectiveness by up to 0.08. The regions between the holes tend to underpredict effectiveness, and the effect increases in the streamwise direction: beyond ten hole diameters, superposition often underpredicts effectiveness by up to 0.08. The areas of greatest accuracy are between the cooling holes and more than five hole diameters downstream of the cooling holes. Recall that the accuracy of superposition, broadly speaking, hinges on the validity of Eq (10) and the local variations exhibited in Figure 15 are a physical manifestation of this principle.

When η is area-averaged across the region of interest, $\bar{\bar{\eta}}$ can be calculated; Table 1 lists values of $\bar{\bar{\eta}}$ for each case where $\xi = 1$ as well as ε_η, the uncertainty in η associated with each case. For the present configuration, the regions in which superposition overestimates η are averaged with the regions in which superposition underestimates η. The greatest difference between estimated and measured area-averages is $\Delta\bar{\bar{\eta}} = 0.042$, which is comparable to the uncertainty in η expected for any particular *point*, i.e. ε_η,

which is 0.036. This does not suggest that superposition is perfect—after all, it was seen that $\Delta\eta$ can vary in certain locations by up to ± 0.08—but the net effect is that, in aggregate, the values of $\Delta\bar{\bar{\eta}}$ are small enough that $\bar{\bar{\eta}}$ of the superposition estimate is a strong predictor of measured $\bar{\bar{\eta}}$.
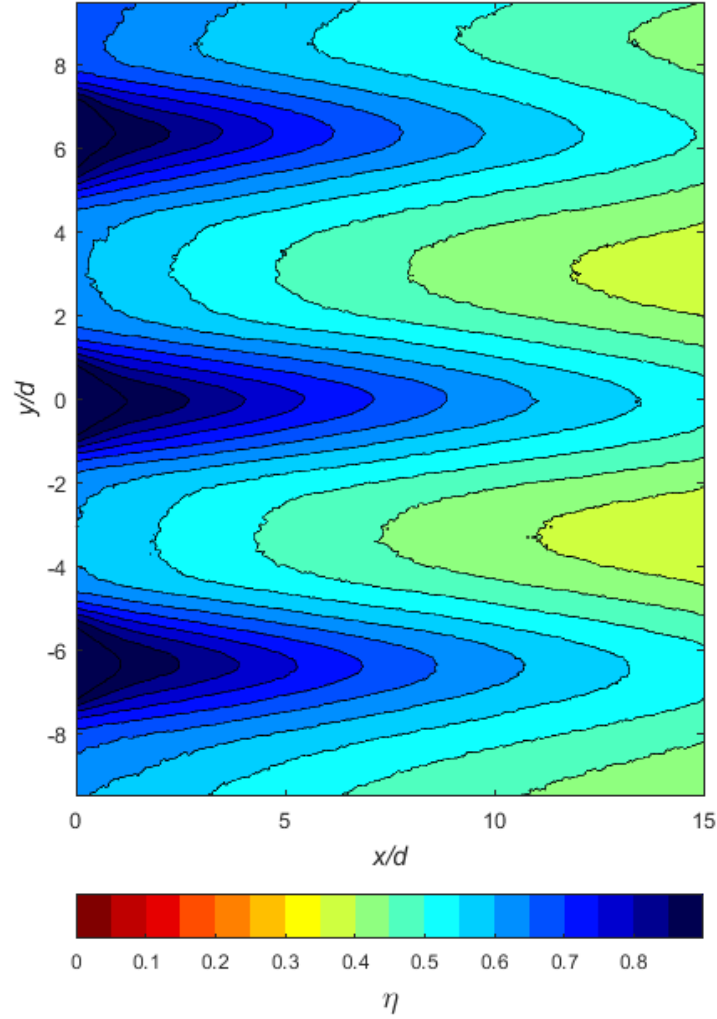
Figure 14. Superposition estimate for $\xi = 1, \ ACR_1 = 0.50, ACR_2 = 0.75$

30
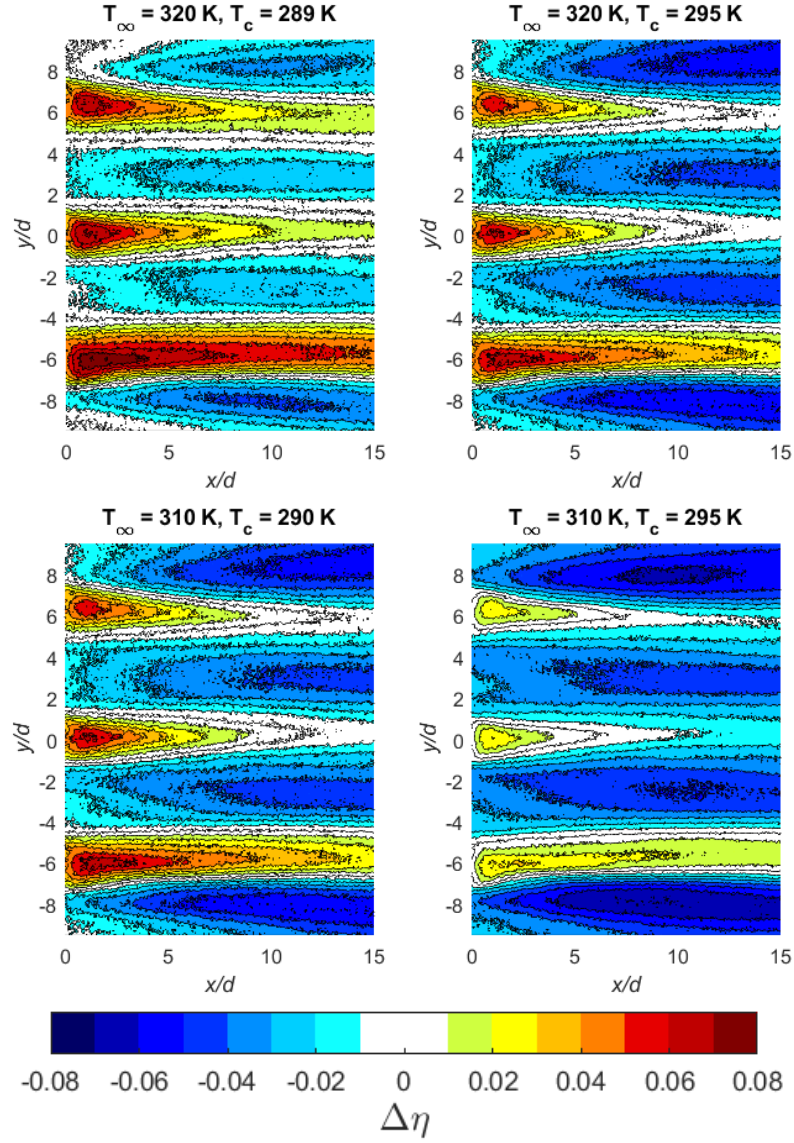
Figure 15. Contours of $\Delta\eta = \eta_{superposition} - \eta_{measured}$ for various T_∞ and T_c

Table 1. Comparison of $\xi = 1$ cases to superposition estimate ($\bar{\bar{\eta}}_{super} = 0.568$)

T_∞ (K)	T_c (K)	$\bar{\bar{\eta}}_{measured}$	$\Delta\bar{\bar{\eta}}$	ε_η
320	289	0.575	-0.007	0.018
320	295	0.593	-0.025	0.022
320	305	0.610	-0.042	0.036
310	290	0.567	+0.002	0.027
310	295	0.583	-0.015	0.036

2.2.3.2 Multiple Coolant Temperature Results

Having established that the present geometry of interest and flow conditions are amenable to traditional superposition, attention turns to the new situation of present interest in which the coolant temperatures do not match. Cases with $T_{c1} \neq T_{c2}$ were run with the baseline *ACR* values and $\hat{\eta}$ was computed using Eq (14). To establish that $\hat{\eta}$ is a function of ξ, four cases are compared in which ξ values are nearly identical but values of T_{∞}, T_{c1}, and T_{c2} are different as shown in Table 2. This initial view is somewhat anecdotal with respect to ξ, but comprehensive with respect to the region of interest. A more comprehensive view of $\hat{\eta}$ with respect to ξ will follow.

Table 2. Comparison cases with $\xi \approx 1.3$ and $\xi \approx 0.8$

ξ	T_{∞} (K)	T_{c1} (K)	T_{c2} (K)	$\overline{\overline{\hat{\eta}}}_{meas}$	$\overline{\overline{\hat{\eta}}}_{super}$	$\Delta\overline{\overline{\hat{\eta}}}$
1.33	320.2	305.3	300.4	0.496	0.469	-0.028
1.33	309.4	295.0	290.2	0.477	0.469	-0.008
0.80	320.3	288.8	295.1	0.543	0.535	-0.008
0.79	320.0	295.0	300.3	0.557	0.533	-0.023

Due to the piecewise nature of $\hat{\eta}$, two cases each were selected for $\xi > 1$ and $\xi < 1$ to test validity of Eqs (20) and (21), respectively, and these cover $\xi \approx 1.3$ and $\xi \approx 0.8$. A comparison in Table 2 indicates that for $\xi \approx 1.3$, values of $\overline{\overline{\hat{\eta}}}$ differ by less than 0.02; the differences are even smaller between the $\xi \approx 0.8$ cases. Contour plots of $\hat{\eta}$ for the $\xi \approx 1.3$ cases are compared in Figure 16 and the two plots bear a strong qualitative resemblance.

Similarly, contour plots of $\hat{\eta}$ for the $\xi \approx 0.8$ cases are shown in Figure 17 and also bear a very strong likeness. Aside from showing the independence of $\hat{\eta}$ from the

choice of T_∞, T_{c1}, and T_{c2} for fixed ξ, a comparison of Figure 16 and Figure 17 allow one

to clearly see that $\hat{\eta}$ is indeed a strong function of ξ as predicted earlier. This is the first

known demonstration of this effect in the literature.
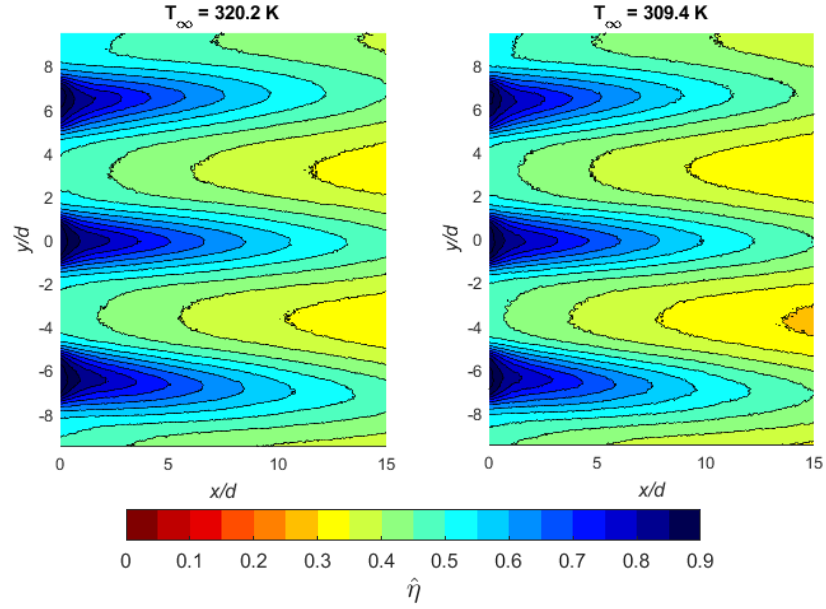
Figure 16**. Comparison of cases with** $\xi \approx 1.3$
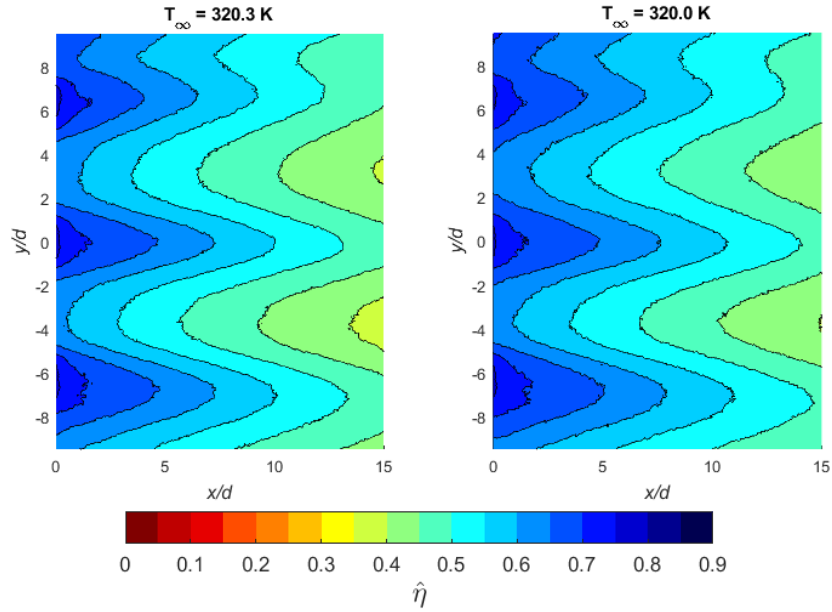
Figure 17. Comparison of cases with $\xi \approx 0.8$

The two-temperature method of superposition in Eqs (20) and (21) was applied to the original η_1 and η_2 distributions from Figure 13 using corresponding values of $\xi = 1.33$ and $\xi = 0.80$. The results are plotted in Figure 18 and it is apparent that the superposition estimates for $\xi = 1.33$ and $\xi = 0.80$ are similar to the respective measured $\hat{\eta}$ profiles. By subtracting $\hat{\eta}$ for the two cases in Figure 16 ($\xi = 1.33$) from the corresponding superposition estimate in Figure 18, similar to the method of Eq (22), $\Delta\hat{\eta}$ values were determined and plotted in Figure 19. Similarly, $\Delta\hat{\eta}$ values were determined for the $\xi \approx 0.8$ cases and plotted in Figure 20.

There is broad similarity between the trends of $\Delta\hat{\eta}$ evidenced in Figure 19 and Figure 20 and the trends of $\Delta\eta$ seen in Figure 15. The trends are the same as those observed in the $\Delta\eta$ plots of Figure 15. The superposition estimates of $\hat{\eta}$ are closest to the measured values at least five hole diameters downstream of the row of holes, with broad swaths of $|\Delta\hat{\eta}| < 0.01$. The estimates overpredict $\hat{\eta}$ in regions within five diameters of the hole exits though typically by $|\Delta\hat{\eta}| < 0.05$. Superposition underpredicts $\hat{\eta}$ between holes, especially beyond five hole diameters downstream of the holes. This is most prominently seen in the white patch in the Figure 19 for 320.2 K, where plot blue area exceeds the color bar bounds; the minimum value is -0.087. To be clear, the shortcomings in the modified superposition theory are the same as those for conventional single-temperature superposition theory: hydrodynamic interactions between the rows reduce the accuracy of the estimates. For the present configuration, these appear most pronounced within five hole diameters of the hole exit, and beyond five hole diameters in the regions between the holes. Referring to Table 2, it is evident that $\Delta\bar{\bar{\hat{\eta}}}$ values are small

and therefore the two-temperature superposition estimates are fairly accurate in predicting area-averaged adiabatic effectiveness, at least for the baseline ACR values used in the present scenario.
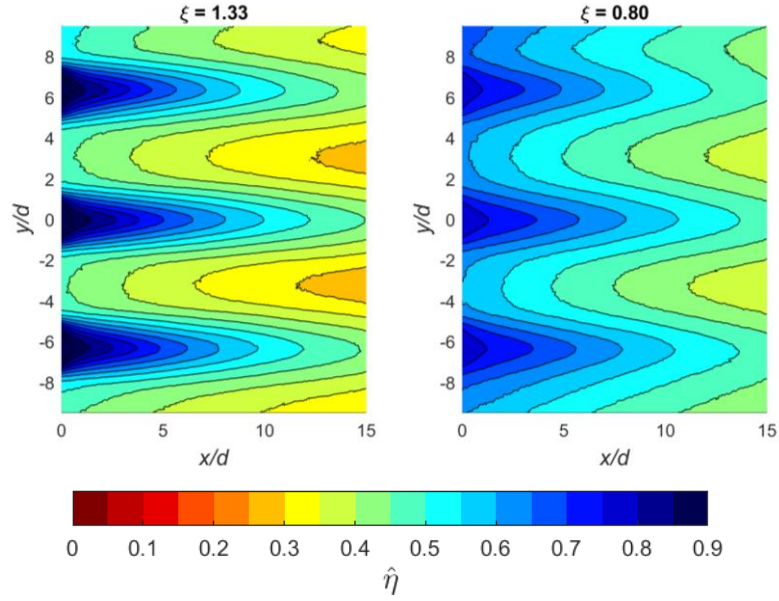
Figure 18. Superposition estimates of $\hat{\eta}$ for $\xi = 1.33$ and $\xi = 0.80$;

$ACR_1 = 0.50, \ ACR_2 = 0.75$
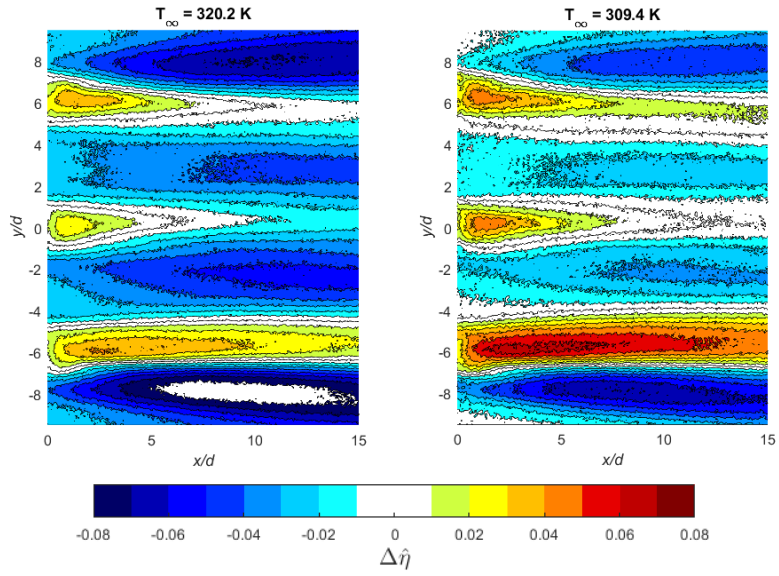
Figure 19. Comparison of $\Delta\hat{\eta}$ for cases with $\xi \approx 1.3$
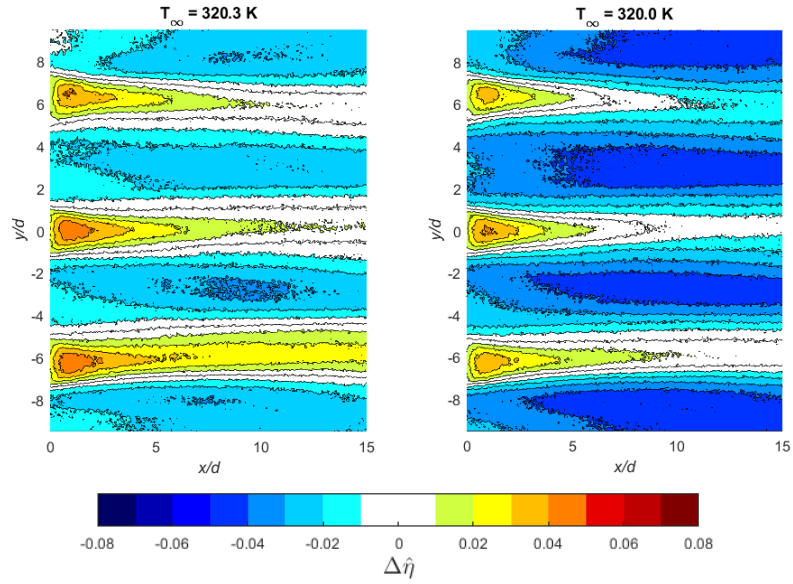
Figure 20. Comparison of $\Delta\hat{\eta}$ for cases with $\xi \approx 0.8$

The comparisons between $\bar{\bar{\hat{\eta}}}_{measured}$ and $\bar{\bar{\hat{\eta}}}_{superposition}$ can be extended to every experimental case, for $T_\infty = 310$ K and $T_\infty = 320$ K. An aggregate of these results is plotted together in Figure 21. The resulting "spike" shape is quite distinctive and is a consequence of the piecewise function used to compute $\hat{\eta}$: for $\xi > 1$, the difference $T_\infty - T_{aw}$ is nondimensionalized by $T_\infty - T_{c2}$, while for $\xi < 1$, it is nondimensionalized by $T_\infty - T_{c1}$. Nevertheless, Figure 21 indicates that $\bar{\bar{\hat{\eta}}}$ is a very strong function of ξ and appears essentially independent of T_∞. Superposition provides fairly accurate estimates—generally within 0.03—even out to extreme values of $\xi = 0.4$ and $\xi = 4.0$.
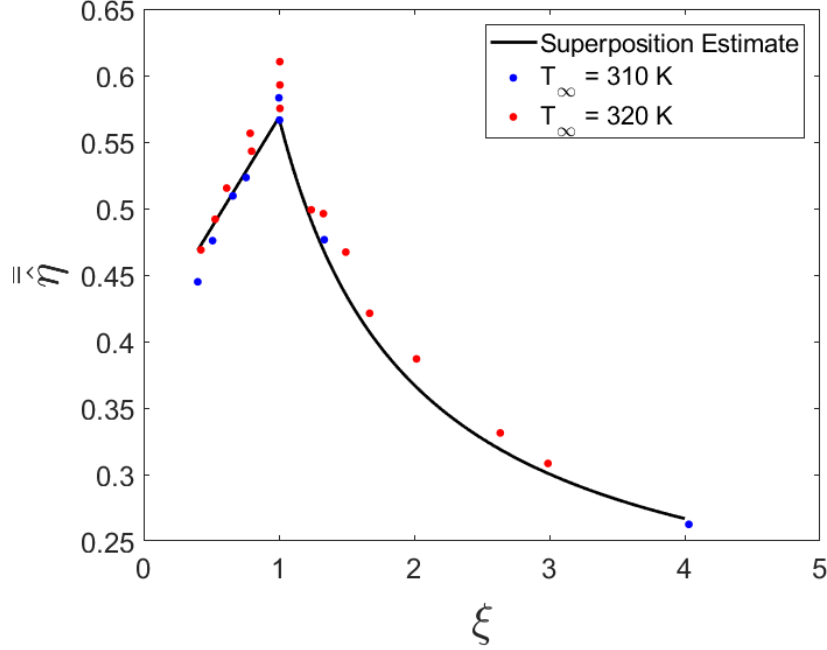
Figure 21. $\bar{\hat{\eta}}$ **vs.** ξ **for measured data and superposition estimates**

However, the variation of $\bar{\hat{\eta}}$ values for the cases of $\xi \approx 1$ deserves additional

analysis; a zoomed-in version of Figure 21 centered on these five cases is shown in

Figure 22 along with error bars corresponding to the uncertainty in η, i.e. ε_η. These are

the verification cases shown above in Figure 11, Figure 12, and Table 1, and the values of

ε_η are drawn from Table 1. For those particular data points, the values of ξ were bounded

by $1.00 < \xi < 1.01$. The greatest and least measured $\bar{\hat{\eta}}$ values differ by 0.044; however,

the uncertainty of measurements made with a large $T_\infty - T_{ref}$ is smaller than that of

measurements with a small $T_\infty - T_{ref}$. The error bars of each sample overlap, although

the samples with highest confidence lie closest to the line of superposition estimates and

therefore imply that the new method of superposition provides a high fidelity $\bar{\hat{\eta}}$ estimate.
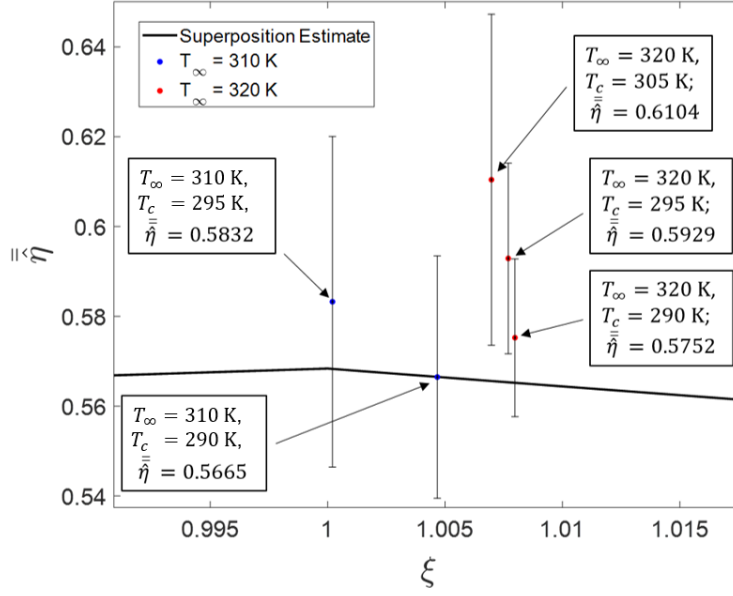
Figure 22. $\bar{\bar{\hat{\eta}}}$ vs. ξ for measured data and superposition estimates near $\xi = 1$

Returning to Figure 21, the cases where $\xi < 1$ offer an interesting insight in that the trend implies that adiabatic effectiveness decreases as ξ decreases below 1.0. This would be the case if, for example, coolant injected from the downstream row had passed through a serpentine internal cooling passage and heated up to a temperature greater than that of the upstream row. The decrease in $\hat{\eta}$ with decreasing ξ occurs simply because warmer coolant issues from the downstream row of holes providing less of a benefit than if that downstream row issued coolant at the same lower temperature as the upstream coolant injection.

More interesting is the observation that if the value of ξ becomes too low, sites within a region of interest downstream of the second row would be better off with *only* the first row issuing, i.e. the second row becomes altogether a detriment. This is demonstrated with a careful review of Figure 23, which depicts the value of $\hat{\eta}$ at a location downstream of a coolant hole in the second row—in this case, the centerline

location at $x/D = 7.0$, $y/D = 0$. Compare the value of η_1, drawn as a horizontal red dashed line, to the values of $\hat{\eta}$ for $\xi < 1$. When $\hat{\eta}$ decreases below η_1, the downstream row actually introduces a *negative* effect. It is important to notice that $\hat{\eta}$ and η_1 are both computed by referencing the quantity $(T_\infty - T_{c1})$ so their comparison is meaningful, although the parameter ξ is meaningless with respect to η_1 because η_1 assumes only the upstream row is issuing coolant. The measured data at the location of interest suggests that $\hat{\eta} = \eta_1$ at $\xi \approx 0.60$, while the superposition curve suggests $\hat{\eta} = \eta_1$ at $\xi \approx 0.50$.
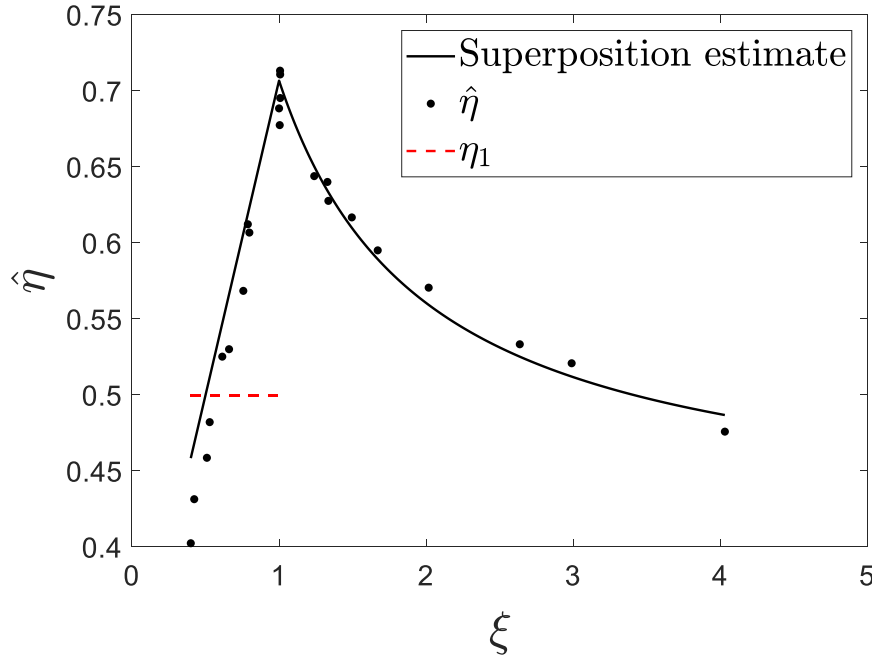
Figure 23. $\widehat{\eta}$ at $x/D = 7.0$, $y/D = 0.0$, baseline ACR values

The very low ξ cases yield distinctive $\hat{\eta}$ contour plots, as shown in Figure 24. To more fully orient the reader to this unusual case, the plot is zoomed out slightly to also show the slot on the first left side and more fully show the gaps between the cooling holes. Regions of low $\hat{\eta}$ are visible immediately downstream of the cooling holes, with

higher $\hat{\eta}$ values in between holes, quite opposite the usual behavior of adiabatic

effectiveness downstream of cooling holes.
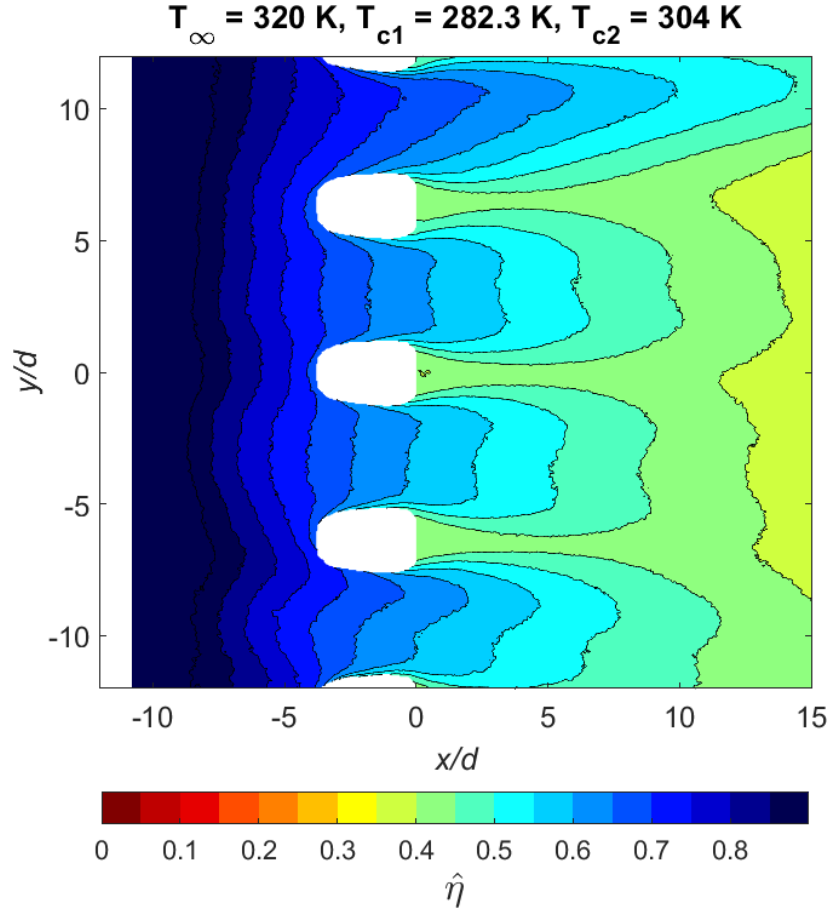
Figure 24. Contours of $\widehat{\eta}$ for $\xi = 0.42$; $ACR_1 = 0.50$, $ACR_2 = 0.75$

To interpret this low ξ behavior in context, at engine conditions with a nominal

value of $T_\infty = 2000$ K, one possible $\xi = 0.60$ equivalency is to have an upstream row

coolant exit temperature of $T_{c1} = 900$ K and a downstream row coolant exit temperature

of $T_{c2} = 1340$ K. This would be quite an extreme situation, and publishable data on the

realistic upper and lower bounds of ξ are not available at this time. However, the point

remains that there could be circumstances under which the second row of coolant holes

may detract from overall cooling performance. That is, even though T_{c2} is less than T_∞, blowing from the second row could have detrimental effects. That situation should be avoided perhaps by routing that warmer coolant through the upstream row, if such an option were available without altering the reason for the coolant temperature difference in the first place. Nevertheless, the value of ξ under which these conditions exist would depend upon the coolant hole configuration and ACR, and also varies spatially on the airfoil surface.

One will notice in Figure 23 that $\hat{\eta}$ also falls below η_1 at large ξ values as well. However, some care should be taken in interpreting Figure 23 with respect to ξ values greater than 1.0. At first glance, the plot implies that there is a ξ value above which the second row of cooling holes detracts from cooling performance; in Figure 23, this is at $\xi \approx 3.5$. However, this would be an erroneous conclusion since η_1 is referenced to the quantity $T_\infty - T_{c1}$, while $\hat{\eta}$ is referenced to $T_\infty - T_{c2}$ for $\xi > 1$; therefore, a direct comparison between the two would not be appropriate. Instead, $\hat{\eta}$ for $\xi > 1$ could be compared to η_2, and it can be found by examining Eq (20) that $\hat{\eta}$ asymptotically approaches η_2 as T_{c1} approaches T_∞. Therefore, any coolant from the upstream row with $T_{c1} < T_\infty$ benefits $\hat{\eta}$ with respect to η_2.

Figure 23 revealed that the measured $\hat{\eta}$ values track the superposition estimates fairly well at $x/D = 7.0$, $y/D = 0.0$, although this had been anticipated after examination of Figure 19 and Figure 20. Even for a complex temperature scenario with an extreme ξ value, the revised superposition method provides a qualitatively representative estimate of the $\hat{\eta}$ distribution, as seen in Figure 25, with local accuracy between $-0.02 < \Delta\hat{\eta} < 0.06$ ($\Delta\hat{\eta}$ contour plot not shown).
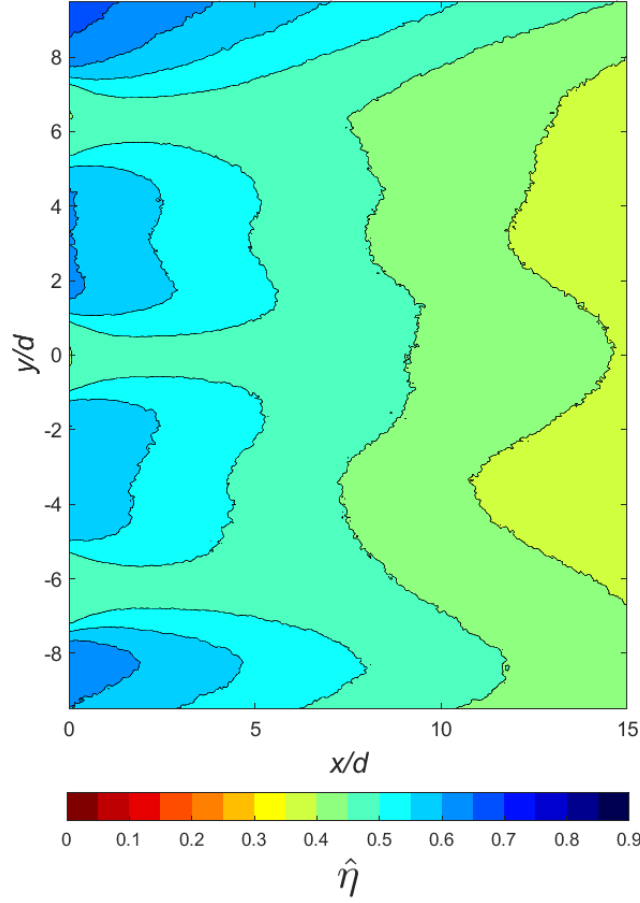
Figure 25. Contours of superposition estimates for $\xi = 0.42$;

$$ACR_1 = 0.50, ACR_2 = 0.75$$

Because superposition holds so well under the present circumstances, it is reasonable to use superposition to estimate—for every location in the region of interest—the *minimum* value of ξ at which the second row would still be expected to bring a benefit; this benefit is present when $\hat{\eta} \geq \eta_1$. Recalling Eq (21), it may be seen that the substitution of $\hat{\eta} = \eta_1$ yields the solution: $\xi = \eta_1$. In other words, such a field of minimum ξ values has already been estimated with the η_1 calculations presented in Figure 13, and one must merely replace η with ξ to arrive at the answer. The interpretation is that any site in the η_1 field

may be vulnerable to degradation if the temperature of the coolant issuing from the second row yields a ξ value less than η_1; whether this is manifested at any site in the region of interest depends of course on the actual locations of downstream holes.

For the present scenario, the minimum η_1 value throughout the region of interest shown in Figure 13 is $\eta_1 = 0.68$ (Figure 13 upper left corner), although the values downstream of the holes are closer to $\eta_1 = 0.66$. Thus, one would expect a second row of cooling holes with $\xi > 0.68$ to improve $\hat{\eta}$ in comparison to η_1. This is precisely what is observed in Figure 17 for $\xi = 0.80$: $\hat{\eta}$ reaches a maximum of $\hat{\eta} = 0.76$ at the exits of the downstream holes and nowhere is $\hat{\eta} < \eta_1$. Contrariwise, one would expect for $\xi < 0.68$ that one would find regions where $\hat{\eta} < \eta_1$ and this is plainly evident in Figure 24. A minimum of $\hat{\eta} = 0.40$ is found at the hole exits, and wide swaths of $\hat{\eta} < 0.45$ are also visible.

This is further corroborated by examining the η_1 distribution in Figure 13 at $x/D = 7.0$, $y/D = 0.0$, it is found that $\eta_1 = 0.500$. This aligns well with the value of ξ at which $\hat{\eta}$ drops below η_1 as seen in Figure 23, which appears to be $\xi \approx 0.50$. This is a strikingly simple method of estimating the effects of coolant issuing at multiple temperatures, assuming one is able to estimate the temperatures of the coolant issuing from each row.

2.2.3.3 Applicability of these findings

These findings are expected to remain valid for a much broader set of film cooling scenarios than were investigated in this study. Recall that the fundamental assumption of superposition, shown in Eq. (10), is that the freestream temperature perceived by the

downstream row is approximately equal to the adiabatic wall temperature when only the upstream row is issuing coolant. This approximation is reasonable in the absence of significant hydrodynamic disturbances such as cooling jet separation or secondary flows resulting from the interaction between successive rows.

The proposed theory relies on the same assumption as conventional superposition and has been experimentally validated for the specific case of two rows. In fact, the conventional superposition theory—in which a single coolant temperature is assumed— could be considered a special case of the more general superposition theory presented in this paper. In essence, if conventional superposition is found to be valid for a cooling scenario, then the multi-temperature extension will also be valid. For example, based on the findings of Saumweber [22], this would include the more familiar geometry of a double-row of fan-shaped cooling holes.

2.2.3.4 Extending the Theory to Multiple Rows

The present theory can also be extended to an unlimited number of rows, each issuing coolant at a different temperature. The original generalization of superposition to n rows comes from Muska [20], in Eq (23), where $\eta_0 = 0$. Superposition estimates are then represented as expressions consisting of several terms that include all product combinations of the rows' η_i values. For example, expanding the expression for $n = 2$ rows results in Eq (12).

$$\eta = \sum_{i=1}^{n} \eta_i \prod_{j=0}^{i-1} (1 - \eta_j) \tag{23}$$

The basic form of the generalized superposition theory with multiple coolant temperatures, given in Eq (24) is similar. However, each term in the expanded expression will have one leading coefficient, ξ_k, for each row k, defined by Eq (25), where T_{ref} is still defined as the coldest of the n coolant temperatures. There are more than n terms in a superposition expression, but only n different coefficient values, and a rules-based approach is necessary to assign coefficient values to the terms in the expression. The rule is actually quite simple: the value of ξ_k for any term corresponds to the furthest upstream row involved in that term. For example, in a triple row superposition expression, one would find the product term $\eta_1\eta_2\eta_3$, which is led by the coefficient corresponding to row 1, i.e. ξ_1. The complete triple row expression is given in Eq (26).

$$\hat{\eta} = \xi_k \sum_{i=1}^{n} \eta_i \prod_{j=0}^{i-1}(1 - \eta_j) \tag{24}$$

$$\xi_k \equiv \frac{T_\infty - T_{c,k}}{T_\infty - T_{ref}} \tag{25}$$

$$\hat{\eta} = \xi_1\eta_1 + \xi_2\eta_2 + \xi_3\eta_3 - \xi_1\eta_1\eta_2 - \xi_1\eta_1\eta_3 - \xi_2\eta_2\eta_3 + \xi_1\eta_1\eta_2\eta_3 \tag{26}$$

With a double row, a single value of ξ as defined in Eqn (20) can be used for a simplified form. It can be verified, for the case in which Row 1 has the colder coolant, that $\xi_1 = 1$ and the expression reduces to Eq (21) (with no subscript on ξ_2). One must exercise care in discerning that in Eq (20), the value of ξ is actually the reciprocal of ξ_1 that would be defined by Eqn (25). For the analysis of more than two rows, it is essential to use the more complete notation with ξ_k coefficients.

2.2.3.5 Conclusions regarding adiabatic effectiveness

The present research adds to the body of knowledge through its development of the analytical tools needed to evaluate adiabatic effectiveness in a region under the influence of multiple rows of coolant at different temperatures. The theory that was developed predicted that the adiabatic effectiveness would be a function of a new nondimensional parameter, ξ, which characterizes the two coolant temperatures relative to the freestream temperature. Additionally, a new superposition technique was devised that would allow prediction of the adiabatic effectiveness under conditions for which $T_{c1} \neq T_{c2}$.

By independently varying the coolant temperatures issuing from a double row cooling configuration, this study experimentally explored the effect of dual-temperature coolant configurations on adiabatic effectiveness. These measurements were made using consistent, baseline *ACR* values for coolant injection, and it was first demonstrated that the experimental setup and data reduction methodology yield results consistent with film cooling literature: that adiabatic effectiveness is independent of the coolant and freestream temperature, provided the various cases do not have temperature differences large enough to have significant variable property effects.

Next, it was demonstrated that the legacy method of superposition can be used to estimate η for this configuration. It should be noted that there were regions identified where the superposition under- or over-estimated local η by up to 0.08, but these variations were largely eliminated through the use of area-averaging. Having confirmed that the necessary condition of applicability of conventional superposition to the film cooling configuration, the new superposition technique was confirmed across a wide

46

range of ξ values, achieved through different combinations of T_{c1}, T_{c2}, and T_∞. The experimental study revealed that revised adiabatic effectiveness as computed for a dual-temperature cooling scenario, $\hat{\eta}$, is indeed a function of ξ, as anticipated from theoretical development. The maximum value of $\hat{\eta}$ occurs at $\xi = 1$ and corresponds to both coolant streams having identical temperatures.

It was further found that adiabatic effectiveness estimates derived from the new superposition methodology described in this dissertation share strong agreement with the experimental data. This was found to be true in terms of site-specific performance within a region of interest and in aggregate by computing $\bar{\bar{\hat{\eta}}}$ as an area-average across the region of interest. The differences in $\hat{\eta}$ between superposition estimates and measured quantities were examined for cases with $\xi > 1$ and $\xi < 1$ and were found to be qualitatively similar to those for $\xi = 1$.

It was discovered that in situations with warmer coolant issuing from the downstream row, it is possible to encounter a circumstance in which the downstream row, in combination with the upstream row, yields poorer adiabatic effectiveness than that of the upstream row alone. It was found that a minimum acceptable ξ can be computed for every site within a region of interest; if the value of ξ for the cooling scenario drops below the minimum acceptable value at any site, then one may expect that adiabatic effectiveness at that site will be worse than for single-row cooling. By applying superposition theory, it was found that the minimum acceptable value of ξ can be closely approximated with the single row measurement of η_1.

Finally, the theory was extended from the double row configuration to an arbitrary number of rows with different coolant temperatures. Because the underlying

assumptions are identical between conventional superposition theory—in which all coolant temperatures are modeled as equal—and this extended theory with different coolant temperatures, it is expected that this theory will be valid for any film cooling scenario in which conventional superposition is found to be valid.

2.3 Overall Effectiveness with Two Local Coolant Temperatures

A logical next step in the investigation of film cooling effectiveness is the evaluation of overall effectiveness. As was observed in the literature review, no research exists describing overall effectiveness in the presence of two local coolant temperatures and hence this is an important step in determining the utility of vortex tubes in film cooling scenarios. Knowledge of the overall effectiveness distribution also has some immediate practical benefits: it can be used to estimate surface temperatures and, implicitly, surface temperature gradients for a given scenario.

2.3.1 *Two-Temperature Analytical Model*

For the case with a single local coolant temperature, such as the double row shown in Figure 26, Eq (13) remains applicable. However, the case with two local coolant temperatures may be depicted as the double row shown in Figure 27. Here, it is not so straightforward to use Eq (13) and it becomes necessary to decide a value for the internal coolant temperature, $T_{c,i}$. The proposed approach is to determine an enthalpy-averaged mean temperature from the two coolant streams, defined in Eq (27), where μ is the relative fraction of coolant enthalpy advected from the upstream row, defined in Eq (28).

For cases in which the temperatures of the coolant streams are not drastically different, μ approximates a mass fraction of coolant injecting from the upstream row. The coolant fraction, μ, bears a relationship to the advective capacity ratio (*ACR*) of the two rows. *ACR*, as proposed by Rutledge and Polanka [17], shown in Eq (29). Fischer et al. [35] showed that by accounting for specific heat differences between the freestream and

49

the coolant, ACR was far superior to blowing ratio and the momentum flux ratio at
scaling adiabatic effectiveness downstream of a 7-7-7 cooling hole.
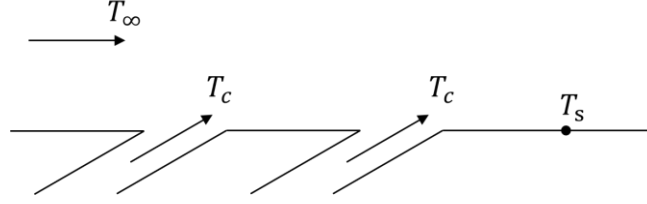
Figure 26. Double row cooling configuration with a single coolant temperature
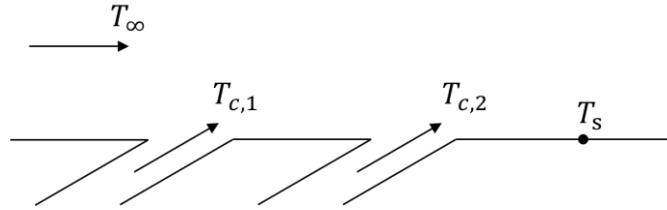
Figure 27. Double row cooling configuration with two coolant temperatures

$$T_{mean} = \mu T_{c,1} + (1 - \mu)T_{c,2} \tag{27}$$

$$\mu \equiv \frac{\dot{m}_{c,1} C_{p,c,1}}{\dot{m}_{c,1} C_{p,c,1} + \dot{m}_{c,2} C_{p,c,2}} \tag{28}$$

$$ACR = \frac{\rho_c C_{p,c} U_c}{\rho_\infty C_{p,\infty} U_\infty} \tag{29}$$

When the mass flow rate of coolant issuing from a row is expressed in the
familiar terms of the one-dimensional continuity equation, that is, Eq (30), it can be
found with some algebraic manipulation that μ may be expressed in terms of the ACR

values of each row and the total cross-sectional areas of the respective rows, as in Eq (31). If the two rows use identical holes, the area ratio is simply the ratio of the number of holes in each row. For a theoretical case with two staggered rows of infinite width and identical holes, $A_{c,2}/A_{c,1} \to 1$ and the coolant fraction reduces to Eq (32).

$$\dot{m}_c = \rho_c A_c U_c \tag{30}$$

$$\mu = \frac{1}{\dfrac{A_{c,2} ACR_2}{A_{c,1} ACR_1} + 1} \tag{31}$$

$$\mu = \frac{1}{\dfrac{ACR_2}{ACR_1} + 1} \tag{32}$$

The representation of coolant fraction in terms of ACR is useful although in practice, of course, such an infinitely extended row of holes cannot exist. However, it can be approximated when $A_{c,2}/A_{c,1} \approx 1$ and it can be shown that edge effects are minimized. The net effect is that mean temperature, T_{mean}, can be computed as a function of the two rows' temperatures and their respective ACRs.

The enthalpy-averaged mean temperature is used in place of $T_{c,i}$ in a revised expression for overall effectiveness, given by Eq (33). There remains some ambiguity though, since T_{mean} is not unique: even while holding ACR constant, infinite combinations of $T_{c,1}$ and $T_{c,2}$ exist for a given T_{mean}. Another parameter must be introduced to measure the relative difference between the two coolant temperatures, since it is hypothesized that the *difference* between the two coolant temperatures is of interest;

it would be desired for a robust model that $\hat{\phi}$ is not dependent on T_{mean} in the same sense

that ϕ should not depend on $T_{c,i}$. The coolant temperature variation parameter, ζ, which

quantifies the dimensionless difference between coolant temperatures, is defined in Eq

(34). The expression for ζ also includes terms representing the difference between the

coolant temperatures and the mean temperature, defined in Eq (35) and Eq (36). Using

the convention in Eq (34), positive values of ζ correspond to the upstream row issuing

the colder coolant and the downstream row issuing the warmer coolant, while negative

values of ζ reflect the opposite.

$$\hat{\phi} = \frac{T_\infty - T_s}{T_\infty - T_{mean}} \tag{33}$$

$$\zeta = \frac{(1 - \mu)\Delta T_{c,2} - \mu \Delta T_{c,1}}{T_\infty - T_{mean}} \tag{34}$$

$$\Delta T_{c,1} = T_{c,1} - T_{mean} \tag{35}$$

$$\Delta T_{c,2} = T_{c,2} - T_{mean} \tag{36}$$

Eq (34) was constructed to weight the temperature differences according to the

same enthalpy weighting parameter, μ, used in determining the mean temperature. While

there remains much work to be done between the film cooling and any eventual

application to vortex tubes, this structure lends itself well to the eventual application of

vortex tubes because μ would be expected to be very similar to a key vortex tube

parameter known as the cold fraction. The second term in the numerator, $\mu \Delta T_{c,1}$, is

subtracted from the first term to ensure that both terms in the numerator contribute to the

overall magnitude of ζ, although the sign of ζ depends on whether colder coolant is being exhausted from the upstream or downstream row. The principal objective of the following experimental work is to determine the extent to which the dual-temperature overall effectiveness, $\hat{\phi}$, is a function of the coolant temperature variation parameter, ζ, for different values of T_{mean}, two values of ACR, and two row spacings.

2.3.2 *Experimental Methodology*

Two new wind tunnel models were constructed to investigate the effect of multiple coolant temperatures on overall effectiveness. Each model consisted of a flat plate of Inconel 718 mounted in a frame of high-density foam (Last-a-Foam™ FR-7120). The Inconel plates were 6.4 mm (0.25 in) thick and each had two rows of laid-back, fan-shaped cooling holes of the 7-7-7 design prescribed by Schroeder and Thole [15] with a metering diameter of $D = 2.1$ mm (1/12 in). Each row of holes was evenly spaced with a pitch of 6 D, with 12 holes in the upstream row and 13 holes in the downstream row. This design was selected to be a close analog to an infinite row, with $A_{c,2}/A_{c,1} = 1.08$ and anticipated minimal edge effects at a region in the lateral middle, the area of interest. As such, Eq (32) was used in this paper to calculate μ since non-unity effects of $A_{c,2}/A_{c,1}$ would be confined outside the region of interest. The plates differed only in the spacing between the two rows; the first model featured a close spacing of 7 D while the second model had more distantly spaced rows at 15 D. The configurations are shown in greater detail in Figure 28 and Figure 29.
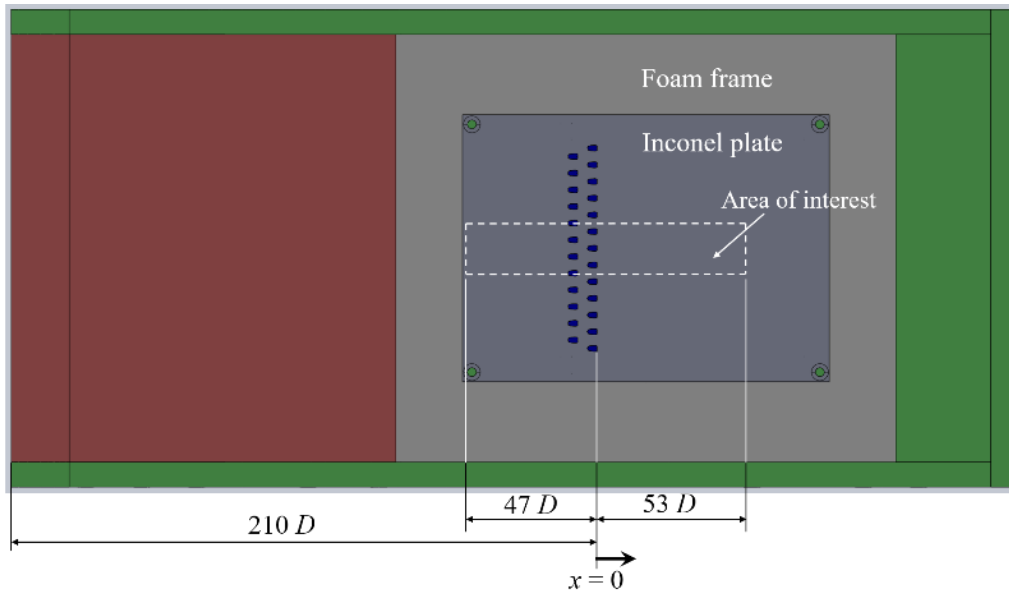
Figure 28. Test rig side view with double row spacing of 7 *D*
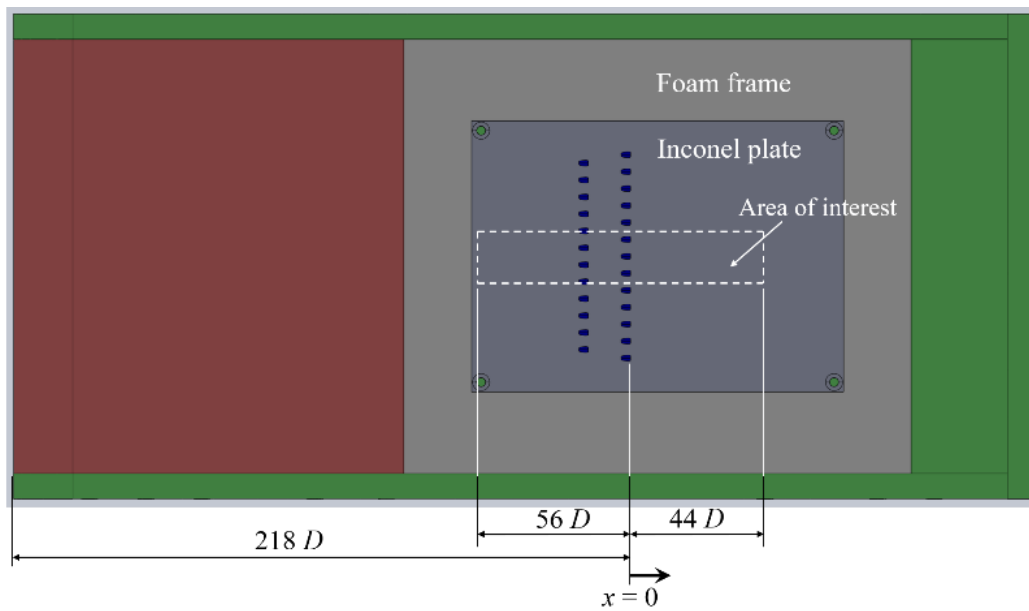
Figure 29. Test rig side view with double row spacing of *15 D*

Two plenums were installed behind the Inconel model to provide backside

cooling and separately feed the two rows of cooling holes at independently controlled

temperatures. This permitted control of the coolant temperature variation parameter, ζ. Each plenum was instrumented with thermocouples to measure the coolant temperature in the internal passages. The plenums were constructed from low-density, low thermal conductivity foam ($k = 0.03$ W/m-K); this foam also formed a sealed thermal barrier between the two plenums. Coolant was supplied to each plenum via a 6.4 mm (0.25 in) diameter copper feeder bar with 1.6 mm (1/16 in) holes. This configuration provided for some impingement in the immediate vicinity of the feeder bar and conventional backside convective cooling everywhere else.

The plenum configurations differ between the two models, as shown in Figure 30. The model with a row spacing of *15 D* features a fairly symmetrical configuration in that the two plenums are identically sized and are positioned approximately in the streamwise middle of the region of interest. The model with a row spacing of 7 *D* features a short upstream plenum and a long downstream plenum, in which the backside coolant flows upstream from the feeder bar before being exhausted through the film cooling holes. The back of the Inconel models apart from the plenums was insulated with low density foam such that the coolant's effect would be largely confined to a region visible to an infrared camera.
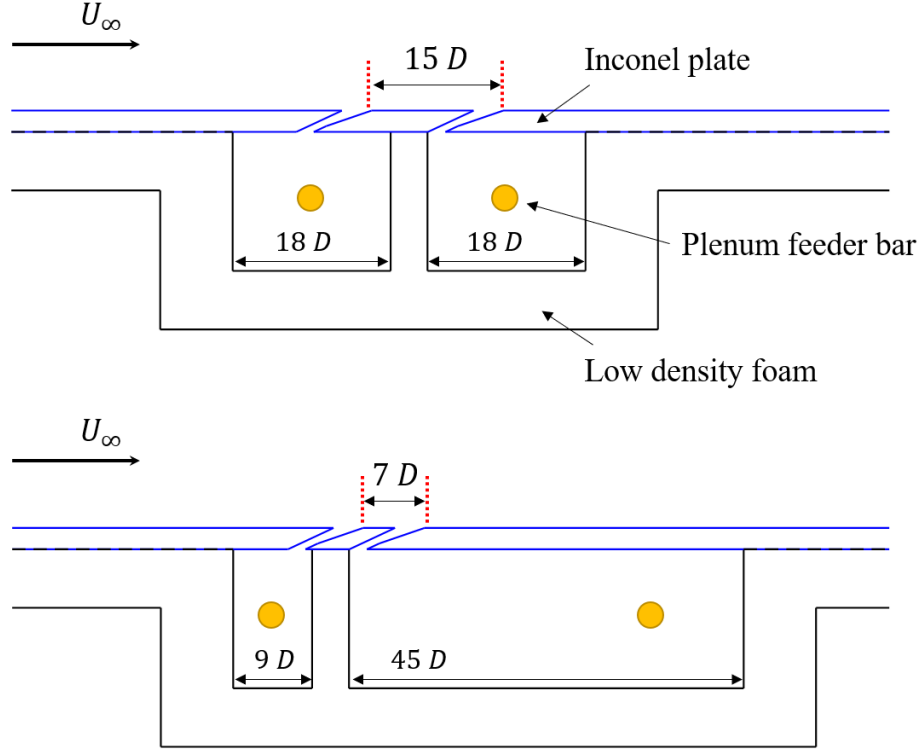
Figure 30. Plenum configurations for models

with row spacing of *15 D* (top), 7 *D* (bottom)

Because the plenums were to be maintained at different temperatures, i.e. $T_{c,1}$ and $T_{c,2}$, some heat transfer across this barrier was unavoidable and expected to be a function of the difference in plenum temperatures. This heat transfer would be expected, in turn, to cause a slight change in temperature, δT, to the coolant in the plenums. It is important to estimate and minimize this effect. Using a one-dimensional heat transfer model based on the resistance analogy and assuming equal heat transfer coefficients on each side of the barrier, the heat transfer between the plenums can be approximated using Eq (37), where L is the thickness of the plenum barrier and A is its cross-sectional area. The change in coolant temperature, δT, attributable to this heat transfer can be estimated using Eq (38).

The change in coolant temperature to either side as a fraction of the difference in coolant temperatures can then be expressed using Eq (39).

$$q = \frac{(T_{c,1} - T_{c,2})}{\frac{L}{kA} + \frac{2}{hA}} \tag{37}$$

$$q = \dot{m}_c C_{p,c} \delta T \tag{38}$$

$$\frac{\delta T}{T_{c,1} - T_{c,2}} = \frac{kA}{\dot{m}_c C_p \left(L + \frac{2k}{h}\right)} \tag{39}$$

The thickness of the barrier, L, in both models was 8.9 mm (0.35 in) and the cross-sectional area, A, was 0.0068 m^2 (10.60 in^2). A worst-case analysis, in which $h \to \infty$ while using an ACR of 1.0 for the upstream row (into a freestream Re_D of 1100), reveals that $\frac{\delta T}{T_{c,1} - T_{c,2}} = 0.05$. For a typical experimental case with $\mu = 0.5$ and $T_\infty - T_{mean} = 30$ K, this contributes an error of approximately 0.001 to the measurements of ζ (which varied between $-0.26 < \zeta < 0.27$ in the present work). This suggests that the practical contribution of heat transfer across the plenum barrier is quite small, and even smaller for cases with an ACR of 2.0.

The Inconel and foam test assemblies were installed in a low-speed, open-loop, temperature-controlled wind tunnel in a manner similar to Fischer et al. [35] and in the afterbody of the 8.89 cm diameter leading edge model of Wiese et al. [36], as seen in Figure 31. The freestream temperature was measured with a thermocouple and the freestream velocity was monitored with a pitot-static system. The freestream Reynolds

number based on cooling hole metering diameter, Re_D, was monitored and controlled to stay within 2% of 1100 with a turbulence intensity of 0.67%.
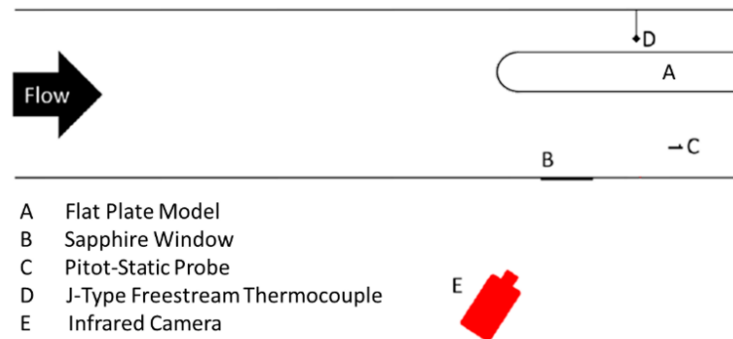
Figure 31. Tunnel test section configuration

An infrared camera was positioned with a line of sight through a viewing window to the Inconel plate. A region of interest with minimal edge effects was selected for this study with a lateral extent of $-9.0 < y/D < 9.0$. The region of interest had a streamwise extent of 100 diameters, with an *x*-origin located at the trailing edge of the downstream row of holes. The position of the downstream row of holes within the area differed slightly between models and hence the x/D coordinates also differed slightly between model; the entire extent was from $-47 < x/D < 53$ or $-56 < x/D < 44$ as seen in Figure 28 and Figure 29.

Due to constraints imposed by the size of the viewing window and focal length of the camera, the entire streamwise extent of the region of interest was not visible in a single image. Instead, measurements were repeated in successive experiments with the camera repositioned to collect overlapping upstream and downstream views, which were brought together in postprocessing to form a composite image. In addition to broadening the net field of view, these successive tests served as checks for day-to-day repeatability.

ACR values of 1.0 and 2.0 were used, and coolant was always injected from both rows at the same *ACR*, which kept a constant value of $\mu = 0.50$. Air was used for the coolant and freestream; the freestream temperature was held at 330K. By varying T_{c1} and T_{c2} between 294 K and 318 K, T_{mean} was varied from 297 K to 316 K. The coolant temperature variation parameter ranged from $-0.26 < \zeta < 0.27$.

Three thermocouples were mounted on the surface of the model directly downstream of the cooling holes at $y/D \approx -18$, a location which permitted variation of surface temperature via the cooling holes but which did not affect the region of interest. Surface temperatures measured with thermocouples were then mapped to infrared counts from the camera to produce a calibration curve for the IR imagery, as shown in Figure 32.
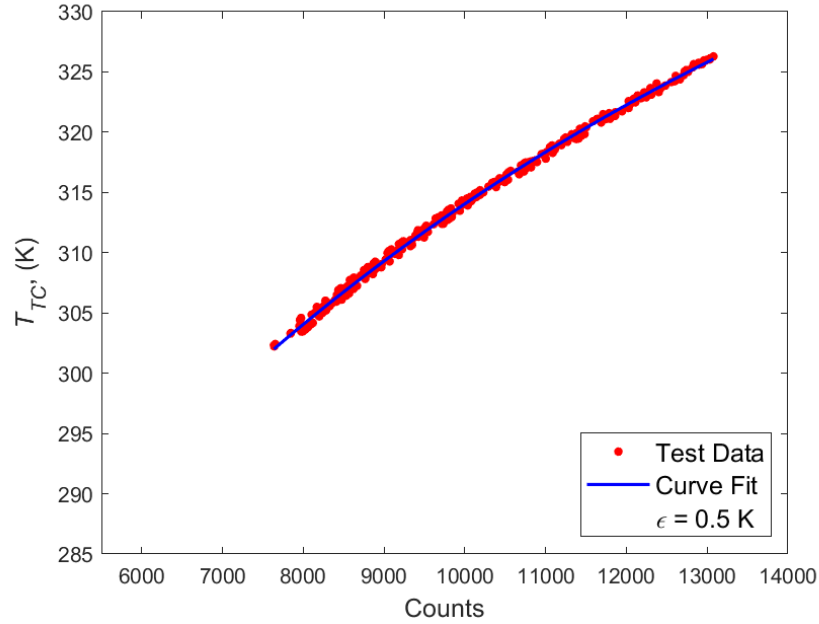
Figure 32. Infrared camera thermal calibration curve

After experimentation, the thermal calibration curve was applied to the IR imagery to estimate surface temperatures across the region of interest. Because all data

59

was taken under similar ambient conditions on successive days with a room temperature of approximately 300 K, and only a single tunnel freestream temperature was used, the same IR calibration curve was applied to all data. Due to time restrictions—taking data for all necessary ζ values for a single ACR and camera angle took approximately 15 hours each day—the thermal calibration curve could not be re-accomplished each day.

Plenum thermocouples and computed ACR values were used to compute μ, T_{mean}, and ζ. Derived surface temperatures, the computed T_{mean}, and the measured freestream temperature were then used with Eq (33) to compute values of $\hat{\phi}$. The accuracy of the thermocouples was 0.5 K, and the uncertainty of the IR measurements was also found to be 0.5 K. The uncertainty of $\hat{\phi}$ within the region of interest, $\varepsilon_{\hat{\phi}}$, was computed using the method of Kline and McClintock [37]. It was found that $\varepsilon_{\hat{\phi}}$ is most strongly a function of the quantity $T_\infty - T_{mean}$ where small values of $T_\infty - T_{mean}$ yield the greatest ε values; these generally occurred for the $ACR = 1.0$ cases when lower mass flow rates yielded higher mean coolant temperatures. The largest value of $\varepsilon_{\hat{\phi}}$ for $ACR = 1.0$ was 0.040 and corresponded to $T_\infty - T_{mean} = 14.5$ K. The largest value of $\varepsilon_{\hat{\phi}}$ for $ACR = 2.0$ was 0.024 and corresponded to $T_\infty - T_{mean} = 24.3$ K.

A significant contributor to repeatability—which cannot be explicitly captured in estimates of uncertainty—is the need for a steady-state condition when taking data. A transient condition may introduce errors in computed $\hat{\phi}$, which are difficult to quantify. For this reason, experimental conditions were permitted to stabilize prior to sampling— typically 25 minutes or more for each test point; steady-state conditions were determined by examining the time history of thermocouples mounted on the test article surface.

Repeatability was confirmed with several experiments performed on different days with $ACR = 2$ and multiple values of ζ. The worst-case repeatability in spatially resolved $\hat{\phi}$ was within 0.025. Additionally, it should be noted that the worst-case repeatability was obtained with an experiment employing a different T_{mean}. While constant property film cooling theory suggests that ϕ (or adiabatic effectiveness, η) is not a function of $T_\infty - T_c$ (or $T_\infty - T_{mean}$), smaller values of $T_\infty - T_c$ tend to cause greater experimental uncertainty.

2.3.3 Results and Discussion

2.3.3.1 Double Row, Double Coolant Temperature Experimental Results

This study begins by examining the model with 15 D row spacing, using the downstream camera view across $-30 < x/D < 44$. Using an ACR of 2.0, $T_\infty = 330$ K, and mean temperatures near 300 K and 305 K, $\hat{\phi}$ was computed for three ζ values: 0.1, 0.0, and -0.1. Conditions for these six cases are summarized in Table 3.

Table 3. Cases evaluating temperature dependence

Case	ζ	T_{mean} (K)	T_{c1} (K)	T_{c2} (K)	μ	ACR
1	0.103	299.7	296.6	302.9	0.497	2.0
2	0.100	304.9	302.4	307.5	0.500	2.0
3	-0.003	300.4	300.5	300.3	0.497	2.0
4	0.000	304.8	304.8	304.8	0.499	2.0
5	-0.102	298.0	301.3	294.8	0.498	2.0
6	-0.103	305.9	308.4	303.4	0.498	2.0

An examination of the results, shown in Figure 33, reveals strong similarities between the $\hat{\phi}$ plots for a given ζ value, irrespective of mean temperature. The comparisons between Cases 1 and 2 as well as Cases 5 and 6 ($\zeta = 0.1$ and $\zeta = -0.1$,

61

respectively) indicate extremely strong agreement: when $\zeta = 0.1$, the two cases agree to within ± 0.005 for virtually the entire frame. For Cases 3 and 4, in which $\zeta = 0.0$, the $\hat{\phi}$ values between the two cases are within ± 0.025 and this represents the contrast with the greatest differences[1]. The strong agreement between results for any given ζ value suggests two encouraging findings: first that $\hat{\phi}$ appears to not be a function of mean temperature; second, that the repeatability of $\hat{\phi}$ as a function of ζ was also reliable.

The invariance of $\hat{\phi}$ with T_{mean} is expected for the same reason that ϕ is invariant with T_c. This is simply a consequence of ϕ being the appropriate nondimensionalization of the surface temperature, T_s, for constant property flow since for such a situation the relation between T_s, T_∞ and T_c is linear. This fundamental independence of cooling effectiveness with selection of T_∞ and T_c is a convenience upon which many an experimentalist has come to rely since accounting for variable property effects present in real engines can generally be accomplished through proper coolant flow rate scaling.

---

[1] The differences between Cases 3 and 4 are not, however, as large as the contours in Figure 33 seem to suggest; rather, the $\hat{\phi}$ values in the region between the two rows of holes are close to the contours. Thus, small differences appear magnified in the plot: Case 3 appears to feature a wide swath between rows where $0.70 < \hat{\phi} < 0.75$, while Case 4 sees only a tiny region of comparable values immediately upstream of the middle hole in the downstream row. To illustrate this point, at the location x/D = -3.4, y/D = 3.0, midway between the upstream breakout of two holes in the downstream row (marked in Figure 33 with a red x), $\hat{\phi} = 0.708$ for Case 3 and $\hat{\phi} = 0.690$ for Case 4—a minor difference. Detailed analysis of the region confirms this trend.
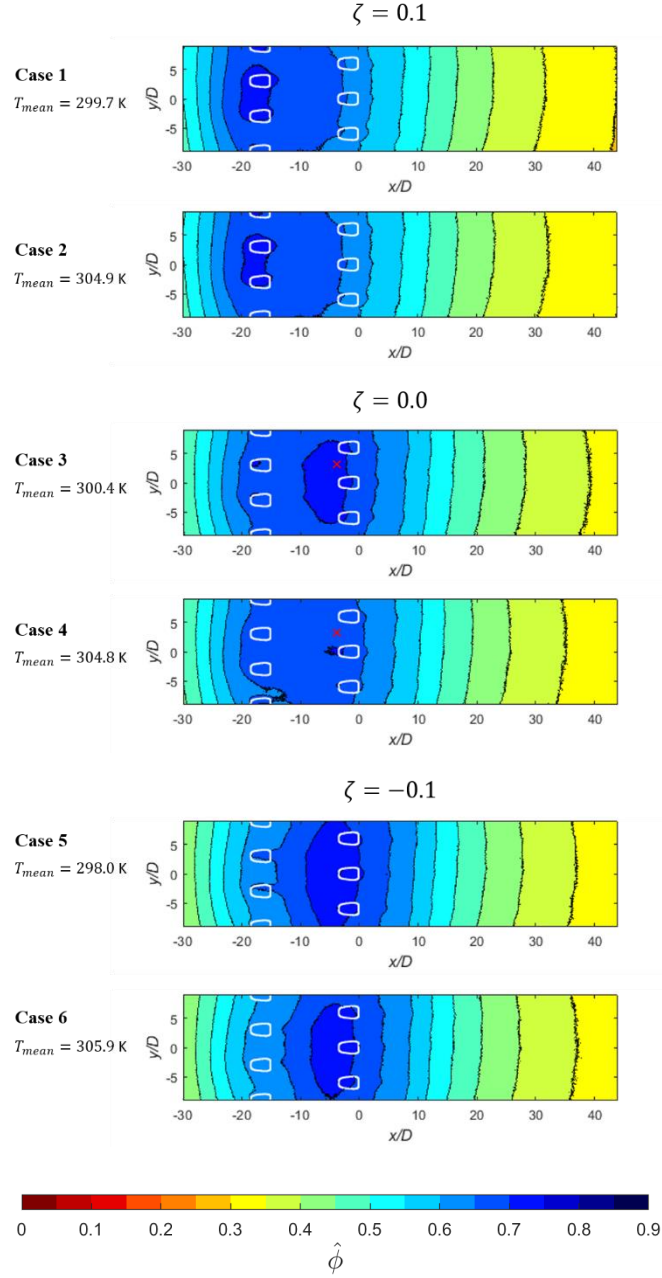
Figure 33. $\hat{\phi}$ for various ζ and T_{mean}, 15 D row spacing

An important deviation from the generally accepted temperature independence of cooling effectiveness becomes apparent when multiple coolant temperatures are present. Indeed, as Figure 33 demonstrates, $\hat{\phi}$ depends upon ζ. Regions of increased cooling

effectiveness are shifted upstream (to the left) with increasing ζ values. This is an expected result, since positive ζ values correspond to colder coolant being exhausted upstream and negative ζ values being exhausted downstream, but it also highlights an important distinction between the $\hat{\phi}$ parameter developed in this dissertation and the conventional parameter, ϕ.

The relationship between $\hat{\phi}$ and ζ has thus far been demonstrated comprehensively with respect to the region of interest, but anecdotally with respect to ζ. While these findings illuminate a fundamental characteristic of the variation of $\hat{\phi}$ as a function of ζ, it would be of great practical interest to better understand the mechanics of this relationship. For this, it is instructive to compile plots of laterally-averaged $\hat{\phi}$, i.e. $\bar{\bar{\hat{\phi}}}$, across the region of interest for an *ACR* of 2.0 and a variety of ζ values. These are plotted for the 15 *D* row spacing model in Figure 34 and for the 7 *D* row spacing model in Figure 35. Both figures include an overlap region from the upstream camera position, which accentuates the high degree of repeatability and dependence of $\hat{\phi}$ on ζ. For further processing, a linear weighting function was applied across an 8 *D* span to smoothly join the data collected from the upstream and downstream viewing; Figure 34 and Figure 35 are plotted without the joining function to highlight repeatability between experiments.
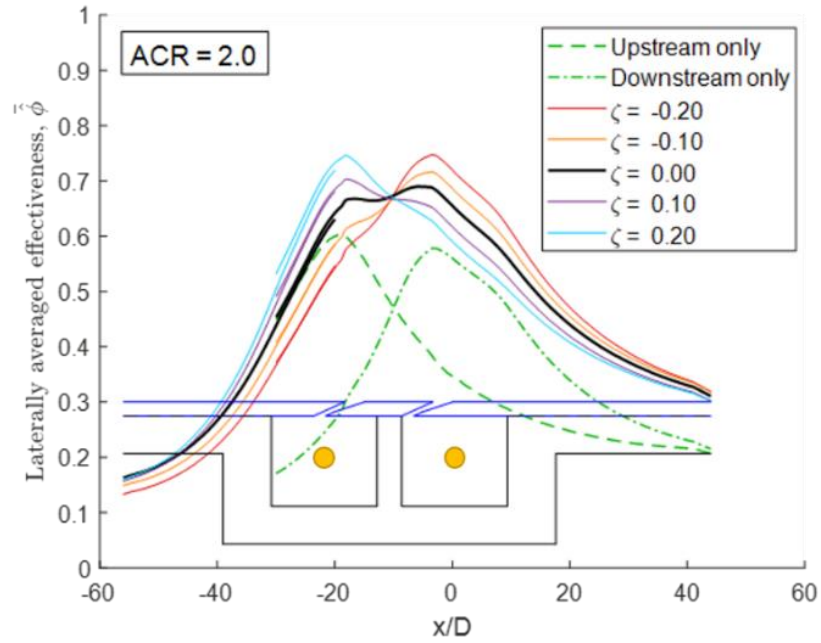
Figure 34. Laterally averaged effectiveness for 15 *D* row spacing (plenum diagram overlaid for reference)
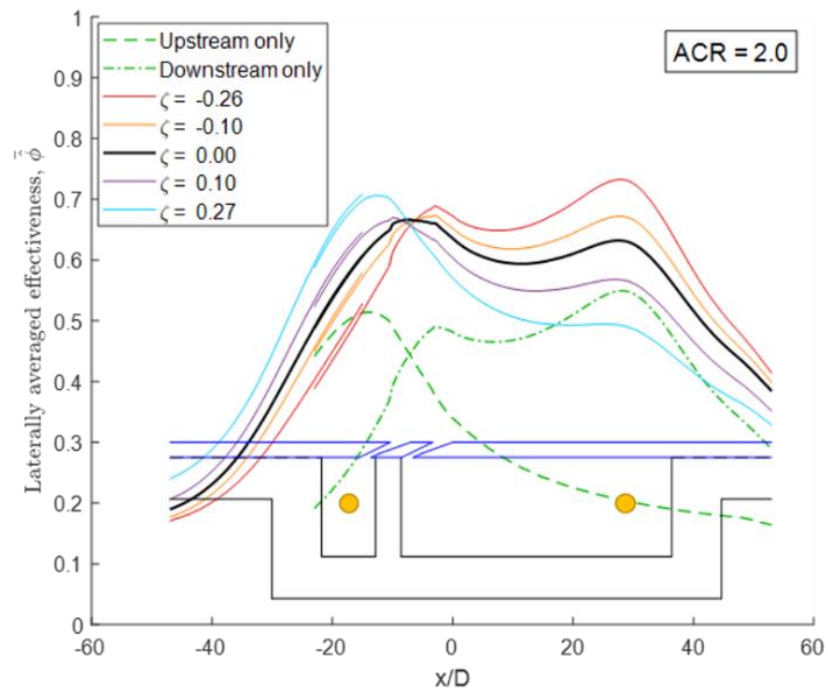
Figure 35. Laterally averaged effectiveness for 7 *D* row spacing (plenum diagram overlaid for reference)

The most salient overall trend is that $\bar{\bar{\phi}}$ increases in regions of decreased coolant temperature; for upstream regions, this corresponds to positive ζ values of increasing magnitude while for downstream regions, this corresponds to negative ζ values of increasing magnitude. For the model with *15 D* row spacing, the greatest $\bar{\bar{\phi}}$ values are in the immediate vicinity of the holes. The model with 7 *D* row spacing sees an additional $\bar{\bar{\phi}}$ increase in the region where the coolant feeder bar supplies the downstream plenum and coolant impinges directly on the internal surface of the model (see Figure 30).

An interesting feature of both plots is the existence of a streamwise location at which $\bar{\bar{\phi}}$ remains constant, regardless of the value of ζ, and that this feature exists for each model despite significant differences between the two configurations. Such a location will be referred to as the pivot point. For the model with *15 D* row spacing, the pivot point is at x/D = -10.2, intuitively positioned above the barrier between plenums. For the model with 7 *D* row spacing, the pivot point is at x/D = -7.0, approximately at the exit of the upstream row of holes.

The location of the pivot point may be deduced without the simultaneous use of both plenums. It can also be seen in Figure 34 and Figure 35 that by evaluating $\bar{\phi}$ with a *single* row issuing coolant at a given *ACR* (and the other row blocked), and then repeating the process with the other row, the location where $\bar{\phi}$ is equal between the two evaluations is actually the pivot point. Significantly, this observation holds for both row spacings examined herein. At this unique *x* location, the thermal state of the model is influenced equally by both the upstream and downstream coolant flows. To the authors' knowledge,

66

the existence of such locations on a film cooled component have never before been documented in the open literature.

Care must be exercised when interpreting Figure 34 and Figure 35. Changing either T_{c1} or T_{c2} alone will influence T_{mean}, and therefore the denominator in Eq (33). For that reason, $\hat{\phi}$ can shift up or down even without a change in T_s. For instance, in Figure 35, $\bar{\bar{\phi}}$ decreases with increasing ζ in the vicinity of $x/D = 20$. While one way to increase ζ is to simply increase T_{c2} (thereby causing an actual increase in surface temperature at $x/D = 20$), another way would be to decrease T_{c1}. That would obviously have the effect of decreasing the surface temperature; however, $\bar{\bar{\phi}}$ would decrease at $x/D = 20$ due to the larger denominator in Eq (33).

2.3.3.2 The Variation of $\hat{\phi}$ with ζ

The variation of $\bar{\bar{\phi}}$ with ζ was evaluated at several streamwise locations on both models for $ACR = 1.0$ and 2.0. The findings suggest that $\bar{\bar{\phi}}$ varies linearly with ζ for both ACR values and models for $-0.26 \leq \zeta \leq 0.27$. A representative portion of this analysis is shown in Figure 36 using the same data set as Figure 34, which covers $-0.20 \leq \zeta \leq 0.20$; the same trend was observed for $-0.26 \leq \zeta \leq 0.27$ for the 7 D row spacing.

This linear variation of $\bar{\bar{\phi}}$ was not confirmed outside the range $-0.26 \leq \zeta \leq 0.27$. Nevertheless, the given range of ζ values is actually quite large: for a scenario involving a freestream temperature of approximately 2000 K, a mean coolant temperature of approximately 1000 K, and a coolant enthalpy weighting of $\mu = 0.50$, it can be seen that $\zeta = 0.20$ corresponds to an upstream coolant temperature of 800 K and a downstream temperature of 1200 K. One can see that the presented range of ζ values is quite wide.

67
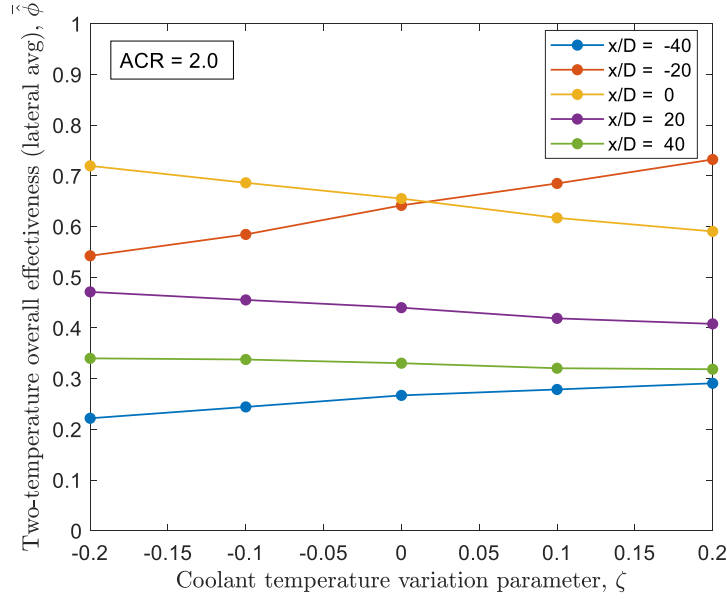
Figure 36. Variation of $\bar{\bar{\phi}}$ with ζ at selected streamwise locations, 15 _D_ row spacing

Adopting the premise that the change in $\bar{\bar{\phi}}$ with respect to ζ is linear across the available range of data, it follows that the partial derivative, $\frac{\partial \bar{\bar{\phi}}}{\partial \zeta}$, can be computed at each streamwise position using a simple linear regression model. The variation of $\frac{\partial \bar{\bar{\phi}}}{\partial \zeta}$ at each x/D location is plotted for the two models in Figure 37. This plot represents functions unique to the respective cooling configurations, indicating the relative sensitivity of each streamwise location to changes in ζ. Notice that $\bar{\bar{\phi}}$ becomes more sensitive to ζ at the higher _ACR_, which would generally be expected to correspond to greater heat transfer coefficients, particularly in the internal passages. This suggests a possible relationship between heat transfer coefficients and sensitivity to ζ.
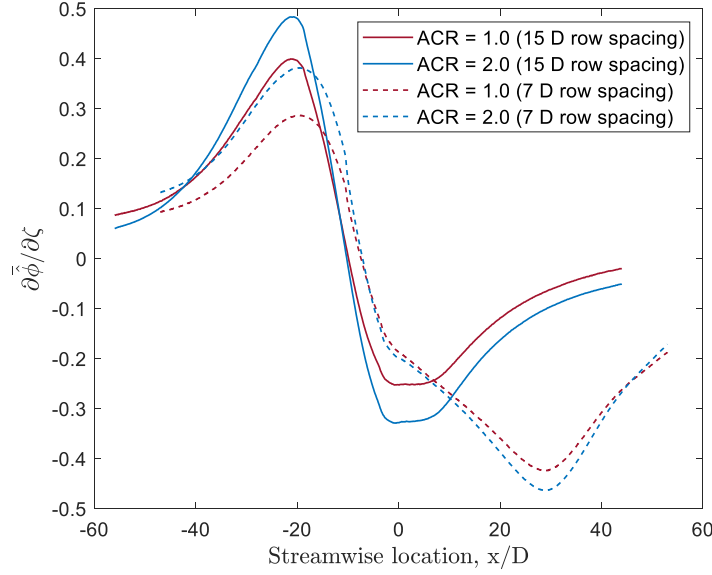
Figure 37. Sensitivity of $\bar{\bar{\hat{\phi}}}$ to ζ with streamwise location, 15 _D_ row spacing

Given a baseline measurement of $\bar{\bar{\phi}}$ when $\zeta = 0$ and the empirical function

$\frac{\partial \bar{\bar{\hat{\phi}}}}{\partial \zeta}(x/D)$, it is possible to estimate the laterally averaged $\hat{\phi}$ for any ζ (within the linear

range) at any _x_/_D_ position using Eq (40). An extension of this model involves using the

partial derivative function derived from the lateral averages, i.e. $\frac{\partial \bar{\bar{\hat{\phi}}}}{\partial \zeta}(x/D)$ to describe

changes in $\hat{\phi}$ at each $(x/D, y/D)$ position within the region of interest. This takes the

mathematical form of Eq (41).

$$\bar{\bar{\hat{\phi}}}(x/D) = \bar{\bar{\phi}}(x/D) + \zeta \left[\frac{\partial \bar{\bar{\hat{\phi}}}}{\partial \zeta}(x/D) \right] \tag{40}$$

$$\hat{\phi}(x/D, y/D) = \phi(x/D, y/D) + \zeta \left[\frac{\partial \bar{\bar{\hat{\phi}}}}{\partial \zeta}(x/D) \right] \tag{41}$$

69

For the model with *15 D* row spacing, the function $\frac{\partial \bar{\bar{\phi}}}{\partial \zeta}(x/D)$ is used to build an

estimate of spatially resolved $\hat{\phi}$ by using ϕ with $\zeta = 0.20$ for $ACR = 2.0$. The estimate is

compared to the experimental results of $\hat{\phi}$ when $\zeta = 0.20$. The results are plotted in

Figure 38, which indicates that the estimate is quite accurate, within ± 0.005 for the

majority of the downstream region and within ± 0.020 in the upstream region. A

conceivable enhancement to the model described by Eq (41) might involve producing a

derivative field function across the entire region of interest, i.e. $\frac{\partial \hat{\phi}}{\partial \zeta}(x/D, y/D)$, by

computing a least squares regression at each $(x/D, y/D)$ position rather than adopting the

simplified $\frac{\partial \bar{\bar{\phi}}}{\partial \zeta}(x/D)$ model. While that may be more appropriate or even essential for

more complex geometries and cooling scenarios, such an approach hardly seems

necessary under the present circumstances.
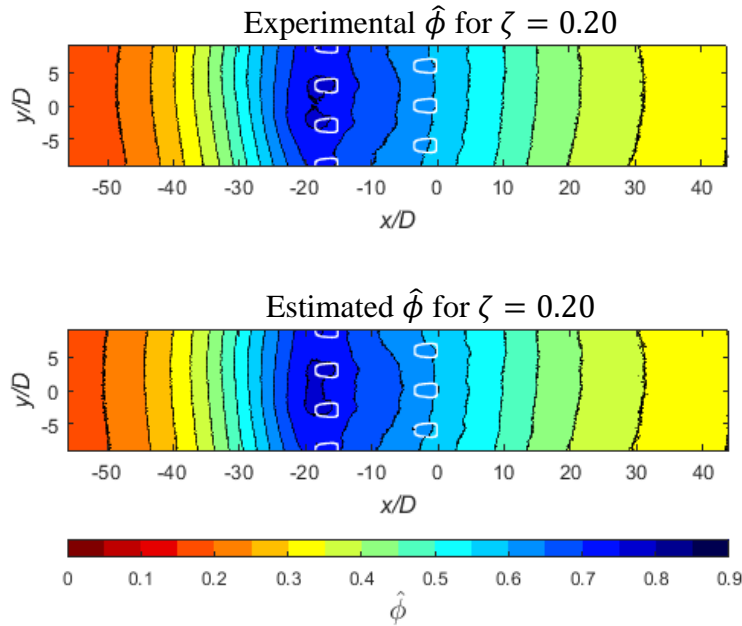
Figure 38. Estimated vs. experimental $\hat{\phi}$ for $\zeta = 0.20, ACR = 2.0, 15 D$ row spacing

That $\frac{\partial \bar{\hat{\phi}}}{\partial \zeta}$ is approximately constant at any (x/D) suggests that the minimum

number of experimental runs required to develop a high-fidelity model—for a given

ACR—is two. Ideally, one of these would be at $\zeta = 0$, but even this is not essential. The

limits of linear variation of $\hat{\phi}$ with ζ are not known, but the present data already suggest a

wide envelope. Despite the variations of local and laterally-averaged $\hat{\phi}$ with ζ, the area-

averaged $\hat{\phi}$ values across the region of interest, i.e. $\bar{\bar{\hat{\phi}}}$, are remarkably insensitive to

changes in ζ. As seen in Figure 39, $\bar{\bar{\hat{\phi}}}$ remains essentially constant across $-0.20 \leq \zeta \leq$

0.20 for the model with *15 D* row spacing. The model with 7 *D* row spacing sees a slight

increase in $\bar{\bar{\hat{\phi}}}$ for decreasing ζ, an effect attributable to its large downstream plenum.
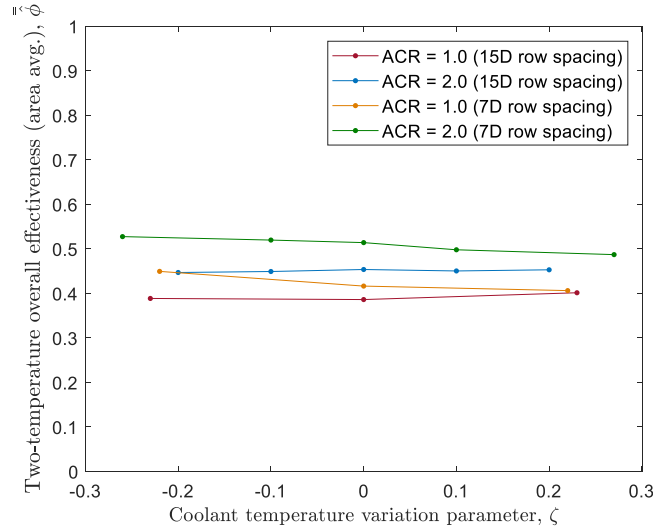
Figure 39. Area averaged $\hat{\phi}$ variation vs. ζ

This observation introduces an intriguing premise: that area-averaged cooling

effectiveness might be increased with non-zero ζ values for some cooling configurations.

Exploiting this potential through optimization could prove rewarding but challenging

since it would require degrees of freedom on both the mechanism of coolant temperature change and the internal geometry—design elements which are often tightly coupled via internal heat transfer characteristics.

2.3.3.3 The Effect of ζ on Temperature Gradients

While the magnitudes of metal temperature on a turbine blade are of considerable concern, spatial temperature gradients also warrant interest because of their contribution to thermal stress. A cursory review of Figure 34 and Figure 35 suggests that ζ modifies the temperature gradients as well, an effect which will be examined more closely.

Scaled, streamwise temperature gradients based on the lateral-mean surface temperature are related to streamwise $\bar{\bar{\phi}}$ gradients by Eq (42). The data shown in Figure 34 and Figure 35 is numerically differentiated and a Savitzky-Golay smoothing filter with a third-order polynomial is applied to reduce numerical noise. Non-physical gradient spikes were also removed: based on the viewing angle, there is a three-dimensional viewing discontinuity between the sharp upstream breakout and the inside of the hole. The resulting scaled temperature gradients, $\frac{d\bar{\bar{\phi}}}{d(x/D)}$, are plotted in Figure 40 for the 15 D row spacing and Figure 41 for 7 D row spacing.

$$\frac{d\bar{T}_s}{d(x/D)} = -\frac{d\bar{\bar{\phi}}}{d(x/D)}(T_\infty - T_{mean}) \tag{42}$$
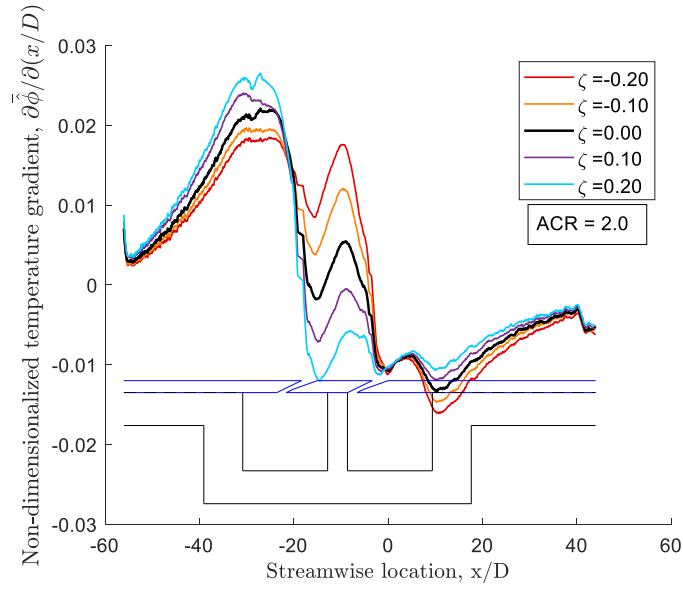
Figure 40. Temperature gradients vs. streamwise location for a range of ζ values, 15 *D* row spacing (plenum diagram overlaid for reference)
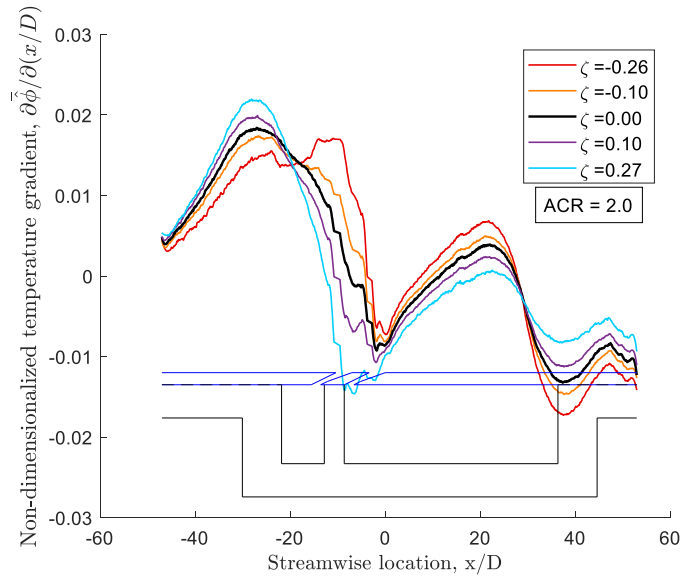
Figure 41. Temperature gradients vs. streamwise location for a range of ζ values, 7 *D* row spacing (plenum diagram overlaid for reference)

The variation of temperature gradients with ζ becomes more apparent in Figure 40 and Figure 41. Some regions where temperature gradients are most sensitive to variations in ζ correspond to regions where gradients are already relatively high, such as those near the boundaries of backside cooling. For those regions, some general trends emerge. For instance, positive ζ values increase temperature gradients in the region upstream of the upstream plenum; for both models, this region is where the greatest temperature gradients are found. Negative ζ values have a similar effect on temperature gradients downstream of the downstream plenum, though the magnitudes are smaller. This suggests, for the regions at the boundaries of backside cooling, that negative ζ values are preferred to positive values—if one has any choice in the matter.

Interestingly, there are also locations where the temperature gradients are approximately invariant with ζ; these correspond to the locations where $\hat{\phi}$ is most sensitive to ζ, as seen in Figure 37. In Figure 40 these can be seen near x/D = -20 and 0, and in Figure 41 these can be seen near x/D = -20 and 29. The apparent increase near x/D = -56 in Figure 40 is an artifact arising from the combined effects of noisy numerical derivatives at the edge of the domain and a limited filtering window.

Although not shown, inspection reveals that the variation of the streamwise temperature gradient, $\frac{d\bar{\bar{\phi}}}{d(x/D)}$, with ζ is also fairly linear. This again permits a linear regression to determine, at every streamwise location, the values of $\frac{\partial^2 \bar{\bar{\phi}}}{\partial(x/D)\partial\zeta}$, i.e. the sensitivity of the streamwise temperature gradient to the value of ζ. The results are seen in Figure 42.
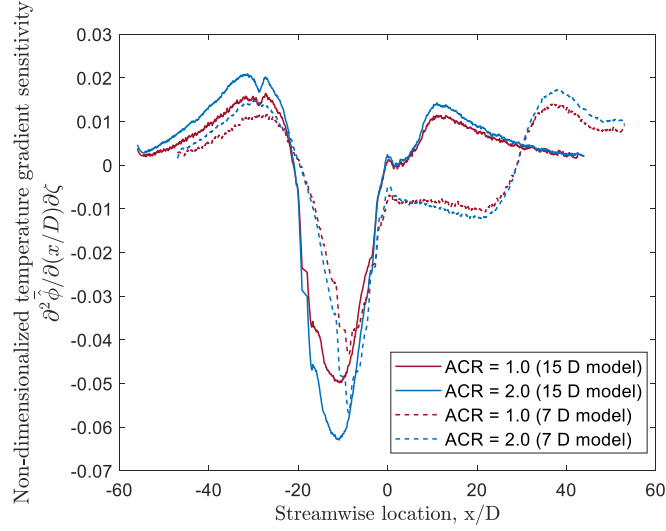
Figure 42. Sensitivity of streamwise temperature gradients to coolant temperature differences, 7 *D* and 15 *D* row spacing

The sensitivity of temperature gradients in the region between the rows is seen quite starkly and it should be noted that the point of greatest sensitivity corresponds to the "pivot point" where $\bar{\bar{\phi}}$ is constant, seen earlier in Figure 34 and Figure 35. The sensitivity of temperature gradients to ζ is generally very similar for *ACR* = 1.0 and 2.0, although a greater *ACR* does increase the sensitivity between the rows. This sensitivity does not differ substantially when the rows are more closely spaced: the 15 *D* row spacing sees a value of $\frac{\partial^2 \bar{\bar{\phi}}}{\partial(x/D)\partial\zeta}$ of -0.063 while the 7 *D* row spacing sees -0.057.

The largest temperature gradients in the region between rows actually occur with negative ζ values, and are nearly identical between the models: for ζ = -0.20, the maximum gradient—which occurs above the plenum wall for the respective models—is 0.0171 for the 7 *D* row spacing and 0.0176 for the 15 *D* row spacing. The values are also comparable between models for ζ = -0.10 and ζ = 0, suggesting that row spacing

75

apparently has little effect for this range of ζ values. For $\zeta > 0$, row spacing has a

pronounced effect: peak gradients increase in magnitude by 51% for $\zeta = 0.1$ and by 23%

for $\zeta = 0.2$. This is perhaps another argument for avoiding $\zeta > 0$, if possible. Minimizing

temperature gradients in the region between rows is, intuitively, best accomplished by

matching the coolant temperatures to achieve $\zeta = 0$. That said, it should be clear that any

ζ value has costs and benefits that apply to these regions of interest; although $\zeta > 0$

causes larger temperature gradients, it also minimizes the surface temperature in a

particular region.

In a manner similar to Eq (40), it is also possible to estimate the temperature

gradient at a particular streamwise location as a function of ζ using Eq (43). Because

$\frac{\partial^2 \bar{\bar{\phi}}}{\partial(x/D)\partial\zeta}$ is approximately constant at any (x/D), only two experiments using different ζ

values will be necessary to produce a model of streamwise temperature gradients.

$$\frac{d\bar{\bar{\phi}}}{d(x/D)} = \frac{d\bar{\phi}}{d(x/D)} + \zeta \left[\frac{\partial^2 \bar{\bar{\phi}}}{\partial(x/D)\partial\zeta}(x/D) \right] \tag{43}$$

Two additional metrics may be useful in characterizing the effect of ζ on

temperature gradients. First, the maximum or greatest magnitude (in the case of negative

values) streamwise temperature gradient within the region of interest; second, the root

mean square (RMS) or standard deviation of the streamwise temperature gradients, which

aggregates non-zero gradients across the region of interest and avoids positive and

negative gradients offsetting each other in a mean value. The maxima may be read

directly from Figure 40 and Figure 41, while the same data is used to compute RMS

76

values; the results are presented in Figure 43. Because the RMS value represents an

aggregate measure of the temperature gradients in a region of interest, it may serve as an

auxiliary metric in combination with measures of local maxima.
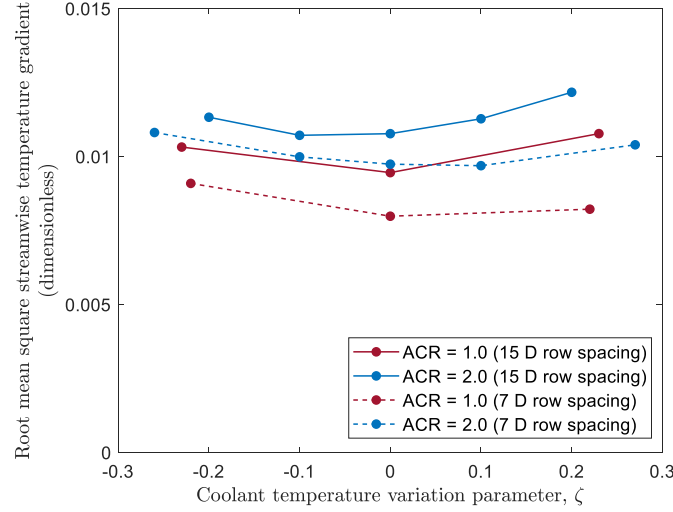
Figure 43. RMS temperature gradients vs. ζ, 7 D and 15 D row spacing

Several interesting similarities and differences emerge in this analysis. For these

geometries, the maximum temperature gradient is more sensitive to positive values of ζ

than to negative values, but across a range of $-0.1 \leq \zeta \leq 0.1$, the maximum temperature

gradient can vary by approximately ±10% for $ACR = 2.0$. It is intuitive that the

temperature gradient RMS increases as the difference between the two temperatures

increases, i.e. for large ζ values, but it is not as sensitive to ζ as is the maximum gradient.

It is somewhat surprising that the minimum RMS value is effectively constant across

$0 \leq \zeta \leq 0.1$ for the 7 D model and $-0.1 \leq \zeta \leq 0$ for the 15 D model.

This highlights an unexpected finding: that non-zero ζ may, under certain

circumstances, present an advantage with respect to temperature gradients. Consider, for

the 15 D row spacing example with $ACR = 2.0$, how the $\zeta = -0.1$ case offers an 11%

reduction in peak temperature gradient and no effective change in RMS, while having no effect on area-averaged $\hat{\phi}$. This, of course, must be balanced against cooling requirements based on surface temperatures in the region of interest since a value of $\zeta = -0.1$ reduces $\hat{\phi}$ upstream of the pivot point. Nevertheless, this would suggest the possibility of permitting warmer coolant to issue from the upstream row without deleterious effects, if such an option is desired.

2.3.3.4 Modeling complex scenarios

This methodology could also be applied to more complex configurations, though some adjustments would need to be made. Significantly, if it is desired to evaluate a model with significant spanwise variations, a more general version of Eq (41) will be needed. Eq (41) considered the overall effectiveness at any streamwise location to be essentially homogenous and therefore well-represented by a spanwise average. Close examination of the experimental values in Figure 38 reveals that this is approximately true, but not exactly, as evidenced by the contours of $\hat{\phi}$ that are curved in the spanwise direction. (As an aside, the configuration of cooling holes and plenum feeder bars was designed to achieve laterally uniform cooling performance, though this was obviously not entirely achieved. The exact reasons for this are not known, but potentially include unintended lateral variations in coolant issuing from the holes drilled in the plenum feeder bar.) However, for a broader spanwise region of interest, prominent edge effects, or configurations such as the mixed use of slots and cooling holes, it may not be reasonable to assume a homogenous spanwise $\bar{\bar{\phi}}$, and instead to let $\hat{\phi}$ at each location be modeled separately with its own linear model. This would involve producing a derivative

78

field function across the entire region of interest, i.e. $\frac{\partial \hat{\phi}}{\partial \zeta}(x/D, y/D)$, by computing a least

squares regression at each $(x/D, y/D)$ position. Thus, for more complex scenarios, Eq

(44) is likely more applicable.

$$\hat{\phi}(x/D, y/D) = \phi(x/D, y/D) + \zeta \left[\frac{\partial \hat{\phi}}{\partial \zeta}(x/D, y/D) \right] \qquad (44)$$

Although no data are currently available for a scenario where $\mu \neq 0.50$, consider

the following. First, assuming the rows have identical cross-sectional areas, Eq (32) may

be used to compute μ for any combination of ACRs. Publishable data are not available on

the range of μ values in actual turbine engines, but the range is finite: even with

dissimilar ACRs of 0.50 and 2.00, μ is still bounded by 0.20 and 0.80, assuming equal

row areas. In the event that the areas are not equal, such as unequal hole diameters, Eq

(31) may be used. Although changes to μ would directly modify the values of T_{mean} and

ζ, the author sees no reason why that would alter the more fundamental relationships

identified, such as the linear nature of $\frac{\partial \hat{\phi}}{\partial \zeta}$ and $\frac{\partial^2 \hat{\phi}}{\partial(x/D)\partial \zeta}$, especially since it has been

determined that $\hat{\phi}$ is independent of T_{mean}.

2.3.3.5   Conclusion regarding overall effectiveness

The present research expands our understanding of turbine cooling scenarios

wherein different temperature coolants issue from different plenums. The analysis

requires the turbine blade surface temperature to be nondimensionalized using a new

reference temperature based on the mean coolant enthalpy of the two rows. The new

theory developed here hypothesized that overall effectiveness in the presence of two

79

coolant temperatures would be a function of ζ, a new parameter characterizing the difference between the coolant temperatures.

The new theory was tested at a variety of reference temperatures and across a wide range of ζ values using two experimental configurations. Each contained two coolant plenums at independently controllable temperatures set behind a flat plate of Inconel 718, with different plenum sizes and row spacings. The experiments confirmed that overall effectiveness is not dependent on the reference temperature but is indeed a function of the coolant temperature variation parameter, ζ. Because overall effectiveness conveniently captures the combined effects of internal and external cooling as well as conduction, with no underlying assumptions regarding hydrodynamic behavior, and because the material used in these experiments has been shown to scale well to engine conditions, the trends observed in this study are expected to remain valid at engine conditions.

Several significant trends emerged with the use of two coolant temperatures. Notably, a location between the two rows was observed at which the overall effectiveness, $\hat{\phi}$, remains constant with ζ; the existence of this location was seen on the two different models, but its placement varied with cooling configuration. Away from this point, it was found that overall effectiveness varies linearly across a wide range of ζ values, permitting the estimation of $\hat{\phi}$ at any location in the region of interest with minimal required experimentation.

Although area-averaged $\hat{\phi}$ values were found to be insensitive to dual-temperature cooling scenarios, streamwise temperature gradients were found to be heavily influenced by ζ. This is most apparent in the region between the rows, where the

80

sensitivity of temperature gradient to ζ is greatest—reaching a maximum at the same location where $\hat{\bar{\phi}}$ remains constant. Similar to the variation of $\hat{\bar{\phi}}$ with ζ, the streamwise temperature gradient, $\frac{d\hat{\bar{\phi}}}{d(x/D)}$, was also found to vary linearly with ζ—permitting the estimation of temperature gradients at various locations with minimal experimental data.

Compared to the baseline ($\zeta = 0$) case, it was found that $\zeta = \pm 0.1$ can increase or decrease peak temperature gradients by approximately 10%. Interestingly, non-zero ζ values may present advantages in terms of *reducing* the maximum temperature gradient in a region of interest as well as the root mean square of the temperature gradient. Regardless of whether this phenomenon can be deliberately exploited, the turbine designer should be aware of the influence that differing local coolant temperatures hold with respect to overall effectiveness, temperature gradients, and—ultimately—blade life.

2.4 Conclusion of Film Cooling Investigations

The two studies presented here—on adiabatic effectiveness in the presence of multiple local coolant temperatures and on overall effectiveness with two local coolant temperatures—have introduced new methodologies for predicting surface temperatures and adiabatic wall temperatures that may be used to evaluate the contribution that a vortex tube has on film cooling performance. For a given film cooling configuration, it may be possible to predict a distribution of adiabatic wall temperatures and actual surface temperatures, the latter of which is directly connected to the blade life.

This page is intentionally left blank

3 Research Objective 2: Characterize the phenomenon of temperature separation as observed in a vortex tube.

Research Objective 2 was accomplished using experimental, analytical, and computational methods, and culminates in a viable theory of vortex tube operation—both in terms of the underlying physics and the manner in which the performance can be scaled. This contributes to Research Objectives 3 and 4, investigate temperature separation under conditions more representative of an engine and how vortex tubes might be best applied to film cooling purposes, respectively.

3.1 Literature Review: Vortex Tubes

3.1.1 Invention and Initial Research

The vortex tube was invented by French engineer Georges Ranque, who gained a French patent in 1933 [38] and a US patent in 1934 [39]. The device languished in obscurity for several years before Hilsch adopted the design for laboratory use and wrote an article describing his experiments [40] [41]; upon its translation into English in 1947, the publication fomented international interest and triggered a flurry of research. Patents for improved designs were awarded in the following decades, such as those to Fulton [42] [43], which served as close forerunners to modern implementations. Vortex tube efficiency is low compared to conventional refrigeration methods. This limitation was recognized immediately by Hilsch [41] and Fulton computed its efficiency as a refrigerator at approximately 1% [44], so its use has been limited primarily to small-scale industrial applications where compressed gas is readily available. Applications include spot cooling in machine shops, cabinet cooling, personal air conditioning, and gas separation.

The most common configuration is the counterflow vortex tube, which uses a central orifice on the cold side and an annular exit on the hot side, as seen in Figure 44. An alternate configuration is the uniflow vortex tube, in which the hot annular exit and cold central orifice are concentric and located on the same side of the tube, opposite the inlets. Although the uniflow configuration is frequently described in the literature and often assumed in theoretical analyses, it is seldom used in actual research and does not appear to be sold commercially.
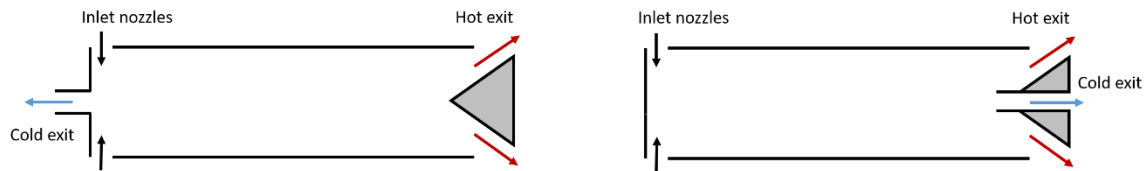
Figure 44. Counterflow vortex tube (left); uniflow vortex tube (right)

Temperature separation is typically manipulated in a counterflow vortex tube by adjusting the inlet pressure and the "cold fraction", μ_c, which is defined as the fraction of the incoming mass flow rate that exits out the cold side; the cold fraction is typically set using a valve on the hot exit, such as the brass piece on the right side of Figure 45. Increasing the inlet pressure corresponds to an increasing degree of temperature separation. Temperature separation varies considerably with cold fraction and although the exact results vary between vortex tubes, the maximum cold side temperature drop is usually achieved with a cold fraction of $0.2 \leq \mu_c \leq 0.5$.

Figure 45. Commercial vortex tube, Exair^{TM} 3208

Figure 46, from Stephan et al. [45], depicts a typical performance diagram for a counterflow vortex tube. The curves indicate changes in total temperature compared to the inlet; the hot and cold exits are shown above and below the horizontal axis, respectively. The horizontal axis indicates cold fraction. Several curves of temperature separation can be seen, which correspond to inlet gauge pressures. Temperature separation can thus be seen as a strong function of cold fraction and inlet pressure, where increased inlet pressures correspond to greater temperature separation for all cold fractions. The maximum temperature drop measured on the cold side occurs at $\mu_C \approx 0.3$; the greatest observed temperature change is approximately -37 K with an inlet pressure of 5.0 bar gauge. Notice that the hot and cold temperature extremes occur at different cold fractions and therefore do not occur simultaneously. The maximum hot exit temperature increase observed occurs at a cold fraction of approximately 0.9, and is nearly 80 K with an inlet pressure of 5.0 bar gauge.
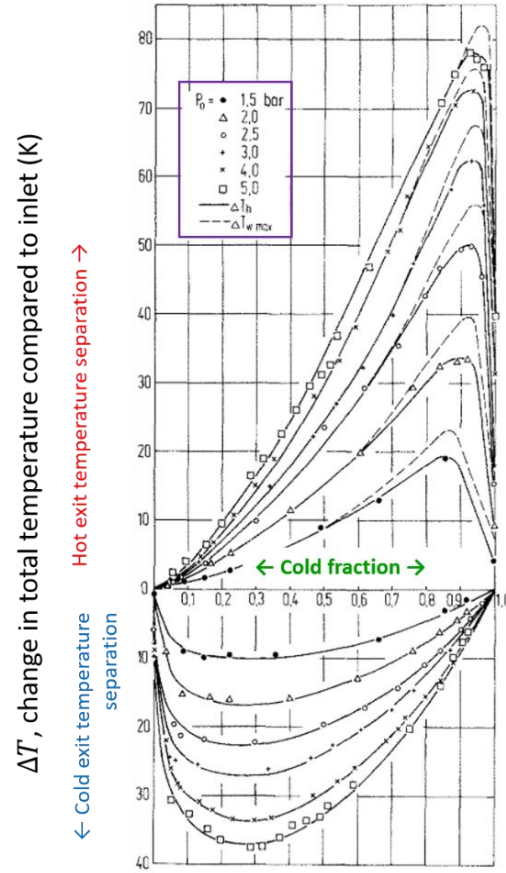
Figure 46. Typical performance curves of a counterflow vortex tube [45]

There remains to this day no consensus on an exact explanation of the mechanism by which the vortex tube achieves temperature separation, but to appreciate the wide array of theories of its operation, it is instructive to understand the progression of early research. Initial experiments, such as those by Hilsch [41], Fulton [44], Schultz-Grunow [46], and Elser [47], were dedicated to system-level performance, such as the influence of inlet pressure, cold fraction, and geometric proportions on temperature separation. Thus the first theories emerged without the benefit of internal flow field measurements; instead they depended primarily on thermodynamic hypotheses, conjecture regarding the flow field, and an influential theoretical paper by Kassner and Knoernschild [48].

86

The original explanation by Hilsch [41] attributes temperature separation to the simultaneous expansion of gas and transfer of kinetic energy between layers in the vortex. Fulton [44] elaborated on this somewhat, assuming the velocity profile proposed by Kassner and Knoernschild [48]. According to Fulton, the explanation is as follows. As gas enters the vortex tube via the nozzles, the gas in the core expands and its static temperature is reduced. The gas in the periphery does not significantly expand and maintains a higher static temperature. Meanwhile, based on the velocity profile conjectured by Kassner and Knoernschild and assumed by Fulton, the flow of gas causes a nearly free vortex (i.e. in which angular momentum in conserved) to form wherein the core flow has a high velocity and the periphery has a lower velocity. The core, by viscous action, transfers kinetic energy to the periphery so that it accelerates and the fluid behaves increasingly like a forced vortex—i.e. solid-body-like rotation with uniform angular velocity. Simultaneously, the warmer periphery transfers heat to the cooler core; however, the rate at which the core performs work on the periphery is greater than the rate at which the periphery transfers heat to the core. The net effect, according to the explanation, is that the core has transferred energy to the periphery and thus has a lower total temperature. As will be seen, however, there are some inconsistencies between this hypothesis and subsequent experimental findings—particularly with respect to the assumed development of the velocity profile.

3.1.2   Internal Flow Examinations

A number of researchers, starting in the early 1950s, began to investigate the inner workings of vortex tubes and measured the velocity, pressure, and temperature distributions. For counterflow vortex tubes of conventional design, the findings of

Scheper [49], Scheller [50], Takahama [51], and Bruun [52] agree that the flow field is dominated by a forced vortex; the lower-resolution data of Martynovskii and Alekseev [53] is also in broad accord. Lay [54] used a uniflow configuration but did not extract a cold fraction and similarly Hartnett and Eckert [55] used a counterflow vortex tube but closed the cold side so it was functionally a uniflow vortex tube; both researchers found a forced vortex. The uniflow experiments were not fully equivalent to the other experiments but are still of a limited analytical utility, as will be seen later.

Figure 47 shows the tangential velocity profile of Hartnett and Eckert [55] and Figure 48 shows the velocity profile of Scheller [50]; both evince compound vortex behavior. The data of Hartnett and Eckert depict the tangential velocity with black dots (the white dots will become relevant later in the analysis) as a function of radius at an axial location 20% of the tube length, i.e. relatively close to the nozzles. Their findings indicate forced vortex behavior extending to 60% of the tube radius (0.9 in), a peak velocity at approximate 80% of the radius (1.2 in), and a rapid decrease in velocity close to the walls.
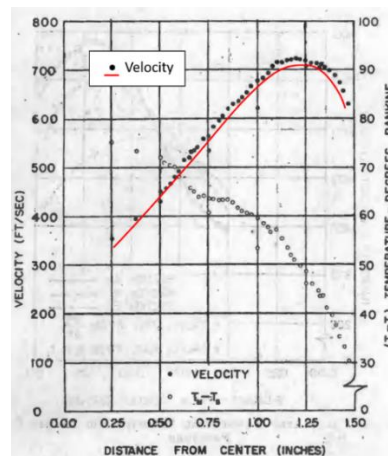
Figure 47. Tangential velocity profile of Hartnett and Eckert (black dots) [55]
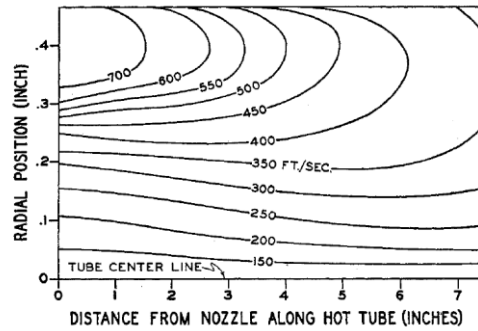
Figure 48. Tangential velocity profile of Scheller [50]

The data of Scheller [50] is presented as contours of velocity with radial position on the vertical axis and axial position on the horizontal axis. The profile suggests a forced vortex at all axial locations, though its peak velocity appears to decrease with distance from the nozzles. The velocity decreases toward the tube wall, but is not shown with sufficient resolution to clearly indicate the no-slip condition.

In aggregate, the experimental evidence indicates that the velocity profile inside the tube is that of a forced vortex for its entire length; there is no clear evidence of a free vortex nor a conversion into a forced vortex. The departure from a forced vortex toward the wall simply appears to be a consequence of the gas approaching a no-slip condition. In essence, this demonstrates that the velocity profile hypothesized by Kassner and Knoernschild [48] was not strictly accurate.

This is significant because the assumed direction of the heat transfer in Fulton's explanation—from periphery to core—was based on the higher-velocity fluid being in the core and corresponding to lower static temperatures. However, based on the velocity distributions observed through experiment, one would easily conclude that the opposite must be the case: with higher velocities in the periphery and lower velocities in the core,

89

that the static temperature profile must lend itself to heat transfer from the core to the periphery. As will be seen, the temperature distribution also became the subject of experimental investigation. Nevertheless, these types of inconsistencies within the theories have proven to be quite persistent and have generally contributed to the diversity of thought surrounding vortex tubes; for example, the direction of heat transfer remained a source debate for over two decades following the study by Kassner and Knoernschild [48].

Hartnett and Eckert also found that subtle changes to exit geometries can have pronounced effects: by modifying the hot exit nozzle in a vortex tube, the hot exit temperature and pressure profiles were shown to exhibit significant variation [55]. They concluded that these changes to exit geometry likely modified the entire internal flow field, but complete data were not taken.

There is a demonstrable explanation for the fundamental qualitative error regarding the assumed velocity distribution and progression by early theorists, such as Kassner and Knoernschild [48]. The influence of exit geometry on other confined vortex flows can be profound. The cyclone separator, which uses a vortex to separate particulates from a fluid, had also been a widely studied system at the time and was possibly an inspiration for Ranque's original invention [44]. Velocity distributions in cyclone separators, such as those observed by Smith [56], are typically dominated by free vortices with a narrow forced vortex at the core due to viscous effects. This trend may explain the original assumption that flow in a vortex tube begins as free vortex.

A demonstration by Chiné [57] reveals the importance of the exit configuration to the flow pattern. Chiné configured two hydrocyclones—both with tangential inlets—with

two different exit geometries. One cyclone featured a central exit orifice on the axis, which is typical of a conventional cyclone separator, while the other had an annular exit, which is typical of the hot exit in a counterflow vortex tube. Although Chiné's working fluid was water, the effect on the velocity distributions was nevertheless quite clear. The velocity profile in the cyclone with the exit orifice was dominated by a free vortex (with a narrow forced vortex at the core), while the cyclone with the annular exit was dominated by a forced vortex extending nearly to the wall.

The vortex tube flow patterns of Reynolds [58] are considerably different than the others and because they are sometimes cited in the literature, they deserve a careful review. Reynolds experimented with a variety of hot and cold exit geometries, no combination of which corresponds to the conventional counterflow design (nor to the uniflow). These included, for example, configurations with orifice exits at both hot and cold ends, an orifice exit at the cold end and a completely open hot exit, and an orifice exit at the cold end and an arrangement of small holes in a plate at the hot end. The configuration of greatest interest to the present study is that with the orifice exits at both hot and cold sides. This unconventional design has a very simple geometry; it could prove useful if it yields appreciable temperature differences. Unfortunately, several factors render Reynolds' results effectively unusable.

Reynolds found—for the case of twin orifice exits—a flow pattern reminiscent of a strong free vortex, although there were some apparent measurement issues near the core. For the case of the open hot exit, he found a flow pattern more consistent with a forced vortex; this finding is expected, given the exit geometry. Although Reynolds did measure radial variation of total temperature at a selection of axial stations for a subset of

91

cases, he did not measure total temperature at the exits for any cases, so the net temperature separation resulting from these internal distributions is poorly quantified. Moreover, no attempt was made to measure or control the cold fraction in the experiments. Most significantly, Reynolds acknowledged that several cases—including that of greatest practical interest to the present study—featured the reverse flow of ambient air back into the vortex tubes, making an energy balance between hot exit, cold exit, and inlet streams extremely difficult. Ultimately, it seems that Reynolds' most significant contribution was illustrating the diversity of flow patterns and internal temperature and pressure distributions that result from unconventional configurations [58].

Researchers also measured internal static and total temperature distributions. At axial stations relatively close to the inlets, most data indicate higher static temperatures in the core of the vortex than in the mid-periphery, with an increase again toward the wall. Scheper [49] found this trend, as did Takahama [51], Scheller [50], and Lay [54]. Figure 49 presents the experimentally measured static and total temperature distributions of Scheper at three axial locations, labeled (1), (2), and (3), at approximately 5%, 10%, and 15% of the tube length, respectively. The profiles closest to the inlet indicate locations of elevated static temperature near the core and the wall—which correspond to the regions of lower tangential velocity identified in the velocity studies. Two regions in particular, circled in red, represent regions where the static temperature gradient with respect to radial position lends itself to heat transfer from the inner layers to the outer layers.
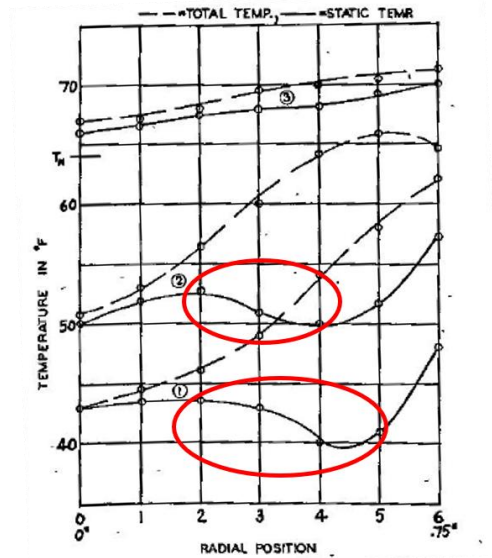
Figure 49. Static temperature distribution adapted from Scheper [49], circles indicate regions where temperature distribution may drive heat transfer

Hartnett and Eckert also measured the temperature distribution, but plotted it as the "temperature depression", i.e. the difference between inlet static temperature and local static temperature [55]. These are the white dots seen in Figure 47 at 20% of the axial length of the tube; they suggest that the static temperature is higher near the wall and decrease away from it. Unlike the other researchers, they did not observe another static increase toward the core; however, their data did not go all the way to the axis.

All researchers found that the radial static temperature gradients became much smaller at axial locations further from the inlets. Total temperature was universally found to be at a minimum at the axis and increased significantly toward the wall; this trend was true at all axial locations. The apparent disagreement between the static temperature measurements of Hartnett and Eckert [55] and those of other researchers does not appear to have been explicitly addressed, and explanations of vortex tubes proposed by

93

subsequent researchers depended greatly on which experimental data were studied. Lastly, static and total pressures were found by all researchers to be at a minimum at the core.

These experimental findings invigorated new theories. Scheper's [49] discovery of higher static temperatures near the core precipitated a theory of heat transfer from the core to the periphery. However, Scheper's theory was presented essentially as an analogy to a counterflow heat exchanger; his fluids model was rough and the underlying analysis made use of correlations for heat transfer coefficients and effectiveness parameters and was not well-received [59]. Other researchers were also espousing heat transfer theories: Scheller [50] posited an unsubstantiated theory of "forced convection", Schultz-Grunow [46] theorized "forced convection in a stratified flow".

Simultaneously, new theoretical efforts were applied to unravel the mystery of the vortex tube. These authors included Rott [60], who wrestled with developing a theoretical static temperature distribution in a compressible, turbulent, viscous core. Van Deemter [61] matured the analysis of energy transfer in a turbulent vortex. He recognized that energy transfer between the cold and hot streams could be attributed only to heat transfer and viscous stresses. The viscous stresses apply only insofar as the velocity profile departs from a forced vortex. Regarding heat transfer, he identified two components. The first was caused by conduction due to a primarily radial temperature gradient within the flow and, like others, van Deemter assumed that the static temperature in the core was lower than at the periphery. The second heat transfer component is unique to a compressible, turbulent flow and suggests that a pressure gradient normal to the direction of flow can also contribute to heat transfer.

94

The principle—according to van Deemter [61]—is that an eddy at a particular static temperature may be buffeted to a region of slightly higher pressure and be slightly compressed. Assuming isentropic compression of the eddy, if that new, compressed temperature is greater than that of the surrounding fluid then heat will be transferred from the compressed eddy as it approaches thermal equilibrium with the surroundings; the reverse would apply to eddies expanded in regions with slightly lower pressure. In this manner, turbulent heat transfer is intensified in the presence of a pressure gradient if the initial static temperature distribution does not adiabatically correspond to the static pressure distribution. Hartnett and Eckert endorsed the pressure-conduction principle [55]; Bruun was also persuaded by this and although he declared that "turbulent heat transport" was the cause of temperature separation, he attributed this primarily to the compression and expansion of eddies [52].

Deissler and Perlmutter [62] agreed with the role of pressure-conduction, extended van Deemter's analysis, and performed limited comparison with experimental work. The temperature distributions in their theoretical analysis qualitatively matched the results of Hartnett and Eckert [55] for static temperature, which they speculated was lower in the core (in contrast to other contemporary experimental findings). In turn, they concluded that the static temperature gradient causes heat transfer from the periphery to the core, while assuming that the static pressure gradient causes heat transfer from the core to the periphery (insofar as the pressure-conduction term is of practical significance). They then asserted that although the two heat transfer mechanisms are each potentially quite large, they act opposite each other and effectively cancel each other out. They ultimately concluded that temperature separation must be primarily attributable to

the viscous stresses between the cold core and the hot periphery, which they described as "shear work" [62].

However, it should be reiterated that other experimental data (i.e. Scheper [49], Takahama [51], Scheller [50], and Lay [54]) indicated that the static temperature distribution was higher in the core, suggesting that heat would be transferred from the core to the periphery, at least at axial stations close to the inlets. In this way, the temperature-gradient and pressure conduction terms would instead be additive in transferring heat from the core to the periphery, rather than canceling each other out. That said, it does not appear that the contribution by the pressure conduction term has ever been mathematically nor experimentally quantified, so its equivalency to any form of energy transfer cannot be concretely established.

Other issues also limit the analysis of Deissler and Perlmutter [62] from broader generalization. First, their treatment did not account for axial variation of flow properties such as pressure, temperature, and velocity; this variation was identified by other researchers such as Sibulkin [63] and Bruun [52] as being so significant that it is essential to a robust analysis. This is especially true since, as Sibulkin [63] observed, "widely divergent theories have given performance curves which agree with Hilsch's measurements".

3.1.3   Internal Flow Boundaries

A second limitation of Deissler and Perlmutter [62] speaks to another challenge of vortex tube analysis: defining the interface between the portion of the inlet flow that will exit via the hot side and that which will exit via the cold side. The earliest speculations regarding the internal flow pattern, such as Fulton's [44] in Figure 50, implied that an

96

internal cold flow would be bounded approximately by a paraboloid, wherein the cold

flow reaches a maximum axial location and then turns around.
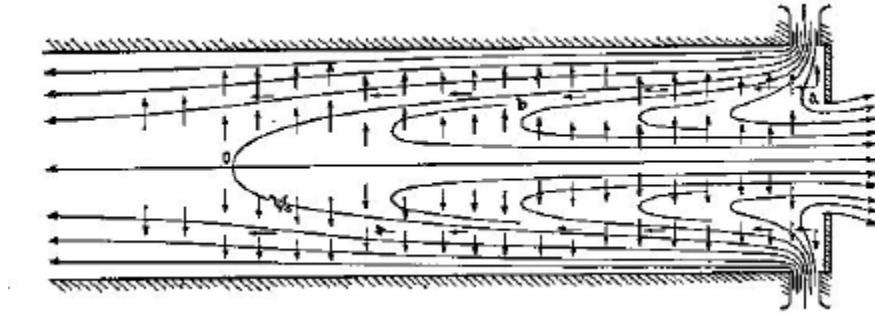
Figure 50. Hypothesized flow pattern from Fulton [44]

Scheper [49] also incorporated in his heat transfer theory the general premise that

a defined interface exists between hot and cold flows inside the vortex tube, though the

interface was characterized as an "imaginary tube", i.e. a cylinder. Deissler and

Perlmutter [62] used a two-layer model which implied a uniflow vortex tube wherein the

hot and cold flows were modeled as concentric cylinders. Some modern researchers such

as Dutta et al. [64] and Xue et al. [65] still imply a paraboloid interface in a counterflow

vortex tube. Computational results vary and several researchers, such as Behera [66],

have concluded that the cold flow extends to the hot exit as shown in Figure 51, though it

does not actually flow out of the hot exit.
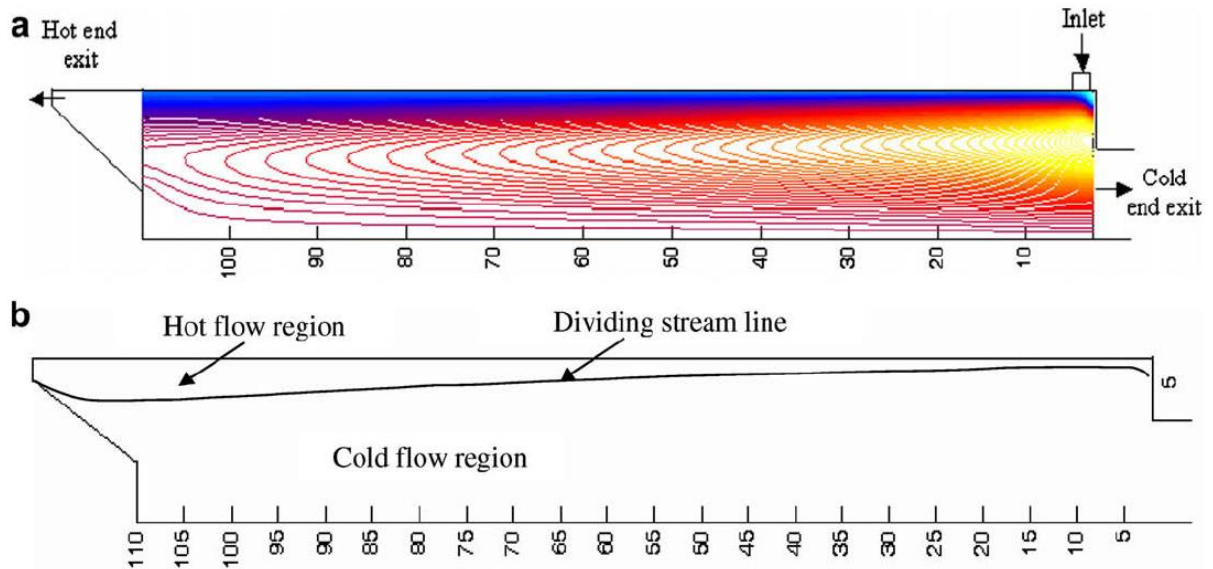
Figure 51. Vortex tube internal streamlines (top);

Hot and cold flows with streamline-derived interface (bottom) [66]

It is surprising that although the community had more or less coalesced on various theories involving transfer of kinetic energy by viscous action, heat transfer, and adiabatic compression and expansion, there had been very little work done on accurately defining the boundaries between the flows and computing the energy transfer across that boundary. Presumably, if this interface were fully defined, then energy transfers across it could be quantified, leading to an overall internal energy balance. Although the general distributions of temperature, pressure, and tangential velocity had been measured, those could only be fully leveraged to solve the problem if the temperature, pressure, and velocity gradients could be determined *at the interface*.

If the interface between hot and cold flows is indeed approximated by a paraboloid, one would expect to find exclusively positive axial flow (in the direction of the hot end) past the maximum cold flow axial station. Unfortunately, the available

experimental data is of very limited resolution, and only two researchers took data that might be used for this purpose—and even that data is incomplete. Takahama's [51] results, taken at $\mu_C = 0.50$, appear consistent with a paraboloid interface, although measurements were only taken to approximately 10% of the length of the tube and thus do not entirely confirm it. To be clear, the analysis of the flow and how it might relate to a notional interface is this author's: Takahama did not draw any conclusions in the original paper regarding an interface. Because of their uniflow configurations, the data of Hartnett and Eckert [55] as well as Lay [54] are not applicable. The only other available and otherwise relevant dataset is that of Bruun [52], taken at $\mu_C = 0.23$. Bruun's velocity profile implies stagnation on the central axis between approximately $30 - 50\%$ of the tube length. However, there also appears to be an area of reverse flow in the mid-periphery, traveling in the opposite direction of the fast-moving air headed toward the hot exit. Thus, the bounds of the hot and cold flows were poorly defined from an experimental perspective.

The matter of the interface was further complicated by experimental measurements made by Ahlborn and Groves [67] in 1997, who *claimed* to have identified a "secondary flow" in the vortex tube. This secondary flow was manifested as a reverse axial flow, i.e. back toward the cold side, of fluid that would otherwise exit the hot side and instead caused some recirculation. Although Bruun had previously found similar flow features for a low cold fraction, Ahlborn and Groves were surprised to find this for $\mu_C = 0$. In fact, this was not an entirely new finding: Hartnett and Eckert found a similar reverse axial flow for $\mu_C = 0$ [55]. In any event, the alleged existence of this flow was hypothesized to be generalizable to all cold fractions and somehow contributing to the

99

temperature separation. However, it must be emphasized that this speculation has not been borne out and the secondary flow does not appear to be as generalizable as Ahlborn and Groves believed. Unfortunately, this added yet another theory and created some confusion in the manner in which an internal energy balance might be accomplished.

3.1.4 Computational Investigations

Computational fluid dynamics (CFD) has also been applied to the understanding of vortex tubes. Perhaps the earliest attempt was by Sibulkin [63] in 1962 who, for a uniflow configuration, approximated the axial progression of temperature separation using numerical techniques with a reduced, nondimensionalized form of the energy equation. Sibulkin's results were qualitatively similar to the experimental results of Lay [54], and Sibulkin concluded that the roles of gas expansion and heat conduction were most significant, while the role of viscous stress was not.

In a more modern sense, the first application of CFD to vortex tubes appears to be Fröhlingsdorf in 1998 [68], who attributed most of the temperature separation to viscous shear and found that the turbulent Prandtl number had a pronounced effect. With some manipulation, he was able to produce a tangential velocity profile that agreed with Bruun's experiments [52]. Early CFD studies focused on proving the emerging techniques by matching experimental data and examining which modeling choices, such as the turbulence model, were best-suited to vortex tube predictions. Skye et al. worked on matching macroscopic performance to experiments [69]. Behera et al. investigated whether they could find Ahlborn's secondary flow with CFD and found that it only existed for very small cold fractions [70]; Oliver et al. also found secondary flow [71], though it was close to the inlets and not in the region originally suggested by Ahlborn.

Eiamsa-ard and Promvonge [72] varied turbulence models and upwinding

schemes in an effort to match the experimental results of Hartnett and Eckert [55] and

found that the algebraic stress model (ASM) outperformed the standard k-ε turbulence

model. Interestingly, their total temperature distribution closely matched the experimental

data, although the CFD *static* temperature distribution disagreed qualitatively with the

experimental data of Hartnett and Eckert [55], but agreed qualitatively with the *other*

experimental findings, such as Lay [54], indicating that static temperature is higher in the

core than in the mid-periphery. Thakare matched the experimental results of Hartnett and

Eckert in terms of tangential and axial velocity profiles and observed the same trend of

static temperature being higher in the core near the inlets [73].

Dutta et al. [74] also investigated turbulence models and found that the standard

k-ε turbulence model closely matched macroscopic experimental performance, although

internal flow distributions were not examined. Farouk pioneered the use of large eddy

simulation (LES) to model vortex tube performance [75] and seemed to find evidence of

secondary flows. However, the hot exit featured a radial exit, which is different from

other experiments, and the resulting flowfield is comparatively messy with considerable

microvortices and the extent to which the simulation is representative of an actual flow

remains unclear. No plots of static temperature were shown. Secchiaroli et al. [76]

modeled a vortex tube using a Reynolds Stress Model (RSM) and LES but did not

validate its performance against experimental results.

The first attempt to compute energy transfer across the boundary between hot and cold

flows was conducted by Aljuwayhel et al. [77] using a two-dimensional, axisymmetric

model with standard and renormalization group (RNG) k-ε turbulence models. The

interface derived from the standard k-ε model with a cold fraction of $\mu_C = 0.3$ is presented in Figure 52. The flow pattern, at least near the inlets, does not correspond well to that of Bruun or Takahama and includes a large recirculation region inside the cold flow. It is unclear whether this is an artifact of CFD or a consequence of their unconventional inlet geometry, which was used for simulation purposes. The researchers claimed to predict macro-level temperature separation within 14% of their own experimental data using a slightly different configuration with similar dimensions.
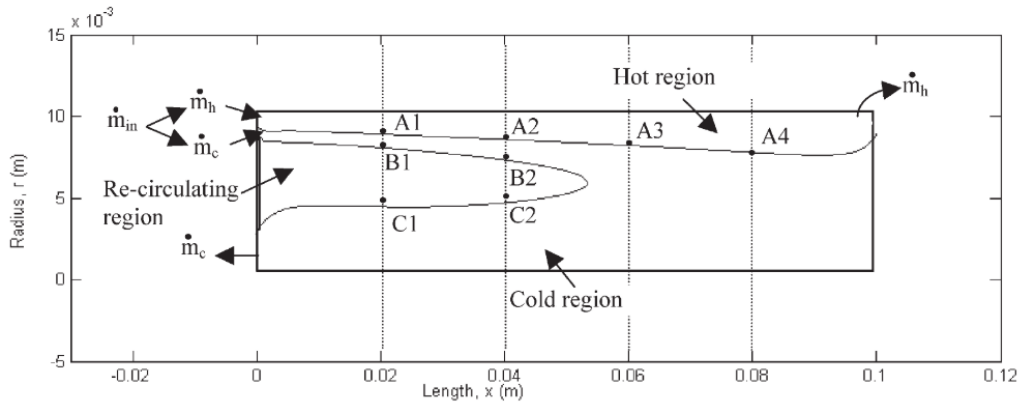
Figure 52. Vortex tube hot/cold interface from CFD ($\mu_C = 0.3$) [77]

The study by Aljuwayhel et al. [77] estimated the viscous work and heat transfer components of the energy transfer between the flows, shown in Figure 53. The viscous work included both tangential and axial components, though they concluded that the tangential component contributed positively to temperature separation while the axial component contributed negatively. The findings also suggested a large heat transfer component as well, though they concluded that the net contribution of heat transfer to temperature separation was actually negative.
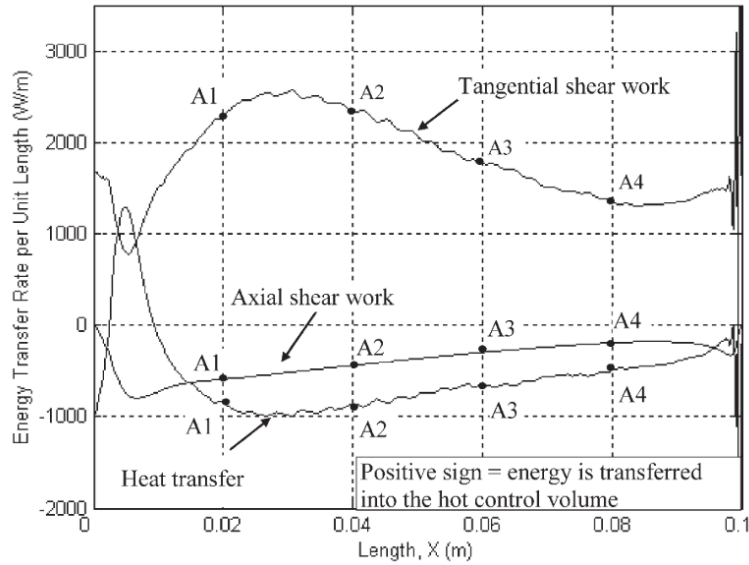
Figure 53. Vortex tube energy transfer components from CFD ($\mu_c = 0.3$) [77]

Behera et al. [66] conducted a subsequent computational investigation similar to that of Aljuwayhel et al. [77], but differed in that the study by Behera et al. [66] was three-dimensional with an axisymmetric flow profile enforced by modeling a 1/6 circumferential wedge—enough to represent a single nozzle—rather than modeling the entirety of the vortex tube in a single mesh. Like Aljuwayhel et al. [77], Behera et al. [66] modeled air as an ideal gas, but Behera et al. [66] only employed the RNG k-ε turbulence model. The two studies examined different cold fraction ranges: Aljuwayhel et al. [77] investigated $0.1 \le \mu_c \le 0.3$ but Behera et al. [66] investigated $0.65 \le \mu_c \le 0.85$. While both studies purported to be experimentally validated, in each case the validation was incomplete with respect to cold fraction and some qualitative differences were observed between the CFD flow profiles and those of experimental investigations.

The energy transfer components estimated by Behera et al. [66] are shown in Figure 54. By comparing the estimated energy transfer components of Behera et al. [66]

103

in Figure 54 with those of Aljuwayhel et al. [77] in Figure 53, it is clear that the contributions of the components with respect to axial position differ considerably between the studies. However, it should be noted that the two sets of curves result from different vortex tube geometries and cold fractions and the former resulted from a standard k-ε turbulence model while the latter is from a RNG k-ε turbulence model. Nevertheless, the findings are qualitatively similar between the two studies, with both research teams concluding that the tangential viscous work drives heat transfer, while the axial work component acts in the opposite direction of the tangential component and therefore decreases temperature separation. Significantly, heat transfer was thought to be of a significant magnitude—around 30% of the tangential work, and larger in magnitude than the axial work component—and also served to *decrease* the temperature separation.
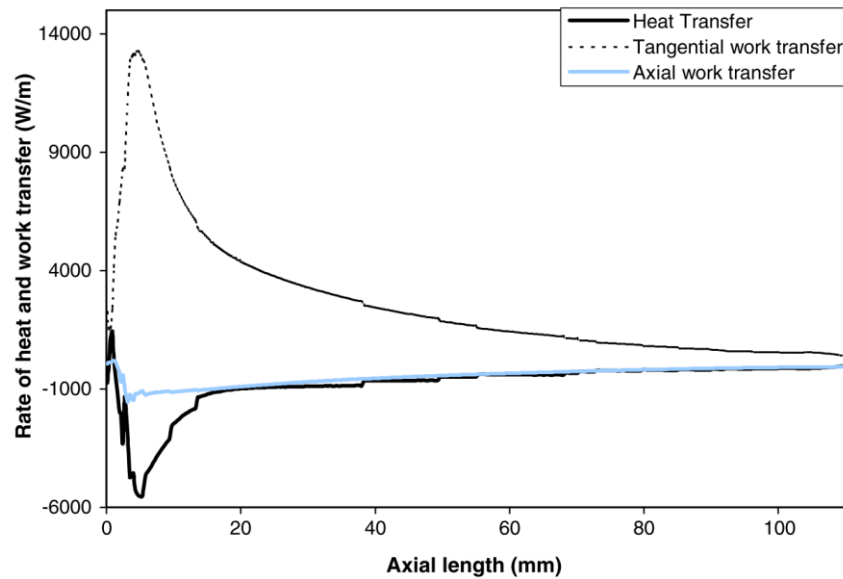
Figure 54. Vortex tube energy transfer components from CFD ($\mu_C = 0.74$) [66]

3.1.5 The Role of Gas Properties

It has always been understood that the temperature separation effect is enhanced by a large pressure drop across the vortex tube. However, the roles of inlet gas and inlet temperature have received considerably less attention and no exhaustive research. Experiments with different gases have generated inconsistent explanations of the role of gas properties. Elser and Hoch [47] experimented with air, H_2, Ar, CH_4, and CO_2 and found that the gases yielded different temperature separation values. H_2 yielded the greatest temperature separation followed by Ar, then air, then CH_4, and CO_2 yielded the least. Elser concluded that the gas properties were probably not very significant because the flow was turbulent, and ultimately no concrete explanation was offered. Martynovskii and Alekseev [53] experimented with air, CO_2, NH_3, and CH_4 and found that air generated the greatest temperature separation, followed by CH_4, then CO_2, and NH_3 had the least. Stephan et al. [78] experimented with air, O_2, and He; He yielded the greatest temperature separation while the temperature separation of air and O_2 at various pressures were virtually identical. Stephan et al. [78] attributed the differences in performance to molecular weight.

The experiments of Elser and Hoch [47] and Martynovskii and Alekseev [53] do not directly support the molecular weight theory. Elser and Hoch's results appear independent of molecular weight in that the temperature separation of air was greater than CO_2 and less than Ar, both of which have greater molecular weights than air. Martynovskii and Alekseev found that air generated the greatest temperature separation of the gases despite being in the middle of the pack in terms of molecular weight. It is worth noting that for both the Elser and Hoch [47] and Martynovskii and Alekseev [53]

experiments, the inlet temperatures of the gases spanned a range of approximately 23 K; Stephan et al. [78] provided no information regarding inlet temperature.

Others have speculated that additional gas properties play a role. Deissler and Perlmutter [62] suggested that temperature separation will increase with decreasing C_p of a gas. Entov [79] held the view that gas properties are not generally significant due to the turbulent flow, with the exception of the ratio of specific heats, γ. Fulton [44] hypothesized a relation to predict the maximum temperature drop in a vortex tube using the maximum isentropic temperature drop that would occur with isentropic expansion, ΔT_s, and the turbulent Prandtl number of the flow; large values of each would increase the maximum possible temperature drop. Note that it can be shown that ΔT_s will increase with γ. Fulton's use of the turbulent Prandtl number was based on an assumed relationship between work flux and heat flux, where work flux was assumed to pass from the cold flow to the hot flow and heat flux was assumed to pass from the hot flow to the cold flow. Martynovskii and Alekseev [53] also subscribed to Fulton's simplified model, though it ultimately provided very little in actually explaining the physics. This author introduces previous attempts at identifying the underlying mechanism of temperature separation for context, and will not necessarily defend all manner of early analytical choices.

In fact, Fulton did perform some initial calculations using an assumed turbulent Prandtl number of 0.75 based on contemporary research on the topic and found that the actual temperature separation was nearly double the maximum predicted value. This difference is probably due at least in part to his faulty assumptions regarding an alleged free vortex velocity distribution and the notion that heat conduction works opposite the

106

viscous stress; it should be reiterated that the net direction of heat conduction has been a matter of debate. However, the theory seemed to give some credence to the roles of γ and turbulent Prandtl number. Nevertheless, there are stark differences in the performance of different gases that are not explained by variations in γ. For example, γ is nearly identical for air and hydrogen, but Elser demonstrated that hydrogen yields enhanced temperature separation compared to air. In other words, there is a body of experimental evidence suggesting that other gas properties must influence temperature separation.

The turbulent nature of the flow does seem to complicate the debate regarding the role played by molecular gas properties in temperature separation. Pope notes that eddy diffusivity values for momentum and heat transfer are significantly greater than their corresponding molecular values, to the point where molecular values are often neglected [80]. This, of course, reflects the prevailing sentiment regarding the flow in a vortex tube. However, Pope places an important caveat on the generalization: this applies particularly for high Reynolds number flows and away from walls. In the case of the vortex tube, tangential velocity—by far the greatest component—increases sharply away from the wall but then *decreases* toward the core. Under these conditions, perhaps there are regions in which molecular properties are not negligible compared to turbulent properties. Moreover, perhaps the relationship between turbulent and molecular properties in such a complex flow has contributed to the challenge of modeling temperature separation in various gases with CFD. In fact, CFD studies repeatedly produce results that are *qualitatively inconsistent* with experimental findings. Pourmahmoud [81] and Rafiee [82] computationally determined that CO_2 yields greater temperature separation than air; this

stands in contrast to the experimental results of Elser and Hoch [47] and Martynovskii and Alekseev [53].

Thakare [73] attempted to match the results of Hartnett and Eckert using CFD; recall that Hartnett and Eckert [55] did not extract a cold fraction and thus did not have separate hot and cold streams. Thakare's metrics of temperature separation instead were the maximum and minimum in the total temperature distribution in the simulated vortex tube. The velocity and total temperature profiles were qualitatively representative, but underpredicted internal total temperature profiles in air by at least 25%; this number increased at different axial stations and with different turbulence models. Because the entirety of the flow was exhausted from a single exit and no theoretical interface existed between hot and cold flows, an internal energy balance was not applicable for this configuration. However, Thakare's results with different gases are qualitatively inconsistent with other experimental data. (Hartnett and Eckert [55] did not experiment with other gases, so this author's comparisons are drawn against the relative magnitudes of temperature separation between gases by other researchers.)

Thakare's CFD model successfully predicted that He and H_2 yield greater temperature separation than air, and that air yields greater than CO_2, but predicted that CH_4 yields greater than air—in contradiction to the results of Elser and Hoch [47] and Martynovskii and Alekseev [53], and with Elser and Hoch controlling for inlet temperature. With respect to gas properties, Thakare concluded that molecular thermal diffusivity is the most significant predictor of temperature separation. It is this author's observation that a correlation between thermal diffusivity and temperature separation

108

suggests that heat transfer plays a significant role, although Thakare's result should still come with some skepticism based on the other inconsistencies.

Thakare [73] also observed a very close correlation between the temperature separation in a gas and its tangential velocity distribution in the simulated vortex tube. Though unstated by Thakare, it is also clear that the relative tangential velocities are—without exception—perfectly correlated to molecular weight where, as one might expect, the lighter gases have higher velocities. Moreover, it can be seen in Thakare's results that molecular weight is, with respect to relative rankings, correlated with relative temperature separation (with H_2 as the only exception). Since the turbulent viscosity, ν_T, is essentially identical between gases at high Reynolds numbers—especially for the standard k-ε model—faster velocities naturally correspond to greater shear stresses and it is not then a great leap to conclude that for Thakare's CFD study, the dominant mode of temperature separation is shear work. However, He was shown to have a slightly higher temperature separation than H_2—the only exception to the molecular weight rule—indicating that the CFD results are factoring in another energy transfer mode such as heat transfer. No researcher has ever compared He and H_2 experimentally, so the CFD findings cannot be independently evaluated.

It is not entirely clear why there are qualitative inconsistencies between the CFD and the experiments. One possibility is that the vortex tube configuration, which in this case was essentially a uniflow tube with no cold fraction, does not lend itself well to comparisons with conventional counterflow vortex tubes. In any event, this is clearly a gap in the literature and a more rigorous comparison between experimental and

computational results with respect to working gas and temperature separation would be helpful.

3.1.6   *The Role of Inlet Temperature*

The role of gas inlet temperature has also received little attention. Elser and Hoch [47] first investigated the effect of inlet temperature and found approximately 30% greater temperature separation when the inlet air was heated to 90°C compared to their baseline case of 25°C [47] but no explanation was offered. Martynovskii and Alekseev [53] anticipated increased temperature separation at higher temperatures, presumably because of their theory relating temperature separation to ΔT_s, since it can also be shown that a greater inlet temperature corresponds to a greater isentropic temperature drop. However, they investigated the effect of inlet temperature across the limited range of 7°C – 25°C and found that it "did not cause any measurable effect" [53]. Torrella [83] experimentally investigated the effect of inlet air temperature ranging from 14°C – 39°C and claimed to have found that increased inlet temperature enhances temperature separation, though the change in performance was not robustly quantified. Pourmahmoud [84] numerically investigated the effect of inlet temperature across the range 21°C – 197°C and found that temperature separation increased by 15 K at the cold exit and 10 K at the hot exit with greater inlet temperature, for a cold fraction of $\mu_C = 0.30$. The most noticeable effect of inlet temperature in the data of Pourmahmoud was greater tangential velocities, which increased by 23% – 26% across the temperature range, though no explicit connection was drawn to increased temperature separation. Unfortunately, no static temperature distributions were shown, nor were any internal energy balances conducted. The research on the variation of temperature separation with

110

respect to inlet temperature remains somewhat anecdotal, and no published studies have investigated the interactions between gas and inlet temperature.

3.1.7   *The Effect of Geometric Scale*

The size of vortex tubes found in the literature varies considerably. Modern commercially available vortex tubes tend to be a few inches long, but Hilsch's original tube was 30 cm long [41], and Scheper used a 36 inch vortex tube [49]. Nevertheless, the effect of geometric scale on vortex tube temperature separation has not been directly evaluated in the literature in that no research has ever been conducted whereby two geometrically identical vortex tubes, differing only in scale, have been compared.

The variation of geometric *proportions* of a vortex tube can have a significant influence on the behavior, and numerous researchers such as Martynovskii and Alekseev [53], Soni [85], and Saidi and Valipour [86] have expended considerable effort to optimize vortex tube performance. Such research typically takes the form of parametric studies of geometric proportion such as the ratios of tube length to diameter, tube diameter to cold exit orifice diameter, and total inlet area to tube cross sectional area; other geometric factors such as the shape and number of inlets, tapering of the tube, and hot exit geometry are also sometimes considered.

Limited research has been performed on small vortex tubes: Dyskin [87] claimed success in testing vortex tubes with diameters down to 1 mm, although the usual performance curves were not presented and the degree of temperature separation was not clear. Hamoudi et al. examined small vortex tubes and small pressure drops [88,89] and the results are much more illuminating. With a tube diameter of 2 mm and an inlet

pressure of 200 kPa, a cold side temperature drop of approximately 9°C was achieved; actual performance was further modulated by varying geometric proportions.

Hamoudi et al. also investigated the effects of inlet pressures in the range of 2.5 kPa – 82 kPa (0.36 – 11.9 psi) for a 2 mm diameter vortex tube. They found that temperature separation disappeared altogether when the inlet pressure dropped below 25 kPa gauge (3.6 psig), and rose to approximately 2°C for an inlet pressure of 69 kPa gauge (10.0 psi). They also considered the influence of inlet channel Reynolds number on temperature separation in that the inlet channel Reynolds number is a function of the pressure difference between the inlet channel and the vortex tube exit. They hypothesized that as the pressure drop and the channel Reynolds number increase, the flow will transition to turbulent flow and that turbulent flow is conducive to temperature separation.

3.1.8   *A Summary of Vortex Tube Explanations in the Literature*

At this point, it is worth recapping the extant theories. The mainstream of researchers recognize viscous shear and heat transfer as the dominant modes of energy transport between the hot and cold flows, and heat transfer was also hypothesized to be enhanced by a pressure gradient when the flow is turbulent. The majority saw viscous work as the dominant mode, with a substantial minority viewing heat transfer as the dominant mode. The conflicting views arose primarily from different understandings of the velocity and temperature distributions inside the tube. This was complicated by a diversity of experimental configurations, some unresolved inconsistencies in measured data, a lack of definition of the boundary between hot and cold flows, and possibly by delays in disseminating the latest results.

Fringe theories have also been proposed; these will not be exhaustively reviewed, but the most prominent will be briefly summarized. Eckert [3], decades after collecting experimental data, attributed temperature separation in vortex tubes to unsteady phenomena; he specifically emphasized the contribution of unsteady pressure forces over that of heat transfer or viscous stress and assumed that the flow inside a vortex tube must be unsteady. A related and oft-cited theory is the "acoustic streaming" hypothesis proposed by Kurosaka [5], which attributes temperature separation to unsteady acoustic interactions that apparently modify vortex behavior and device performance. This fascinating phenomenon is apparently not essential for vortex tube operation and remains beyond the scope of this paper. In recent years, several more theories have emerged which do not directly explain vortex tube operation, such as Ahlborn's secondary flow [67], the cumulative effect of Görtler vortices [45], partial stagnation and multi-circulation [65], and angular propulsion [90]. None of these will be seriously considered.

The present research will only consider explanations that are rooted in the energy equation and therefore will attempt to determine the relative contributions of work and heat transfer inside the vortex tube based on a rigorous characterization of the velocity and temperature distributions.

3.2 Characterization of the Phenomenon of Temperature Separation as Observed in a Vortex Tube

The second research objective, "Characterize the phenomenon of temperature separation as observed in a vortex tube", is multi-faceted and successful completion depended upon analytical, experimental, and computational methods. First and foremost, it was important to establish as rigorous an experimental footing as possible. Therefore,

113

research began via experimental investigations into governing properties in vortex tubes. Following the initial experimental investigation, all results were nondimensionalized using a methodology established in a subsequent analytical study. Computational methods, validated through favorable comparison with experimental results, were also applied to determine the underlying mechanism of temperature separation and to identify any influences of geometric scale on temperature separation.

Conventional vortex tube configurations apply an inlet pressure of several atmospheres and vent to ambient pressure. Temperature separation may be manipulated by adjusting the cold fraction, μ_C, defined as the fraction of the inlet mass flow rate exhausted via the cold exit. The cold fraction is typically adjusted using a valve on the hot exit, and the greatest temperature drop is usually achieved with $0.2 < \mu_C < 0.5$. Performance characteristics are conventionally plotted as a set of curves in which the difference in temperature between exits and inlet are plotted as a function of cold fraction; the hot exit results will be seen as a curve of positive values, while the corresponding cold exit curve will be a set of negative values. The results herein will be reported in this fashion, similar to that of Figure 46.

3.2.1   *Experimental methodology: characterization of vortex tube performance*
The experimental evidence indicates that inlet flow conditions and gas properties are significant to temperature separation, but little progress has been made in understanding these dependencies. The present effort experimentally investigates the contribution of inlet flow conditions and gas properties to temperature separation and two

properties will be considered, which have not historically been of interest in vortex tube investigations: nozzle velocity and volumetric heat capacity, ρC_p.

The degree of temperature separation in a vortex tube is at least partially linked to the intensity of the vortex. Since the flow profile inside the tube is established by the high-velocity flow passing through the nozzles, it stands to reason that nozzle velocity is of considerable interest in an investigation of temperature separation. Nozzle velocity has not historically been of interest in vortex tube investigations; only Sibulkin [63] measured the velocity at the nozzle, and even then the purpose was to verify boundary conditions for a numerical study rather than as a parameter to vary. The volumetric heat capacity, ρC_p, reflects a combination of flow properties, such as temperature and pressure, and gas properties such as molecular weight and C_p. Moreover, wherever density is found in the energy equation, it is multiplied by C_p; see Panton [91]. The present study examines the effects of inlet temperature, pressure, mass flow rate, and working gas on nozzle velocity and ρC_p and—in turn—on temperature separation.

The model of vortex tube used in this study was a commercially available Exair™ 3208, shown in Figure 55, which indicates the locations and flow paths for the inlet, hot exit, and cold exit. A component known as a vortex generator, which contains the tangential nozzles that impart the swirl of the vortex, was installed internally at the site depicted in Figure 55. The vortex generator was the Exair™ model 8R, seen in Figure 56. The 8R vortex generator contains six rectangular-channel nozzles, each of which has a height of 0.794 mm, a width of 0.660 mm, and a hydraulic diameter of 0.721 mm. The outside diameter of the vortex generator matches the inside diameter of the cavity near

the cold exit, so when the vortex generator is sealed inside the cavity, the annular recess forms an annular chamber. Gas flows into the vortex tube via the inlet and then into the annular chamber. Next, it passes through the nozzles and into the tube, where the complex vortical flow occurs. A fraction of the gas exits the vortex tube via the nearby cold exit, while the rest exits via the hot exit at the opposite end of the tube.
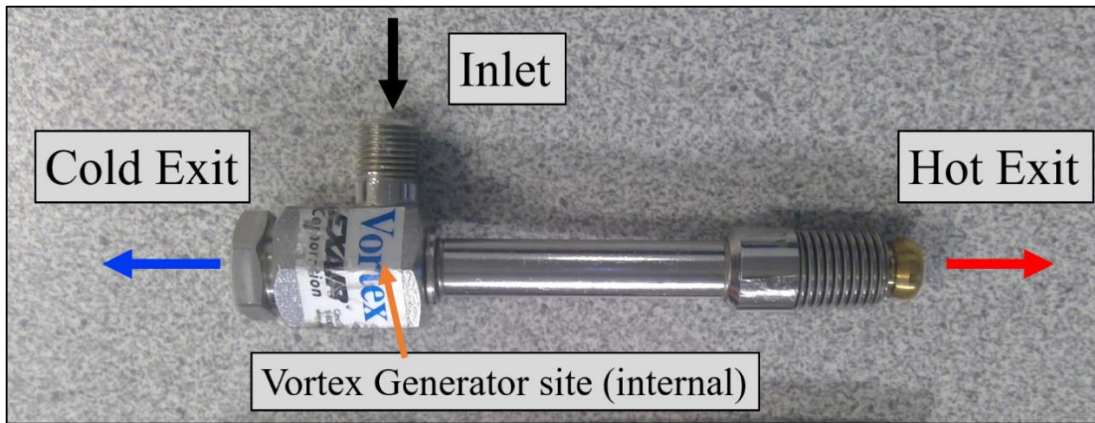
Figure 55. Exair™ 3208 vortex tube used in the study
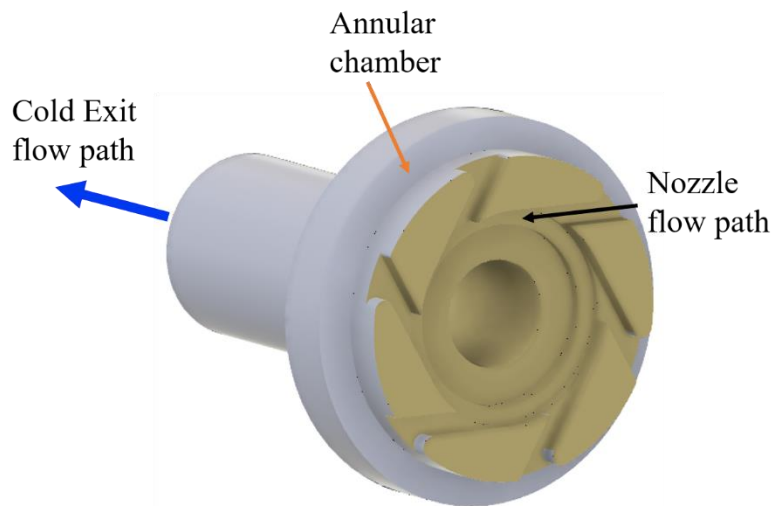
Figure 56. Exair™ 8R vortex generator

For this investigation, it was necessary to independently control the mass flow

rate, static temperature, and static pressure of a gas through the nozzles. A vortex tube

laboratory was assembled to meet these requirements as shown in Figure 57. Pressurized

dry air and bottled CO_2 were used in the experiments. The gas was passed through a

manual pressure regulator to set the inlet pressure, and then through a heat exchanger to

achieve the desired inlet temperature. At the inlet to the vortex tube, a NetScanner

pressure transducer measured static pressure and an Omega grounded-junction K-type

thermocouple measures temperature.

Figure 57. Vortex Tube Laboratory Configuration

The gas was exhausted through both ends of the vortex tube where the pressure

and temperature were measured using identical pressure sensors and thermocouples as at

the inlet. The mass flow rate through each side of the vortex tube was independently

controlled with a dedicated Omega 2612A digital mass flow controller; these can control

flow rates of up to 500 standard liters per minute (SLPM). The mass flow controllers

have an operating range of -10°C to +50°C, so the gas was passed through a heat

exchanger upstream of the controllers to remain within this range. The location of the

mass flow controllers was a unique feature of this laboratory: by installing them

downstream of both exits, the inlet pressure and mass flow rates were largely decoupled. Whereas conventional experiments could not set a high inlet pressure and a low mass flow rate, such independent variation was possible here. Obviously, some *minimum* inlet pressure was still required for a particular mass flow rate.

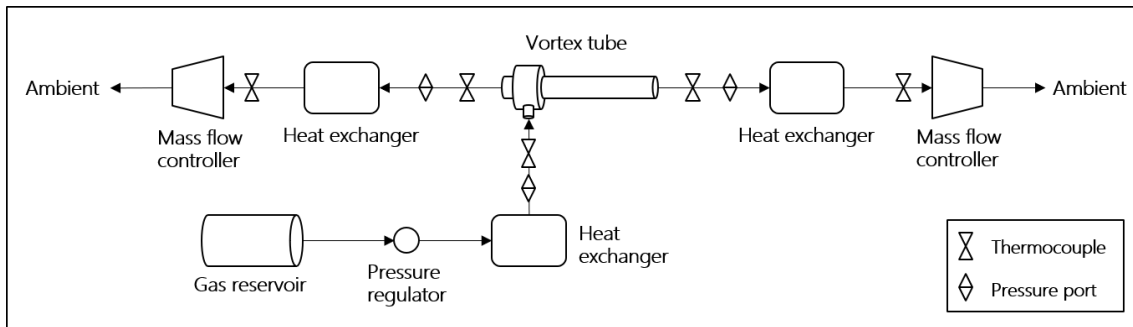For each test point, ten samples of temperature and pressure at the inlet and exits as well as mass flow rate at the exits were collected at a rate of 1 Hz and then averaged. The nominal accuracy of the thermocouples and pressure sensors were 0.5°C and 0.05 psi, respectively. However, the thermocouple standard error for each test point was typically less than 0.05°C and rarely greater than 0.07°C; note that the standard error reflects the experimental precision of the measurement technique, not the underlying accuracy of the measurements. Nominal accuracy of pressure measurements was 0.05 psi; the standard error was typically less than 0.01 psi and rarely above 0.02 psi. The nominal accuracy of the mass flow controllers was the sum of 0.2% of full scale (500 SLPM) and 0.8% of measured; because most experiments used flow rates between 50 – 100 SLPM, this corresponded to a nominal accuracy of 1.1 – 2.6% for each flow meter where lower flow rates have a higher percentage error. Uncertainty in nozzle velocity was estimated using the method of Kline & McClintock [37]. Using the nominal accuracies of the sensors yielded typical velocity uncertainties between 2 – 4% of the calculated value; this was dominated by uncertainty in mass flow rate. In essence, it was more difficult to reliably match nozzle velocity for low mass flow rates.

Precision uncertainty of the results was analyzed with an assessment of repeatability. The three cases of greatest interest—Cases 5.1 – 5.3, to be introduced in Section 3.2.2—were repeated after a period of several days. For example, the Case 5.1

118

temperature separation curves for both days are shown in Figure 58. The repeatability was aggregated for hot and cold curves across all cold fractions for all three repeated cases and normalized by observations. The results are presented as a histogram in Figure 59, which reveals that their distribution is approximately normal with a nearly zero (0.0012 K) mean. 64.1% of the data points had repeatability within ±0.05 K, while 97.4% were within ±0.15 K. The remaining two data points, within ±0.25 K, occurred on the cold exit curves for a cold fraction of 0.20, which is an especially challenging data point due to corresponding mass flow rates.
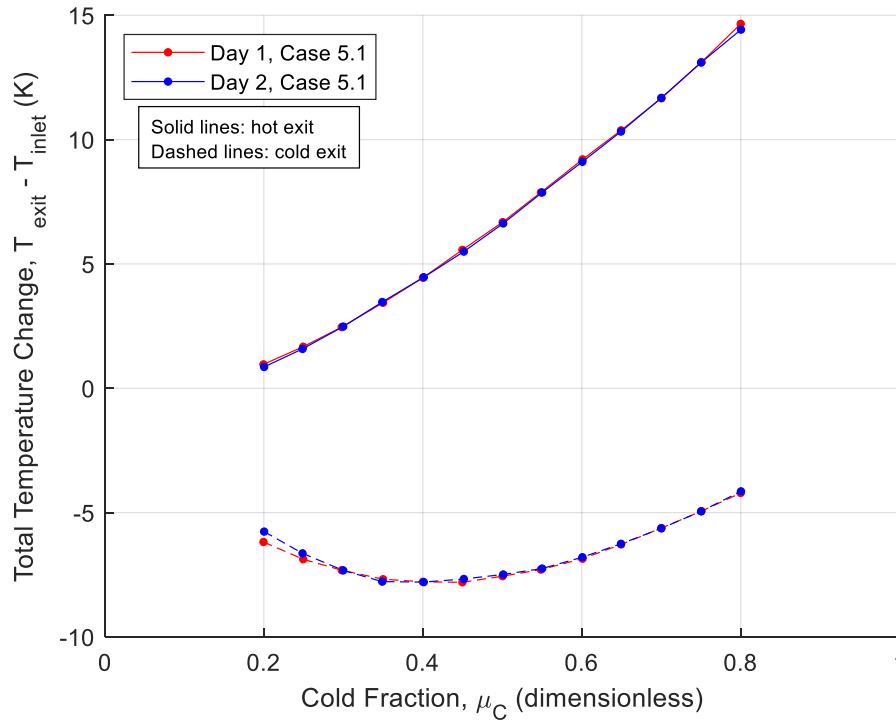
Figure 58. Day-to-day repeatability of experimental test cases
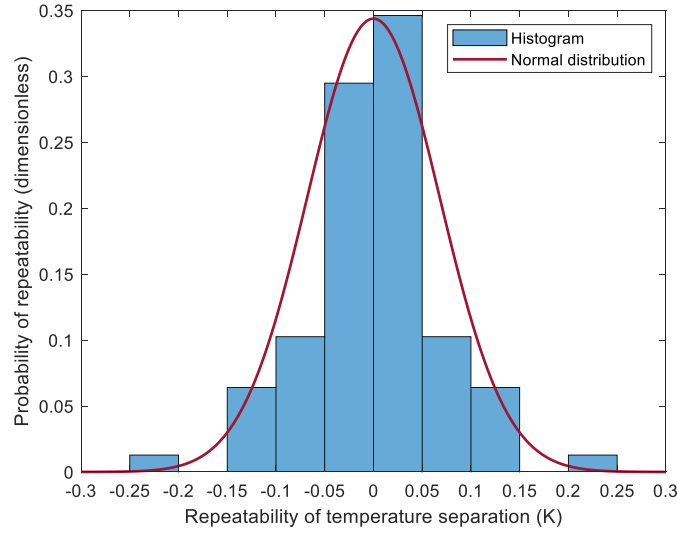
Figure 59. Histogram of experimental precision uncertainty

The experiments require control of the flow conditions through the nozzles,

including a means of determining the velocity and ρC_p, but the size and placement of the

nozzles made direct instrumentation prohibitive; moreover, instrumenting an inlet was

expected to distort the flow path. Flow conditions were instead measured slightly

upstream of the nozzles at the vortex tube inlet; in Figure 57, this location is between the

heat exchanger and the vortex tube. Nozzle flow conditions were computed using

compressible flow relations based on foundational thermodynamic and fluids theory; see

John [92] for Eqs (45) – (49), which outline the solution process for nozzle properties.

The path from the instrumented inlet to the vortex tube nozzles is approximately

7 cm long and consists mostly of tubing followed by a constriction inside the vortex tube

as the flow enters the nozzles, which are 2.5 mm in length, and is accelerated; the flow in

this study does not exceed Mach 0.30. The total pressure losses along this path are

certainly not zero but, based on these observations, the losses are expected to be small

enough that the flow path is modeled ideally as an isentropic converging nozzle. However, once the flow exits the nozzles, the total pressure losses inside the tube are substantial. To avoid confusion, the term "inlet" refers to the instrumented station upstream of the vortex tube, while the term "nozzles" will be reserved for the passages through which gas is injected to form the vortex.

At the inlet, total temperature and static pressure are measured, and mass flow rate is computed as the sum of the mass flow rates measured at the tube exits. Inlet bulk velocity, static temperature, and Mach number were computed using the two total temperature relations in Eq (45) and (46). The combined cross-sectional area of the nozzles is 3.144×10^{-6} m^2. The area ratio between all of the nozzles and the inlet is $\frac{A_{nozzles}}{A_{inlet}} = 0.172$. The Mach number at the nozzles is computed by calculating the nozzles' critical ratio from the inlet critical ratio in Eq (47) and relating the critical area ratio to Mach number with Eq (48) [92]. Nozzle static temperature is computed using Eq (45), and finally nozzle bulk velocity is calculated from the Mach number using Eq (49). Through experimentation with air, it was found that the Mach numbers through the inlet and exits were low—in all cases, $M \leq 0.061$—implying that the thermocouple measured total temperature. Due to mass flow rate limits imposed by the lab configuration, the Mach number through the nozzles could not exceed 0.40 and remained at 0.35 or below for the cases of interest.

$$T_t = T \left(1 + \frac{\gamma - 1}{2} M^2 \right) \tag{45}$$

$$T_t = T + \frac{V^2}{2 C_p} \tag{46}$$

$$\frac{A_{nozzles}}{A^*} = \frac{A_{inlet}}{A^*} \frac{A_{nozzles}}{A_{inlet}} \tag{47}$$

$$\frac{A}{A^*} = \frac{\left(\frac{\gamma + 1}{2} \right)^{-\frac{\gamma+1}{2(\gamma-1)}} \left(1 + \frac{\gamma - 1}{2} M^2 \right)^{\frac{\gamma+1}{2(\gamma-1)}}}{M} \tag{48}$$

$$V_{nozzles} = \sqrt{\gamma R T_{nozzles}} M_{nozzles} \tag{49}$$

Two data sets were taken separately using this laboratory configuration: a multi-μ_C set and a single-μ_C set, which were used for slightly different purposes. For the multi-μ_C set, comparison cases were developed for six scenarios and data was taken for cold fractions across a range of $0.20 \leq \mu_C \leq 0.80$. The first five scenarios use air, while the last extends the investigation using CO_2. For air, the first three scenarios involved varying either mass flow rate, temperature, or pressure while holding the other two quantities constant. These are the three operating conditions that are directly adjusted, and these were independently varied at first. The fourth scenario investigated temperature separation while matching nozzle velocity and varying ρC_p, while the fifth matched nozzle velocity and ρC_p for three different combinations of inlet temperature and pressure. Finally, the sixth scenario matched nozzle velocity and ρC_p in CO_2. For brevity,

experiments were named according to the scenario and the comparison case; for example, the third case within the fifth scenario was named Case 5.3.

For multi-μ_C experiments in air, mass flow rates varied from 0.945 – 1.776 g/s (47.9 – 90.0 SLPM), inlet total temperatures ranged from 20°C to 60°C, and inlet static gauge pressures varied 2.00 – 5.00 bar (29.01 – 72.52 psig). Combinations of these parameters were carefully set to achieve nozzle velocities ranging from 62.85 to 98.95 m/s, with Mach numbers ranging from 0.183 to 0.295. Several sets of experimental data were taken using carefully selected combinations of mass flow rates, temperatures, and pressures. The resulting curves of temperature separation are plotted against cold fraction for each of the comparison cases.

The single-μ_C data set was taken only for a cold fraction of $\mu_C = 0.40$, which is in the range of cold fractions near which the coldest temperatures are typically observed, and thus was expected to yield readily discernable results. The inlet temperatures were set to 20°C, 40°C, or 60°C; inlet static pressures ranged from 2.0 to 5.0 bar (gauge), and mass flow rates varied from 9.85×10^{-4} to 2.37×10^{-3} kg/s (approximately 50 – 120 SLPM). 36 data points were collected using combinations of these settings. Nozzle velocities ranged from 44.4 to 127.5 m/s, Reynolds numbers from 11,222 to 30,112, and Mach numbers from 0.130 to 0.353. The only use for the single-μ_C data set in the dimensional investigation of temperature separation is to characterize the relationship with nozzle velocity; however, the full utility of this data set will become clear following the nondimensionalization of temperature separation in Section 3.2.4.

Nozzle velocity uncertainty was most significantly affected by uncertainty of the mass flow controllers, which was computed as 0.2% of full scale (500 SLPM) plus 0.8%

of the measured value. For the cases with the lowest flow rates of 9.85×10^{-4} kg/s

(50 SLPM), velocity uncertainty ranged from 3.4% to 3.9% of the computed velocity.

This decreased to 2.3% or less for flow rates of 1.97×10^{-3} kg/s (100 SLPM) and higher.

3.2.1.1 Heat Loss Correction

To minimize heat losses, the vortex tube and the instrumentation stations were

wrapped with foam insulation. However, heat losses from the vortex tube were inevitable

at elevated inlet temperatures and it was necessary to account for these losses to avoid

distorting the results, especially when comparing results from different inlet

temperatures. Heat losses were computed using Eq (50), where heat lost through the

vortex tube was equal to the difference in specific total enthalpy between the inlet and

exits, where total enthalpy is defined by convention as $h_t \equiv h + \frac{V^2}{2}$.

$$q = \dot{m}_{hot} h_{t,hot} + \dot{m}_{cold} h_{t,cold} - \dot{m}_{inlet} h_{t,inlet} \qquad (50)$$

Values of specific enthalpy, h, and specific heat at constant pressure, C_p, were

computed at the inlets and exits as functions of static temperature and pressure from the

data of NIST REFPROP 9.1 for air [93], and from the data of NIST Webbook for CO_2

[94]. Moreover, to ensure accurate calculations of heat losses, conditions were monitored

for steady-state operation prior to data collection. This typically took two minutes or

more, depending on mass flow rate and was determined by monitoring the exit

thermocouple time histories.

To correct for heat losses, a function was devised to apportion a fraction of the

overall lost heat back to each exit as appropriate; as expected, this apportionment fraction

was a function of the cold fraction, μ_C, and is described by Eq (51), where $\frac{q_{hot}}{q}$ is the

fraction of lost heat apportioned to the hot exit. This simple linear function performs well

for $0.20 \leq \mu_C \leq 0.90$ and is remarkably robust against variations in inlet temperature,

mass flow rate, and degree of insulation. The function was validated for flow rates from

20 – 100 SLPM, inlet temperatures of 20°C – 60°C, and for both insulated and

uninsulated cases. A temperature correction was then computed based on the C_p and mass

flow rate and added to the temperature measured at the hot and cold exits. For example,

the hot side temperature correction was computed using Eq (52).

$$\frac{q_{hot}}{q} = -0.60\mu_C + 0.88 \tag{51}$$

$$\Delta T_{t,hot} = \frac{q_{hot}}{\dot{m}_{hot}C_{p,hot}} \tag{52}$$

An extreme example of the corrected versus uncorrected results is shown in

Figure 60, where the inlet total temperature is 60°C, inlet static gauge pressure is

5.00 bar, and mass flow rate is 0.00197 kg/s (100 SLPM). Tests were run with and

without insulation on the vortex tube: in the top plot of Figure 60, insulated and

uninsulated cases are shown before correction. After the same heat loss correction

function was applied to both results, nearly identical corrected curves can be seen in the

bottom plot. All subsequent results are corrected for heat losses.
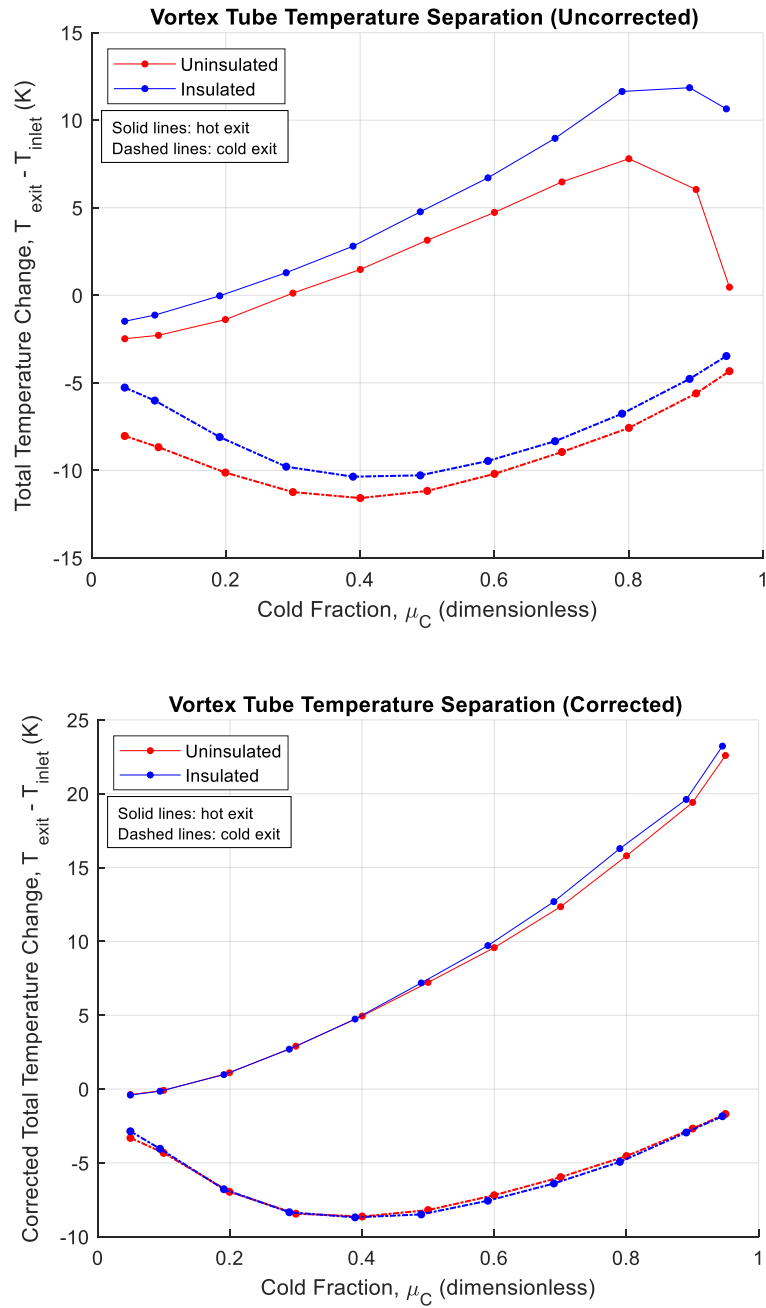
Figure 60. Comparison of Temperature Separation Curves:

Uncorrected (top), with Heat Loss Correction (bottom)

3.2.2 Results and discussion: experimental characterization of vortex tubes

3.2.2.1 Analysis of the multi-μ_C data set

The results of the multi-μ_C data set will be reviewed first. Scenario 1 investigated the influence of varying mass flow rate while holding inlet total temperature and static gauge pressure constant at 20°C and 3.0 bar. This had the effect of directly varying nozzle velocity; the increased velocity slightly decreased nozzle static pressure and temperature, causing a small net decrease in nozzle density and hence ρC_p across the cases. Nozzle properties were carefully maintained at target values with respect to cold fraction; see for example the plot of nozzle velocity in Figure 61. Therefore, key values will be averaged across the cold fractions and tabulated for each case, such as in Table 4.
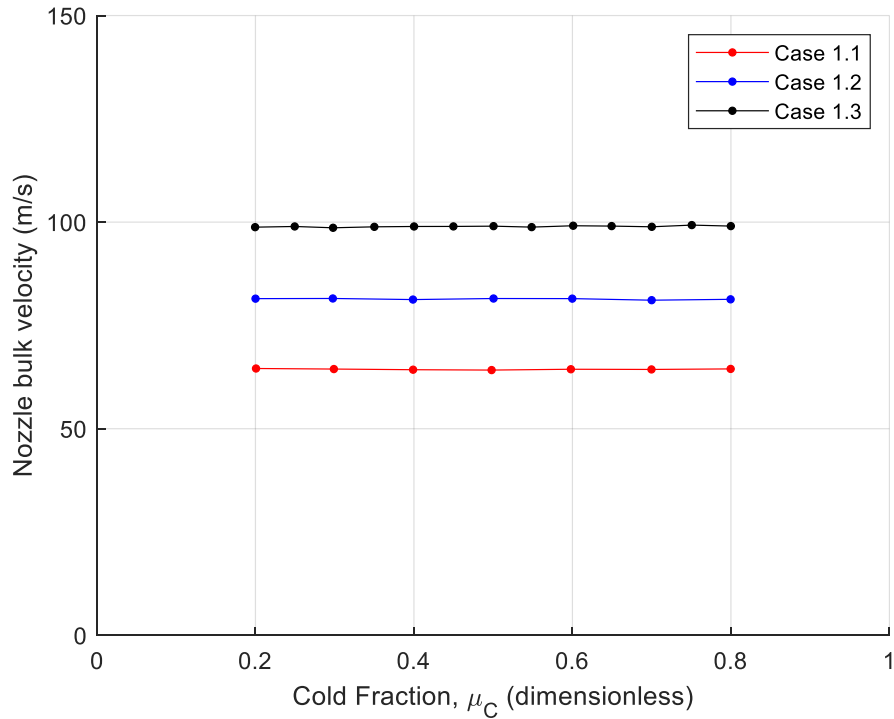
Figure 61. Constant nozzle bulk velocity with cold fraction for three mass flow rates

127

Table 4. Flow conditions for Scenario 1: varied mass flow rate, constant T_t and P_{static}

	Case 1.1	Case 1.2	Case 1.3
Mass flow rate (kg/s)	9.454×10^{-4}	1.183×10^{-3}	1.420×10^{-3}
Inlet T_{total} (K)	293.3	293.3	293.2
Inlet P_{static} (bar, gauge)	3.001	3.001	3.000
Velocity (m/s)	**64.39**	**81.38**	**98.95**
ρC_p (kJ/m³-K)	**4.724**	**4.676**	**4.616**
Mach number	0.188	0.238	0.291
Re_{D_h}	11910	14955	18034
ρ (kg/m³)	4.669	4.622	4.563
C_p (kJ/kg-K)	1.012	1.012	1.012
μ (μPa-s)	18.20	18.14	18.05
Nozzle T_{static} (K)	291.3	290.0	288.3
Nozzle P_{static} (Pa, absolute)	390293	384687	377571

As seen in Figure 62, the increase in mass flow rate—and consequently velocity—correlates with a large increase in temperature separation. Intuitively, the increased temperature separation is also correlated with increased nozzle Mach number and Reynolds number based on hydraulic diameter, Re_{D_h}. The value of ρC_p is nearly constant between the cases, decreasing by only 2.3%.
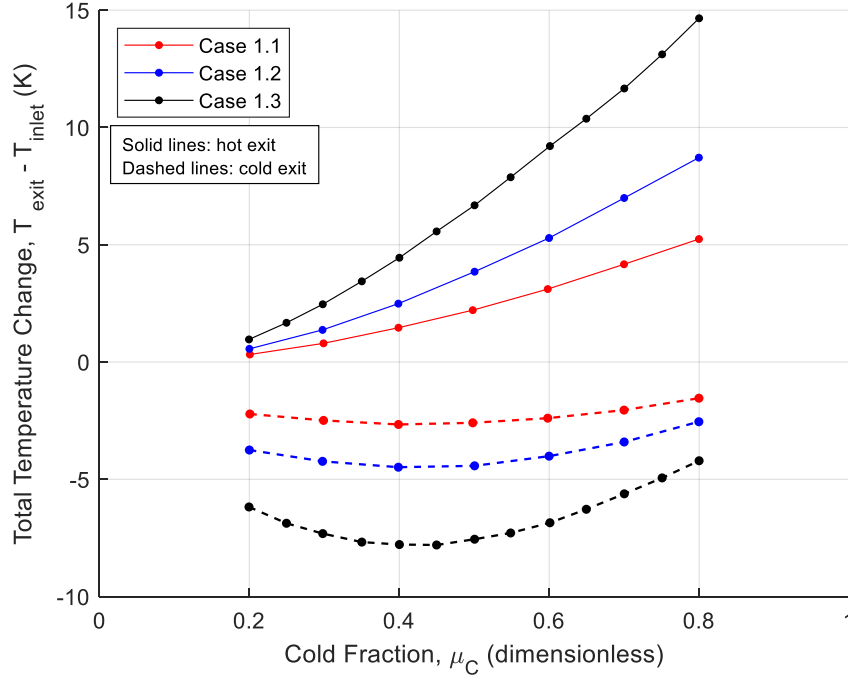
Figure 62. Temperature separation in air for varied mass flow rates (Scenario 1)

Scenario 2 examined the influence of inlet temperature on temperature separation. Temperature profiles are shown in Figure 63 and, consistent with other findings, temperature separation increased with inlet temperature. However, it now appears probable that the contribution of inlet temperature was primarily attributable to its corresponding influence on nozzle velocity, which increased by 14% between Cases 2.1 and 2.3, and potentially also to its influence on ρC_p, which decreased by 12% between the cases. Counterintuitively, temperature separation correlates with *decreasing Re_{D_h}*, as can be seen by reading the values of Re_{D_h} corresponding to the cases from Table 5, suggesting that nozzle Reynolds number alone is a poor predictor of temperature separation.

Table 5. Flow conditions for Scenario 2: varied T_t, constant mass flow rate and P_{static}

	Case 2.1	Case 2.2	Case 2.3
Mass flow rate (kg/s)	1.183×10^{-3}	1.184×10^{-3}	1.184×10^{-3}
Inlet T_{total} (K)	293.3	312.7	332.7
Inlet P_{static} (bar, gauge)	3.001	3.000	3.003
Velocity (m/s)	**81.38**	**87.11**	**92.86**
$\boldsymbol{\rho C_p}$ **(kJ/m³-K)**	**4.676**	**4.372**	**4.105**
Mach number	0.238	0.247	0.255
Re_{D_h}	14955	14251	13602
ρ (kg/m³)	4.622	4.322	4.056
C_p (kJ/kg-K)	1.012	1.012	1.012
μ (μPa-s)	18.14	19.05	19.96
Nozzle T_{static} (K)	290.0	308.9	328.4
Nozzle P_{static} (Pa, absolute)	384687	383127	382210
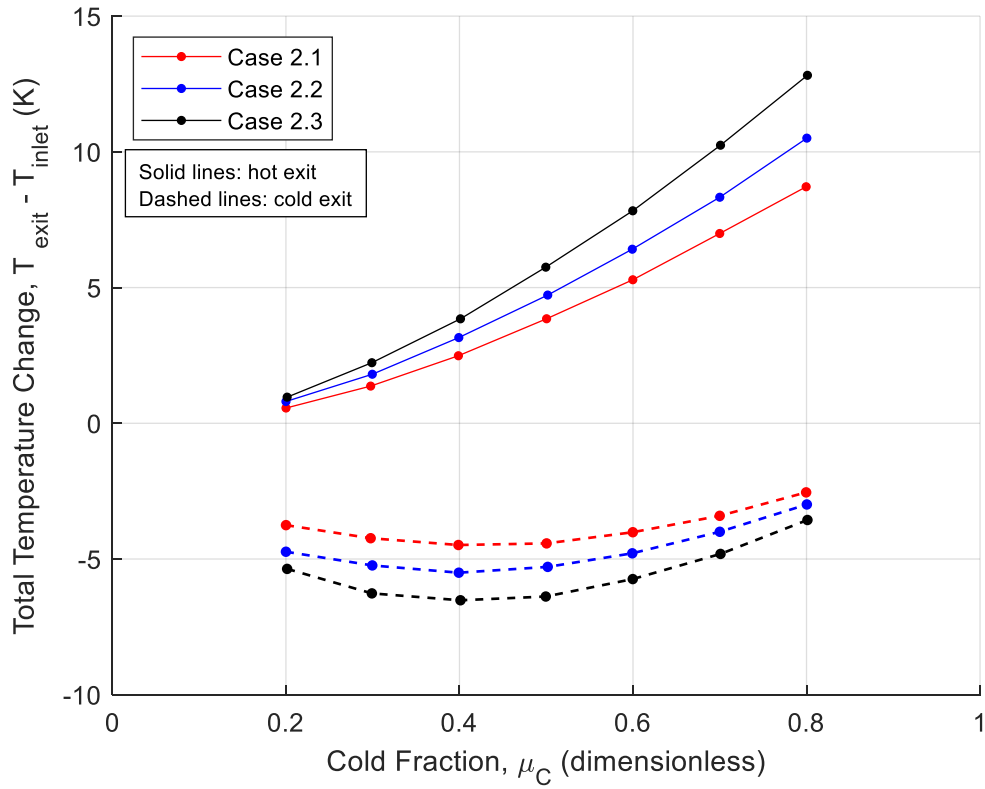
Figure 63. Temperature separation for air with varied inlet temperatures (Scenario 2)

Scenario 3 investigated the effect of pressure; these cases highlight both a unique capability of this laboratory and a potential challenge in using vortex tubes in high pressure environments. Typical vortex tube configurations feature an intrinsic coupling between the inlet pressure and the mass flow rate: higher inlet pressures are inherently linked to greater mass flow rates due to a lack of flow rate control at *both* exits; typical control is exerted by adjusting a valve only at the hot exit. The linkage between inlet pressure and mass flow rate means that higher pressures are conventionally linked to higher nozzle velocities and greater temperature separation.

For the configuration with dual mass flow controllers at the exits, an increase in inlet pressure effectively increases the pressure at the exits as well, which increases the flow density at the nozzle. When the mass flow rate is held constant, the increased nozzle density causes a reduction in nozzle velocity, as seen in Table 6. The consequence, as seen in Figure 64, is reduced temperature separation with increased nozzle pressure as long as mass flow rate is held constant. The effect of inlet pressure on temperature separation for this configuration obviously stands in contrast to conventional vortex tube configurations and reiterates the roles of nozzle velocity in inducing temperature separation. Notice that Re_{D_h} was the same for Cases 3.1 and 3.2, again indicating that Reynolds number alone cannot be used to predict temperature separation.

Table 6. Flow conditions for Scenario 3: varied P_{static}, constant mass flow rate and T_t

	Case 3.1	Case 3.2

131

Mass flow rate (kg/s)	$1.382{\times}10^{-3}$	$1.383{\times}10^{-3}$
Inlet T_{total} (K)	293.4	293.8
Inlet P_{static} (bar, gauge)	5.001	3.000
Velocity (m/s)	**62.80**	**96.59**
ρC_p (kJ/m³-K)	**7.102**	**4.604**
Mach number	0.183	0.283
Re_{D_h}	17366	17520
ρ (kg/m³)	6.996	4.551
C_p (kJ/kg-K)	1.015	1.012
μ (µPa-s)	18.24	18.09
Nozzle T_{static} (K)	291.4	289.1
Nozzle P_{static} (Pa, absolute)	585213	377643

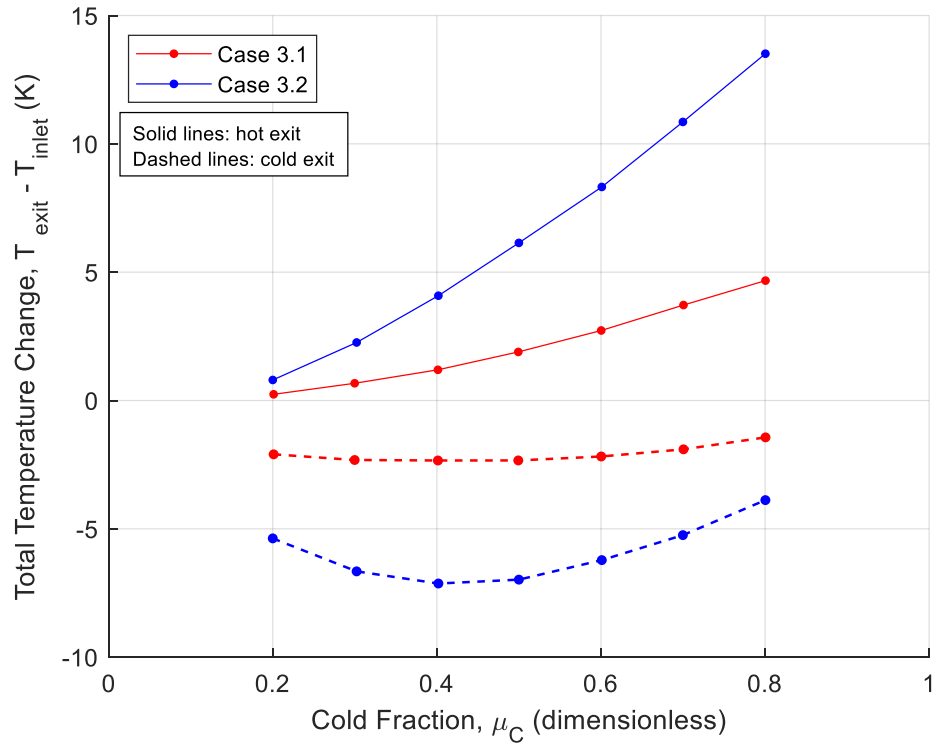**Figure 64. Temperature separation for air with varied inlet pressures (Scenario 3)**

The three scenarios thus far have found that increases in temperature separation

correlate with increases in nozzle velocity, as expected. The scenarios have also found,

without exception, that temperature separation is correlated with decreasing ρC_p. What is thus far lacking, however, is an indication of the sensitivity of temperature separation to ρC_p alone. Scenario 4 tested just that: nozzle bulk velocity was held constant for three cases, while nozzle ρC_p was varied by using combinations of mass flow rate and inlet pressure. This permitted a 42% decrease in ρC_p between Cases 4.1 and 4.3, shown in Table 7.

Table 7. Flow conditions for Scenario 4: matched V but varied $\rho\ C_p$

	Case 4.1	Case 4.2	Case 4.3
Mass flow rate (kg/s)	1.776×10^{-3}	1.420×10^{-3}	1.027×10^{-3}
Inlet T_{total} (K)	293.3	293.3	293.4
Inlet P_{static} (bar, gauge)	4.183	3.154	2.000
Velocity (m/s)	**95.29**	**95.04**	**95.21**
ρC_p **(kJ/m³-K)**	**6.009**	**4.808**	**3.463**
Mach number	0.280	0.279	0.279
Re_{D_h}	22508	18010	13029
ρ (kg/m³)	5.928	4.751	3.429
C_p (kJ/kg-K)	1.014	1.012	1.010
μ (μPa-s)	18.09	18.08	18.06
Nozzle T_{static} (K)	288.8	288.8	288.8
Nozzle P_{static} (Pa, absolute)	491365	393842	284320

Figure 65 suggests that temperature separation is a function of the product ρC_p, but not a strong function. Greater temperature separation appears correlated with lower ρC_p. Case 4.3 yields a small but consistent increase: at a cold fraction of $\mu_C = 0.4$, at which the greatest cold exit temperature separation is observed the difference between Case 4.3 and Case 4.1 is 0.51 K at the cold exit and 0.55 K at the hot exit. However, the differences between Cases 4.1 and 4.2 are so slight that they are on the same order as the

133

standard error of the experiment. This scenario ultimately reveals that the performance of the vortex tube is not sensitive to changes in ρC_p of the magnitude seen in these Scenarios, which further implies that the differences between cases in Scenarios 2 and 3 are largely attributable to differences in nozzle velocity.
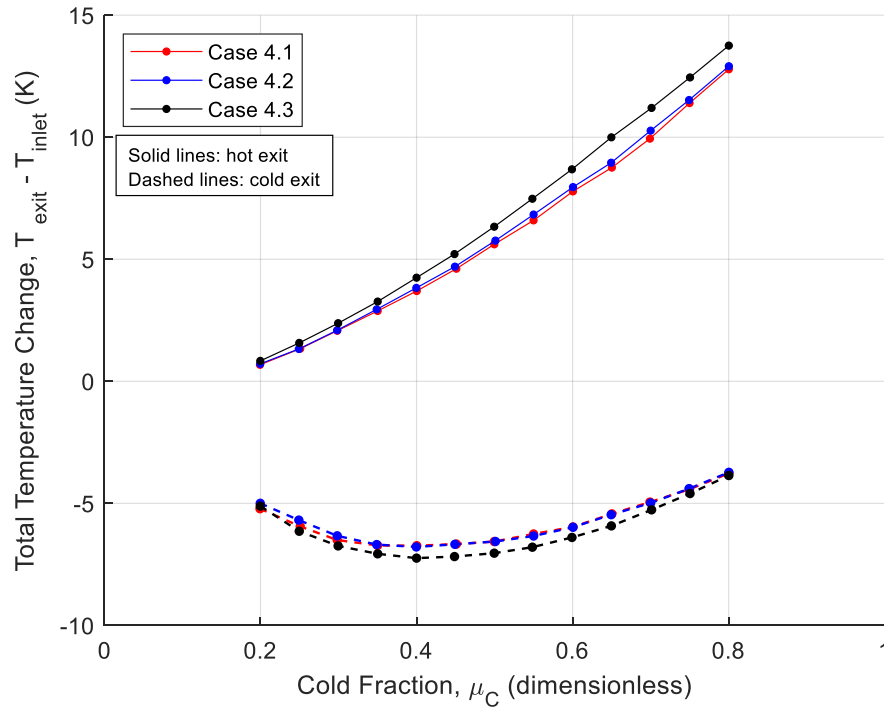
Figure 65. Temperature separation for air with

constant nozzle bulk velocity but varied ρC_p (Scenario 4)

Scenario 5 presents a novel comparison: the nozzle bulk velocity and ρC_p are matched for all three cases by varying temperature and pressure while holding mass flow rate constant, as presented in Table 8. Mach number and Reynolds number vary slightly between the cases. The net effect, shown in Figure 66, is striking: the performance curves are essentially identical between the three cases. This is the first instance in the known literature in which temperature separation in a vortex tube has been matched between

134

cases with dissimilar pressures and temperatures. This also suggests that dimensional

temperature separation is governed by two dimensional parameters: nozzle velocity and

ρC_p, though nozzle velocity has a vastly stronger influence than ρC_p. Moreover, velocity

apparently provides the link between temperature and pressure that has thus far proven

elusive. It has been long understood that increasing inlet pressure or inlet temperature

alone will increase temperature separation, but no explanation has thus far been offered

regarding any possible relationship between the two. Using standard fluid dynamics

analysis techniques, the relationship between the two is now clear—they both serve to

modify nozzle velocity by means of compressible flow relations.

Table 8. Flow conditions for Scenario 5: matched nozzle velocity and $\rho\ C_p$

	Case 5.1	Case 5.2	Case 5.3
Mass flow rate (kg/s)	1.420×10^{-3}	1.420×10^{-3}	1.421×10^{-3}
Inlet T_{total} (K)	293.2	313.3	333.1
Inlet P_{static} (bar, gauge)	3.000	3.275	3.549
Velocity (m/s)	**98.95**	**98.79**	**98.52**
$\boldsymbol{\rho C_p}$ **(kJ/m³-K)**	**4.6163**	**4.6262**	**4.6452**
Mach number	0.291	0.280	0.271
Re_{D_h}	18034	17111	16322
ρ (kg/m³)	4.563	4.571	4.587
C_p (kJ/kg-K)	1.012	1.012	1.013
μ (μPa-s)	18.05	19.03	19.96
Nozzle T_{static} (K)	288.3	308.4	328.2
Nozzle P_{static} (Pa, absolute)	377571	404644	432078

Figure 66. Temperature separation for air with matched V and ρC_p (Scenario 5)

Scenario 6 repeated the investigation of varying temperature and pressure while maintaining nozzle bulk velocity and ρC_p constant, but with CO_2 instead of air, shown in Table 9. Based on the findings in air, one might expect that the temperature separation curves would again be exactly aligned. However, this time the hot exit curves in Figure 67 collapse as expected but the cold exit curves reveal a variation such that temperature separation decreases with increasing inlet temperatures and pressures.

Table 9. Flow conditions for Scenario 5: matched nozzle velocity and $\rho\,C_p$

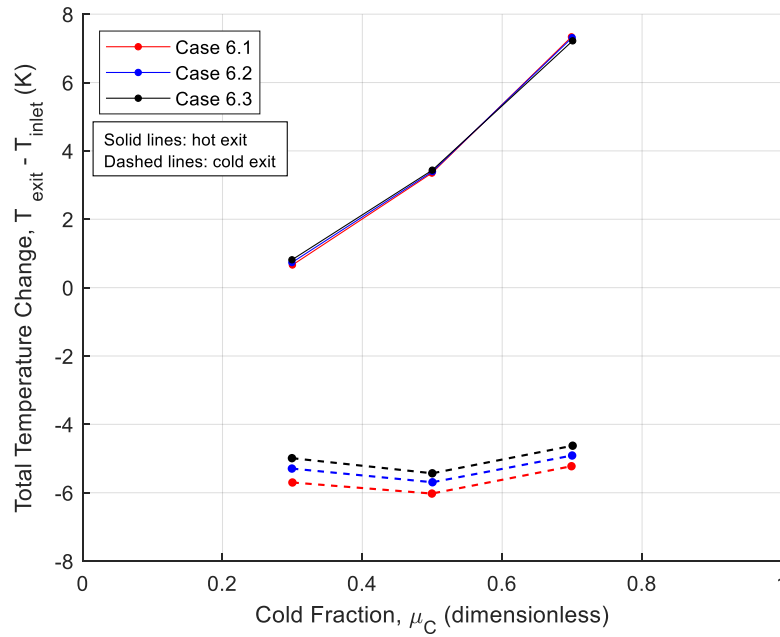|	Case 5.1	Case 5.2	Case 5.3
Mass flow rate (kg/s)	1.420×10^{-3}	1.420×10^{-3}	1.421×10^{-3}
Inlet T_{total} (K)	293.2	313.3	333.1
Inlet P_{static} (bar, gauge)	3.000	3.275	3.549
Velocity (m/s)	**98.95**	**98.79**	**98.52**
ρC_p **(kJ/m³-K)**	**4.6163**	**4.6262**	**4.6452**
Mach number	0.291	0.280	0.271
Re_{D_h}	18034	17111	16322
ρ (kg/m³)	4.563	4.571	4.587
C_p (kJ/kg-K)	1.012	1.012	1.013
μ (µPa-s)	18.05	19.03	19.96
Nozzle T_{static} (K)	288.3	308.4	328.2
Nozzle P_{static} (Pa, absolute)	377571	404644	432078

Figure 67. Temperature separation for CO₂ with matched V and ρC_p (Scenario 5)

This intriguing result indicates that at least one other relevant gas or flow property has not been matched. Reynolds number and Mach number seem unlikely culprits, since the variations between the cases are comparable to those in Scenario 5 in air. However,

137

the Joule-Thomson coefficient, μ_{JT}, which has not thus far been under consideration, is a likely contributor to this finding because its value is known to be much larger in CO_2 than in air and it inherently governs temperature changes across a pressure drop. Table 10 lists the values of μ_{JT} at the nozzle for each case in K/bar. The variation of μ_{JT} between cases for air (Scenarios 1 – 5) is approximately 0.06 K/bar at most, while Scenario 6 sees a total variation of 0.32 K/bar from 20°C to 60°C—a difference which alone is larger than the entire magnitude of μ_{JT} in air in any of the previous cases.

Table 10. Joule-Thomson coefficients at the nozzle for each scenario and case

μ_{JT} (K/bar)	Case 1	Case 2	Case 3
Scenario 1	0.2343	0.2345	0.2348
Scenario 2	0.2345	0.2043	0.1776
Scenario 3	0.2327	0.2338	-
Scenario 4	0.2337	0.2344	0.2351
Scenario 5	0.2348	0.2034	0.1768
Scenario 6	1.1466	0.9634	0.8260

The Joule-Thomson coefficient relates a change in pressure to a corresponding isenthalpic change in temperature. For a given pressure change, a larger value of μ_{JT} results in a larger temperature change, and the observations in CO_2 at the cold exit are consistent with this trend. For example, consider how the cold exit curves of Case 6.1, where $\mu_{JT} = 1.1466$, depict a greater temperature drop than those of Case 6.3, where $\mu_{JT} = 0.8260$. Figure 68 reveals the static pressure drop between the nozzle and the exits.
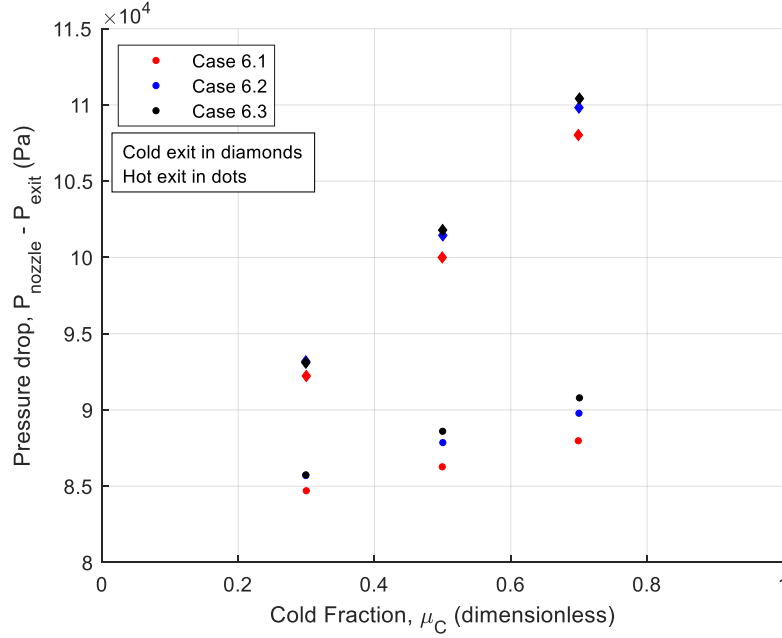
Figure 68. Static pressure drop between nozzle and exits: cold (diamonds) and hot (dots)

A decrease in pressure upon exiting the nozzle will also decrease the temperature of the gas. The static pressure drop between the nozzle and the cold exit is larger for all cases than the pressure drop between the nozzle and hot exit, so it is not surprising that the temperatures at the cold exit are more sensitive to changes in μ_{JT} than are temperatures at the hot exit. However, that these variations in μ_{JT} have no discernable effect on the hot exit temperatures is somewhat surprising. While the present findings suggest that μ_{JT} is indeed a governing property for temperature separation, deducing the exact manner in which it modulates the temperature separation likely requires a detailed internal flow analysis. The role of μ_{JT} will be further examined during the nondimensionalization of temperature separation, starting in Section 3.2.3.

3.2.2.2 Analysis of the single-μ_C data set

The dimensional investigation concludes with a direct investigation of the relationship between temperature separation and nozzle velocity. Recall that the single-μ_C data set was taken for $\mu_C = 0.40$ at various combinations of inlet temperatures, pressures, and mass flow rates to achieve a wide range of nozzle velocities. Inlet temperatures were 20°C, 40°C, and 60°C, inlet gauge pressures ranged from 2.0 – 5.0 bar, and mass flow rates varied from $9.85{\times}10^{-4}$ to $2.37{\times}10^{-3}$ kg/s (approximately 50 – 120 SLPM). The temperature separation for the test points has been aggregated and plotted in Figure 69.
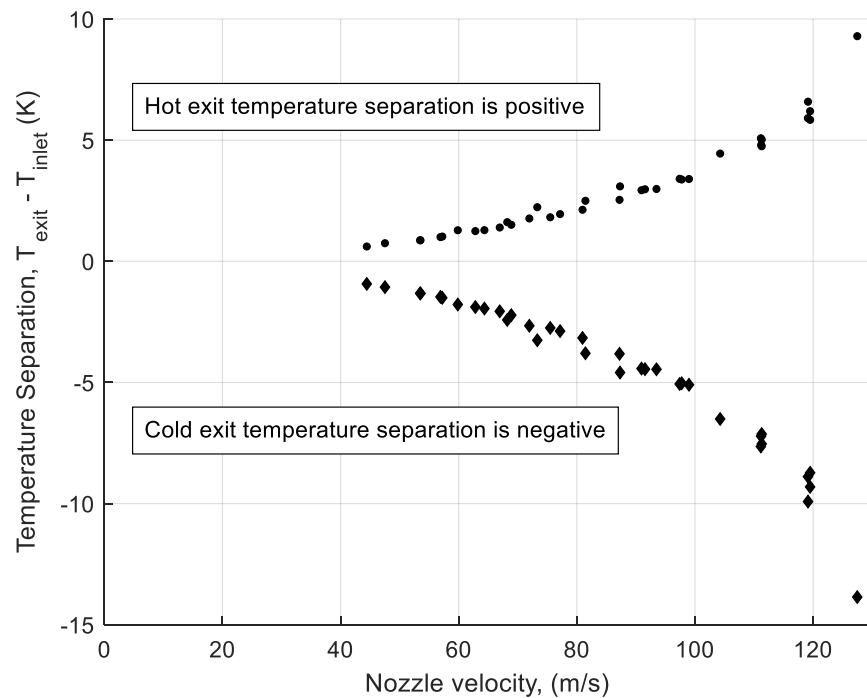

Figure 69. Temperature separation vs. nozzle velocity ($\mu_C = 0.40$)

The results form essentially a single curve for either the hot or cold exit temperature separation, which indicates that nozzle velocity is indeed a strong governing

140

parameter for dimensional temperature separation rather than solely pressure or temperature. Moreover, the strong curvature implies that temperature separation is a higher-order function of nozzle velocity. This result also implies that the sensitivity of temperature separation to nozzle velocity increases at higher velocities or, by association, higher mass flow rates.

3.2.2.3 Conclusions on dimensional investigation of temperature separation

The present study extends our understanding of vortex tubes by identifying gas and flow properties which at least partially govern temperature separation in a vortex tube. Using a novel vortex tube laboratory configuration, experiments were conducted in which mass flow rate, inlet pressure, inlet temperature were independently varied, permitting by extension independent control of the nozzle velocity and volumetric heat capacity, ρC_p. It was found through experiments in air that temperature separation increases with increasing nozzle velocity and decreasing values of ρC_p, though the results are relatively insensitive to changes in ρC_p. It was also found that the greater temperature separation observed with greater inlet temperatures is actually attributable to the greater nozzle velocities associated with the higher inlet temperatures and, to a lesser extent, the slightly lower values of ρC_p. This is the first explanation ever offered regarding the influence of inlet temperature on temperature separation.

Most notably, it was demonstrated that by matching nozzle velocity and ρC_p between cases—even though the pressures, temperatures, Reynolds numbers, and Mach numbers differ—the resulting temperature separation curves are identical. This is the first known demonstration of such a principle, and it suggests that nozzle velocity is

141

fundamental to scaling the performance of a vortex tube, while the nozzle volumetric heat capacity is also relevant to its behavior. Counterintuitively, it was found that nozzle Reynolds number apparently has little influence on temperature separation.

An investigation with CO_2 also found that temperature separation could be closely—but not exactly—matched when nozzle velocity and ρC_p were matched. Observable differences between the cases seem attributable to the Joule-Thomson coefficient of CO_2, and its relatively high sensitivity to nozzle temperature compared to air. This suggests that real gas effects can influence the temperature separation characteristics of a vortex tube and yield pronounced differences between gases.

Finally, it appears that temperature separation has a higher-order dependency on nozzle velocity, as discovered through a data set taken for $\mu_C = 0.40$. Although the data were taken at a variety of inlet pressures, temperatures, and mass flow rates, the results reveal that the temperature separation points collapse almost entirely into a single curve with respect to nozzle velocity. Moreover, even a cursory visual examination reveals a prominent curvature signaling a higher-order increase in temperature separation with nozzle velocity. These findings and those from the multi-μ_C data set suggest that, in air, temperature separation is almost exclusively a function of nozzle velocity and that the influence of mass flow rate, pressure, or temperature on temperature separation is largely due to the influence of that parameter on nozzle velocity. The analysis of the dimensional data sets must now transition to a more fundamental review. The results will be examined in greater detail as a part of a nondimensionalization study to understand the influence of governing dimensionless parameters on dimensionless temperature separation. This will

then permit a deeper understanding of the scaling of the temperature separation phenomenon.

3.2.3 *Developing a method of nondimensionalization for vortex tubes*

While the previous findings represent significant developments, their dimensional nature still belies an incomplete characterization of temperature separation. To demonstrate a more complete understanding of the phenomenon, it is essential to cast it in dimensionless terms. Some partial nondimensionalizations of the governing equations have been undertaken previously, although these have typically relied upon assumed velocity profiles—the realism of which has been debated over the years—with the aim of modeling the internal flow field and explaining the underlying mechanism of temperature separation. These efforts largely predate modern computational codes and include classic works by Kassner and Knoernschild [48], Deissler and Perlmutter [62], and perhaps most comprehensively, Sibulkin [63].

Dimensionless descriptions of temperature separation results have also emerged over the decades, with varying degrees of physical connection to the problem. For instance, Stephan et al. [78] normalized temperature separation curves by the maximum observed change in temperature and found that the performance curves involving different inlet pressures and gases were geometrically similar—an intriguing result that nevertheless offers little prescriptive power. Likewise, Ahlborn et al. [95] and Hamoudi et al. [89] normalized the temperature changes by the inlet temperature, though the basis for this choice of temperature scale appears arbitrary.

The present effort identifies the nondimensional parameters which govern temperature separation as well as the appropriate reference scales for temperature

143

separation, and proposes a means by which results may be nondimensionalized according to meaningful experimental properties. However, this study makes no assumptions regarding the internal flow field nor the actual mechanism of temperature separation; it does not require constant properties, nor even that the working gas behaves ideally. To that end, it does not include the momentum equations, within which several flow field assumptions must be applied. Rather, the analysis focuses on the total energy equation, which accounts for the contributions of work, heat transfer, and real gas effects in a compressible fluid. While the principal aim herein is to identify the defining nondimensional parameters which govern temperature separation in a vortex tube, the resulting equation is valid for a broad range of applications.

But what use is nondimensionalizing temperature separation without probing its underlying mechanism? Supposing for a moment that the underlying mechanism behind temperature separation were identified for a particular case—and it will be in Section 3.2.9 by computational investigation —it still would not necessarily answer a broader question of practical concern: the question of scaling. Given what is known about a vortex tube's performance in one scenario, what conclusions can be drawn about scaling its performance to other scenarios? For the designer with finite experimental and computational resources, this question is significant and can be answered via proper nondimensionalization of the problem.

3.2.3.1 Energy Equation Analysis

The differential form of the total energy equation in index notation, see Panton [91], is Eq (53) where $\partial_0()$ represents the time derivative, $\frac{\partial()}{\partial t}$, and $\partial_i()$ is the spatial

derivative, $\frac{\partial ()}{\partial x_i}$. The left-hand side of the equation may be distributed and the product rule

applied such that the left-hand side is rewritten using eight terms, each of which is

lettered as seen below in Eq (54). Eq (55) represents the continuity equation in index

notation.

$$\partial_0 \left[\rho\left(e + \frac{1}{2}v^2\right)\right] + \partial_i \left[\rho v_i\left(e + \frac{1}{2}v^2\right)\right] = -\partial_i q_i + \partial_i(T_{ij}v_j) + \rho v_i F_i \qquad (53)$$

$$\begin{array}{cccccccc} \text{A} & \text{B} & \text{C} & \text{D} & \text{E} & \text{F} & \text{G} & \text{H} \end{array}$$

$$\rho\partial_0 e + e\partial_0\rho + \frac{v^2}{2}\partial_0\rho + \rho\partial_0\left(\frac{v^2}{2}\right) + e\partial_i(\rho v_i) + \rho v_i\partial_i e + \frac{v^2}{2}\partial_i(\rho v_i) + \rho v_i\partial_i\left(\frac{v^2}{2}\right)$$

$$= -\partial_i q_i + \partial_i(T_{ij}v_j) + \rho v_i F_i \qquad (54)$$

$$\partial_0\rho + \partial_i(\rho v_i) = 0 \qquad (55)$$

It can be seen, by way of Eq (55), that Terms B and E in Eq (54) sum to zero, as

do Terms C and G. The remaining terms may then be rewritten as Eq (56). The left side

of Eq (56) may alternatively be expressed using the substantial derivatives of internal and

kinetic energy, as shown in Eq (57). It may also be shown, such as in Panton [91], that

the substantial derivative of internal energy has the equivalency shown in Eq (58), where

β is the isobaric thermal expansion coefficient and T represents static temperature (not to

be confused with the stress tensor, T_{ij}). Substituting this equivalency into the energy

equation yields, with some rearranging, Eq (59).

$$\rho\partial_0 e + \rho v_i\partial_i e + \rho\partial_0\left(\frac{v^2}{2}\right) + \rho v_i\partial_i\left(\frac{v^2}{2}\right) = -\partial_i q_i + \partial_i(T_{ij}v_j) + \rho v_i F_i \qquad (56)$$

$$\rho\partial_0 e + \rho v_i \partial_i e + \rho\partial_0\left(\frac{v^2}{2}\right) + \rho v_i \partial_i\left(\frac{v^2}{2}\right) = -\partial_i q_i + \partial_i(T_{ij} v_j) + \rho v_i F_i \tag{57}$$

$$\frac{De}{Dt} = C_p \frac{DT}{Dt} - \frac{\beta}{\rho} T \frac{DP}{Dt} - \frac{P}{\rho}\partial_i v_i \tag{58}$$

$$\rho C_p \frac{DT}{Dt} + \rho \frac{D\left(\frac{v^2}{2}\right)}{Dt} = -\partial_i q_i + \partial_i(T_{ij} v_j) + \rho v_i F_i + \beta T \frac{DP}{Dt} + P\partial_i v_i \tag{59}$$

It is worth recalling that manipulating the energy equation to the form in Eq (59)

required no assumptions and is applicable to all fluids. It is here that the first assumption

is introduced: the fluid in question is Newtonian, with stress tensor defined by Eq (60),

where τ_{ij} are the components of the viscous stress tensor. With some substitution and by

applying the product rule and the appropriate index notation manipulations, the work

done by fluid stresses can be represented using the equivalency in Eq (61). Substituting

this expression back into the energy equation, recalling that the substantial derivative of

static pressure can be expressed as $\frac{DP}{Dt} = \partial_0 P + v_i\partial_i P$, yields Eq (62).

$$T_{ij} = -P\delta_{ij} + \tau_{ij} \tag{60}$$

$$\partial_i(T_{ij} v_j) = -v_i\partial_i P - P\partial_i v_i + \partial_i(v_j\tau_{ij}) \tag{61}$$

$$\rho C_p \frac{DT}{Dt} + \rho \frac{D\left(\frac{v^2}{2}\right)}{Dt} = -\partial_i q_i + \partial_i(v_j\tau_{ij}) + (\beta T - 1)v_i\partial_i P + \beta T\partial_0 P + \rho v_i F_i \tag{62}$$

Body forces such as gravity are expected to be insignificant to vortex tube operation, nor is there any expectation that the presence of a gravitational field is required for the operation, so it is assumed that $\rho v_i F_i = 0$. Using standard thermodynamic relations (for example, see Demirel and Gerbaud [96]), the isobaric thermal expansion coefficient may be expressed using the Joule-Thomson coefficient, μ_{JT}, where $\beta T - 1 = \rho C_p \mu_{JT}$. With these substitutions, the energy equation may now be represented using Eq (63).

$$\rho C_p \frac{DT}{Dt} + \rho \frac{D\left(\frac{v^2}{2}\right)}{Dt} = -\partial_i q_i + \partial_i\left(v_j \tau_{ij}\right) + \partial_0 P + \rho C_p \mu_{JT} \frac{DP}{Dt} \tag{63}$$

Next, the equation may be nondimensionalized by choosing appropriate scales for length, r, velocity, v, density, ρ, specific heat at constant pressure, C_p, Joule-Thomson coefficient, μ_{JT}, dynamic viscosity, μ, and thermal conductivity, k. Nondimensionized values of temperature, pressure, time, viscous work, and heat transfer employ a combination of these scales and are indicated in Table 11. The appropriate scale for viscous work arises from the form of the viscous stress tensor for a Newtonian fluid in Eq (64). Likewise, the scale for heat transfer is obvious from Fourier's law, in Eq (65). The temperature scale, $\frac{v_0^2}{C_{p,0}}$, follows naturally from the aforementioned scales.

$$\tau_{ij} = -\frac{2}{3}\mu\partial_k v_k \delta_{ij} + \mu\left(\partial_i v_j + \partial_j v_i\right) \tag{64}$$

$$q_i = -k\partial_i T \tag{65}$$

Table 11. Nondimensionalization of relevant gas and flow properties

$r^* = \dfrac{r}{R_0}$	$v^* = \dfrac{v}{V_0}$	$\rho^* = \dfrac{\rho}{\rho_0}$	$C_p^* = \dfrac{C_p}{C_{p,0}}$
$\mu_{JT}^* = \dfrac{\mu_{JT}}{\mu_{JT,0}}$	$T^* = \dfrac{T - T_0}{\dfrac{V_0^2}{C_{p,0}}}$	$P^* = \dfrac{P - P_0}{\rho_0 V_0^2}$	$t^* = \dfrac{tV_0}{R_0}$
$\partial_i^*\big(v_j^*\tau_{ij}^*\big) = \dfrac{R_0^2}{\mu_0 V_0^2}\,\partial_i\big(v_j\tau_{ij}\big)$		$\partial_i^* q_i^* = \dfrac{R_0^2}{k_0\dfrac{V_0^2}{C_{p,0}}}\,(\partial_i q_i)$	

Substitution of the nondimensionalized values yields Eq (66). The terms in the brackets may be rewritten as the substantial derivative of total temperature plus a new term involving the substantial derivative of $C_p{}^*$, using the equivalency of Eq (67) and the substantial derivative of the total temperature defined using Eq (68).

$$\rho^* C_p^* \left[\frac{DT^*}{Dt^*} + \frac{1}{C_p^*}\frac{D\left(\dfrac{v^{*2}}{2}\right)}{Dt^*} \right] \tag{66}$$

$$= \frac{k_0}{\rho_0 C_{p,0} V_0 R_0}\left(-\partial_i^* q_i^*\right) + \frac{\mu_0}{\rho_0 V_0 R_0}\,\partial_i^*\big(v_j^*\tau_{ij}^*\big) + \partial_0^* P^* + \rho_0 C_{p,0}\mu_{JT,0}\rho^* C_p^* \mu_{JT}^* \frac{DP^*}{Dt^*}$$

$$\frac{1}{C_p^*}\frac{D\left(\dfrac{v^{*2}}{2}\right)}{Dt^*} = \frac{D\left(\dfrac{v^{*2}}{2C_p^*}\right)}{Dt^*} + \frac{v^{*2}}{2C_p^{*2}}\frac{DC_p{}^*}{Dt^*} \tag{67}$$

$$\frac{DT_t^*}{Dt^*} = \frac{DT^*}{Dt^*} + \frac{D\left(\dfrac{v^{*2}}{2C_p^*}\right)}{Dt^*} \tag{68}$$

148

While arbitrary, the reference property values used in the scales identified in

Table 11 will be defined at the nozzle for convenience. Since the nozzle velocity drives

the internal velocity profile, it will be used for the velocity scale, V_0. The length scale, R_0,

will be the nozzle hydraulic diameter, D_h. The gas properties will each be evaluated at the

static pressure and temperature in the nozzle unless specified otherwise. In this way, the

Reynolds number will be defined using Eq (69) and the Prandtl number using Eq (70).

With these substitutions, the reader at last arrives at Eq (71). This dimensionless form is

valid for any Newtonian fluid with negligible work done by body forces; it does not

assume steady flow nor any constant properties and because it is in a differential form, it

is valid for any point in the flow.

$$Re = \frac{\rho_0 V_0 D_h}{\mu_0} \tag{69}$$

$$Pr = \frac{C_{p,0}\mu_0}{k_0} \tag{70}$$

$$\rho^* C_p^* \left(\frac{DT_t^*}{Dt^*} + \frac{v^{*2}}{2C_p^*} \frac{DC_p^*}{Dt^*} \right)$$

$$= \left(\frac{k_0}{\rho_0 C_{p,0} V_0 D_h} \right) (-\partial_i^* q_i^*) + \left(\frac{\mu_0}{\rho_0 V_0 D_h} \right) \partial_i^* (v_j^* \tau_{ij}^*) + \partial_0^* P^* + \left(\rho_0 C_{p,0} \mu_{JT,0} \right) \rho^* C_p^* \mu_{JT}^* \frac{DP^*}{Dt^*} \tag{71}$$

The left side of Eq (71) contains the substantial derivative of total temperature,

$\frac{DT_t^*}{Dt^*}$, as well as the substantial derivative of the specific heat, $\frac{DC_p^*}{Dt^*}$. The latter term may

appear unfamiliar, but it is necessary in the case of variable properties; for a scenario with

a near-constant C_p, its value approaches zero. Eq (71) reveals that changes in the total

temperature of a fluid depend on the contributions of the four terms on the right side: heat

transfer, work due to viscous stresses, pressure fluctuations, and the effects of intermolecular forces introduced via the Joule-Thomson coefficient, μ_{JT}.

The term $\frac{k_0}{\rho_0 C_{p,0} V_0 D_h}$ is readily identifiable as the reciprocal of the Péclet number, which is simply the product of the reciprocals of the Prandtl and Reynolds numbers, as in Eq (72). A slight rearrangement yields the final equation, Eq (73). Three nondimensional parameters are evident: the Reynolds number, the Prandtl number, and a new parameter, $\rho_0 C_{p,0} \mu_{JT,0}$.

$$\frac{1}{Pe} = \left(\frac{1}{Pr}\right)\left(\frac{1}{Re}\right) \tag{72}$$

$$\rho^* C_p^* \left(\frac{DT_t^*}{Dt^*} + \frac{v^{*2}}{2C_p^{*2}} \frac{DC_p^{*}}{Dt^*}\right) = \left(\frac{1}{Re}\right)\left[\left(\frac{1}{Pr}\right)(-\partial_i^* q_i^*) + \partial_i^*\left(v_j^* \tau_{ij}^*\right)\right] + \partial_0^* P^* + \left(\rho_0 C_{p,0} \mu_{JT,0}\right)\rho^* C_p^* \mu_{JT}^* \frac{DP^*}{Dt^*} \tag{73}$$

3.2.3.2 The Roles of Gas and Flow Properties in Temperature Separation

All of the gas and flow properties relevant to temperature separation can be found in the three dimensionless parameters in Eq (73) and in the associated scales in Table 11. Eq (73) indicates that the diffusion of kinetic energy in the flow, $\partial_i^*\left(v_j^* \tau_{ij}^*\right)$, is governed by $\frac{1}{Re}$, and that the diffusion of heat, $-\partial_i^* q_i^*$, is governed by $\frac{1}{Re}$ and $\frac{1}{Pr}$. The contribution of intermolecular forces, $\rho^* C_p^* \mu_{JT}^* \frac{DP^*}{Dt^*}$, to a change in total temperature along a streamline—which, for a gas, is equivalent to real-gas effects—is governed by the parameter $\rho_0 C_{p,0} \mu_{JT,0}$. However, $\rho_0 C_{p,0} \mu_{JT,0}$ has distinctly different behavior than Re and Pr due to the nature of μ_{JT}. For gases below the inversion point, $\mu_{JT} > 0$ and a pressure decrease drives a corresponding decrease in temperature. At the inversion point $\mu_{JT} = 0$, as does

150

$\rho_0 C_{p,0} \mu_{JT,0}$. For gases above the inversion point, $\mu_{JT} < 0$, which serves to increase the temperature with a pressure drop. In fact, it is conceivable that $\mu_{JT} < 0$ and $\mu_{JT} > 0$ at different points in the flow field inside a vortex tube, if the inlet temperature is sufficiently close to the inversion point. This qualitatively different variation presents a slight challenge in reporting differences in $\rho_0 C_{p,0} \mu_{JT,0}$ between cases. For example, while differences in Re_{D_h} are often reasonably reported as a percentage of a reference value, it is not hard to imagine two contrasting cases near the inversion point in which the value of $\rho_0 C_{p,0} \mu_{JT,0}$ decreases by more than 100% (or more perplexingly, increases in magnitude by a negative percentage), even if the actual magnitude of differences is very small. For this reason, differences in $\rho_0 C_{p,0} \mu_{JT,0}$ will simply be compared simply in terms of magnitude.

In theory, vortex tube flows with identical Re, Pr, and $\rho_0 C_{p,0} \mu_{JT,0}$ should yield identical nondimensional profiles of $\rho^* C_p^* \left(\frac{DT_t^*}{Dt^*} + \frac{v^{*2}}{2C_p^{*2}} \frac{DC_p^{*}}{Dt^*} \right)$, though the dimensional profiles may differ. However, a subtle but important limit to nondimensional scaling lies in the manner in which dimensionless parameters vary with respect to each other. For example, μ_{JT} for air is much more sensitive to temperature near 300 K than 500 K; if the variation of μ_{JT}^* with respect to T^* differs between cases, then even the nondimensional profiles of $\rho^* C_p^* \left(\frac{DT_t^*}{Dt^*} + \frac{v^{*2}}{2C_p^{*2}} \frac{DC_p^{*}}{Dt^*} \right)$ will differ between cases. Significantly, the temperature scale was found to be $\frac{V^2}{C_p}$, suggesting that *dimensional* temperature differences compared to a reference temperature scale with the square of nozzle velocity and inversely with C_p.

Eq (73) has broad application to compressible and incompressible flows of Newtonian fluids including many liquids, such as water. Because $\mu_{JT} < 0$ for liquid water under most conditions, the contribution of $\rho_0 C_{p,0} \mu_{JT,0}$ serves to increase temperature across a pressure drop. This may help explain why cases in which one fluid stream becomes *colder* than the inlet temperature and the other becomes hotter have not thus far been observed in incompressible fluids.

Pressure fluctuations also show up in the equation via the term $\partial_0^* P^*$ and in the time component of the substantial derivative $\frac{DP^*}{Dt^*}$. The assumption of steady flow could be made on the logical basis that pressure fluctuations have a zero mean, i.e. $\partial_0 P = 0$, but such a choice should not be made arbitrarily: there has been considerable discussion of the potential contribution of unsteady pressure fluctuations to temperature separation, such as Eckert [3]. There has also been a rich study of the complex interaction between acoustic phenomena and temperature separation, such as Kurosaka [5] and Seol and Goldstein [6]. Although the role of acoustic interactions is out of scope of the present research, perhaps a non-zero-mean coupling of pressure fluctuations into the fluid may indeed contribute to temperature separation via the term $\left(\rho_0 C_{p,0} \mu_{JT,0}\right) \rho^* C_p^* \mu_{JT}^* \frac{DP^*}{Dt^*}$.

One must still interpret the analytical findings with caution. The total temperature differences across a vortex tube are certainly attributable to the combined action of the terms identified in the energy equation. However, due to the complexity of the flow in a vortex tube, it should not be assumed that increasing or decreasing any of the parameters automatically or universally relates to increased or decreased temperature separation. The signs of the nondimensional terms, i.e. $-\partial_i^* q_i^*$, $\partial_i^* \left(v_j^* \tau_{ij}^*\right)$, $\partial_0^* P^*$, and $\rho^* C_p^* \mu_{JT}^* \frac{DP^*}{Dt^*}$, could

be positive or negative in different parts of the flow, and the relative magnitudes of the governing parameters may serve to alternately intensify or diminish the temperature separation.

3.2.3.3 Selecting a Dimensionless Form

The application of Eq (73) has not yet been fully specified. The hot and cold vortex tube exits are points on the solution at which flow properties have been measured, and at least two relevant choices are available to nondimensionalize the results. The first is more straightforward: compare the dimensionless changes in total temperature, T_t^*, where $T_t^* = \frac{T_{t,exit} - T_{t,inlet}}{\frac{V^2}{C_p}}$. This bears a resemblance to historical dimensional temperature separation plots and is justified on the basis that T_t^* alone is inside the substantial derivative in Eq (73).

There is also a theoretical basis for evaluating the dimensionless product $\rho^* C_p^* T_t^*$, effectively the dimensionless volumetric energy density, since the left side of Eq (73)—with some manipulation and use of Eq (55)—has the equivalency shown in Eq (74). Eq (74) shows that indeed, the product $\rho^* C_p^* T_t^*$ may be treated as a dependent variable itself. With this method, exit static pressure and temperature are used to compute exit density and C_p, which are then converted to ρ^* and C_p^* using nozzle properties. Both methods of nondimensionalizing temperature separation will be compared.

$$\rho^* C_p^* \left(\frac{DT_t^*}{Dt^*} + \frac{v^{*2}}{2C_p^{*2}} \frac{DC_p^{\ *}}{Dt^*} \right) = \frac{D\left(\rho^* C_p^* T_t^* \right)}{Dt^*} + \rho^* \left(T_t^* - \frac{v^{*2}}{2C_p^*} \right) \frac{DC_p^{\ *}}{Dt^*} + \rho^* C_p^* T_t^* \partial_i^* v_i^* \tag{74}$$

3.2.4   *Nondimensionalization of experimental vortex tube results*

The method of nondimensionalization is now applied to the experimental data sets, each of which serves a different analytical purpose. First, results for the twelve cases using air in the multi-μ_C data set, which stem from the investigations of the influence of mass flow rate, temperature and pressure, are plotted in Figure 70, and these will help establish the most appropriate method of nondimensionalizing results. The corresponding nozzle flow conditions are listed in Table 12 where they are now labeled as Cases A – L.

The results for each of the cases were then nondimensionalized; curves of T_t^* are presented in Figure 71 and curves of $\rho^* C_p^* T_t^*$ are in Figure 72. The latter reveals a tighter collapse of the performance curves and remarkable insensitivity to changes in flow conditions for a single working gas. The range of $\rho^* C_p^* T_t^*$ values at the hot and cold exits is a function of cold fraction such that the range of $\rho^* C_p^* T_t^*$ is larger at the cold exit for small cold fractions and larger at the hot exit for large cold fractions. In essence, the spread of $\rho^* C_p^* T_t^*$ values at an exit appears to increase with decreasing mass flow through that exit. At the cold exit, the range of $\rho^* C_p^* T_t^*$ values is at a minimum of 0.0189 for $\mu_C = 0.75$ and a maximum of 0.104 for $\mu_C = 0.20$ while the mean values range from -0.31 to -0.55; this equates to being within ±4% of the mean value for most cold fractions, and up to ±12% at $\mu_C = 0.20$. At the hot exit, the range of $\rho^* C_p^* T_t^*$ values is at a minimum of 0.0235 for $\mu_C = 0.25$ and a maximum of 0.087 for $\mu_C = 0.80$ while the mean values range from 0.06 to 1.10; this equates to being within ±5% of the mean value for most cold fractions except for cold fractions of $\mu_C \leq 0.30$ where the mean values of $\rho^* C_p^* T_t^*$ are small. Contrast this with the curves of T_t^*, which feature larger, though also

qualitatively different, variations of T_t^*. For example, values of T_t^* at the cold exit feature

a larger spread for the middle cold fractions and smaller variations at the extremes: for

$\mu_C = 0.40$, T_t^* remains within ±14% of the mean value, but at $\mu_C = 0.80$, T_t^* remains

within ±8% of the mean value. This analysis suggests that $\rho^* C_p^* T_t^*$ is the more appropriate

method for nondimensionalizing temperature separation. This is the first instance in the

known literature in which a diverse set of vortex tube performance curves have been

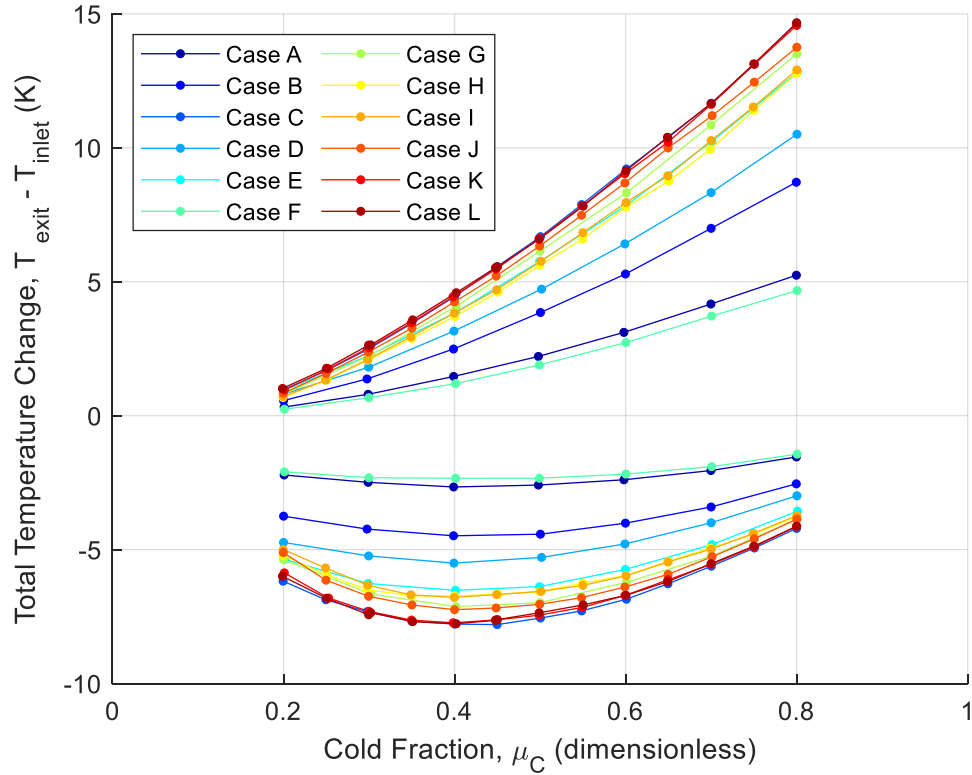reduced to similarity based on the intrinsic fluid properties of the experiment.

Figure 70. Summary plot of temperature separation for air cases

155

Table 12. Cases for nondimensionalization of temperature separation curves

| Case:	A	B	C	D	E	F	G	H	I	J	K	L
Mass flow rate (kg/s)	1.183×10^{-3}	1.183×10^{-3}	1.420×10^{-3}	1.184×10^{-3}	1.184×10^{-3}	1.382×10^{-3}	1.383×10^{-3}	1.776×10^{-3}	1.420×10^{-3}	1.027×10^{-3}	1.420×10^{-3}	1.421×10^{-3}
Inlet T_{total} (K)	293.3	293.3	293.2	312.7	332.7	293.4	293.8	293.3	293.3	293.4	313.3	333.1
Inlet P_{static} (bar, gauge)	3.001	3.001	3.000	3.000	3.003	5.001	3.000	4.183	3.154	2.000	3.275	3.549
Re	**14955**	**14955**	**18034**	**14251**	**13602**	**17366**	**17520**	**22508**	**18010**	**13029**	**17111**	**16322**
Pr	**0.721**	**0.721**	**0.721**	**0.718**	**0.716**	**0.722**	**0.721**	**0.722**	**0.721**	**0.720**	**0.718**	**0.716**
$\rho_0 C_{p,0} \mu_{JT,0}$	**0.011**	**0.011**	**0.0108**	**0.0089**	**0.0073**	**0.0165**	**0.0108**	**0.0140**	**0.0113**	**0.0081**	**0.0094**	**0.0082**
Velocity (m/s)	81.38	81.38	98.95	87.11	92.86	62.80	96.59	95.29	95.04	95.21	98.79	98.52
Mach number	0.238	0.238	0.291	0.247	0.255	0.183	0.283	0.280	0.279	0.279	0.280	0.271
ρ (kg/m³)	4.622	4.622	4.563	4.322	4.056	6.996	4.551	5.928	4.751	3.429	4.571	4.587
μ (μPa-s)	18.14	18.14	18.05	19.05	19.96	18.24	18.09	18.09	18.08	18.06	19.03	19.96
k (mW/m-K)	25.45	25.45	25.32	26.83	28.23	25.64	25.38	25.40	25.37	25.33	26.81	28.24
C_p (kJ/kg-K)	1.012	1.012	1.012	1.012	1.012	1.015	1.012	1.014	1.012	1.010	1.012	1.013
μ_{JT} (K/bar)	0.2345	0.2345	0.2348	0.2043	0.1776	0.2327	0.2338	0.2337	0.2344	0.2351	0.2034	0.1768
Nozzle T_{static} (K)	291.3	290.0	288.3	308.9	328.4	291.4	289.1	288.8	288.8	288.8	308.4	328.2
Nozzle P_{static} (Pa, absolute)	390293	384687	377571	383127	382210	585213	377643	491365	393842	284320	404644	432078
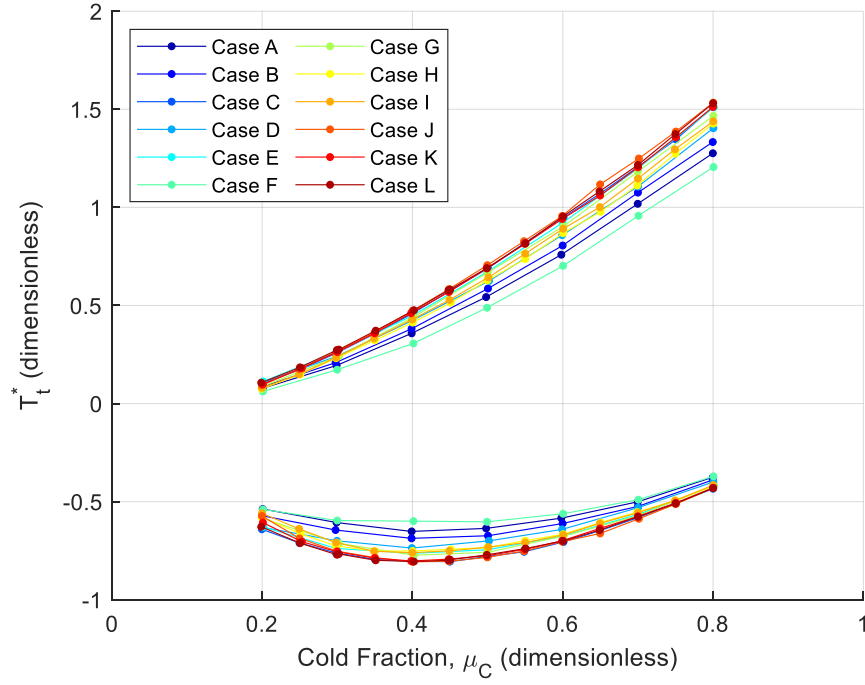
Figure 71. Summary nondimensional total temperature profiles, T_t^*, for all air cases
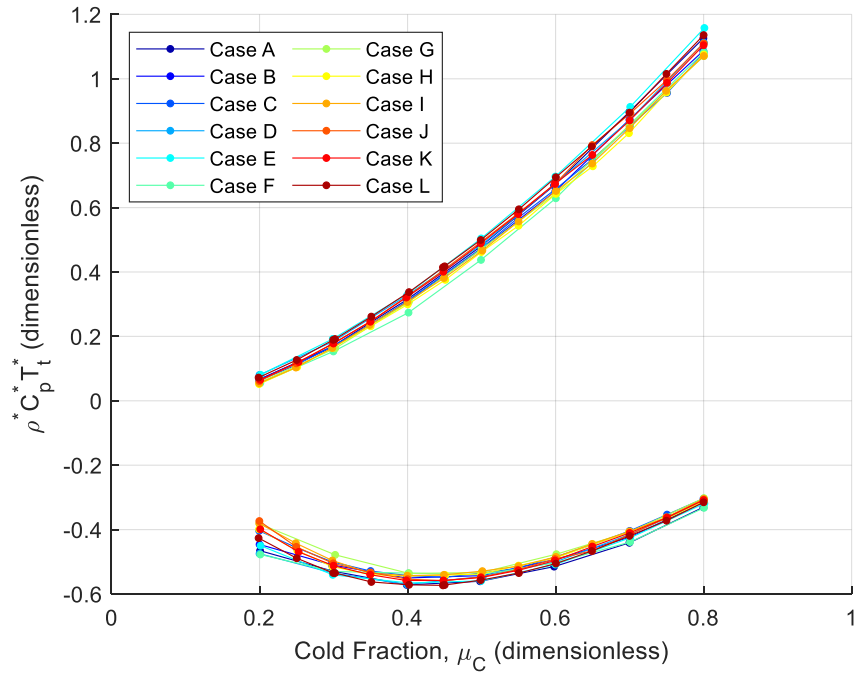

Figure 72. Summary nondimensional total temperature profiles, $\rho^* C_p^* T_t^*$, for all air cases

3.2.4.1 Temperature Separation Sensitivity to Governing Nondimensional Parameters

Although it has been shown analytically that Re, Pr, and $\rho_0 C_{p,0} \mu_{JT,0}$ would be expected to govern temperature separation, and demonstrated with experimental data that $\rho^* C_p^* T_t^*$ is an appropriate nondimensionalization of temperature separation, it is not yet clear how sensitive the dimensionless profiles actually are to variations in Re, Pr, and $\rho_0 C_{p,0} \mu_{JT,0}$. A major objective of the present study is to more fully understand the influence of Re and $\rho_0 C_{p,0} \mu_{JT,0}$ on $\rho^* C_p^* T_t^*$; the Prandtl number of air is nearly constant across the range of achievable flow conditions and thus its influence cannot be independently evaluated. The single-μ_C data set taken at $\mu_C = 0.40$ was analyzed for this purpose, due to a wider range and higher resolution of Re. Recall that Figure 69 (see page 140) revealed that the temperature separation increased as a higher order function of nozzle velocity. This is now expected, given the analytical finding that dimensional temperature separation scales with $\frac{V_0^2}{C_{p,0}}$ based on nozzle properties.

The data from Figure 69 were nondimensionalized to $\rho^* C_p^* T_t^*$ and plotted against nozzle Reynolds number in Figure 73. There is some noticeable dispersion in $\rho^* C_p^* T_t^*$ values for the lower Reynolds numbers between 11,000 and 15,000, which is probably attributable to the increased experimental uncertainty associated with lower mass flow rates. However, on the whole, the results do not imply a generalizable trend of $\rho^* C_p^* T_t^*$ with respect to Re, and even suggest that $\rho^* C_p^* T_t^*$ is not a function of Reynolds number across the range of observed values. It is surprising that a governing parameter like the Reynolds number does not apparently exert a strong influence on dimensionless

158

temperature separation, but this is consistent with the earlier finding that Reynolds

number is not a consistent predictor even of dimensional temperature separation.

Although the nondimensionalization process did not yield Mach number as a governing

parameter, the influence of Mach number on $\rho^* C_p^* T_t^*$ is shown in Figure 74 for the tested

range of approximately 0.13 to 0.35. Figure 74 reveals that Mach number does not have a
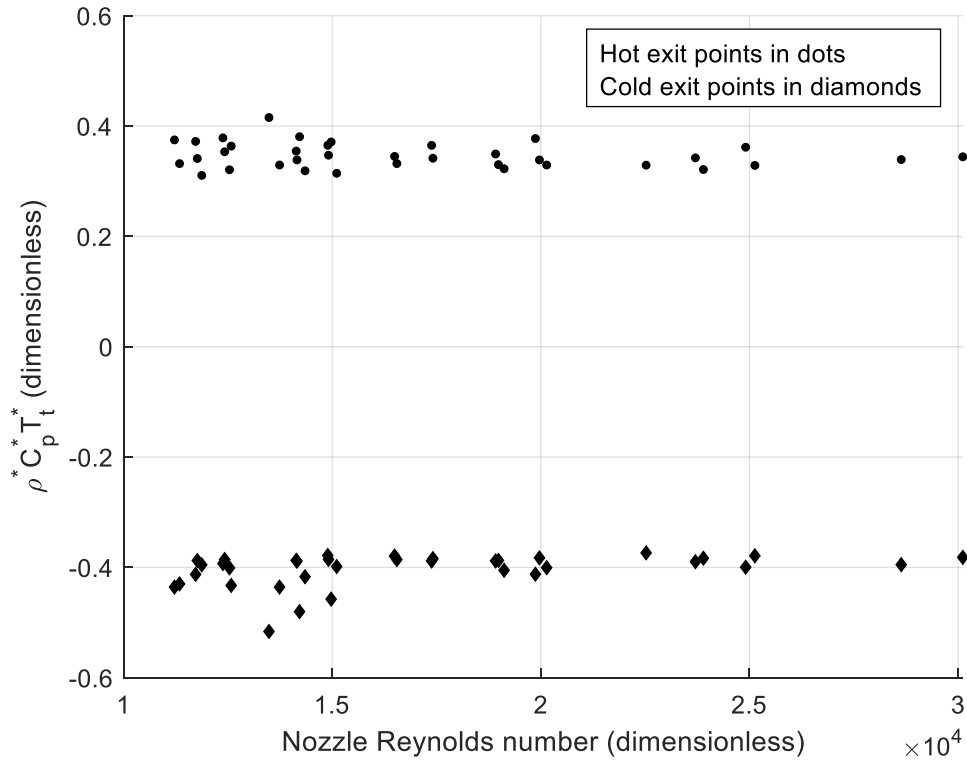
discernable influence on $\rho^* C_p^* T_t^*$.

Figure 73. Dimensionless temperature separation $\rho^* C_p^* T_t^*$ vs. Re ($\mu_C = 0.40$)
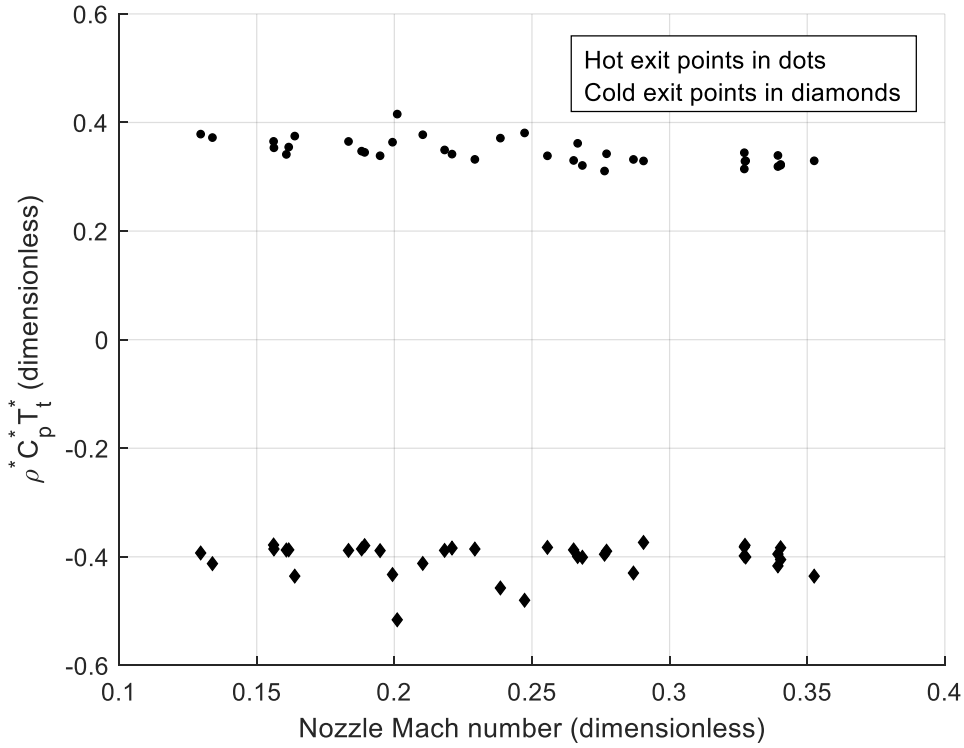
Figure 74. Dimensionless temperature separation $\rho^* C_p^* T_t^*$ vs. Mach number ($\mu_C = 0.40$)

The investigation was extended by plotting $\rho^* C_p^* T_t^*$ against $\rho_0 C_{p,0} \mu_{JT,0}$ in Figure 75 for a tested range of $0.00532 \leq \rho_0 C_{p,0} \mu_{JT,0} \leq 0.0167$. In a similar fashion, the data do not reveal any trends in $\rho^* C_p^* T_t^*$ with respect to $\rho_0 C_{p,0} \mu_{JT,0}$ and likewise imply that $\rho^* C_p^* T_t^*$ is not a function of $\rho_0 C_{p,0} \mu_{JT,0}$ across this range of values, in which the maximum is approximately triple the smallest value. It is again surprising that a governing parameter does not strongly influence dimensionless temperature separation, but less so than with respect to Reynolds number. It is well known that real gas effects, including the influence of μ_{JT}, are not prominent in air and therefore air is frequently—and reasonably—modeled as an ideal gas in various fluids problems.
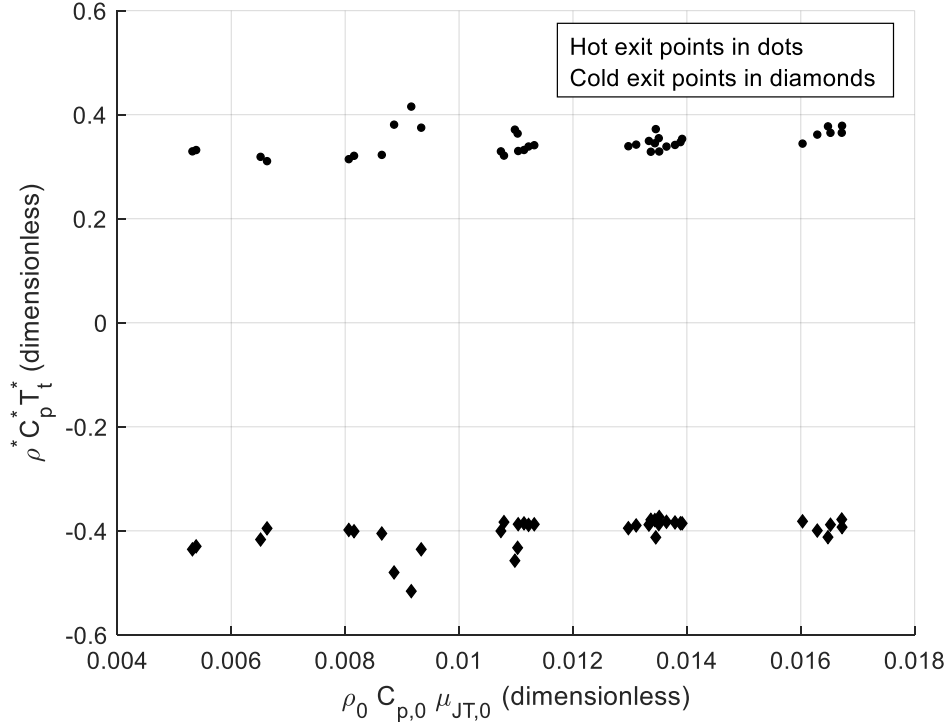
160

Figure 75. Dimensionless temperature separation $\rho^* C_p^* T_t^*$ vs. $\rho_0 C_{p,0} \mu_{JT,0}$ ($\mu_C = 0.40$)

Finally, the investigation returns to the data set in which experiments were conducted using CO_2 as the working gas for a variety of cold fraction (see Section 3.2.2.1). The nozzle flow parameters are listed in Table 13; also listed are two cases from the cases using air, which feature comparable nozzle Reynolds numbers as the CO_2 cases. The Prandtl number differs by 8% between CO_2 and air. However, the most striking difference lies in the magnitude of $\rho_0 C_{p,0} \mu_{JT,0}$, which is approximately six times greater for the CO_2 cases than those using air; it also varies by up to 0.0172 across the cases, nearly twice the greatest variations seen in air (see cases E and F in Table 12).

161

Table 13. Flow conditions for compared cases using CO_2 and Air

Case:	M (CO_2)	N (CO_2)	O (CO_2)	H (Air)	I (Air)
Mass flow rate (kg/s)	1.410×10^{-3}	1.420×10^{-3}	1.393×10^{-3}	1.776×10^{-3}	1.420×10^{-3}
Inlet T_{total} (K)	292.9	313.6	333.5	293.3	293.3
Inlet P_{static} (bar, gauge)	2.771	3.040	3.216	4.183	3.154
$\boldsymbol{Re}$	**22196**	**20920**	**19336**	**22508**	**18010**
$\boldsymbol{Pr}$	**0.780**	**0.770**	**0.762**	**0.722**	**0.721**
$\boldsymbol{\rho_0 C_{p,0} \mu_{JT,0}}$	**0.0652**	**0.0560**	**0.0480**	**0.0140**	**0.0113**
Velocity (m/s)	68.13	68.44	68.26	95.29	95.04
Mach number	0.256	0.248	0.240	0.280	0.279
ρ (kg/m^3)	6.580	6.599	6.489	5.928	4.751
μ (μPa-s)	14.56	15.56	16.52	18.09	18.08
k (mW/m-K)	16.12	17.79	19.44	25.40	25.37
C_p (kJ/kg-K)	0.864	0.880	0.896	1.014	1.012
μ_{JT} (K/bar)	1.1466	0.9634	0.8260	0.2337	0.2344
Nozzle T_{static} (K)	290.1	310.8	330.7	288.8	288.8
Nozzle P_{static} (Pa,	360604	387422	405373	491365	393842

The curves of dimensional temperature separation of Cases M, N, and O from the original study were shown originally in Figure 67 as Cases 6.1, 6.2, and 6.3, respectively. The differences between the dimensional cold exit curves were attributed to differences in μ_{JT} between cases, which are approximately four to six times greater in CO_2 than in air. However, when reduced to $\rho^* C_p^* T_t^*$, as shown in Figure 76 the resulting CO_2 curves reveal the same dimensionless similarity to each other that was found in air. That is not to say that the curves for air and CO_2 are identical; on the contrary: curves of $\rho^* C_p^* T_t^*$ for cases H and I—which used air—are also shown in Figure 76 and illustrate that the two gases yield pronounced differences in dimensionless performance.
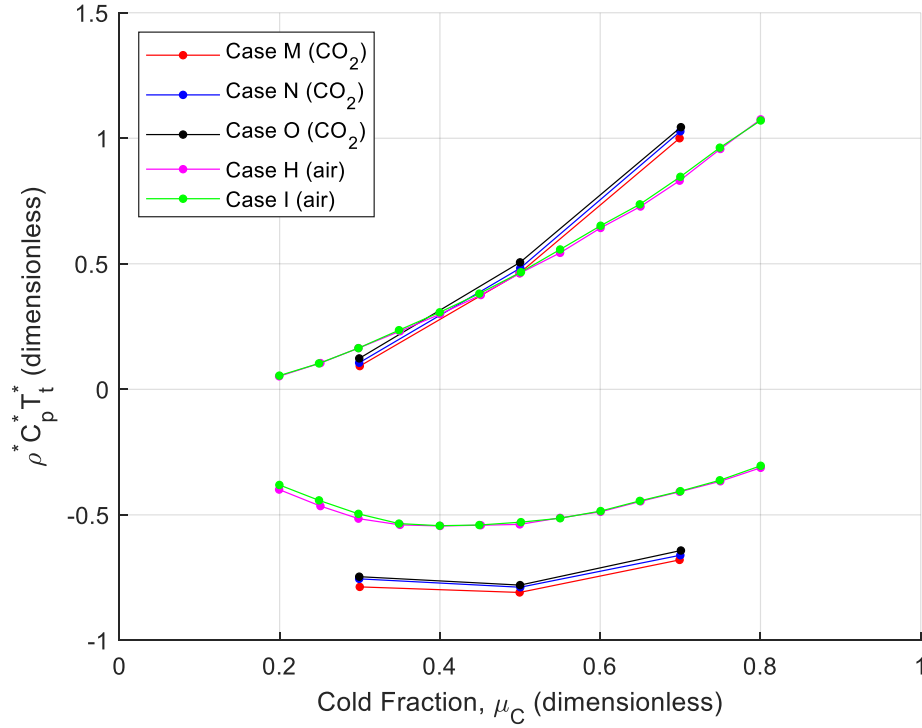
Figure 76. Nondimensional temperature separation, $\rho^* C_p^* T_t^*$, for CO_2 and air

The reason for the differences seems most likely related to $\rho_0 C_{p,0} \mu_{JT,0}$, which

ranges from 0.0480 to 0.0652 for CO_2, but only between 0.0113 and 0.0165 for air. If

$\rho_0 C_{p,0} \mu_{JT,0}$ is indeed responsible for the different curves, it is interesting that the

differences in $\rho_0 C_{p,0} \mu_{JT,0}$ between the gases are large enough to manifest as different

shaped curves, though the differences in $\rho_0 C_{p,0} \mu_{JT,0}$ between cases of the same gas—

particularly CO_2—are not large enough to cause a noticeable dispersion.

3.2.4.2 Conclusions regarding nondimensionalization

The present study extends our understanding of vortex tubes first through a

nondimensionalization of the total energy equation, which casts variations in total

temperature in terms of viscous work, heat transfer, pressure changes, and real gas

effects. This form identified three dimensionless parameters which govern changes in total temperature and, in turn, contribute to the temperature separation phenomenon: Reynolds number, Prandtl number, and a new parameter, $\rho_0 C_{p,0} \mu_{JT,0}$, which governs the contribution of real gas effects. The inherent temperature scale for temperature separation is $\frac{V^2}{C_p}$, based on the bulk velocity and specific heat at the nozzle. A set of experimental temperature separation curves were nondimensionalized using two methods: first, by converting the temperature differences between the exits and the inlet to a dimensionless total temperature difference, T_t^*; second, by converting differences in the volumetric energy density between the inlet and exits to the novel dimensionless product $\rho^* C_p^* T_t^*$.

When the experimental results are converted to $\rho^* C_p^* T_t^*$, the performance curves spanning cold fractions from $0.20 \leq \mu_C \leq 0.80$ collapse tightly to nearly a single curve—much more so than those of T_t^*—suggesting that $\rho^* C_p^* T_t^*$ is the more appropriate dimensionless characterization of temperature separation. Variations of the governing parameters did not strongly influence the dimensionless performance of the vortex tube for a single gas; in air, Re ranged from approximately 12,000 to 22,500. This is the first such nondimensionalization of vortex tube performance curves based on fluid properties relevant to the flow problem.

The addition of a new high-resolution experimental data set collected for a cold fraction of $\mu_C = 0.40$ permitted an analysis of the variation of $\rho^* C_p^* T_t^*$ in air with respect to Reynolds number across $11222 \leq Re \leq 30112$ and with respect to the new parameter $\rho_0 C_{p,0} \mu_{JT,0}$ across $0.0053 \leq \rho_0 C_{p,0} \mu_{JT,0} \leq 0.0167$. The findings revealed that $\rho^* C_p^* T_t^*$ was nearly constant with no discernable trends across these ranges with respect to either

parameter. This does not imply that $\rho^* C_p^* T_t^*$ is entirely independent of Re and

$\rho_0 C_{p,0} \mu_{JT,0}$; rather, it suggests that this range of values is may not be broad enough to

evince any underlying dependence. It is surprising that the governing parameters hold

such little influence on dimensionless temperature separation for this device, across the

given range of values, in air, but this finding is consistent with the investigation of

dimensional temperature separation, in which Reynolds number had virtually no

predictive power. Such robustness may actually serve to increase the utility of the product

$\rho^* C_p^* T_t^*$ in predicting dimensional temperature separation—an application which will be

investigated in Section 3.2.6. It should not be expected that the curves of $\rho^* C_p^* T_t^*$ will be

identical between vortex tubes; rather, curves of $\rho^* C_p^* T_t^*$ are likely tied to a specific

geometry.

Investigations with CO_2 also found that nondimensionalizing according to $\rho^* C_p^* T_t^*$

is appropriate. The dimensional experimental results differed between cases due to

differences in μ_{JT}, but despite substantial differences in $\rho_0 C_{p,0} \mu_{JT,0}$ between the CO_2

cases—twice those in air—the curves of $\rho^* C_p^* T_t^*$ similarly collapsed to nearly a single

curve. However, the curves of $\rho^* C_p^* T_t^*$ with respect to cold fraction for air and CO_2 are

markedly different, revealing a more fundamental dissimilarity in behavior between

gases. The cases compared between CO_2 and air featured nearly identical Reynolds

numbers, Prandtl numbers differing by 8%, and differences in $\rho_0 C_{p,0} \mu_{JT,0}$ by a factor of

4.66; this led to the conclusion that the nondimensional differences between gases should

be attributed to the contribution of $\rho_0 C_{p,0} \mu_{JT,0}$ and hence real gas effects.

3.2.5   *Pressure drop across the vortex tube*

The vortex tube contains, of course, an example of a pressure-driven flow and the pressure drop across the device is relevant to modeling its performance and ultimately to its utility in a turbine engine. Conventional vortex tube configurations vent both exits to atmospheric pressure and the pressure drop is typically characterized as the inlet gauge pressure. However, in keeping with the present convention of referencing flow properties to the nozzle, the following analysis will consider the static pressure at the nozzle as the entering pressure, and the exiting pressure as the static pressure at the respective exits.

The pressure drop for flow exiting via the hot exit is slightly different than that exiting via the cold exit, and both pressure drops vary as a function of cold fraction. A plot of dimensional pressure drop as a function of cold fraction for three different cases is shown in Figure 77; these correspond to the cases in Scenario 1 in the dimensional characterization of temperature separation, see Table 4 and Figure 62 starting on page 128 for their corresponding inlet properties and temperature separation curves. As one might expect, a greater pressure drop corresponds to a greater degree of temperature separation.

The relationship between the pressure drop and nozzle velocity is evidently based partly—but not exclusively—on the square of nozzle velocity, a trend seen in Figure 78 based on the experimental single-μ_C data set from Section 3.2.2.2 on page 140. This is consistent with the modeling of a pressure drop by means of a pressure loss coefficient, ξ, which relates a change in pressure to the density and velocity through a device via the relationship shown in Eq (75). Such a relationship will be drawn in the present analysis; however, because the flow through a vortex tube is compressible with considerable

166

variations in velocity, a suitable reference density and velocity must be chosen. These will be evaluated at the nozzle.

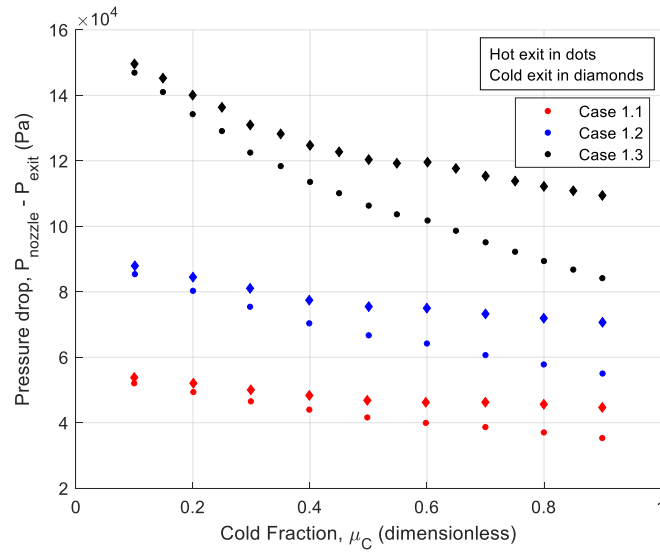$$\Delta P = \xi(\frac{1}{2}\rho V^2) \qquad (75)$$

Figure 77. Pressure drops across vortex tube for cases in air (see page 128)
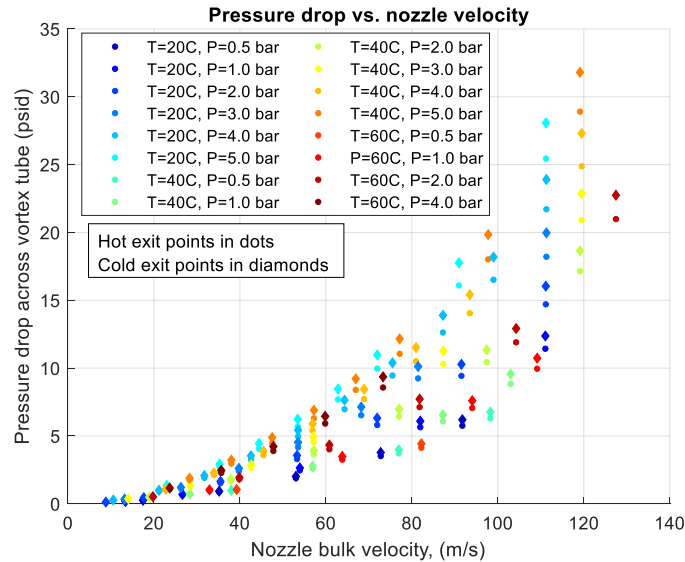

Figure 78. Pressure drop vs. nozzle velocity for cases in air (see page 140)

167

The data from Figure 78 are further analyzed in Figure 79, which illustrates the relationship between pressure drop between the nozzle and hot exit and nozzle dynamic pressure, $\frac{1}{2}\rho V^2$. A constant value of the loss coefficient would be manifested as a straight line; Figure 79 reveals a quasi-linear trend, but it is evident from the dispersion that the loss coefficient is not constant and may be a function of the nozzle properties.
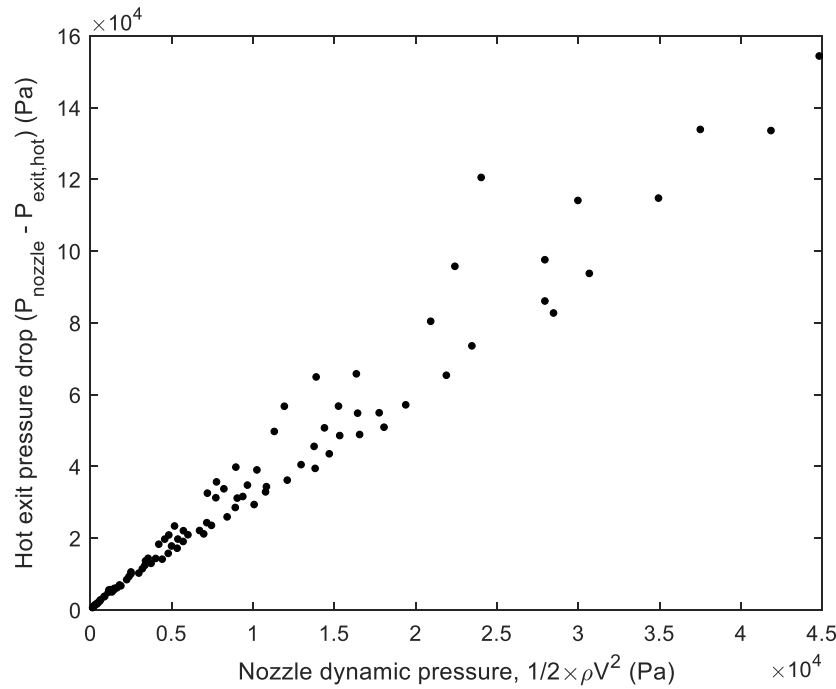

Figure 79. Hot exit pressure drop as a function of nozzle dynamic pressure

It was hypothesized that the loss coefficient might be a function of nozzle Reynolds number, but the large scatter in Figure 80 reveals that Reynolds number does not dominate the coefficient value. However, modeling the pressure drop across much simpler devices—never mind a vortex tube—is still challenging: even for an asymmetric T-junction, the pressure loss coefficient between the inlet and the dual exits is not a straightforward function of inlet Reynolds number.
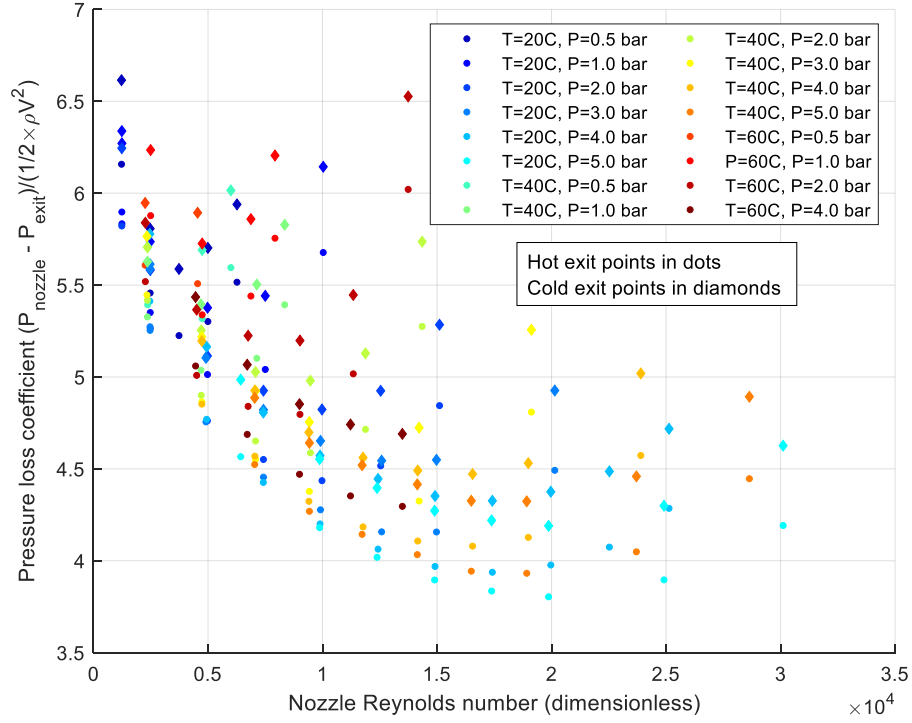
Figure 80. Loss coefficient as a function of Reynolds number

The experimental data set under present review was taken at a variety of pressures and temperatures, so it was thought that some empirical relationship could be deduced between the loss coefficient and the static temperature and pressure at the nozzle; this is shown in a general sense in Eq (76). A multiple linear regression model was developed for the data set using a zero-intercept construct described by Eq (77). The regression statistics and resulting coefficients are presented in Table 14. Both pressure and temperature were found to be significant to estimating the loss coefficient, though their contributions were opposite: nozzle static temperature was found to increase ξ by 0.01606/K, while nozzle static pressure was found to decrease ξ by 3.0126×10^{-6}/Pa.

$$\frac{\Delta P}{\left(\frac{1}{2}\rho V^2\right)} = \xi(P, T) \tag{76}$$

$$\xi = \beta_T T + \beta_P P \tag{77}$$

Table 14. Statistics of linear model for hot exit loss coefficient

	Coefficients	*Standard Error*	*t Stat*	*P-value*
Temperature	0.01606	0.00035	46.515	3.344×10^{-66}
Pressure	-3.0126×10^{-6}	2.6461×10^{-7}	-11.385	2.532×10^{-19}

Regression Statistics	
Multiple R	0.9950
R Square	0.9900
Adjusted R Square	0.9791
Standard Error	0.3883
Observations	95

Figure 81 demonstrates a verification of the model. For each data point, the loss coefficient is estimated as a function of static temperature and pressure, which permits estimation of the pressure drop. The estimate is plotted against the experimentally observed pressure drop; perfect equality would be indicated by a linear relationship with a slope of 1.0. The data indeed collapses to a near line with slight dispersion. A zero-intercept best-fit line is plotted through the data, which reveals a near-identity between the estimated and actual pressure drops with $R^2 = 0.9945$. This suggests that the linear model is quite adequate across this range of pressures and temperatures. The process was completed for both the multi-μ_C and single-μ_C experimental data sets and both exits. The resulting model coefficients are listed in Table 15.
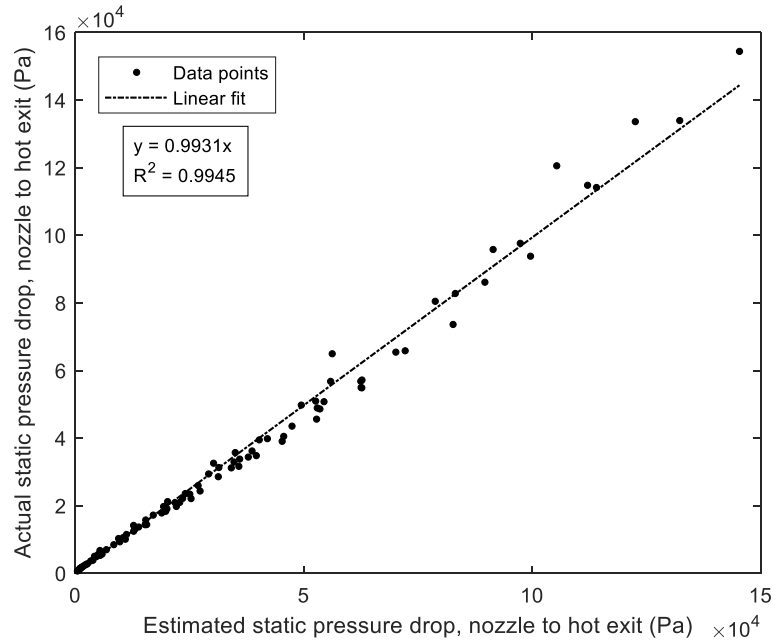
Figure 81. Verification of linear model of pressure loss coefficient for hot exit

Table 15. Temperature and pressure parameters for pressure loss coefficient

		Temperature coefficient, β_T (1/K)	Pressure coefficient, β_P (1/Pa)
Multi-μ_C data set	Hot exit	0.02090	-3.3496×10^{-6}
	Cold exit	0.02261	-3.4225×10^{-6}
Single-μ_C data set	Hot exit	0.01606	-3.0126×10^{-6}
	Cold exit	0.01730	-2.9934×10^{-6}

This linear regression ultimately provides the user with a means of anticipating the pressure drop across the vortex tube for a given inlet condition, and the inlet condition can be determined uniquely as a function of inlet pressure, temperature, and mass flow rate. This is of practical concern and speaks to the utility of scaling temperature separation. For example, perhaps a particular application requires a certain cold exit temperature and is constrained by pressure drop—it may be possible to investigate

171

operating conditions that would be suitable for such an application based on known

dimensionless performance curves of temperature separation for a particular vortex tube.

However, to complete such an analysis, a method must be devised to estimate

dimensional exit temperatures based on dimensionless curves. It is this problem which

will be solved next.

3.2.6 *Reconstituting dimensional temperature separation from dimensionless curves*

That differing dimensional temperature separation curves from a particular vortex

tube can be reduced to nearly identical dimensionless curves of $\rho^* C_p^* T_t^*|_{exit}$—i.e. $\rho^* C_p^* T_t^*$

evaluated at the exits—was a revelation, but the greatest utility of this discovery lies in

the potential ability to predict dimensional temperature separation without the need for

additional experiments. The method for such a prediction is laid out here. The full

expansion of $\rho^* C_p^* T_t^*|_{exit}$ is shown in Eq (78). For a particular vortex tube, the value of

$\rho^* C_p^* T_t^*|_{exit}$ is known for both hot and cold exits across a range of cold fractions. The

nozzle conditions, including the product ρ_{nozzle}, V_{nozzle}^2, and $T_{t,nozzle}$, correspond to the

scenario of interest. The goal is to determine $T_{t,exit}$. By rearranging Eq (78), one arrives

at Eq (79). By adopting the ideal gas law as the equation of state and substituting the sum

of static temperature and velocity components at the exit in place of the total temperature,

one arrives at Eq (80). One more rearrangement permits a solution for the static

temperature at the exits, as shown in Eq (81).

$$\rho^* C_p^* T_t^*|_{exit} = \left(\frac{\rho_{exit}}{\rho_{nozzle}}\right)\left(\frac{C_{p,exit}}{C_{p,nozzle}}\right)\left(\frac{T_{t,exit} - T_{t,nozzle}}{\frac{V_{nozzle}^2}{C_{p,nozzle}}}\right) \tag{78}$$

$$\frac{\rho_{nozzle}V_{nozzle}^2}{\rho_{exit}C_{p,exit}}\rho^*C_p^*T_t^*|_{exit} = T_{t,exit} - T_{t,nozzle} \tag{79}$$

$$\left(\frac{RT_{exit}}{P_{exit}}\right)\frac{\rho_{nozzle}V_{nozzle}^2}{C_{p,exit}}\rho^*C_p^*T_t^*|_{exit} = T_{exit} + \frac{V_{exit}^2}{2C_{p,exit}} - T_{t,nozzle} \tag{80}$$

$$T_{exit} = \frac{T_{t,nozzle} - \frac{V_{exit}^2}{2C_{p,exit}}}{1 - \frac{\rho_{nozzle}V_{nozzle}^2 R\rho^*C_p^*T_t^*|_{exit}}{P_{exit}C_{p,exit}}} \tag{81}$$

Considerable experimentation has revealed that the velocities and Mach numbers at the exits are small and therefore the total temperature at the exit can be approximated using the static temperature at the exit. In the most extreme case, observed during initial testing of the vortex tube lab configuration, helium achieved sonic flow through the nozzles but still only saw Mach 0.11 flow through the exits. In other words, the term $\frac{V_{exit}^2}{2C_{p,exit}}$ is negligible, leading to Eq (82).

$$T_{exit} = \frac{T_{t,nozzle}}{1 - \frac{\rho_{nozzle}V_{nozzle}^2 R\left(\rho^*C_p^*T_t^*|_{exit}\right)}{P_{exit}C_{p,exit}}} \tag{82}$$

Eq (82) is not entirely a closed form solution, since the specific heat at the exit is—strictly speaking—a function of the static temperature at the exit. However, if the specific heat does not vary significantly across the vortex tube such that $C_{p,exit} \approx C_{p,nozzle}$, then a value of T_{exit} may be determined analytically; obviously, a more rigorous solution will be achieved numerically by determining $C_{p,exit} = f(T_{exit})$.

173

The author does have a means of performing such refinement, but the practical difference is negligible for most applications.

To determine the static pressure at the exit, P_{exit}, it becomes necessary to incorporate the pressure drop model such that $P_{exit} = f(T_{nozzle}, P_{nozzle})$. The earlier pressure drop models were determined for $\mu_C = 0.40$. Greater fidelity may be achieved by expanding the model to additional cold fractions, assuming sufficient data exists. However, Figure 77 revealed that the pressure drop associated with $\mu_C = 0.40$ lies approximately in the middle of the range of expected values. The model will be evaluated while assuming a constant pressure drop for all cold fractions based on $\mu_C = 0.40$. Figure 82 plots the estimated dimensional temperature separation against the actual experimental values for Case 1.3, first seen in Figure 62 (see p129). In this plot, the dimensional estimate is reconstituted from the curve of $\rho^* C_p^* T_t^*|_{exit}$ from the exact same case. The estimated and actual temperature separation curves differ slightly between the cold curves at low cold fractions and the hot curves at high cold fractions due to the use of constant exit pressure; the differences at each end are less than 1 K.
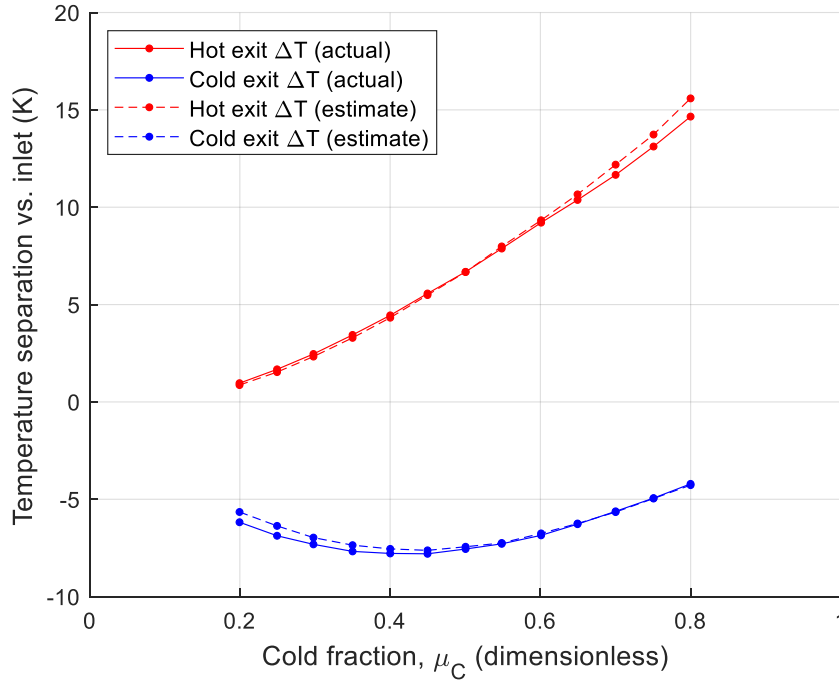
Figure 82. Estimated dimensional temperature separation vs. actual (Case 1.3)

With dimensionless temperature separation curves of $\rho^* C_p^* T_t^*|_{exit}$ and a relevant pressure drop model at hand, it has now become possible to predict the temperature separation for a vortex tube at desired nozzle conditions. Some experimentation is required to initially determine the curves of $\rho^* C_p^* T_t^*|_{exit}$, though this could be as little as a single sweep through the desired cold fractions. The use of a single cold fraction to establish the pressure drop model is evidently adequate, since the assumption of a constant pressure drop with respect to cold fraction yielded a favorable comparison with experiment in Figure 82 with minor deviations at the extreme cold fractions. The use of validated linear models for the purposes of interpolation comes with confidence intervals and other metrics of uncertainty, but the same cannot be said for extrapolation. Therefore,

to maximize the accuracy of temperature separation estimates, the pressure drop model should encompass as broad an extent of relevant pressures and temperatures as possible.

An obvious use of dimensional temperature separation estimates, however, *is* extrapolation: to predict the performance of a vortex tube at conditions that cannot be achieved experimentally, such as conditions approaching those of a turbine engine compressor section. It is not known how well the pressure drop function will perform beyond the range of temperatures and pressures used in the lab, and this presents a risk to the accuracy of the estimates.

3.2.7 *Experimental investigation of modified vortex tube performance*

Several research tasks involve the use of CFD to simulate vortex tube performance, and it was desired to validate the CFD results with a favorable comparison to experimental results. Ideally, such a comparison would be based on identical geometries for both the experimental and computational efforts. However, the off-the-shelf Exair™ 3208 vortex tube hardware incorporates several complex features that made exact computational replication difficult. These included a component known as a "taper sleeve", which is located adjacent to the 8R nozzles, a cruciform metal insert set inside the tube near the hot exit, and a set of "steps" on the 8R nozzles, and a radial hot exit valve. The cruciform insert and original hot exit geometry are shown in Figure 83. The brass fitting is identical to that installed at the hot exit in Figure 55 and can be adjusted like a valve to limit flow from the hot exit and thereby adjust the cold fraction. The original set of experimental investigations incorporated all of the complex features described here except the brass hot exit valve, which was removed since the mass flow controllers were used to adjust the cold fraction.

176

Figure 83. Exair^{TM} 3208 vortex tube cruciform insert (left)

and original hot exit geometry (right)

To assist with experimental validation of the subsequent computational effort, the vortex tube hardware was modified slightly. The taper sleeve and cruciform blades were removed, a simplified 8R nozzle was manufactured, and a hot exit geometry was installed. This could be replicated almost exactly in the CFD software. The original and modified versions of the 8R nozzles—with and without the "steps", respectively—can be seen in Figure 84.
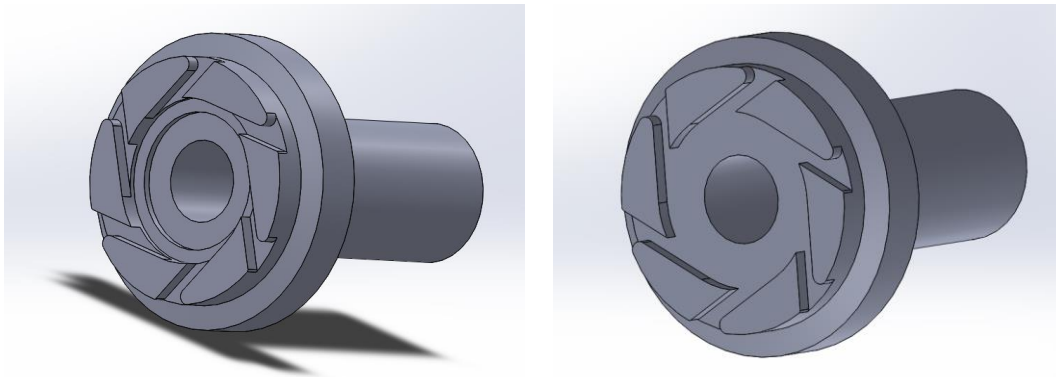

Figure 84. Nozzles for Exair^{TM} 3208 vortex tube: original (left) and simplified (right)

Two new new hot exit geometries were machined: one included an annular exit and one used an orifice exit, as seen in Figure 85. The annular exit has an outside diameter of 5.7 mm and an inside diameter of 2.2 mm. The conical axial obstruction has a

60° half-angle and blocks 15% of the area circumscribed by the outer diameter, not counting the spokes, which are 0.6 mm wide. The diameter of the orifice exit is 4.0 mm.
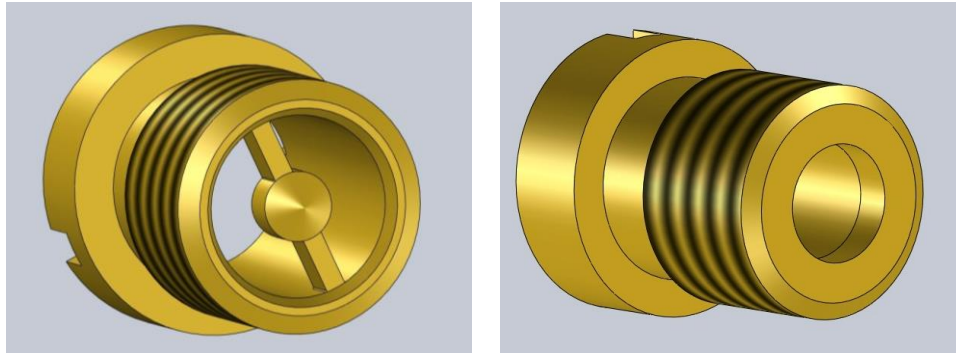

Figure 85. Modified hot exit geometries for Exair^{TM} 3208 vortex tube

The simplified vortex tube, when equipped with the two new hot exit geometries, essentially constituted two new configurations. The operating conditions, in Table 16, were identical between the three configurations: the unmodified vortex tube and the modified tube with each exit geometry. Figure 86 compares dimensional performance of the three configurations. The dimensional temperature separation of the original configuration exceeded that of each modified configuration.

Table 16. Operating conditions for original and modified vortex tubes

	Original	Annulus	Orifice
Mass flow rate (kg/s)	1.420×10^{-3}	1.421×10^{-3}	1.420×10^{-3}
Inlet T_{total} (K)	293.2	293.3	293.1
Inlet P_{static} (bar, gauge)	3.000	3.001	3.004
Re_{D_h}	18034	18045	18041

Pr	0.721	0.721	0.721
$\rho C_p \mu_{JT}$	0.0108	0.0108	0.0108
Nozzle bulk velocity (m/s)	98.95	99.30	99.07
Nozzle Mach number	0.291	0.292	0.291
ρ (kg/m^3)	4.563	4.551	4.558
μ (µPa-s)	18.05	18.05	18.05
k (mW/m-K)	25.32	25.33	25.31
C_p (kJ/kg-K)	1.012	1.012	1.012
μ_{JT} (K/bar)	0.2348	0.2346	0.2349
Nozzle T_{static} (K)	288.3	288.3	288.2
Nozzle P_{static} (Pa, absolute)	377571	376614	377051
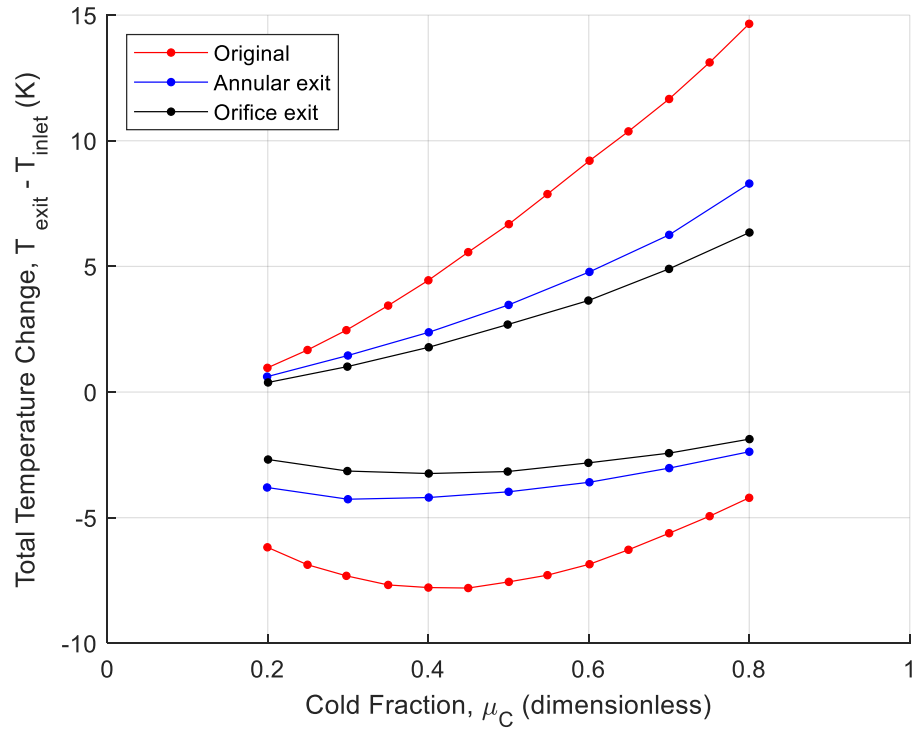
Figure 86. Dimensional temperature separation across modified vortex tubes

The magnitudes of temperature separation yielded by the geometries are quite different, especially between the modified and original tubes. It was established in the literature review that the hot exit geometry exerts an influence on the entire velocity distribution in a vortex tube, and the modified vortex tube with its new brass hot exit

geometries differs from the otherwise open hot exit of the "original" configuration.

However, the metal insert in the tube is likely driving the large difference in performance

between the original and modified configurations. The insert straightens out the flow—

eliminating the tangential component of velocity and constraining the flow to almost

entirely axial flow. This would be expected to dramatically influence the velocity profile

and may serve to enhance tangential components upstream of the insert, thereby

intensifying the vortex in that region and increasing overall temperature separation.

Because the internal flow fields between the vortex tubes are do not share a dynamic

similarity, it is not surprising that the dimensionless temperature separation curves of

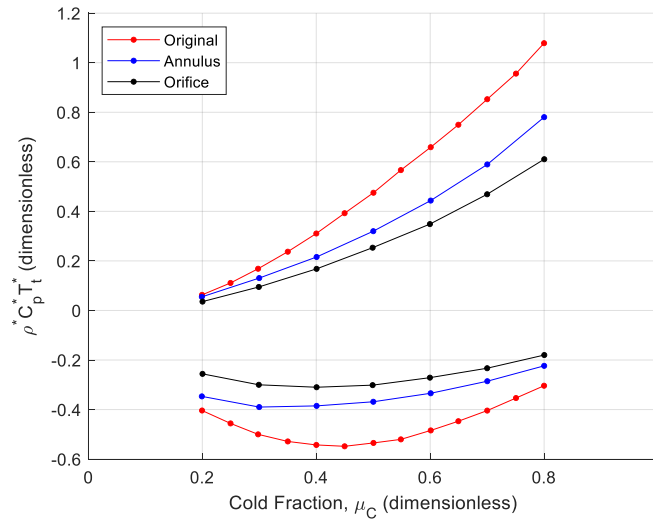$\rho^* C_p^* T_t^*$ are also different, as seen in Figure 87.

Figure 87. Dimensionless temperature separation across modified vortex tubes

The pressure drops associated with the three configurations are shown in Figure

88. The pressure drops across the modified vortex tubes are significantly less than for the

original design—on the order of 20-30% of the original pressure drop, depending on cold

fraction. This is evidently correlated with a reduction in temperature separation.
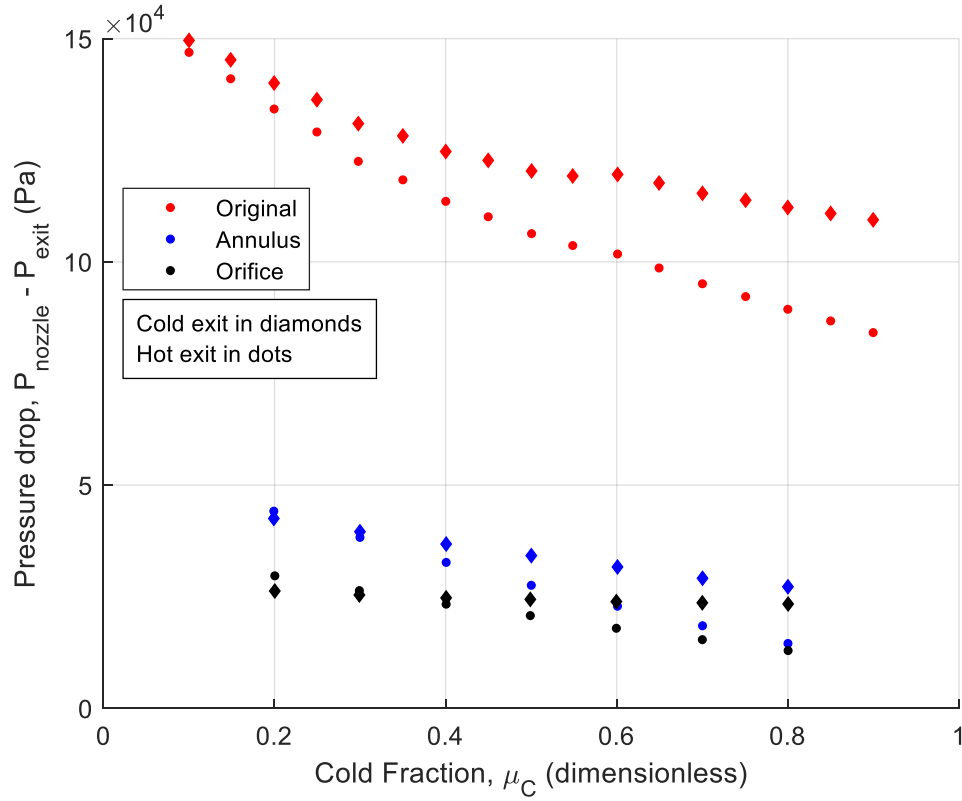
**Figure 88. Pressure drops across original and modified vortex tubes**

The purpose of the modifications to the vortex tube geometry was to establish a

simple configuration that could be easily replicated in CFD and therefore provide an easy

means of experimental validation for the CFD results, and this objective was

accomplished. However, gathering this additional data provided some insights into vortex

tube operation. First, it reveals that there is an intrinsic relationship between a particular

flow pattern in a vortex tube and the resulting temperature separation. The collapse of the

nondimensional temperature separation curves of $\rho^* C_p^* T_t^*$ in Figure 72, which were all

gathered for the same vortex tube geometry but with different nozzle conditions,

suggested a dynamic similarity between the flow patterns. However, when the vortex

tube geometry was altered, such as by removing the cruciform tube insert and adding a

181

new hot exit geometry, the flow pattern is no longer dynamically similar and the curves of $\rho^* C_p^* T_t^*$ are no longer the same. This implies that geometry governs flow patterns, which in turn govern $\rho^* C_p^* T_t^*$ in a vortex tube. Lastly, the investigation revealed a relationship between pressure drop and temperature separation in a vortex tube, where increased pressure drop is evidently correlated with increased temperature separation.

3.2.8 *Computational characterization of vortex tube performance*

3.2.8.1 Geometry and solution methodology

Vortex tube performance was modeled with ANSYS FLUENT v17.2 computational fluid dynamics (CFD) software, and a major objective was to validate the computational effort by matching the experimental work as closely as possible. To that end, the computational geometry was based on the modified vortex tube with the annular exit, which was straightforward to implement in the software. Figure 89 depicts the geometry implemented, with tube walls in gray, inlet faces in green, cold exit orifice face in blue, and hot exit annulus face in red; these are the faces at which nozzle and exit properties are computed.
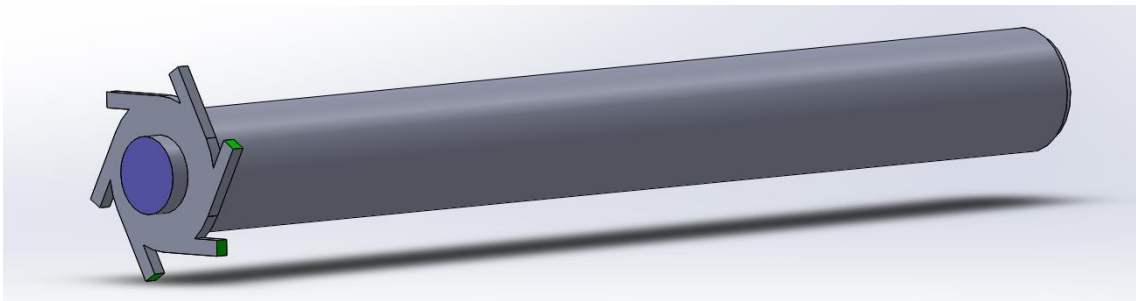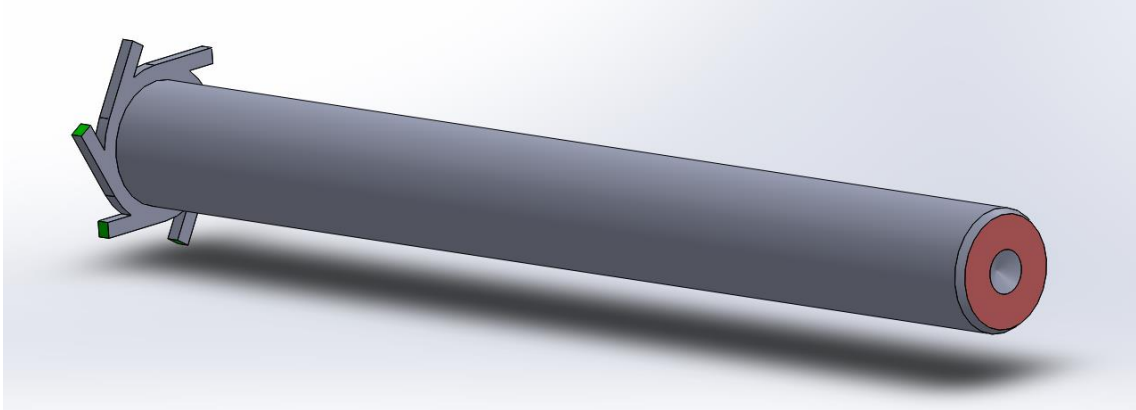
Figure 89. Geometry used for computational investigations: walls in gray, cold exit face in blue (top), hot exit face in red (bottom), nozzle faces in green

A three-dimensional unstructured mesh was created from the basic geometry using Pointwise v18.0 via its automated hybrid mesh generation method known as anisotropic tetrahedral extrusion, or "T-Rex". A closeup view of the mesh is shown in Figure 90; however, for reasons to be described, the mesh required further modification at the exits to achieve satisfactory solutions.
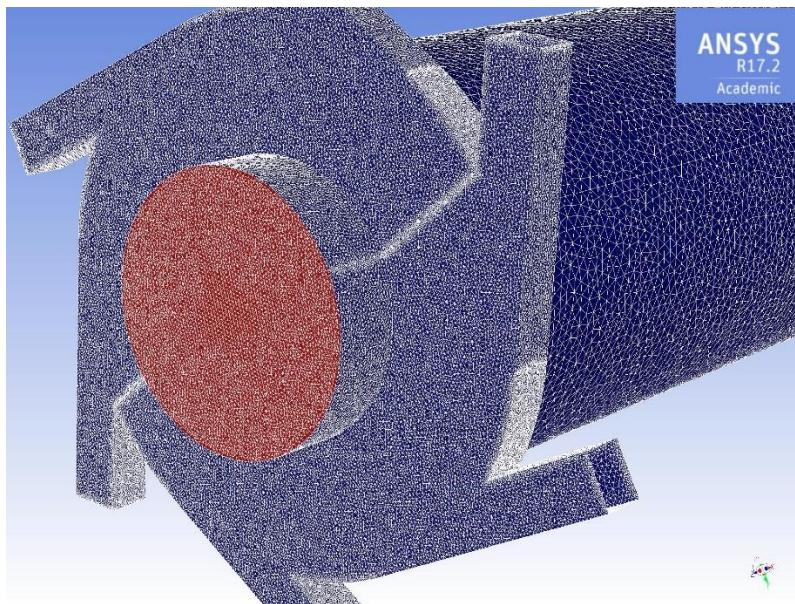

Figure 90. Unstructured mesh used for CFD modeling (cold orifice exit face in red)

The CFD code ANSYS FLUENT v17.2.0 was used to model the flow. The intrinsic complexity of the flow field inside a vortex tube greatly complicated the computational study, and considerable effort was exerted to identify the most appropriate turbulence model, solver settings, gas model, and boundary conditions. In many cases, it was not possible to reach a converged solution, or else the solution yielded distorted temperature distributions that were visibly asymmetric and yielded virtually no temperature separation.

Ultimately, a turbulence model and solver settings were identified which yielded reliable, stable temperature separation profiles. The standard k-ε model was implemented with a standard wall function; viscous heating and compressibility effects were enabled. A pressure-based solver was adopted with a semi-implicit method for pressure-linked equations (SIMPLE) pressure-velocity coupling scheme. Spatial discretization was accomplished with the Green-Gauss node-based method for gradients, the FLUENT v17.2 "standard" method for pressure, second-order upwinding for density and momentum, and Quadratic Upstream Interpolation for Convective Kinematics (QUICK) for turbulent kinetic energy, turbulent dissipation rate, and energy. A real gas model was applied based on the NIST REFPROP database resident in FLUENT.

The use of the wall function in the turbulence model dictated a needed range of wall y^+ values; in FLUENT 17.2, this range was approximately 30 to 500. Figure 91 illustrates the actual y+ values for the mesh that was actually utilized in the study, which generally lie in the desired range except for the region closest to the hot exit.
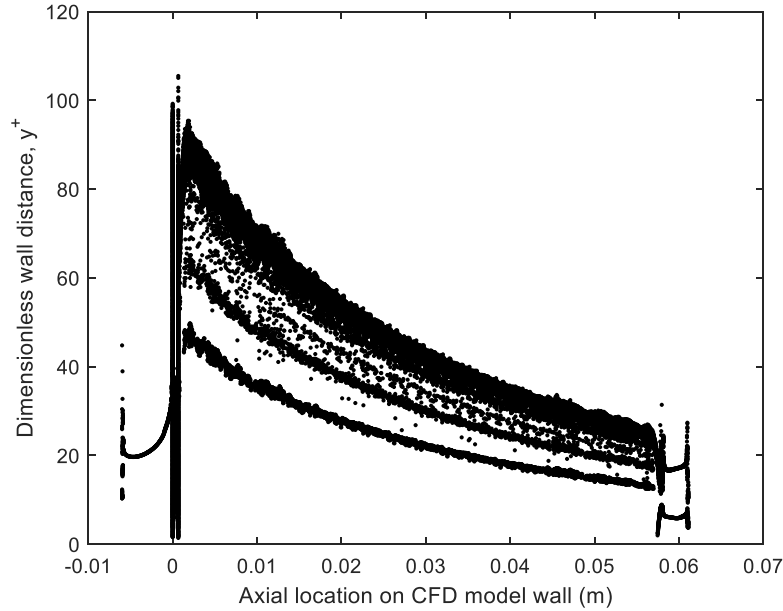
184

Figure 91. Dimensionless wall distance, y$^+$, along the vortex model tube walls

The CFD boundary conditions represented a challenging aspect of matching the experimental characteristics. One of the most fundamental variables to control when modeling vortex tube operation is the cold fraction, and building a characteristic set of performance curves requires precise prescription of both the mass flow rate entering the vortex tube and that exiting from the cold side. Because the mesh inlet faces were actually the nozzles, the terms "inlet" and "nozzles" are synonymous here; this contrasts with the distinction between terms with respect to the experimental configuration.

The inlet boundary condition is best modeled using a mass flow rate condition. In FLUENT, the total temperature of the entering fluid is also specified, which is convenient because this is also a known experimental boundary condition. The pressure at the inlet (or nozzles), however, is not known *a priori* and emerges from the flow solution. The exit boundary conditions introduced a new wrinkle. Because it is essential to model the flow

185

using a compressible solver, the exit boundary conditions available in the software are somewhat restricted. FLUENT prohibits the use of "outflow" boundary conditions—in which the mass flow rate at the exits would be defined—for compressible flow.

However, a workaround is available to achieve a desired mass flow rate at the exits: both exits must be defined as pressure outlet boundary conditions—which are permissible for the compressible flow solver—and FLUENT offers a capability to automatically adjust the exit static pressure at a pressure outlet to achieve a target mass flow rate across that boundary. In practice, the inlet mass flow rate is set to the desired value and the cold exit is set to a pressure outlet with a target mass flow rate that corresponds to the desired cold fraction. FLUENT then makes the necessary adjustments to achieve this cold fraction during the course of iterating to a converged solution. The simultaneous processes of converging the flow solution for a complex flow field while modifying it by adjusting the cold fraction contributes to a greatly protracted solution time. This is particularly true when using a real gas model, which approximately doubles the time required for each solver iteration. Nevertheless, this process guarantees that a desired cold fraction will be achieved.

However, there are some remaining boundary conditions that must be specified. The hot exit pressure outlet must be specified to an arbitrary static pressure. The choice is significant because it directly affects the pressure that emerges at the nozzles, although the relationship between the two is not straightforward. Consider the following: a typical use case for the CFD investigations herein is to achieve a desired nozzle velocity or value of ρC_p, which in turn would permit deliberate control of the nozzle's governing dimensionless parameters. However, this requires a precise nozzle static pressure which,

thus far, cannot be directly set and can only be determined *a posteriori* from the flow solution.

The procedure then is to set the hot exit static pressure according to an anticipated static pressure drop between the nozzle and the hot exit, which is also very much an empirical finding. After iterating the solution to completion, i.e. achieving the desired cold fraction, an inspection of the properties at the nozzle reveals whether the target pressure and velocity were achieved. If not, the hot exit static pressure is adjusted and the solution process is repeated. Unfortunately, this is not a matter of simply adjusting the hot exit static pressure and running for a few more iterations. Adjustment to the hot exit pressure outlet reinitiates FLUENT's goal-seeking process at the cold exit pressure outlet, and a large number of iterations—typically 6000 or more—must be completed if the target cold fraction will be reliably achieved with a converged flow solution.

There is still another set of boundary conditions that requires close attention. With pressure outlet boundary conditions, there is the possibility that the overall pressure distribution may cause a reverse flow condition wherein gas is ingested into the flow field from beyond the exits. Because the reverse flow obviously originates from the mesh, this requires arbitrary specification of the total temperature of the reverse flow. This, in turn, presents an interesting challenge in replicating experimental results. If such a reverse flow pattern actually existed under experimental conditions—and it should be emphasized that evaluating such flow patterns is beyond the scope of the present research—the reverse flow temperatures would clearly be based on the temperatures of the gas being exhausted from the exits. Unfortunately, such a linkage cannot be established in the software being utilized. Instead, after achieving a converged flow

solution, the temperature profile at each exit plane must be inspected for reverse flow and mismatches between the exiting flow and the reverse flow.

Mismatches essentially represent an arbitrary energy source or sink. Imagine, for example, a non-physical situation in which the reverse flow entering the cold exit is much warmer than the solution flow; the warm gas would mix with the cold gas, pass back out of the cold exit again, and distort the temperature separation results. Because the flow at each exit has a radial temperature profile, even in the absence of reverse flow, it is not entirely straightforward to determine what the appropriate reverse flow temperature actually should be and some subjective judgment is required to establish the reverse flow boundary conditions. Because of the non-physical nature of this artifact, "perfect" settings may not even be achievable.

However, to mitigate the influence of reverse flow on the solution, extensions were added to the exits in the computational mesh. These extensions, 3.0 mm on the hot exit and 5.0 mm on the cold exit, permitted some reverse flow circulation to take place beyond the original exit plane and reduced its influence on the main body of the solution. The original and extended meshes can be seen in Figure 92, which depicts three planes: 1) extending along the axial length of the tube, labeled the "Axial-diametric plane", 2) the circular cold exit plane, and 3) the annular hot exit plane. Please note that the contours of axial velocity are not necessary to interpret the figure.
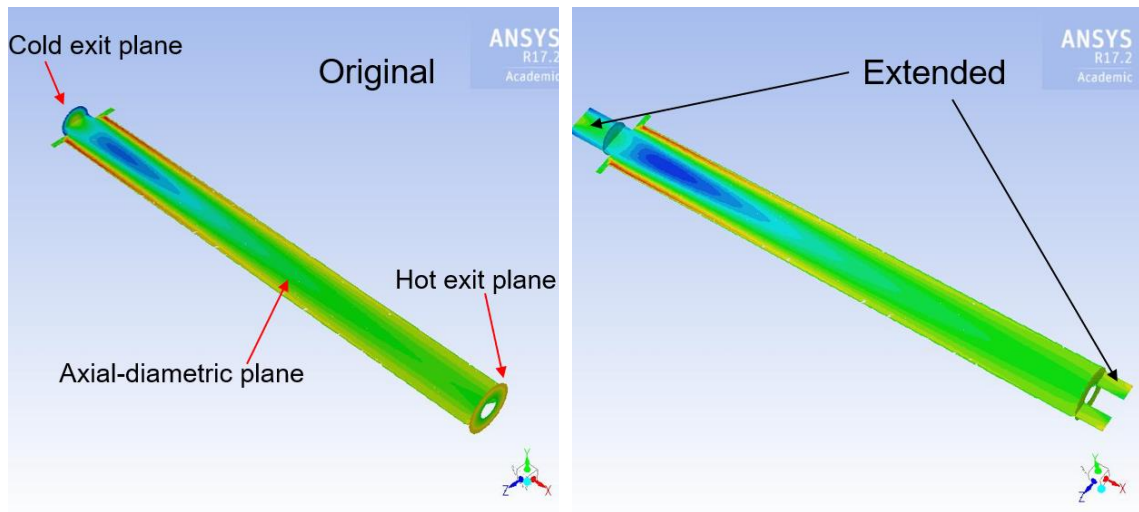
Figure 92. Exit extensions on vortex tube unextended (left) and extended (right)

Although the original exit planes were no longer, strictly speaking, the actual exit

planes of the solution, they remained the locations at which exit properties were

evaluated. In principle, if the exit extensions were made infinitely long, then the reverse

flow would never re-enter the vortex tube and its contribution would be completely

eliminated. Unfortunately, the extensions represented an additional computational burden

and their length had to be limited. The new procedure for adjusting the reverse flow

temperature was then an inspection of the temperature profiles at both the measurement

plane (the original exit plane) and the solution exit plane (at the end of the extension),

and changing the reverse flow temperature if it appeared that the solution exit plane had

an exaggerated influence on the measurement plane.

The nature of the boundary conditions meant that each solution was typically run

at least twice: first, with the desired nozzle mass flow rate and total temperature, cold

fraction exactly achieved, and guesses for the hot exit static pressure and both exits'

reverse flow temperatures; second, with updated guesses for the hot exit static pressure

and both exits' reverse flow temperatures. With some experience, two runs were often sufficient to achieve the target nozzle conditions while minimizing reverse flow effects to an acceptable degree.

Once the proper solution settings were identified and procedures were developed to set the boundary conditions, a mesh sensitivity study could be conducted. Five meshes were prepared, with cell counts of 1.6×10^6, 2.5×10^6, 5.2×10^6, 9.4×10^6, and 16×10^6, respectively. Inlet boundary conditions were specified with a mass flow rate of 0.00142 kg/s (72 SLPM) and a total temperature of 293.4 K. The cold exit pressure outlet was set to achieve a cold fraction of 0.40, which typically yields the greatest cold exit temperature change. The hot exit pressure outlet used a static pressure of 345 kPa. The meshes were compared in terms of temperature separation, quantified as the difference in mass-averaged total temperature between the exit measurement planes and the inlet plane. An additional measurement was included to assess net changes in the flow field: a volume-integrated x-vorticity. This was selected because the x-vorticity is one of the most prominent indicators of the swirl of the vortex; in the present configuration, the x-axis spans the length of the vortex tube. By integrating the x-vorticity across the volume of the mesh, a single indicator could aggregate large-scale changes in the flow pattern.

The results of the sensitivity study are presented in Figure 93. Hot and cold exit temperature separation are shown in the red and blue traces, respectively, scaled with the left vertical axis. The x-vorticity is scaled according to the right vertical axis. Temperature separation and integrated x-vorticity are fairly sensitive to mesh size from 1.6×10^6 to 5.2×10^6 cells, but much less sensitive from 5.2×10^6 to 16×10^6 cells. Hot exit and cold exit temperature separation increase by 32% and 28% from 1.6×10^6 to 5.2×10^6

190

cells, while they increase by only 5.7% and 5.9%, respectively, from 5.2×10^6 to 16×10^6

cells. Similar trends occur in x-vorticity, though the maximum observed value is at

9.4×10^6 cells. Since the purpose of the mesh sensitivity is to balance concerns of

accuracy with computational cost, it was decided to use the mesh with 5.2×10^6 cells for

all subsequent investigations. The average cell size for this grid was 5.31×10^{-4} mm^3. The

run time with available resourcing was sixteen hours to achieve a converged solution for

a single cold fraction in an adiabatic vortex tube with 6000 iterations; creating a cold

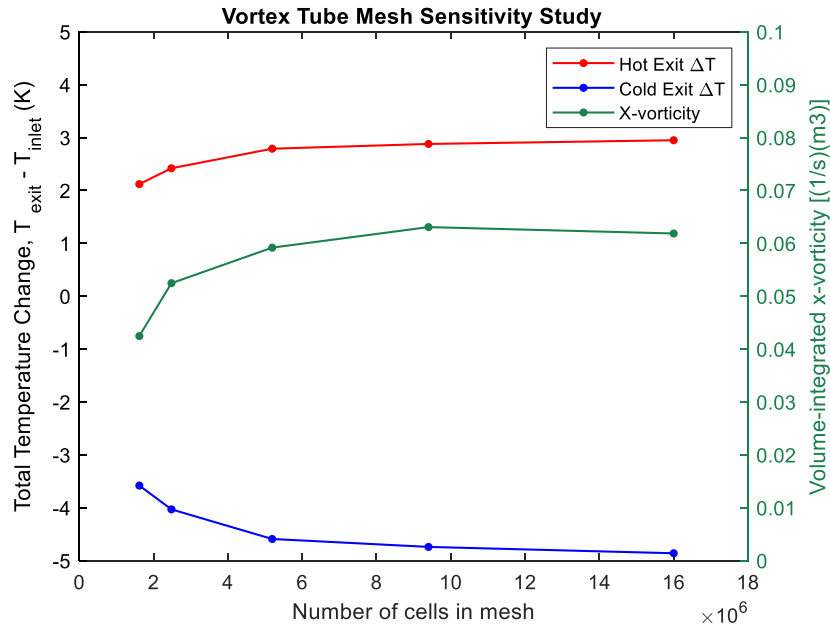fraction curve from $0.2 \leq \mu_C \leq 0.8$ thus required 112 hours of run time.

Figure 93. Vortex tube mesh sensitivity results ($\boldsymbol{\mu_C = 0.40}$)

3.2.8.2 Examination of internal flow field for CFD solution

The internal flow field was examined in terms of temperature, pressure, and

velocity and compared to historical experimental data. The CFD vortex tube geometry

was constructed to match the author's experimental geometry, not any specific historical geometry; therefore, the purpose of the comparison to historical data is to qualitatively determine the extent to which the CFD flow profiles are consistent with previously observed trends. No single source contained a complete set of desired temperature, pressure, and velocity profiles; therefore, three sources of experimental data were used for comparison. The examination consisted of contours across a plane spanning the axial and radial extent, as well as a set of radial cuts at axial positions of 2.9 mm, 5.8 mm, 11.6 mm, 29.05 mm, and 40.7 mm, which correspond to 5%, 10%, 20%, 50%, and 70% of the tube length, respectively; see Figure 94. Note that a plane extending radially from the zero axial location is coincident with the side of the nozzles nearest the cold exit, and the hot exit plane lies at an axial position of 58.1 mm. The radius of the tube is 3.1 mm.
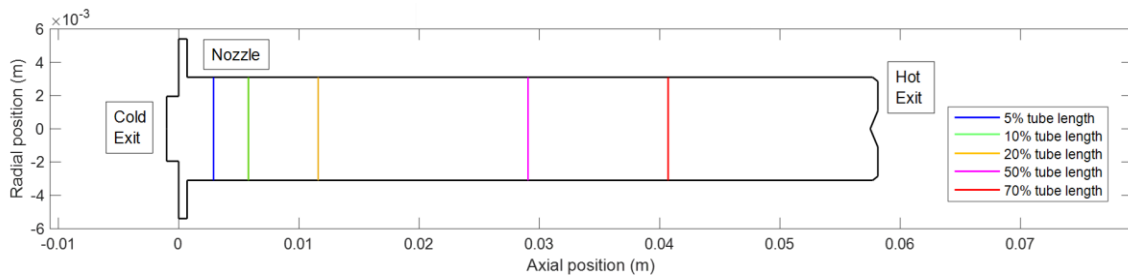

Figure 94. Vortex tube CFD model cross-section

Experimental data on static and total temperature along the tube cross section at various axial positions comes from Scheper [49]. Figure 95 depicts static and total temperatures profiles from experiment (left) and this author's CFD (right). In the left plot, the solid lines of static temperature and dashed lines of total temperature are taken for axial positions (1), (2), and (3), which correspond approximately to 5%, 10%, and 15% of the tube length, respectively; experimental data are only shown for one half of the

192

radial profile. The measurements and CFD results display a strong qualitative

consistency, especially the relative curvature of the static and total temperature in the

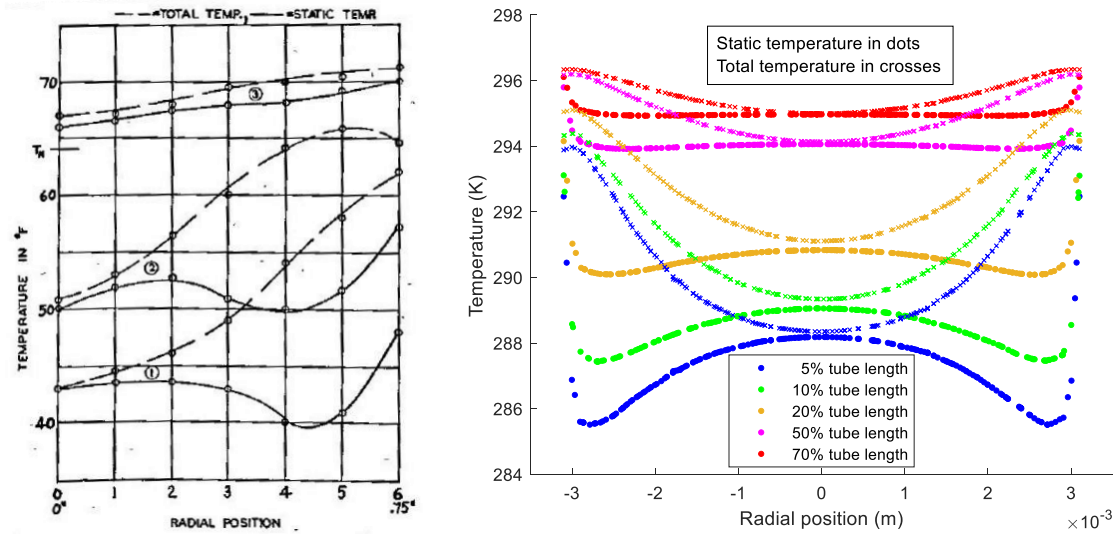radial direction as well as the progression of the profiles in the axial direction.

Figure 95. Comparison of temperature profiles from

experiment [49] (left) to CFD (right)

Experimental pressure data were taken from Hartnett and Eckert [55]. Radial

profiles of static and total pressure are compared between experiment and CFD in Figure

96. The experimental data was taken at an axial position of 40% of the tube length

(measured from the nozzles toward the hot exit), while this author's CFD data is shown

for axial positions of 20% and 50% of tube length. The CFD curves again bear a strong

resemblance to the experimental data, particularly the distinctly different curvatures of

static and total pressure with respect to radial position. Static and total pressure

distributions are also shown for additional axial positions in Figure 97. An experimental

profile of tangential velocity is also drawn from the results of Hartnett and Eckert [55]

and compared to CFD in Figure 98. Qualitatively speaking, there is yet again a strong resemblance, though the experimental data does not extend all the way to the central axis of rotation inside the vortex.
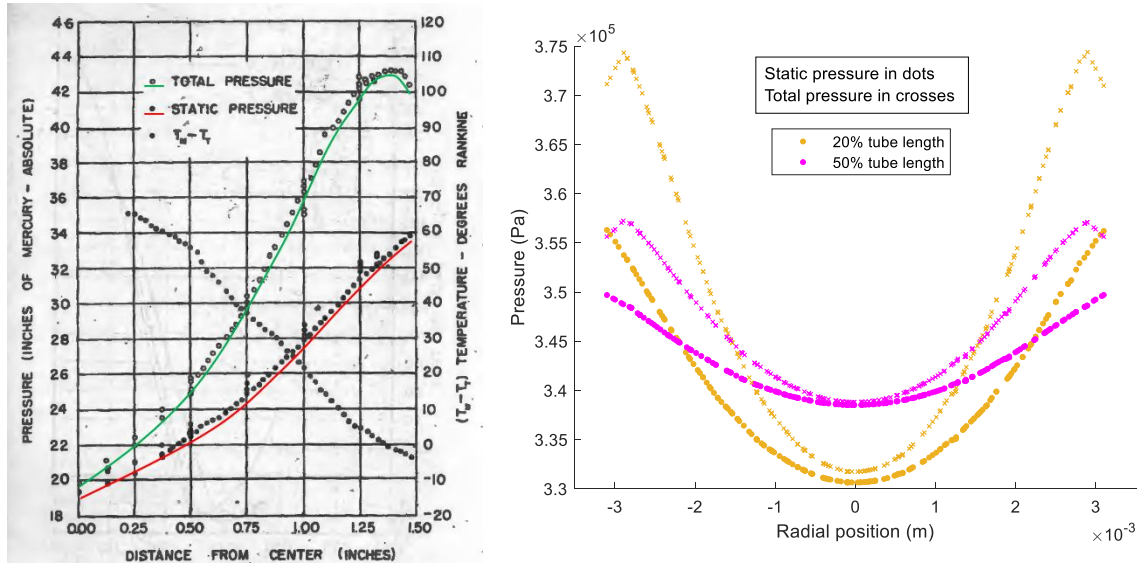

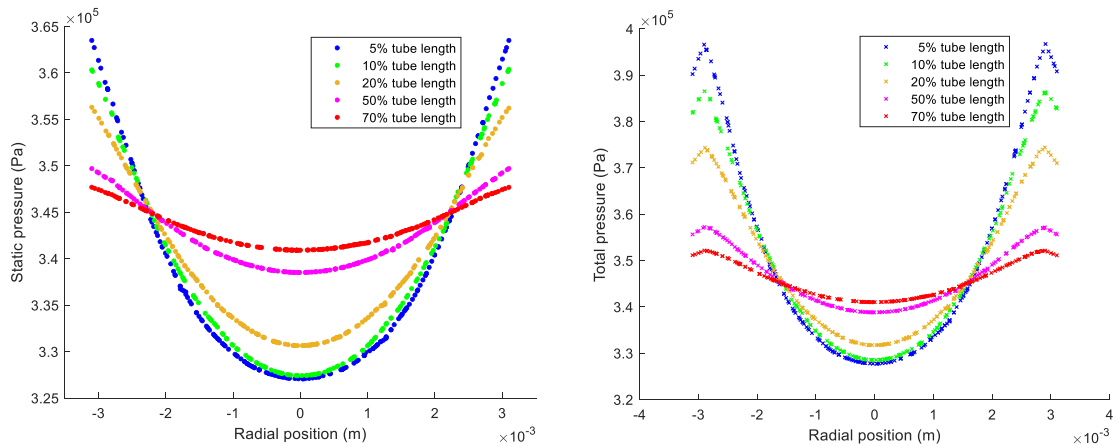**Figure 96. Comparison of static and total pressure profiles from experiment [55] (left) to CFD data (right)**

Figure 97. Static pressure (left) and total pressure (right) profiles from CFD results
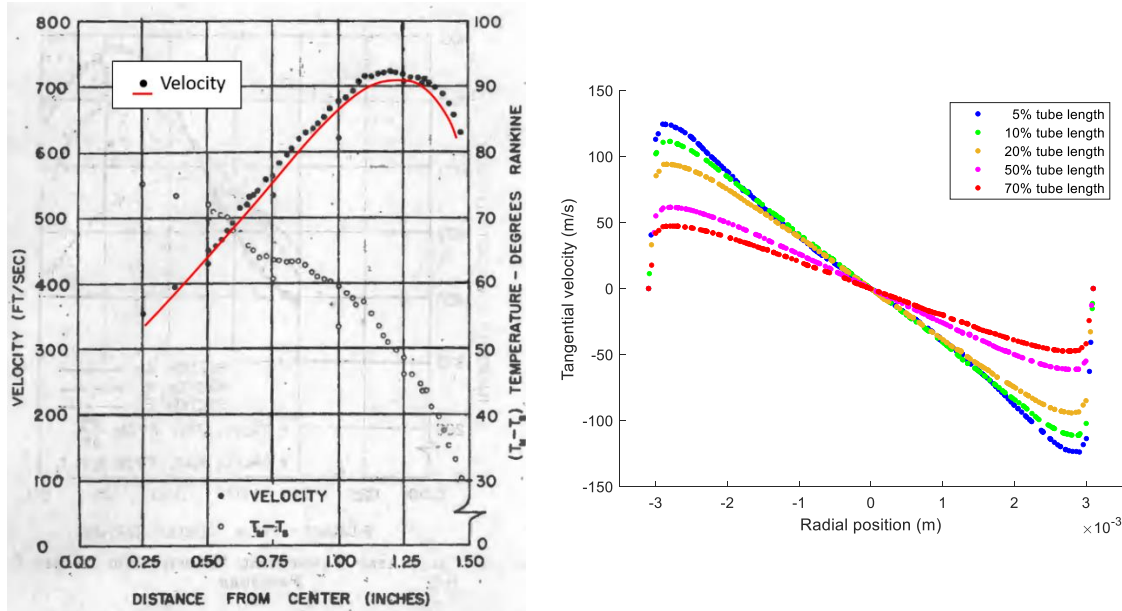
194

Figure 98. Comparison of tangential velocity profiles from experiment [55] (left) to CFD data (right)

The experimental data of Scheller [50], which was originally plotted as a set of contours, also forms a basis for comparison. Scheller's data were taken for a cold fraction of 0.506 and, given a tube length of 43 inches, are only shown for the first 17% of the tube. Contours were prepared from the CFD data, both to acquaint the reader with a broader characterization of the flow and to further establish that the CFD results are representative of experimentally evaluated vortex tube flow. Contours of static temperature from experiment [50] are shown in Figure 99 and CFD results are in Figure 100. Elevated static temperatures near the core are plainly evident in both figures, though this effect becomes less pronounced near the hot exit.
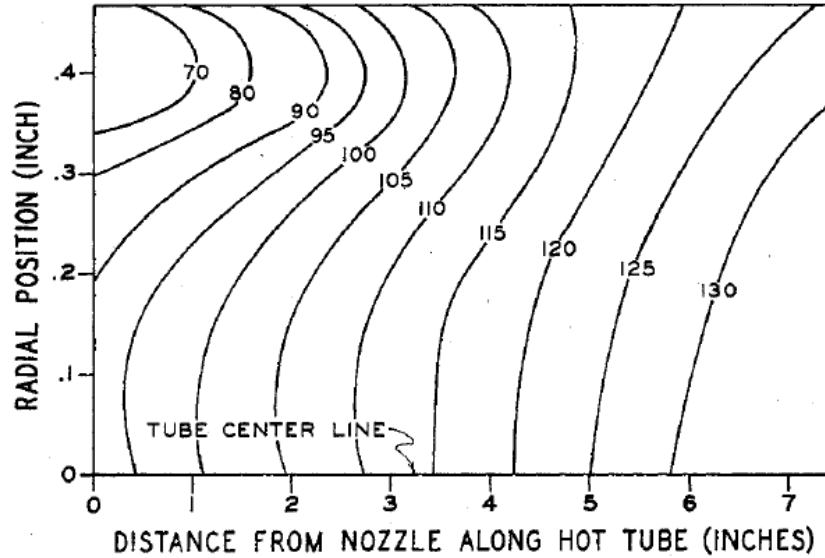
Figure 99. Contours of static temperature (°F) from experiment [50]

282.0 283.0 284.0 285.0 286.0 287.0 288.0 289.0 290.0 291.0 292.0 293.0 294.0 295.0 296.0 297.0

Figure 100. Contours of static temperature (K) from CFD

Contours of total temperature from experiment [50] are shown in Figure 101 and CFD results are in Figure 102. In contrast to the static temperature profiles, the total temperature plots reveal that the temperature along the axis of rotation is universally colder than the surrounding gas, though in some regions the total temperature decreases again toward the wall—a finding also observed earlier in Figure 95. The experimental and computational results again compare favorably in a qualitative sense.

196

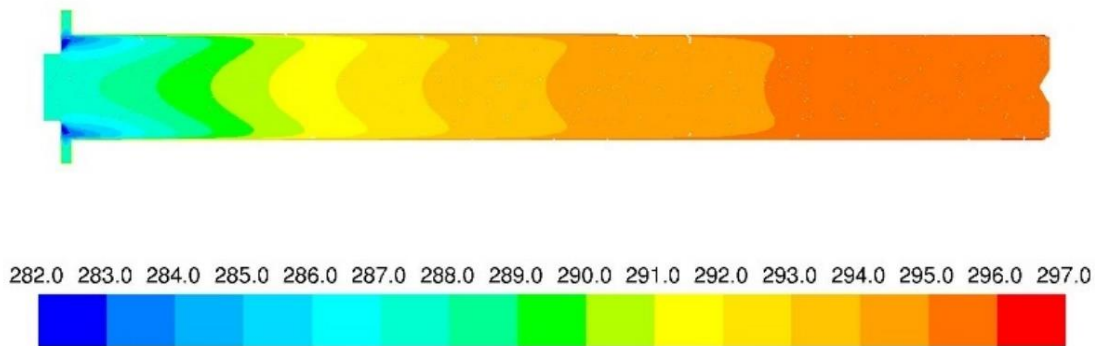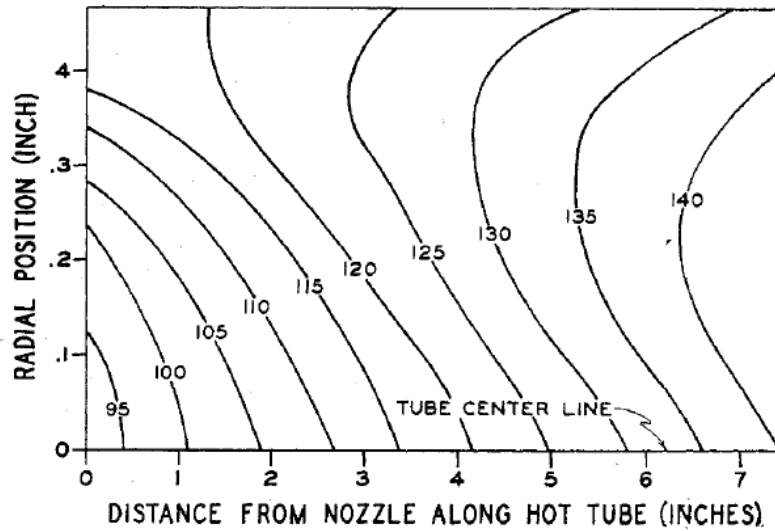**Figure 101. Contours of total temperature (°F) from experiment [50]**

Figure 102. Contours of total temperature (K) from CFD

Contours of static pressure from experiment [50] are shown in Figure 103 and

CFD results are in Figure 104, while total pressure is compared between experiment and

CFD in Figure 105 and Figure 106, respectively. Most striking in these plots is the

fidelity by which CFD replicates the pressure distributions near the cold exit, which are

distinct. The static pressure forms a depression near the cold exit, though there is

apparently a slight adverse static pressure gradient for the flow exiting via the cold side,

197

evidenced by an increase in static pressure along the axis of rotation as the cold exit is approached; for example, follow the "Tube Center Line" in Figure 103 from 4.0 inches toward 0.0 inches. This is apparently manifested at axial locations less than 5% of the tube length, which is why it is not seen in Figure 97. The total pressure does not exhibit this type of variation along the central axis and again the CFD successfully replicates the experimental profile.
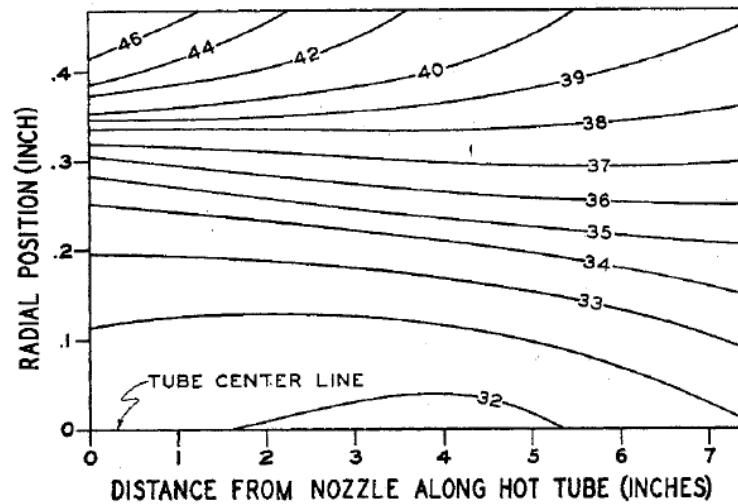
Figure 103. Contours of static pressure (in. Hg) from experiment [50]
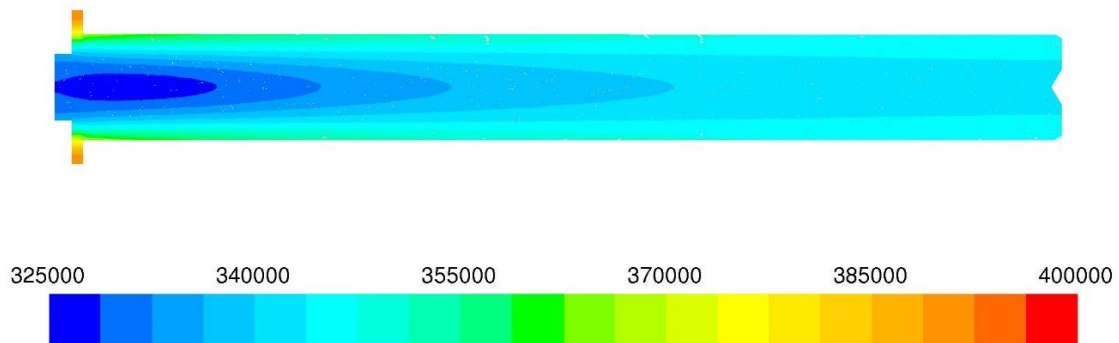
Figure 104. Contours of Static Pressure (Pa) from CFD

198

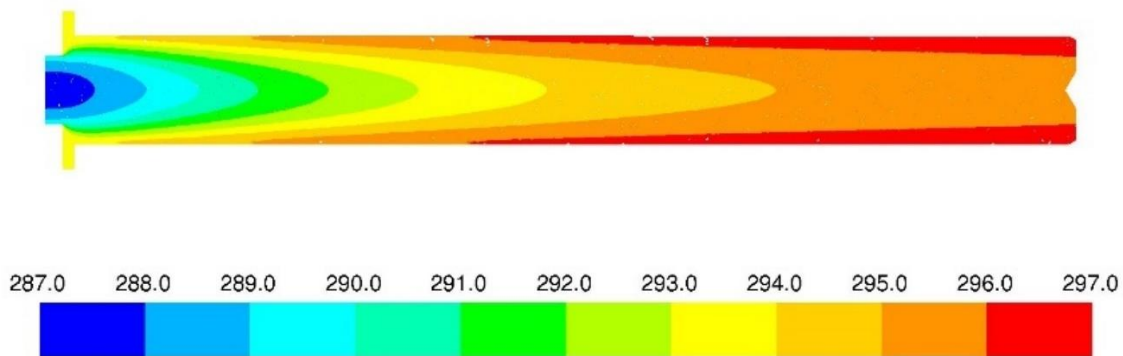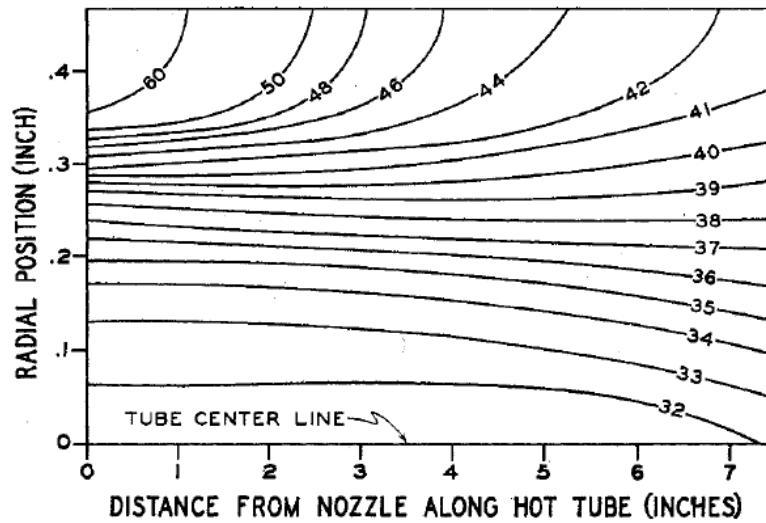**Figure 105. Contours of constant total pressure (in. Hg) from experiment [50]**
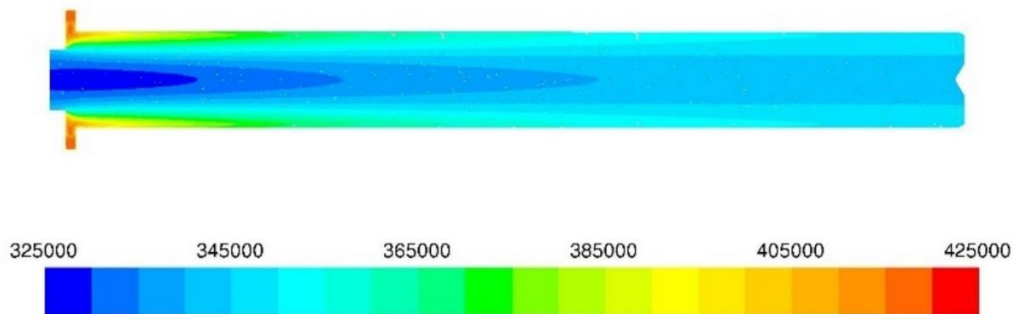
Figure 106. Contours of Total Pressure (Pa) from CFD

Contours of tangential velocity from experiment [50] are shown in Figure 107 and CFD results are in Figure 108. The comparison is again favorable. In all CFD-derived profiles of temperature, pressure, and velocity, the flow displays axisymmetry. In summary, a detailed review of the CFD-derived profiles of temperature, pressure, and velocity suggests that the flow is qualitatively representative of historical experimental

199

findings. Furthermore, this indicates that this CFD solution is likely suitable for detailed

internal flow analysis, including deducing the underlying physics of temperature

separation; this assumes a favorable comparison with experiment regarding device-level

temperature separation.
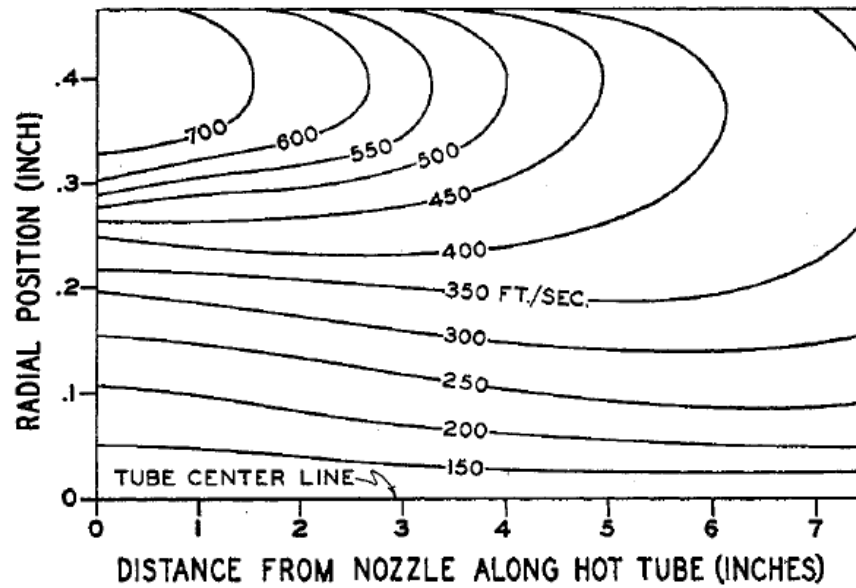
Figure 107. Contours of constant tangential velocity (ft/s) from experiment [50]
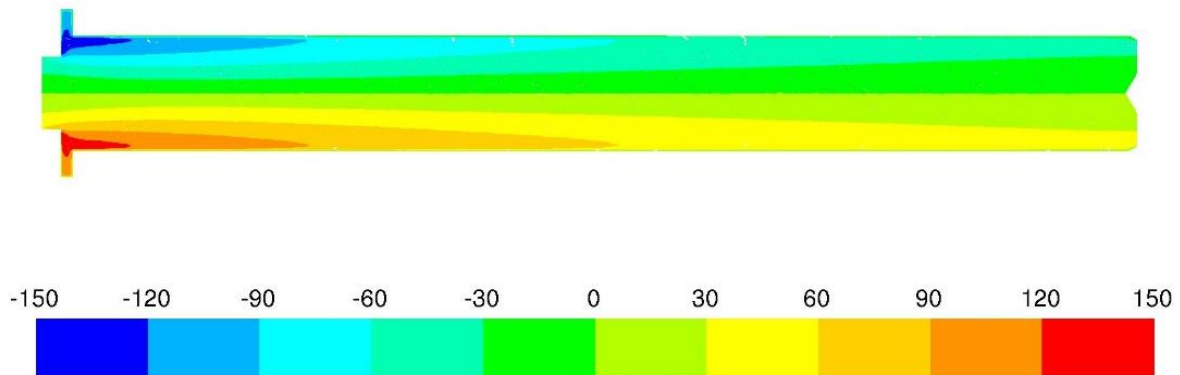
Figure 108. Contours of Tangential Velocity (m/s) from CFD

3.2.8.3 Examination of temperature separation performance

The CFD case was then compared to experiment with respect to quantified temperature separation. By adjusting the cold fraction, it was possible to create the characteristic vortex tube performance curves. Figure 109 compares the CFD results to experiment, indicating a very close match and a strong experimental validation. The hot curves consistently differ by approximately 0.4 K. The most prominent difference between CFD and experiment is for the cold exit at low cold fractions, especially $\mu_C = 0.2$ and 0.3, which differ by up to 1.5 K. It is likely that the differences are attributable to reverse flow, the effects of which are strongest for these cold fractions and are almost entirely absent by $\mu_C = 0.4$. The hot exit does have some reverse flow that increases at higher cold fractions, although this apparently does not have a strong influence on the result.
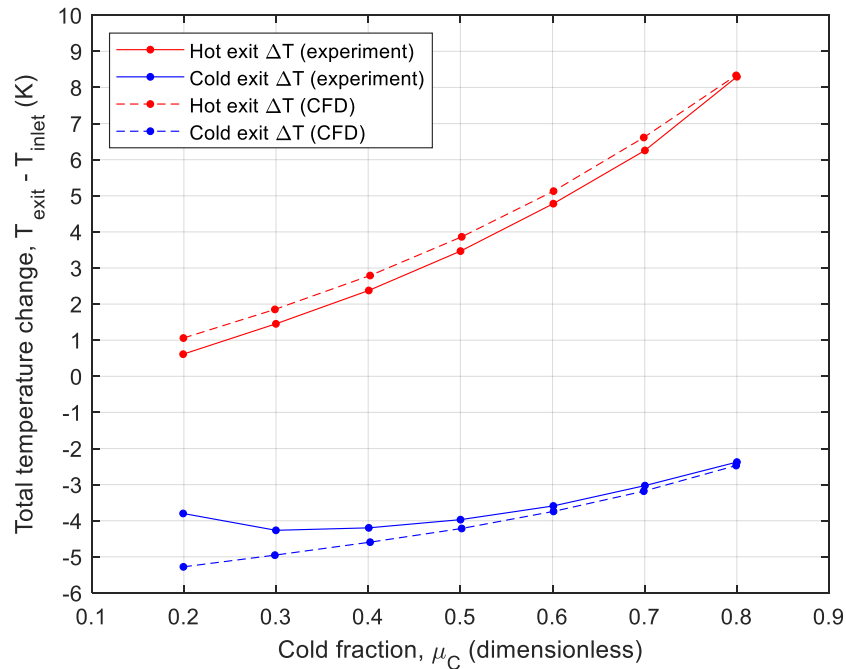
Figure 109. CFD vs. experimental temperature separation, matched hot exit static pressure

The boundary conditions play an important role in matching CFD to experiment. The hot exit pressure outlet, which is the only manually adjustable pressure boundary condition available, was carefully matched to the experimentally measured hot exit static pressures. This is shown with the red traces in Figure 110. The resulting static pressure at the cold exits compares favorably with the experiment, within 10 kPa. The most prominent difference between CFD and experiment is for the static pressure at the inlet. The CFD solution apparently predicts that the static pressure drop between the nozzles and the exits is essentially constant with respect to cold fraction, while the experimental findings suggest that the pressure drop decreases with increasing cold fraction. FLUENT overpredicts the pressure drops in each case, though it is especially glaring at high cold fractions. An important effect is that the computed nozzle static pressure increases with cold fraction; in turn, this increases density and—perhaps most significantly—decreases nozzle velocity. This becomes evident when nozzle velocity is plotted as a function of cold fraction, as in Figure 111.

Figure 110. CFD vs. experimental static pressures, matched hot exit static pressure
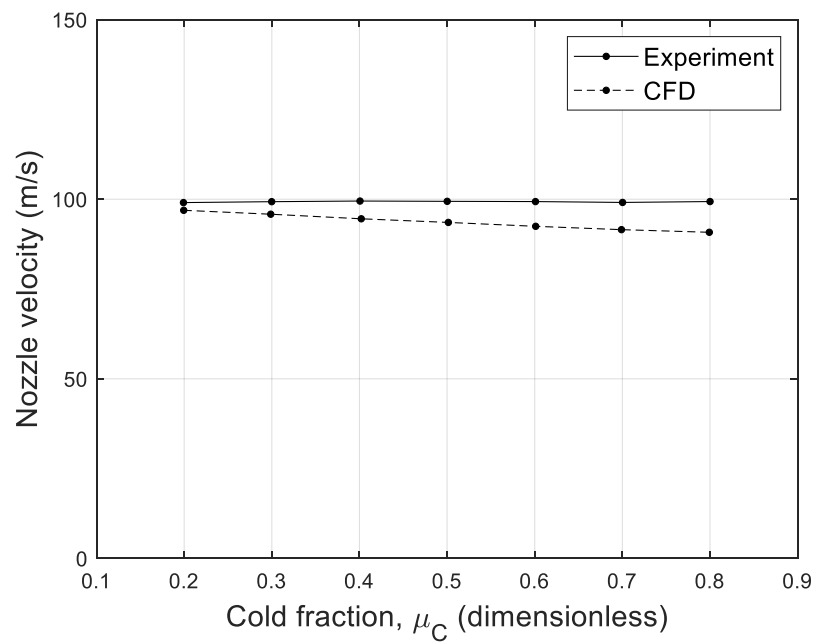
Figure 111. CFD vs. experimental nozzle velocities, matched hot exit static pressure

Since the predicted pressure drop across the vortex tube is basically constant, an alternative approach is to specify a constant hot exit static pressure to achieve a target nozzle static pressure—ideally equal to the experimental value. With these boundary conditions applied, the resulting pressure curves can be seen in Figure 112. In this case, the static pressure at the nozzle is essentially constant and is closely matched to the experimental values. The predicted static pressure at the exits is up to 40 kPa lower than the experimental values. The nozzle velocities, shown in Figure 113, are nearly identical between CFD and experiment for the range of cold fractions.
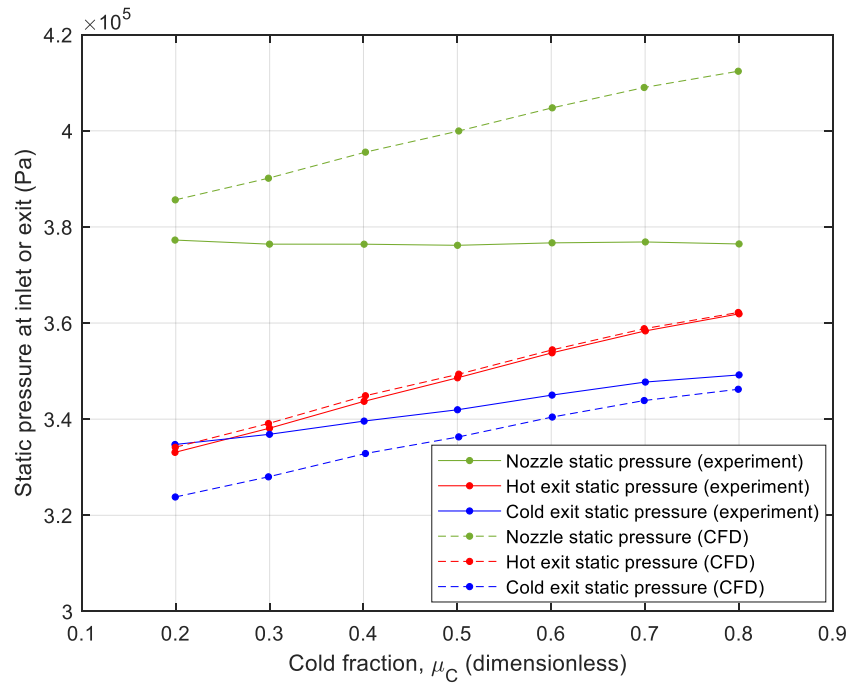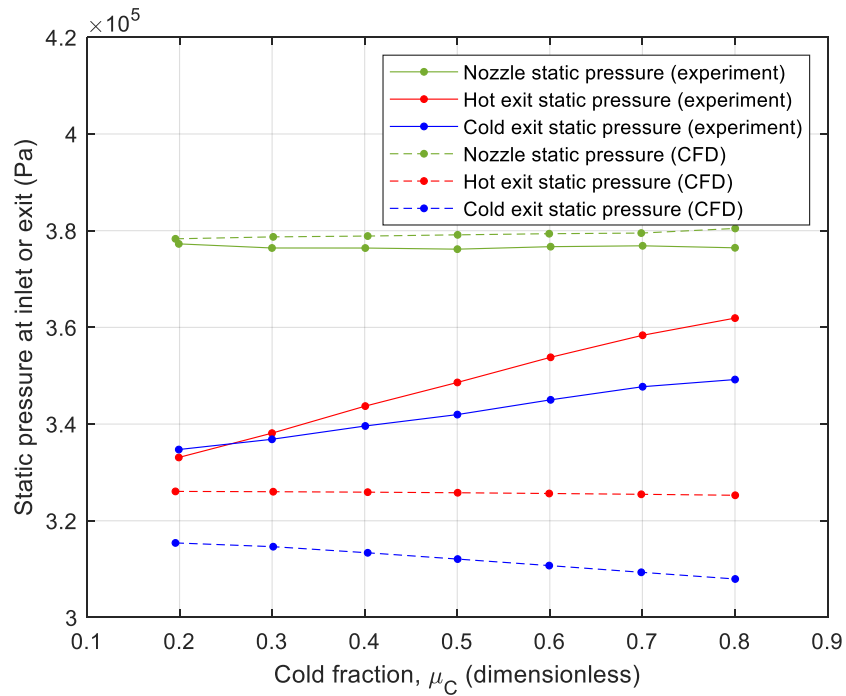

Figure 112. CFD vs. experimental static pressures, matched nozzle static pressure
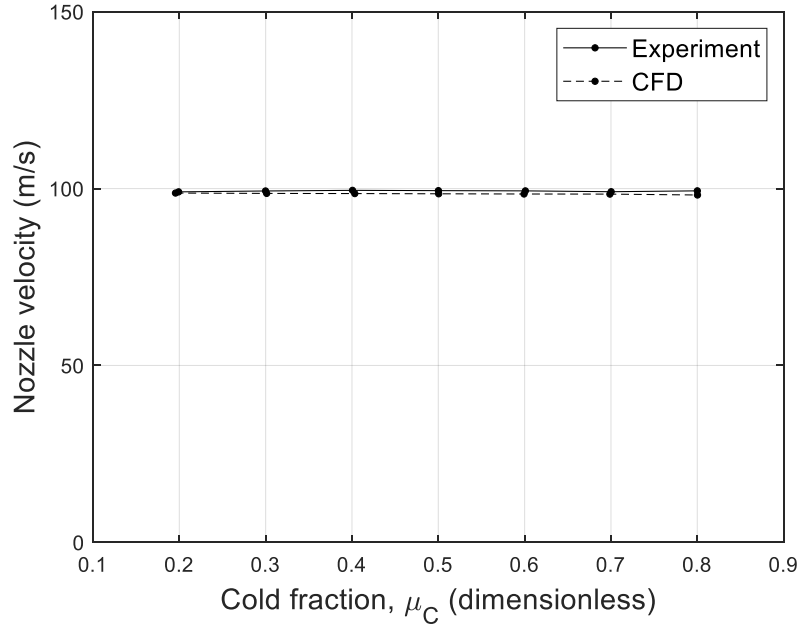
Figure 113. CFD vs. experimental nozzle velocities, matched nozzle static pressure

Nozzle properties for the CFD and experimental cases with matched nozzle static pressures are averaged across cold fractions and presented in Table 17, which indicates that the nozzle properties between CFD and experiment are nearly identical. This was not computed for the CFD case with the matched hot exit static pressure boundary condition since it yielded variations of nozzle properties with respect to cold fraction; averaging the properties across cold fraction would have masked these modeling nuances. It can be seen in Figure 114 that by matching nozzle static pressure, the CFD solution overpredicts temperature separation, resulting in a less favorable comparison with experiment. This highlights the importance of boundary conditions in matching dimensional temperature separation. It also appears that the trend of overpredicting the pressure drop across vortex tubes is correlated with the overprediction of dimensional temperature separation.

Table 17. Nozzle properties, CFD vs. Experiment (matched nozzle static pressure)

	Experiment	CFD
Mass flow rate (kg/s)	1.421×10^{-3}	1.420×10^{-3}
Inlet T_{total} (K)	293.3	293.4
Inlet P_{static} (bar, gauge)	3.001	-
Re_{D_h}	**18045**	**18027**
Pr	**0.721**	**0.721**
$\rho C_p \mu_{JT}$	**0.0108**	**0.0112**
Velocity (m/s)	99.30	98.58
Mach number	0.292	0.289
ρ (kg/m³)	4.551	4.582
μ (μPa-s)	18.05	18.06
k (mW/m-K)	25.33	25.34
C_p (J/kg-K)	1011.6	1010.8
μ_{JT} (K/bar)	0.2346	0.2424
Nozzle T_{static} (K)	288.3	288.5
Nozzle P_{static} (Pa, absolute)	376614	378890
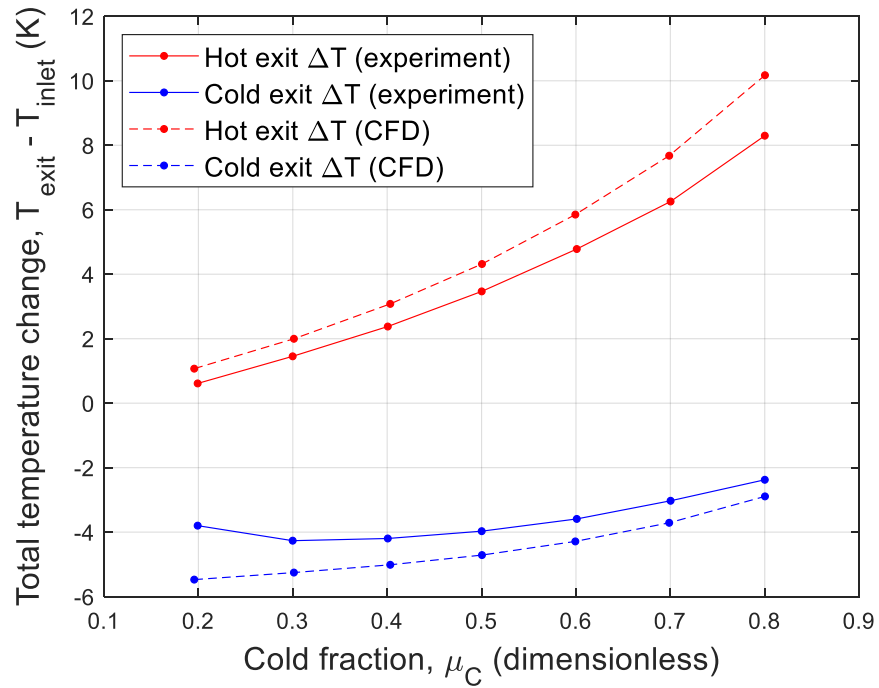
Figure 114. CFD vs. experimental temperature separation (matched nozzle pressure)

The most favorable comparison between CFD and experiment—the cases with matched hot exit static pressures—are compared in terms of non-dimensionalized temperature separation, with T_t^* in Figure 115 and $\rho^* C_p^* T_t^*$ in Figure 116; the curves of $\rho^* C_p^* T_t^*$ compare slightly more favorably than those of T_t^*. The inaccuracy of CFD in predicting the relative magnitudes of temperature and pressure changes across a vortex tube is manifested in a disparity between the dimensionless CFD and experimental results; nevertheless, the comparison in Figure 116 suggests that the fundamental characteristics of vortex tube temperature separation are indeed replicated in CFD and that this simulation forms a legitimate basis for the investigation of its underlying behavior.
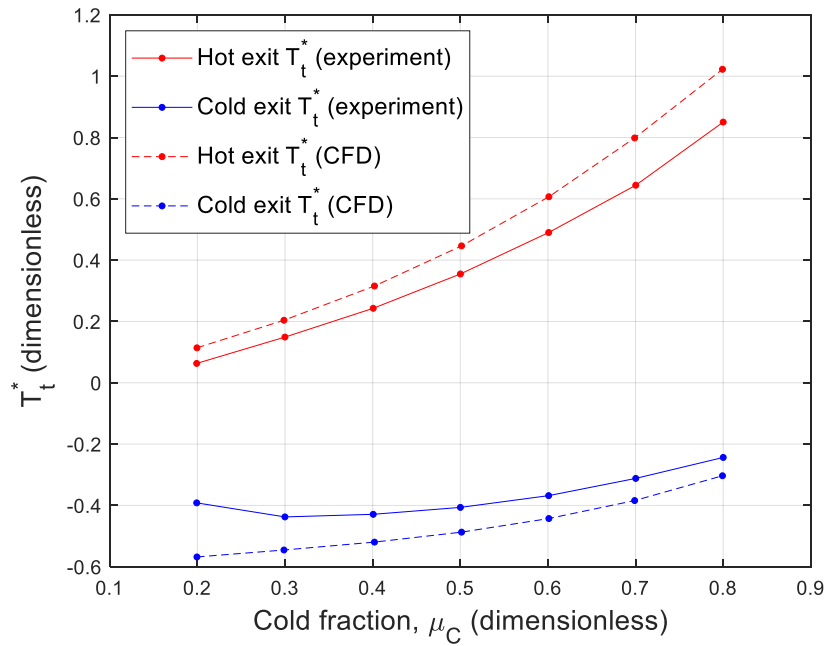
Figure 115. Dimensionless temperature separation, T_t^*, CFD vs. experiment

(matched hot exit static pressures)
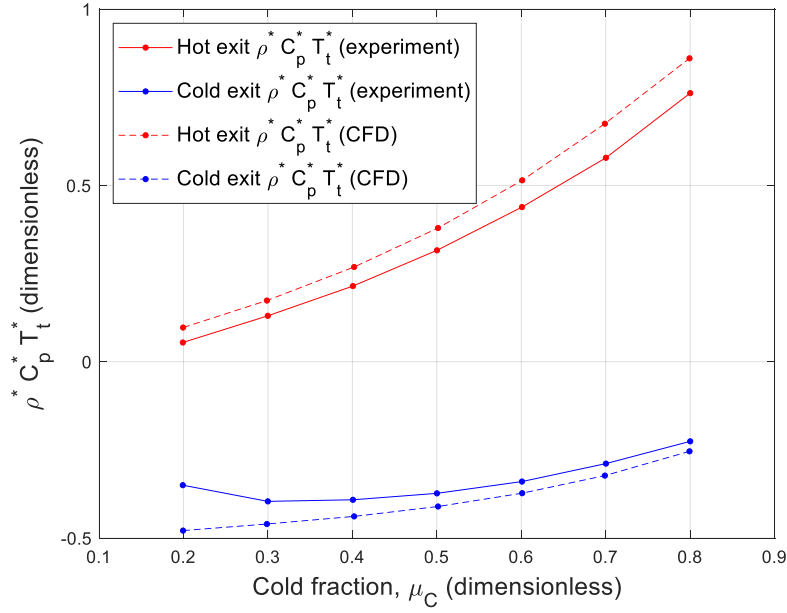
Figure 116. Dimensionless temperature separation, $\rho^* C_p^* T_t^*$, CFD vs. experiment (matched hot exit static pressures)

In general, when evaluating temperature separation for a variety of CFD test cases where experimental data is not available, it is simpler to use the same hot exit boundary condition for each cold fraction rather than speculate about a potential pressure drop function. Changing the boundary conditions—matching either the hot exit static pressure or nozzle static pressure to experiment—obviously changed the dimensional temperature separation characteristics between the CFD cases, which are now directly compared in Figure 117. It is also a matter of interest to see how much these changes altered the non-dimensional temperature separation characteristics of the solution. It turns out that the two solutions yield virtually identical results in terms of $\rho^* C_p^* T_t^*$, as seen in Figure 118; hence, at a fundamental, dimensionless level, it does not matter whether the hot exit static pressure is varied or kept constant.

208
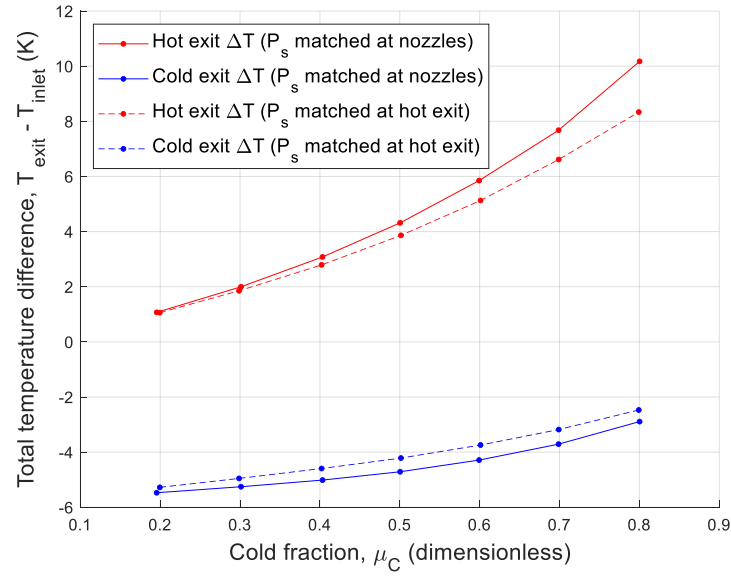
Figure 117. Dimensional CFD temperature separation with static pressures matched to experiment at either nozzle or hot exit
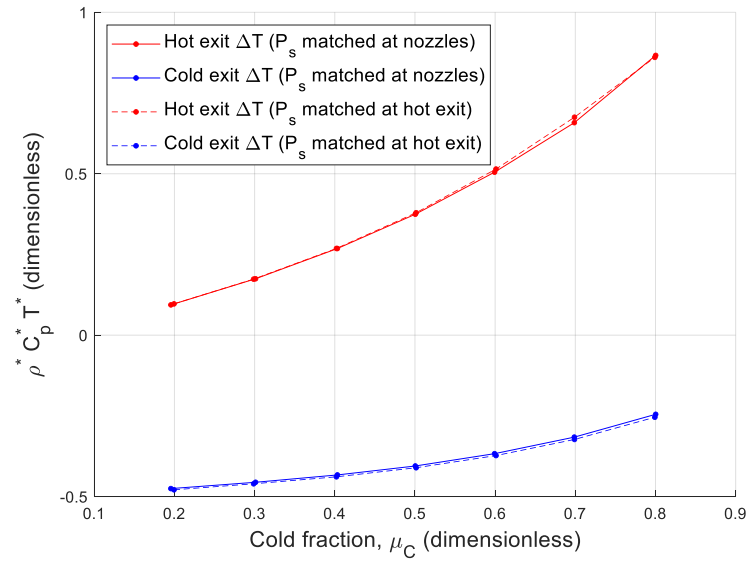
Figure 118. Dimensionless CFD temperature separation, $\rho^* C_p^* T_t^*$, with static pressures matched to experimental values at either nozzle or hot exit

Interestingly, a comparison of T_t^* between the two CFD cases, shown in Figure 119, finds that the results are essentially identical. Because the dimensionless profiles are essentially identical regardless of boundary condition strategy, subsequent CFD test cases will employ a constant hot exit static pressure boundary condition for all cold fractions.
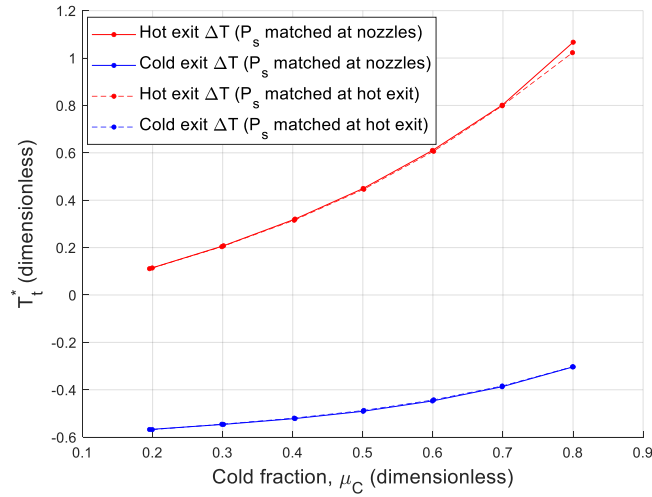
Figure 119. Dimensionless CFD temperature separation, T_t^*, with static pressures matched to experimental values at either nozzle or hot exit

3.2.9 *The underlying mechanism of temperature separation*

Attention now turns to deducing the underlying mechanism of temperature separation. This endeavor requires a complete picture of all flow properties throughout the vortex tube—a job best suited for CFD. A previous study by Aljuwayhel et al. [77] was conducted in two dimensions, while Behera et al. [66] performed a study in three dimensions but with a periodic boundary. Both sets of researchers enforced axisymmetric conditions but incorporated very limited experimental validation. This is the first such analysis using a full three-dimensional flow characterization based on robust experimental validation, no flow constraints, and incorporating real-gas effects. The flow

solution used in the analysis corresponds to that in Figure 109 on page 201, which was shown to compare favorably with experiment, for a cold fraction of $\mu_C = 0.40$.

The analysis will incorporate an energy balance conducted for an appropriate control volume, one surface of which must be the interface between hot and cold regions of the flow. The "hot region" of the vortex tube contains flow which enters via the nozzles and exits exclusively via the hot exit. It is an annulus bounded on the outside by the tube walls and it circumscribes the "cold region" on the inside via an interface, though the radius of the interface between the two regions varies with axial position.

The control volume will be assigned to the fluid in the hot region. The flow in this region has four surfaces: (1) an annular "inlet" face adjacent to the nozzles, (2) an annular "outlet" face at the hot exit, (3) the interface between the hot and cold flows, and (4) the tube wall, which is defined in CFD as adiabatic and therefore has no energy transferred across it. The energy advected via the inlet and outlet surfaces will be quantified along with the energy transfer across the interface. The energy transfer across the interface is of primary interest since this is expected to explain the mechanism of temperature separation.

The integral form of energy equation will be used for the analysis. The differential form in Eq (73) can be converted to an integral form, Eq (83), for an arbitrary region (see Panton [91]). Although the total internal energy term, e_t, is conventionally defined as $e_t \equiv e + \frac{1}{2}v^2 + gZ$, the gravitational potential energy, gZ, will not be considered.

$$\frac{d}{dt}\int_{AR}\rho e_t d\Psi + \int n_i(v_i - w_i)\rho e_t dS$$

$$= -\int n_i q_i dS + \int_{fluid} n_i \tau_{ij} v_j dS - \int_{fluid} n_i v_i \, P \, dS + \int_{solid} n_i T_{ij} v_j dS \tag{83}$$

The analysis will assume steady flow, i.e. $\frac{d}{dt}\int_{AR}\rho e_t d\Psi = 0$; this is both a

principled and pragmatic decision. The possibility exists that short-period fluctuations

occur which may temporarily increase or decrease the energy in the control volume;

however, the present analysis assumes that these fluctuations have a zero mean. From a

pragmatic standpoint, the mesh that was validated against the experimental data is not

well suited to a transient CFD solution. Experimentation with transient solutions revealed

immediate instabilities for time steps greater than one nanosecond. Assuming the results

of a nanosecond-scale time step simulation are satisfactory, the computational time

required to achieve a flow-relevant time scale vastly exceeded time available for this

research. The results shown are therefore the result of a steady CFD simulation.

Since the boundaries of the control volume are stationary, all components of the

surface velocity vector, $\boldsymbol{w}$, are zero. The control volume encompasses only a fluid region,

so no solid regions will be considered. Finally, by applying the definition of total

(stagnation) enthalpy [92], shown in Eq (84), the flow work term, $\int_{fluid} n_i v_i \, p \, dS$, is

combined with the advection term on the left side of the equation. The integral form

which will be used is Eq (85), which contains three terms: the term $-\int n_i v_i \, \rho \, h_t \, dS$

represents the total enthalpy advected across the surfaces; the term $-\int n_i q_i dS$ represents

heat transfer by conduction across the surfaces; and finally $\int n_i \tau_{ij} v_j dS$ represents the

viscous work performed at the surfaces.

$$h_t \equiv e + \frac{p}{\rho} + \frac{1}{2}v^2 \qquad (84)$$

$$0 = -\int n_i v_i\, \rho\, h_t\, dS - \int n_i q_i dS + \int n_i \tau_{ij} v_j dS \qquad (85)$$

The form of the energy equation represented by Eq (85) is especially well-suited to the present task because it requires only surface integrals to be computed, and any real gas effects are incorporated into the variation of specific enthalpy by means of the real gas model resident in the CFD code. By contrast, the conversion of Eq (63) on page 147 to integral form yields two volume integrals—a flow work term involving spatial gradients of static pressure and the Joule-Thomson coefficient, and another term necessary to correct the total temperature distribution for spatial variations in C_p—the evaluation of which would complicate the analysis considerably.

Many of the terms in Eq (85) are readily available from the CFD solution, including velocity, density, and specific total enthalpy, which permit the evaluation of the advection integral for a defined surface. However, evaluation of the heat conduction and viscous work terms requires additional information not provided explicitly by the CFD solution. For instance, heat flux is defined using Eq (86). Evaluation of the heat flux at any point requires a measure of effective thermal conductivity, k_{eff}, which is also directly available from the CFD, and the static temperature gradients, $\partial_i T$, which must be calculated separately based on the distribution of static temperature. Effective thermal conductivity accounts for contributions from both the molecular gas property as well as its turbulent counterpart.

$$q_i = -k_{eff}\partial_i T \tag{86}$$

The components of the viscous stress tensor, τ_{ij}, will be computed based on cylindrical, three dimensional coordinates using Eqs (87) – (93) [91]; the axis of rotation runs down the length of the tube and the positive z direction is oriented toward the hot exit. The effective viscosity, μ_{eff}, is drawn from the CFD solution and likewise accounts for both molecular and turbulent properties.

$$\tau_{rr} = \mu_{eff}\left[2\frac{\partial v_r}{\partial r} - \frac{2}{3}(\nabla \cdot \boldsymbol{v})\right] \tag{87}$$

$$\tau_{\theta\theta} = \mu_{eff}\left[2\left(\frac{1}{r}\frac{\partial v_\theta}{\partial \theta} + \frac{v_r}{r}\right) - \frac{2}{3}(\nabla \cdot \boldsymbol{v})\right] \tag{88}$$

$$\tau_{zz} = \mu_{eff}\left[2\frac{\partial v_z}{\partial z} - \frac{2}{3}(\nabla \cdot \boldsymbol{v})\right] \tag{89}$$

$$\tau_{r\theta} = \tau_{\theta r} = \mu_{eff}\left(r\frac{\partial}{\partial r}\left(\frac{v_\theta}{r}\right) + \frac{1}{r}\frac{\partial v_r}{\partial \theta}\right) \tag{90}$$

$$\tau_{\theta z} = \tau_{z\theta} = \mu_{eff}\left(\frac{\partial v_\theta}{\partial z} + \frac{1}{r}\frac{\partial v_z}{\partial \theta}\right) \tag{91}$$

$$\tau_{zr} = \tau_{rz} = \mu_{eff}\left(\frac{\partial v_z}{\partial r} + \frac{\partial v_r}{\partial z}\right) \tag{92}$$

$$\nabla \cdot \boldsymbol{v} = \frac{1}{r}\frac{\partial}{\partial r}(rv_r) + \frac{1}{r}\frac{\partial v_\theta}{\partial \theta} + \frac{\partial v_z}{\partial z} \tag{93}$$

The inlet and outlets to the control volumes are simply defined as annular faces with outside radii equal to the tube radius of 3.1 mm and internal radii equal to radius of the interface at the corresponding axial locations. Because the solutions of Aljuwayhel et al. [77] and Behera et al. [66] enforced an axisymmetric flow constraint, the interface separating hot and cold regions is easily defined by selection of the proper streamline. Although the three-dimensional spiraling flow in the present solution is nearly axisymmetric (a characteristic consistently observed in the internal flow examinations), the solution was not constrained as such during its development. Therefore, it is not—

formally-speaking—an axisymmetric flow and the streamline technique cannot be applied here. The consequence is that defining the interface for this flow is not a straightforward process.

The adopted approach was to generate a set of high-resolution, three-dimensional pathlines in FLUENT, which were separated into those exiting via the hot side and those exiting the cold side. A total of 1,105 hot pathlines and 569 cold pathlines were produced, each using a step size of 0.01 mm; this was the maximum feasible resolution with the given solution. The pathlines were analyzed and the innermost hot pathline and the outermost cold pathline were identified, shown in Figure 120, which illustrates the paths in a two-dimensional plane of lateral position against axial position. The two pathlines originate from separate nozzles and spiral down the length of the tube and the cold pathline reverses direction at the hot exit of the tube before traversing back the entire length again to leave via the cold exit. Although the two spirals are offset circumferentially—the number of pathlines available was high but nonetheless finite—this method was believed to closely approximate the interface.
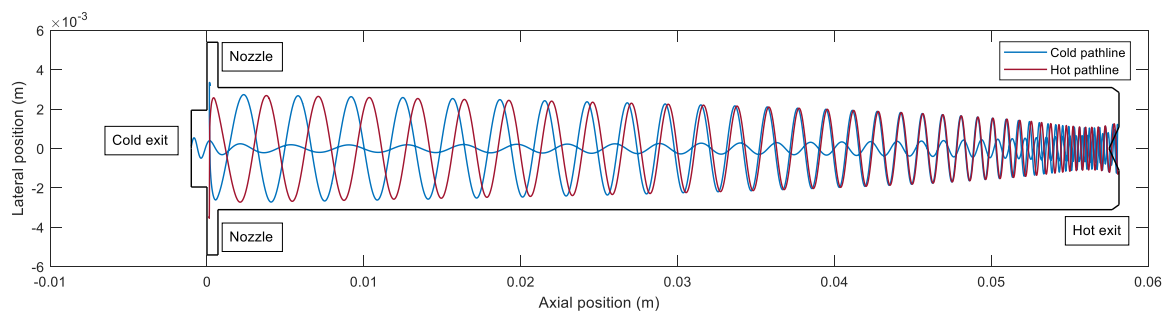
Figure 120. Hot and cold pathlines used to define hot/cold interface

The radius of each pathline was computed for each axial position and, upon further examination, it was verified that the radii lie exceptionally close to each other at

215

any given axial location, generally separated by less than 0.04 mm. The actual two-dimensional interface curve was defined by the mean radius of the hot and cold pathlines for each axial location. The three radius lines—hot, cold, and mean interface—are shown in Figure 121. Because the hot, cold, and mean lines are so close as to be nearly indistinguishable at the scale of Figure 121, a closeup view of a region near the hot exit is also provided in Figure 122, in which the pathlines lie particularly far apart and are more readily distinguishable. Also shown in Figure 121 are the axial extents of the control volume, with the inlet face depicted as a blue dotted line and the outlet face as a red dotted line. The axial position origin is coincident with the side of the nozzles nearest the cold exit, and the axial extent of the nozzles is 0.70 mm. The flow at the immediate exit of the nozzles is chaotic and disordered, and the large-scale flow features have not yet been established in this region. The inlet face of the control volume was therefore specified at an axial location of 1.0 mm to improve the quality of the interface, the principal measure of which is the magnitude of the mass flux through it.
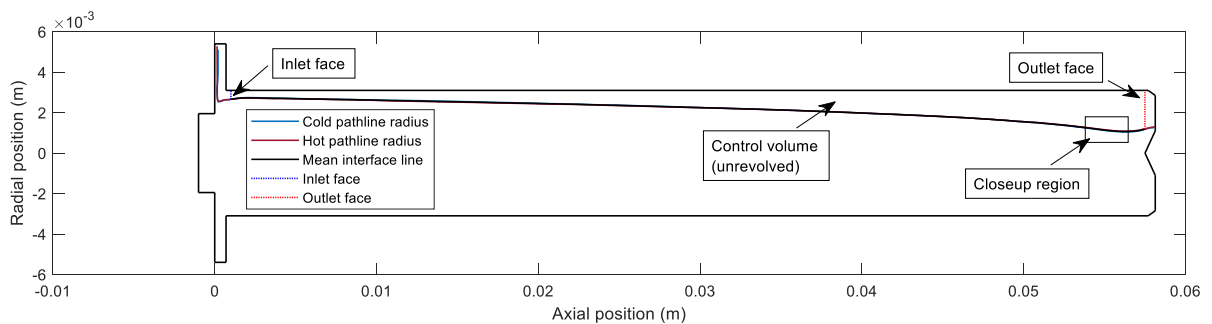
Figure 121. Unrevolved hot/cold interface

216
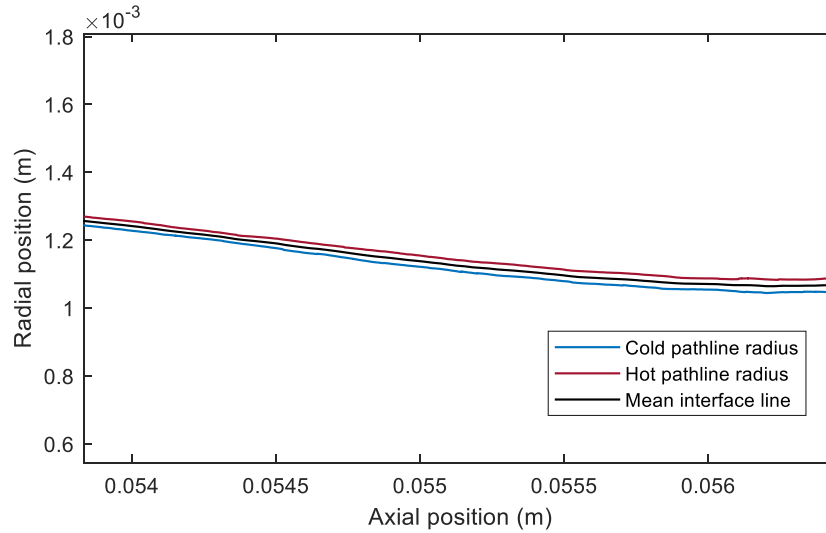
Figure 122. Closeup revealing innermost "hot" pathline, outermost "cold" pathline, and mean interface line

Ideally, the interface would have zero mass flux; however, because it is a notional interface in a turbulent flow, this can never be truly the case. Moreover, the interface was defined here on an empirical basis from computed pathlines and its quality may be impacted by computational artifacts. Nevertheless, for the accuracy of the calculations, it is important to select an interface such that its axial extent is maximized to ensure all contributions to temperature separation are included, while minimizing the mass flux and corresponding advection. The outlet face was positioned at an axial location of 57.5 mm, upstream of the hot exit geometry features that begin at 57.7 mm and the hot exit plane at 58.1 mm. The region bounded by the tube wall, the inlet face, the outlet face, and the mean interface line, labeled "Control volume (unrevolved)" in Figure 121, was revolved around the central axis to form a full three-dimensional control volume.

For practical use, the interface surface and all equations were discretized. The inlet and outlet annular faces were divided radially and circumferentially into a set of

polar rectangles. The three-dimensional interface surface was sliced into a set of axial segments, each of which was approximated as the lateral surface of a conical frustum. Each of the frusta was further subdivided into a set of circumferential faces in a manner similar to that shown in Figure 123.
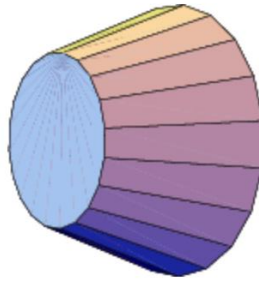
Figure 123. Notional conical frustum with circumferential faces [97]

Although the near-axisymmetry of the flow would imply that the circumferential subdivision into separate faces was unnecessary and rather, the flow properties for the entire frustum could be adequately deduced from a single point anywhere on the frustum, it was understood that computational artifacts might cause small circumferential variations. To mitigate this influence, the subdivision was deemed necessary and had a net effect of averaging out the properties at each face.

The FLUENT solution was imported into the software package Tecplot 360 EX 2020 R2, which permitted the interpolation of flow properties at any point in the domain. This was important because the locations at which flow data was desired did not generally correspond exactly to the cell centroids of the FLUENT solution, which was generated for an unstructured mesh. An example low-resolution point cloud of inlet, outlet, and interface centroids is shown in Figure 124. The inlet, whose face centroids are plotted in blue, contains 250 faces at 5 radial stations and 50 circumferential stations. The

218

interface is in yellow with 50 circumferential stations and 40 longitudinal stations, and hence 2000 faces. The outlet is in red with 10 radial stations and 50 circumferential stations, and 500 faces.
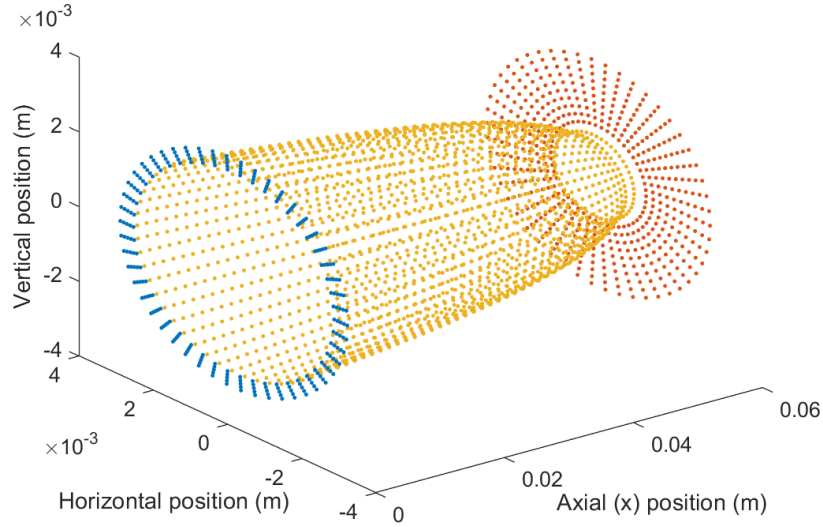
Figure 124. Example low-resolution point cloud of face centroids on inlet (blue), interface (yellow), and outlet (red)

Flow properties were interpolated at the desired locations using an inverse distance algorithm in Tecplot. Flow properties for each face on the inlet, outlet, and interface were evaluated at the corresponding centroid, including velocity components, density, total enthalpy, effective thermal conductivity, and effective viscosity. Advection, heat flux, and work computations need a surface unit normal vector for each face. For the inlet and outlet faces, each normal vector was aligned entirely in the axial direction. For the faces on the interface, the process was more involved. The two-dimensional curve of radius as a function of axial position was numerically differentiated to determine the slope, $\frac{dr}{dz}$, at the centroid, essential to computing the normal vector. Numerical

differentiation is an inherently noisy process, and a smoothing algorithm was applied to minimize erratic surface normal vectors.

The heat flux and viscous stress tensor calculations also use gradients of static temperature and velocity, which required interpolated values at locations offset some distance from the face. In every case, gradients were computed using central difference approximations. For example, the viscous stress tensor component τ_{rz} was computed using Eq (94). Suitable offset distances were found to be $\Delta r = \Delta z = 0.05$ mm.

$$\tau_{rz} = \mu_{eff}\left(\frac{\partial v_z}{\partial r} + \frac{\partial v_r}{\partial z}\right) \approx \mu_{eff}\left(\frac{v_z(r+\Delta r,\theta,z) - v_z(r-\Delta r,\theta,z)}{2\Delta r} + \frac{v_r(r,\theta,z+\Delta z) - v_r(r,\theta,z-\Delta z)}{2\Delta z}\right) \tag{94}$$

The use of faces distributed across the inlet, outlet, and interface surfaces introduces a "grid-within-a-grid" concept. To that end, the results are introduced with a brief grid sensitivity study to ensure that the overlaid grid resolution is not unduly influencing the results. The inlet and outlet are varied from 2,500 to 100,000 faces, while the interface is varied from 5,000 to 2,000,000 faces. The mass flow rate and advection across the surfaces are monitored for convergence for all three surfaces, and mass-averaged (bulk) total temperature is also monitored for the inlet and outlet, as seen in Table 18.

Table 18. Grid sensitivity study

	Circumferential segments	Radial segments	Total faces	Mass flow rate (kg/s)	Advection (W)	T_{mean} (K)
Inlet	50	50	2500	-9.080×10^{-4}	-380.52	293.53
	200	100	20000	-9.082×10^{-4}	-380.59	293.53
	500	200	100000	-9.083×10^{-4}	-380.63	293.53
Outlet	Circumferential segments	Radial segments	Total faces	Mass flow rate (kg/s)	Advection (W)	T_{mean} (K)
	50	50	2500	8.319×10^{-4}	350.9744	296.20

	Axial segments	Radial segments	Total faces	Mass flow rate (kg/s)	Advection (W)	
	200	100	20000	8.320×10^{-4}	351.0158	296.20
	500	200	100000	8.319×10^{-4}	350.9906	296.20
Interface	100	50	5000	-1.052×10^{-4}	-44.016	
	500	200	100000	2.802×10^{-5}	11.8094	
	1000	500	500000	6.549×10^{-5}	27.5542	
	2000	1000	2000000	6.232×10^{-5}	26.2828	

The inlet and outlet are almost entirely insensitive to grid resolution across this range, with negligible changes in the response values; the increase in total temperature across the control volume remains constant at $\Delta T = 2.67$ K. The interface, however, is quite sensitive to changes in resolution: between 5,000 and 100,000 faces, the net mass flow rate and advection reverse directions; between 500,000 and 2,000,000 faces, the mass flow rate and advection have apparently stabilized. Recall that the entire mesh in the FLUENT solution consists of approximately 5,200,000 cells, so characterizing the interface alone with 2,000,000 faces is needlessly oversampling the surface. Thus, the interface with 500,000 faces will be used for the analysis with the inlet and outlets with 2,500 faces.

A note regarding sign convention: the surface unit normal vectors point outward from the control volume. In the advection term, $\int n_i v_i \, \rho \, h_t \, dS$ in Eq (85), repeated below, mass flow into the control volume via a surface is seen as positive, while flow out is seen as negative. On the right side of Eq (85), positive values of $-\int n_i q_i dS$ and $\int n_i \tau_{ij} v_j dS$ refer to heat transfer and work *into* the control volume.

$$0 = -\int n_i v_i \, \rho \, h_t \, dS - \int n_i q_i dS + \int n_i \tau_{ij} v_j dS \tag{85}$$

The continuity balance is shown in Table 19. The mass flow rate via the inlet is greater than that via the outlet, suggesting that there must be a net positive mass flux via the interface. In other words, some mass is entering via the inlet but leaving via the interface before it reaches the outlet; this obviously implies that the quality of the interface is imperfect.

Table 19. Continuity balance for control volume

Surface	Mass flow rate (kg/s)
Inlet	9.080×10^{-4}
Outlet	-8.319×10^{-4}
Interface	-6.549×10^{-5}
Sum	*1.063×10^{-5}*

The difference in mass flow rates between the inlet and outlet indicate that there should be 7.612×10^{-5} kg/s flowing out of the interface, equivalent to 8.4% of the flow that entered via the inlet, but calculations at the interface find only 6.549×10^{-5} kg/s, or 7.2% of the inlet mass flow rate, actually crossing the interface. This means that present analysis cannot account for 1.063×10^{-5} kg/s or 1.2% of the mass flow entering via the inlet. The apparent sensitivity of the interface fluxed to grid resolution and the relatively complex math required for the calculations (compared to the inlet and outlet) suggest that the error may be attributable to computational challenges at the interface. Naturally, the mass flow rate is very sensitive to the pointing angle of the surface normal vectors with respect to the local flow velocity, and any pointing errors will result in an apparent mass flow rate across the interface. This is compounded somewhat in three dimensions since the surface normal vectors are a revolved version of the two-dimensional interface.

The mean mass flux values for each of the 1000 axial frusta are plotted in Figure 125. The occasional large values are likely due to unusual angles of surface normal vectors, despite efforts to reduce this effect. The majority of the mass flux apparently occurs nearest the nozzles and although the magnitude decreases toward the hot exit, it is never entirely eliminated.
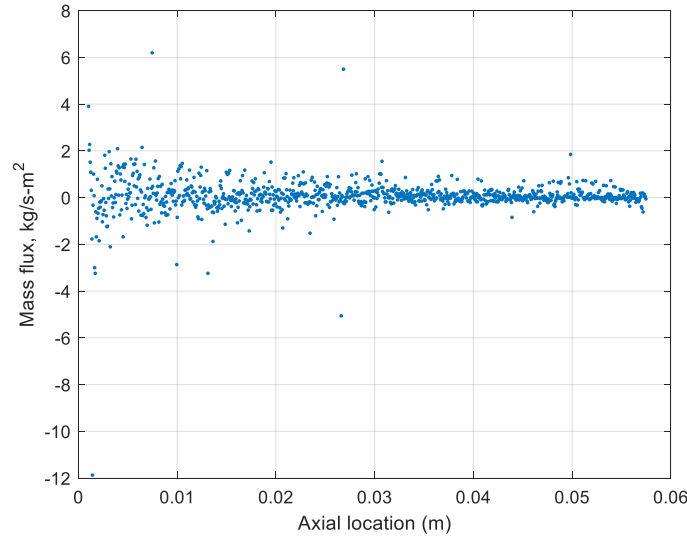
Figure 125. Mass flux across interface vs. axial location

The contributions of each of the nine components of the viscous stress tensor as well as the heat transfer were summed across the surface area of the interface. The results are listed in Table 20. The calculated energy transfer across the interface by means of work and heat transfer is 2.893 W, of which 0.294 W (10.1%) is via heat transfer and 2.597 W is via viscous work. Note that the computed values of $\int n_r \tau_{r\theta} v_\theta dS$ and $\int n_r \tau_{rz} v_z dS$ are not as sensitive to pointing errors in the normal vector as are the mass flux computations. This is due partly to the fact that in the region where the greatest work is done, $n_r \approx 1$; it is also partly because the shear stress terms, $\tau_{r\theta}$ and τ_{rz}, are driven by

calculated velocity gradients—and small computational artifacts in the velocity field are damped out somewhat by the central differencing method.

Table 20. Contributions of heat and stress tensor components to energy transfer

Contributing component	Power across interface (W)
$\int n_r\, q_r\, dS$	0.3077
$\int n_z\, q_z\, dS$	-0.0133
$\int n_r\, \tau_{rr} v_r\, dS$	1.9653×10^{-4}
$\int n_r\, \tau_{r\theta} v_\theta\, dS$	4.2827
$\int n_r\, \tau_{rz} v_z\, dS$	-1.6860
$\int n_\theta\, \tau_{\theta r} v_r\, dS$	0
$\int n_\theta\, \tau_{\theta\theta} v_\theta\, dS$	0
$\int n_\theta\, \tau_{\theta z} v_z\, dS$	0
$\int n_z\, \tau_{zr} v_r\, dS$	9.3779×10^{-4}
$\int n_z\, \tau_{z\theta} v_\theta\, dS$	2.2129×10^{-3}
$\int n_z\, \tau_{zz} v_z\, dS$	-1.3585×10^{-3}

Heat flux as a function of axial position is presented in Figure 126. Close to the nozzles, positive values of heat flux—in which heat is transferred into the control volume—are quite large, approaching 20 kW/m^2, though the heat flux decreases rapidly down the length of the tube. At approximately 5 mm, the heat flux reverses direction and heat is transferred from the hot flow to the cold flow, though at much smaller magnitudes. This effect disappears around an axial location of 20 mm, beyond which the contribution of heat transfer is negligible.
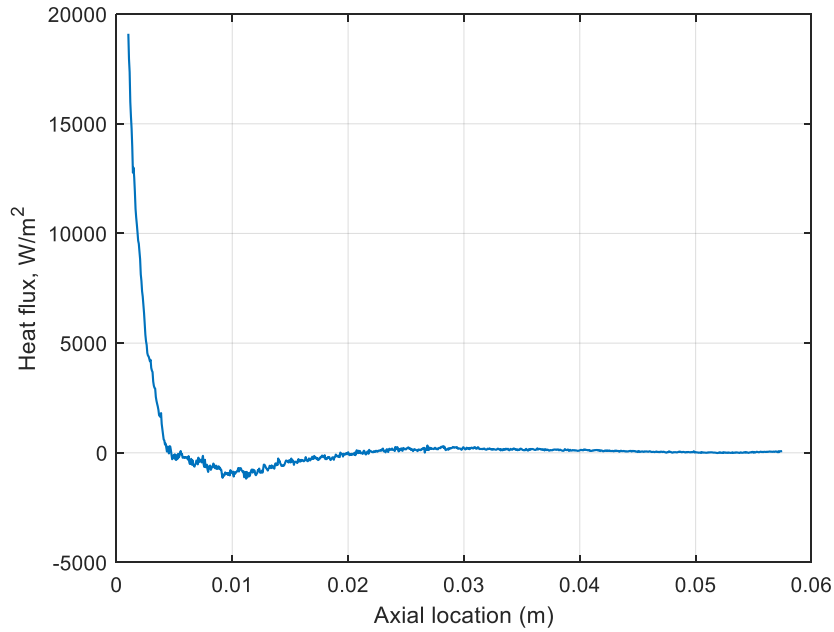
Figure 126. Heat flux across interface vs. axial location

The overall work flux from all viscous stress tensor components is plotted against axial location in Figure 127. Just beyond the nozzles, work is transferred from the hot region to the cold, but past 1.7 mm this trend reverses in dramatic fashion as the work flux spikes to 11,000 W/m^2 near an axial location of 5 mm and then slowly decreases with axial location. At 25 mm, the work flux is at less than 20% of its peak value, and slowly approaches zero toward the hot exit, becoming negligible beyond approximately 40 mm.
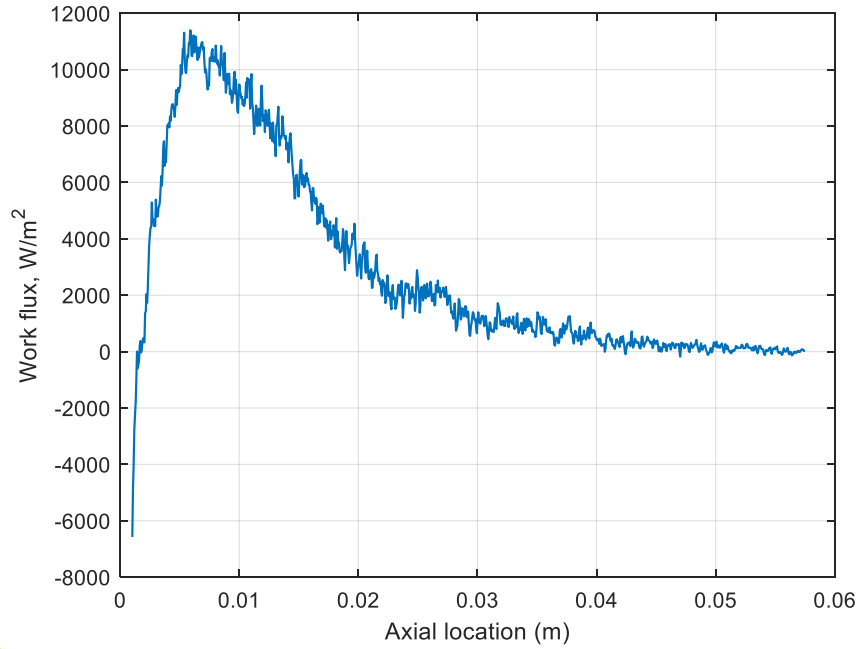
Figure 127. Work flux from all viscous stress tensor components vs. axial location

Only two components of the viscous stress tensor contribute significantly: $\tau_{r\theta}$ and τ_{rz}, though the two components perform work in opposite directions, with $\tau_{r\theta}$ contributing to increased temperature separation and τ_{rz} decreasing it. The heat flux and the work flux of the significant components is plotted in Figure 128. Recall that the experimental validation of the present CFD solution included examinations of radial profiles of velocity and temperature taken at a variety of axial locations (see Figure 94); the vertical dot-dashed lines indicate axial locations of 1.45 mm (2.5% of 58.1 mm tube length), 2.9 mm (5%), 5.8 mm (10%), 11.6 mm (20%), and 29.05 mm (50%).
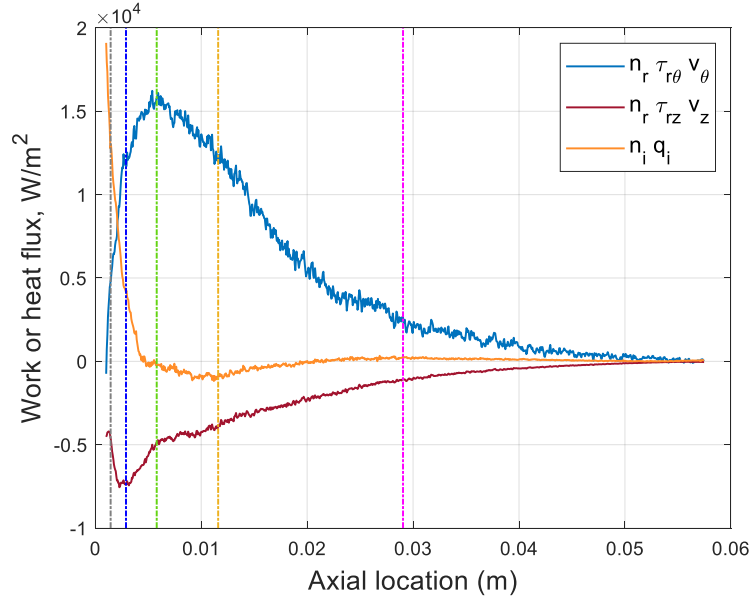
Figure 128. Heat and work flux from significant components: q_i, $\tau_{r\theta}$, and τ_{rz}

These findings are broadly in line with those of Aljuwayhel et al. [77] and Behera et al. [66], who similarly identified that viscous work in the tangential direction was most significant, while the work in the axial direction partially counteracted its contribution; see Figure 53 and Figure 54. However, recall that both sets of researchers suggested a much larger role of heat transfer, with a net contribution *out* of the control volume with a magnitude equivalent to 30% of the tangential work component transfer *into* the control volume; in other words, they concluded that the effect of heat transfer is to significantly reduce temperature separation. Moreover, they assessed that the magnitude of the heat transfer was comparable to or greater than that of the axial work, though the two efforts used different cold fractions and cannot be compared directly. The most significant difference between the previous works and the present study is that heat transfer has been found here to contribute *positively* to temperature separation, though the magnitude

estimated herein is much smaller, at 7% of the tangential work component and 10% of the overall energy transfer.

Radial profiles of tangential velocity and angular velocity taken at the planes indicated in Figure 128 are shown in Figure 129 and Figure 130, respectively, with the radial locations of the interface marked in black on each respective curve.
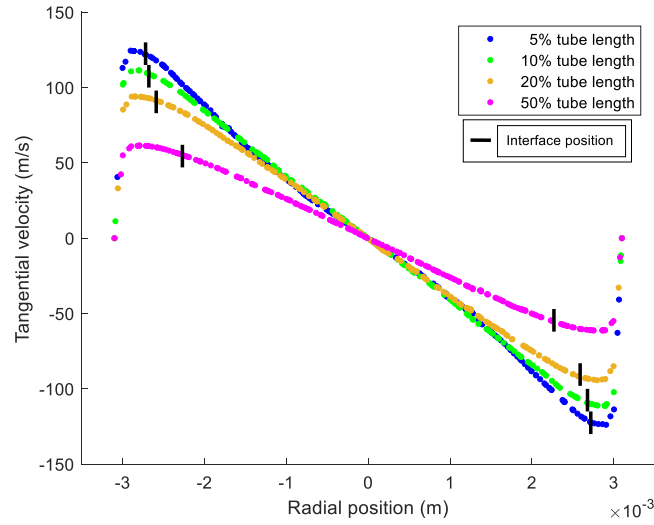
Figure 129. Tangential velocity profiles with radial position of hot/cold interface
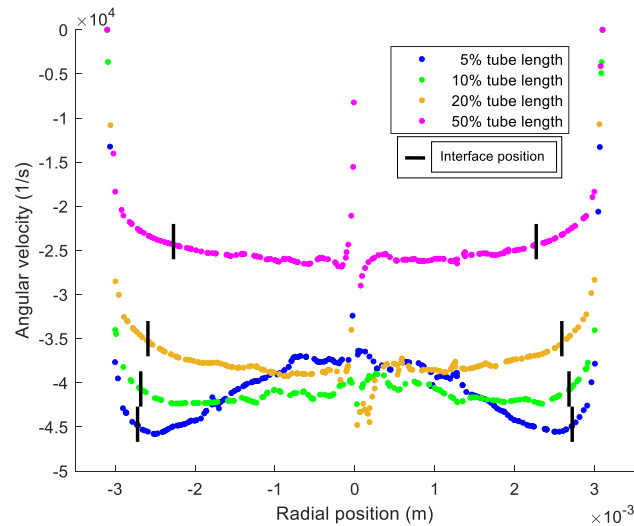
Figure 130. Angular velocity profiles with radial position of hot/cold interface

The work is dominated by the $\tau_{r\theta}$ component, and its contribution is not surprising. Tangential velocity, v_θ, can be defined in terms of angular velocity, Ω , and radial position, r, according to $v_\theta = \Omega r$. Assuming axisymmetric flow, substituting this definition into Eq (90), yields Eq (95).

$$\tau_{r\theta} = \mu_{eff} \left(r \frac{\partial \Omega}{\partial r} \right) \tag{95}$$

Eq (95) reveals that the viscous work of the component $\tau_{r\theta}$ depends on the extent to which the angular velocity is *not* constant with respect to radius, i.e. the extent to which the velocity profile deviates from solid body like rotation. The interface, as seen in Figure 130, consistently lies at a radial position just beyond the solid body like rotation, when the tangential velocity begins to decrease toward the no-slip condition at the wall.

Radial profiles of static temperature with interfaces are shown in Figure 131. The original discovery of elevated static temperatures in the core of the vortex by Scheper [49] led to a hypothesis that heat transfer may be a significant factor in temperature separation. Figure 131 reveals that the radial position of the interface does not generally coincide with the regions of greatest radial static temperature gradients; in fact, for axial locations at 5% of the tube length and beyond, the radial position of the interface is such that the radial temperature gradient is at nearly a minimum. However, at regions very close to the nozzle, such as at 2.5%, the interface lies near the maximum static temperature gradient and therefore the local heat flux is quite large.
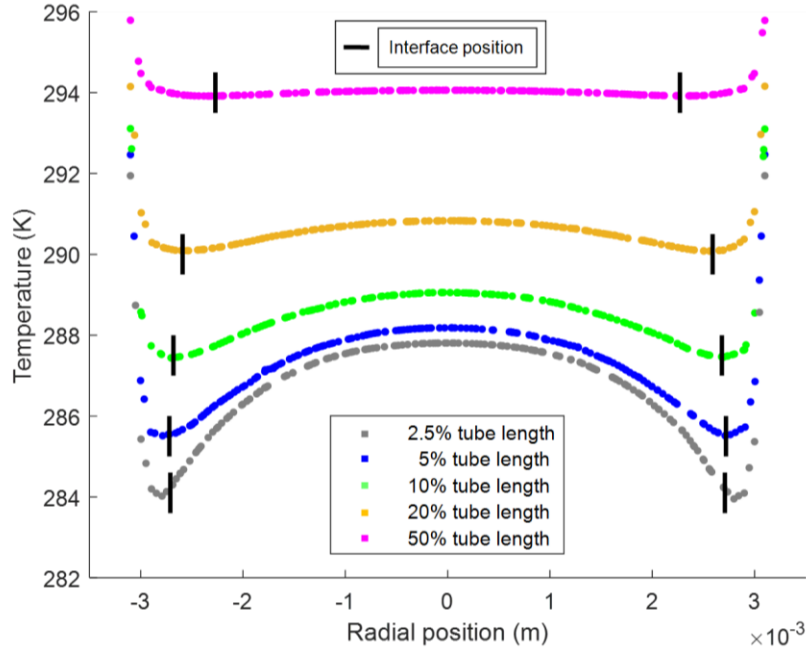
Figure 131. Static temperature profiles with radial position of hot/cold interface

The mean total temperature, as seen in Table 18, increased by ΔT = 2.67 K between the inlet and the outlet. The power required to raise the temperature of the outlet mass flow rate, 8.319×10^{-4} kg/s, by 2.67 K may be easily approximated from bulk transport properties by Eq (96). The mean C_p across the inlet and outlet is 1010.4 J/kg-K.

$$w + q = \dot{m} C_p \Delta T \qquad (96)$$

Assuming a constant C_p, a ΔT of 2.67 K requires that $w + q = 2.244$ W. If instead this were applied to the entire flow rate through the inlet, a ΔT of 2.67 K requires that $w + q = 2.450$ W. This compares favorably with the calculated 2.893 W transferred across the interface, especially given the mass flux is greatest in the region where the most energy transfer takes place, accounting for 7.2% of the inlet mass flow rate.

The calculations of heat and work crossing the interface also compare favorably with experimental data. In the experimental case used to validate the CFD solution, shown in Figure 109, the difference in total temperature between the inlet and the hot exit was 2.38 K; this is similar to but obviously slight less than the computational result. The mass flow rate through the hot exit was 8.523×10^{-4} kg/s and the mean C_p value of the inlet and hot exits was 1011.5 J/kg-K. Applying Eq (96), the experimental data suggests that 2.05 W must have crossed the interface.

The energy balance is presented in Table 21. Work and heat transfer were also calculated for the inlet and outlet surfaces, which were shown to be negligible. There is more energy advected in via the inlet than out via the outlet, which is due to the net mass flow rate out of the interface; the 27.554 W advection across the interface corresponds to 7.2% of that advected in via the inlet—identical to the fraction of the inlet mass flow rate that crosses the interface. The overall energy balance error is 4.887 W, or 1.28% of that advected in via the inlet face. This is comparable to the 1.17% discrepancy in the mass flow balance, and it would appear that the two discrepancies are related. In other words, the energy balance error is most likely attributable to difficulties computing the mass flux and advection across the interface rather than wild inaccuracies in calculating the work and heat transfer across the interface.

Table 21. Energy balance within the vortex tube control volume

Surface	Mode	Energy rate (W)
Inlet	Advection	380.523
	Work	2.86×10^{-5}
	Heat transfer	-9.42×10^{-5}
Outlet	Advection	-350.974
	Work	2.32×10^{-4}
	Heat transfer	3.49×10^{-4}
Interface	Advection	-27.554
	Work	2.599
	Heat transfer	0.294
	Sum	*4.887*

While the energy balance was not closed as tightly as desired, it should be noted that the estimate of heat and work transfer—derived from a complex set of numerical surface integrals over an interface defined empirically from flow patterns—differs from the estimate derived from a bulk transport approximation by only 0.443 W to 0.649 W (depending on the calculation method used, as described on page 230). If the energy balance were to be tightened such that the overall energy balance discrepancy was reduced to within 10% of the combination of work and heat transfer derived from the surface integrals, or 0.29 W, this would correspond to 0.076% error—as a percentage of the energy advected in via the inlet—a stringent standard indeed.

This is the first full, unconstrained, three-dimensional analysis of the energy transfer within a vortex tube. It was developed to incorporate the greatest realism practicable, including real gas effects. The solution has been rigorously validated against experiments: qualitatively, the flow profiles compare favorably with historical experiments; quantitatively, the temperature separation characteristics compare favorably with current experiments across a range of cold fractions. Through numerical integration

across an empirically-defined internal interface between hot and cold portions of the flow, contributions of heat transfer and viscous work were quantified and examined. Based on these results, the phenomenon of temperature separation appears attributable primarily to viscous work, with a lesser contribution by heat transfer.

3.2.10 *Computational investigation of the influence of geometric scale on vortex tube temperature separation*

Geometric scale represents an important consideration for the practical application of vortex tubes. To that end, it is important to understand the extent to which geometric scale influences temperature separation. The nondimensionalized total energy equation, Eq (73), revealed that length scale appears in one of the governing parameters, the Reynolds number, which influences the contributions of both viscous work and heat transfer to changes in total temperature. However, the findings thus far have suggested that the influence of Reynolds number on dimensionless temperature separation is low, and that the appropriate temperature scale is $\frac{V^2}{C_p}$ at the nozzle.

The effect of geometric scale was investigated computationally, while considering both the dimensional and dimensionless aspects of performance. Three CFD cases were compared. The first is the same case as originally shown in Table 17, in which the static pressure was matched to experiment. The scale of the mesh was then doubled such that the reference length scale—the hydraulic diameter—was also doubled and the cross-sectional area of the nozzles was quadrupled. Solutions were then computed for two additional cases. One used a mass flow rate approximately four times the original flow rate in order to closely match the nozzle velocity of the original case, but yielding a Re_{D_h} approximately double the original. The other used a mass flow rate approximately double

233

the original flow rate to match the nozzle Re_{D_h}, though with approximately half of the

original nozzle velocity. The other dimensionless governing properties, Pr and $\rho C_p \mu_{JT}$,

were matched between cases. The flow and gas properties and key parameters for all

three cases are shown in Table 22.

Table 22. CFD cases used to investigate the effect of geometric scale

	1x scale	2x scale, matched velocity	2x scale, matched Re_{D_h}
Hydraulic diameter, D_h (m)	**7.21×10^{-4}**	**1.442×10^{-3}**	**1.442×10^{-3}**
Mass flow rate (kg/s)	1.42×10^{-3}	5.60×10^{-3}	2.86×10^{-3}
Inlet T_{total} (K)	293.40	293.40	293.40
Re_{D_h}	**18027**	**35623**	**18013**
Pr	0.721	0.721	0.720
$\rho C_p \mu_{JT}$	0.01123	0.01102	0.01094
Velocity (m/s)	**98.58**	**99.02**	**49.64**
Mach number	0.289	0.290	0.145
ρ (kg/m^3)	4.582	4.497	4.581
C_p (J/kg-K)	1010.8	1010.7	1010.9
μ (μPa-s)	18.06	18.06	18.24
k (mW/m-K)	25.34	25.34	25.61
μ_{JT} (K/bar)	0.2424	0.2425	0.2362
Nozzle T_{static} (K)	288.54	288.50	292.17
Nozzle P_{static} (Pa, absolute)	378890	371810	383651
ΔP_{hot} (Pa)	52973	52378	13115

The dimensional temperature separation curves of the three cases are shown in

Figure 132, in which the curves of the two cases with matched velocity are nearly

identical, while the resulting temperature separation from the matched Reynolds number

but reduced velocity is considerably lower. The dimensionless curves of T_t^* and $\rho^* C_p^* T_t^*$

are shown in Figure 133 and Figure 134, respectively, and reveal that—despite the large

dimensional differences between curves—the dimensionless characteristics are very

similar. Interestingly, the dimensionless $\rho^* C_p^* T_t^*$ results for the scaled-up cases are

virtually identical despite the differences in Re_{D_h}, while the 1x and 2x scale cases with

identical Re_{D_h} still show slight differences. The 1x and 2x scale cases with matched

velocity are clearly not *exactly* identical, though the two sets of curves are vertically

offset by approximately 0.5 K. The reason for this is not precisely known, but is likely

attributable to computational artifacts—the two grids are, after all, geometrically similar

but are nevertheless distinct.
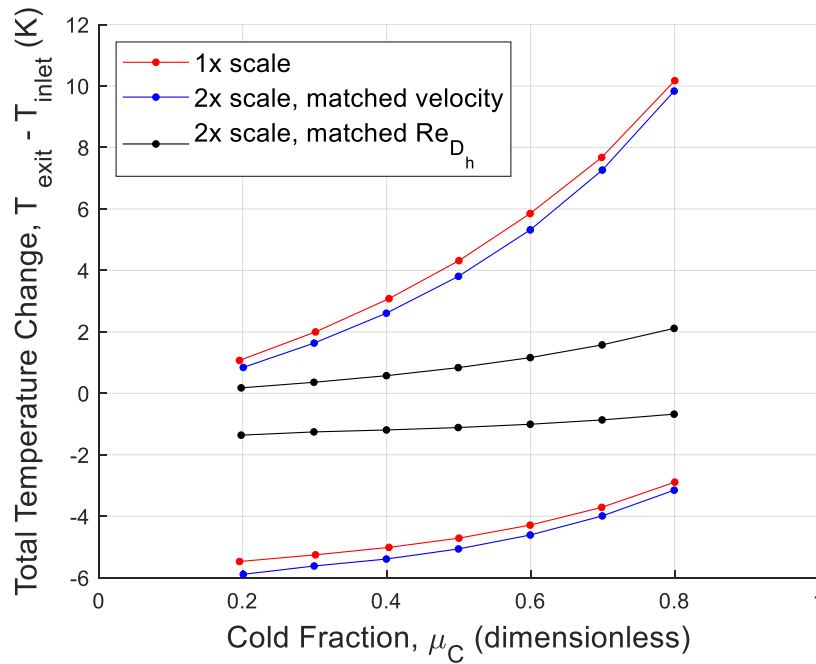
Figure 132. Dimensional temperature separation for different scales
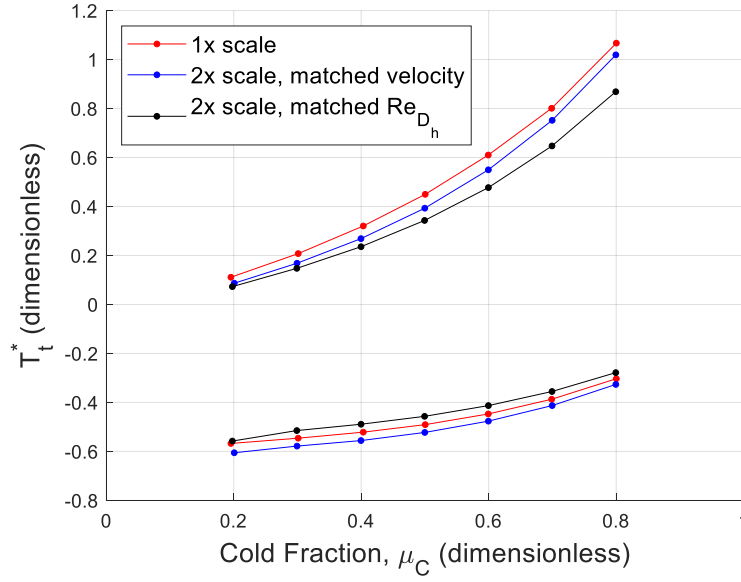
Figure 133. Dimensionless temperature separation, T_t^*, for different scales
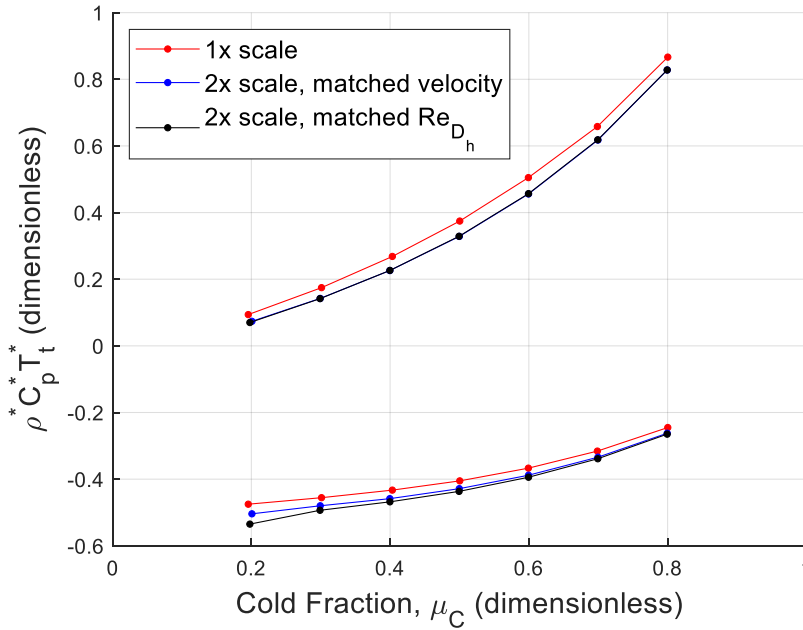
Figure 134. Dimensionless temperature separation, $\rho^* C_p^* T_t^*$, for different scales

In essence, this appears to demonstrate that the influence of geometric scale on dimensionless temperature separation, at least for the range of values considered here, is

small. The influence of geometric scale on *dimensional* temperature separation is also small, provided that sufficient mass flow is provided to maintain the same nozzle velocity. However, this raises an important, if obvious, point: since all areas in the configuration (such as the cross-sectional area of the nozzles) scale with the *square* of the change in length scale, the geometric scale still plays a significant practical role with respect to mass flow rate requirements.

These findings do not necessarily imply that the role of Reynolds number could never be significant—in fact, there are important qualitative changes in fluid behavior at low Reynolds numbers. Significantly, $Re_{D_h} \approx 2300$ is a typical benchmark for the onset of transition from laminar to turbulent internal flow [98]. However, the 1x scale vortex tube would need to be scaled down considerably before encountering such a scenario. For instance, assuming an approximately 1/9 scale vortex tube with the mass flow rate reduced to 1/81 of its value in the full-scale case, one would find $Re_{D_h} \approx 2000$ and the potential for fully laminar flow may exist, which might fundamentally modify the dimensionless characteristics of the vortex tube. However, the nozzles of such a vortex tube would have a hydraulic diameter of 80 µm, placing them into the distinctive category of microfluidic devices which, according to convention, lie in the range of $0.1\ \mu\text{m} \leq D_h \leq 100\ \mu\text{m}$ [98] and would require additional analysis. Moreover, it would remain to be seen what mass flow rates could be achieved through such small channels. In any event, such microfluidic devices are at smaller scales than would be of interest in film cooling applications.

4   Research Objective 3: Quantify the degree of temperature separation achievable at engine conditions

Research Objective 3 centers on the characteristics of vortex tubes at engine conditions. The temperatures and pressures inside a gas turbine engine present formidable operating conditions, and it remains to be seen how well a vortex tube might perform in such an environment. The experimental findings in Section 3.2.2 (see page 127) revealed that the contribution of inlet temperature to temperature separation was to increase the nozzle velocity; it has also been found that the appropriate temperature scale for temperature separation is based on the square of nozzle velocity. The temperatures in an engine are very high and this, on its face, provides inspiration for the practical use of vortex tubes in gas turbine engines.

It is also important to consider operational factors and constraints that may affect temperature separation in an engine, and two distinctive characteristics leap to mind. First, recall that the research herein has been performed using adiabatic or corrected-to-adiabatic vortex tubes; however, it seems unrealistic to expect an adiabatic tube wall for a vortex tube installed in an engine. In fact, for a vortex tube installed anywhere near a turbine section, it seems reasonable that some amount of heat would be conducted into the vortex tube. The influence of such a boundary condition on temperature separation is of great interest.

Second, it should be emphasized that a vortex tube operates as a pressure-driven flow, and the pressure drop available has a direct influence on the achievable mass flow rates and nozzle velocities. This represents an important constraint in its application—one that must be carefully considered within the context of gas turbine engines.

4.1 Literature review: application of vortex tubes to gas turbine engines

Because the application of vortex tubes to gas turbine engine cooling is a novel concept, no literature exists to directly quantify vortex tube performance at engine conditions. The highest temperature experimentally achieved in air was 363 K (90°C) by Elser and Hoch [47], while Takahama et al. achieved 494 K in steam [99]. No literature was found describing temperature separation under the conditions of heat addition.

However, it is possible to describe the pressure drop available in the cooling architecture of a gas turbine engine, which is dictated by the pressure difference between the high pressure compressor section and the high pressure turbine section. Using representative engine performance figures, it is possible to estimate this difference analytically based on methods described in Mattingly [1].

The difference between the total pressure exiting the high-pressure compressor, P_{t3}, and the total pressure entering the high-pressure turbine, P_{t4}, represents the maximum total pressure drop available to a vortex tube if used in the cooling architecture. This can be expressed using Eq (97). The value of P_{t3} can be computed with respect to the total pressure entering the compressor section, here assumed to be P_{t1} (the inlet total pressure considering ram effect), using the total pressure ratio across the compressor, π_c, as described by Eq (98). The value of P_{t4} can be computed with respect to the total pressure exiting the compressor section using the total pressure ratio across the combustor, π_b, as described by Eq (99). By combining Eqs (97) – (99), it can be seen that the total available pressure difference is a function of the compressor pressure ratio, the combustor pressure ratio, and the inlet pressure as in Eq (100).

$$\Delta P_t = P_{t3} - P_{t4} \tag{97}$$

$$P_{t3} = \pi_c P_{t1} \tag{98}$$

$$P_{t4} = \pi_b P_{t3} \tag{99}$$

$$\Delta P_t = \pi_c(1 - \pi_b)P_{t1} \tag{100}$$

Some relevant performance figures are found in Mattingly [1]. Modern high-performance military aircraft engines may have an overall pressure ratio on the order of 30. A typical modern combustor pressure ratio, π_b, is approximately 0.95, and future combustors may have a pressure ratio of 0.96. Consider an aircraft at 30,000 ft altitude, though hypothetically with zero airspeed (this simplification will be improved upon in the methodology presented in Section 4.2.4.1). The ambient static pressure for a standard atmosphere at 30,000 ft is 30,148 Pa (4.37 psia). Using modern nominal values of $\pi_c = 30$ and $\pi_b = 0.95$, $\Delta P_t = 45{,}222$ Pa (6.56 psid). With future nominal values of $\pi_c = 50$ and $\pi_b = 0.96$, $\Delta P_t = 60{,}296$ Pa (8.74 psid). At sea level static conditions on a standard day, $P_{t1} = 101325$ Pa (14.7 psia) and the pressure drop increases to $\Delta P_t = 151{,}988$ Pa (22.1 psid) for modern aircraft.

The severity of the constraints imposed on vortex tubes by engine operating conditions are now much more apparent. At sea level static conditions—a reasonable approximation for ground taxi or even for takeoff and landing—the maximum pressure drop is approximately 1.5 bar. Recall Figure 46 (page 86) with typical counterflow vortex tube performance curves—the lowest inlet gauge pressure used was 1.5 bar, and Stephan

et al. [45] achieved a cold-side temperature drop of 10°C. It has been shown that the pressure drop available at altitude is approximately 30% of that at takeoff, not considering the contribution of airspeed. However, additional contributions to pressure drop between the compressor and turbine sections besides that of a vortex tube have not been considered either. It appears that for vortex tubes to be viably applied to film cooling, the performance will need to be improved compared to the cases in the literature thus far.

4.2   Quantification of temperature separation at engine conditions

Completion of the third research objective, "Quantify the degree of temperature separation available at engine conditions", depends primarily upon experimental and computational methods while incorporating some analytical methods developed thus far, such as the principles of dimensional and dimensionless scaling. The efforts here will focus primarily on three research strands. First is a characterization of temperature separation under the conditions of heat addition. Second is an experimental investigation of the extent to which the scaling principles identified at low temperatures can be reproduced at high temperatures using a new laboratory configuration. Finally, a computational investigation quantifies the temperature separation expected for a notional vortex tube at conditions approximating those of air exiting a high-pressure compressor in the absence of heat addition.

4.2.1 *Experimental characterization of temperature separation with heat addition*

The use of vortex tubes in a gas turbine engine would likely expose the devices to elevated temperatures of varying magnitudes, depending on the chosen embodiment. This would be especially severe if, for instance, tiny vortex tubes were incorporated directly into the cooling passages in a turbine blade. Under those circumstances, one would expect—by design—a large heat flux from the turbine blade into the gas inside the vortex tube. This is a novel configuration and no published research was found describing the effects of heat addition on temperature separation and vortex tube performance. In the present body of research, pains have been taken to model the vortex tube as adiabatic, such as the experimental heat loss correction function and the choice of boundary conditions in CFD. Attention now turns to characterizing vortex tube behavior under the more realistic assumption of heat addition. This was investigated first via experiment and then computationally.

4.2.1.1 Experimental Methodology

The experimental configuration for this investigation is largely identical to that employed in the experimental work in Section 3.2.1 (see page 114). The laboratory was modified to incorporate an Omega HTC-030 heater cord and a Staco 3PN1510B variable transformer to drive the heater. A length of 50.8 cm of the heater cord was coiled tightly around the length of the vortex tube. This modified configuration can be seen in Figure 135.
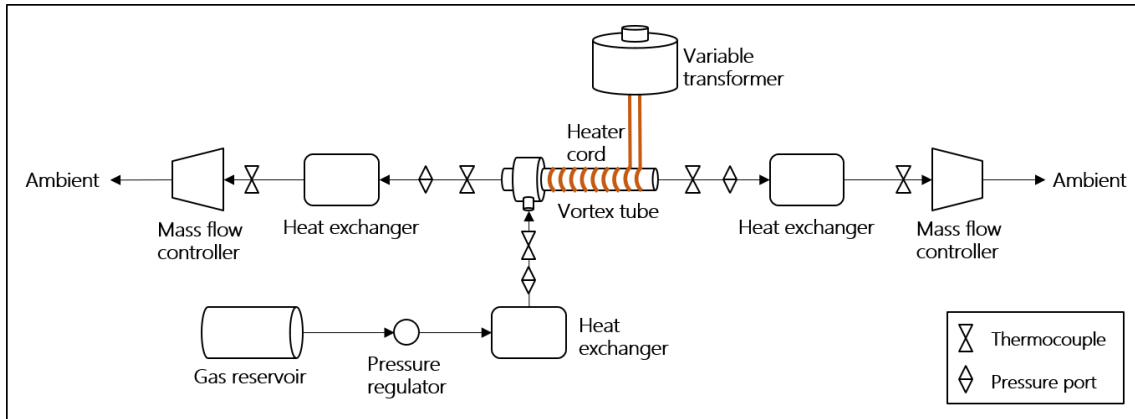
Figure 135. Vortex tube configuration for heat addition investigation

Heat addition to the vortex tube was controlled by adjusting the voltage output by the variable transformer to the heater cord, specified as a percentage of the transformer's rated voltage of 120 VAC. Test cases were run in increments of 20% of the rating, from 0% to 80%. The baseline case of 0% voltage, i.e. with the heater off, was conducted using an inlet temperature that was closely matched to ambient conditions, nominally 302 K, to minimized heat transfer between the tube and the surroundings; the vortex tube was also insulated with foam rubber. This inlet temperature was then held approximately constant for all tests. The flow rate for the tests was nominally 1.420×10^{-3} kg/s (72 SLPM) and inlet gauge pressure was nominally 3.0 bar. Actual nozzle conditions for all cases, averaged across the cold fractions, are shown in Table 23.

Table 23. Nozzle conditions for heat addition cases

Case:	0% rating	20%	40%	60%	80%
Mass flow rate (kg/s)	1.420×10^{-3}	1.422×10^{-3}	1.421×10^{-3}	1.419×10^{-3}	1.419×10^{-3}
Inlet T_{total} (K)	301.9	301.6	301.7	302.0	302.2
Inlet P_{static} (bar, gauge)	3.001	2.999	2.999	3.000	2.999
Re	17638	17675	17654	17616	17612
Pr	0.720	0.720	0.720	0.720	0.720
$\rho_0 C_{p,0} \mu_{JT,0}$	0.0098	0.0099	0.0099	0.0098	0.0098
Velocity (m/s)	102.33	102.42	102.38	102.28	102.44
Mach number	0.296	0.297	0.296	0.296	0.296
ρ (kg/m^3)	4.413	4.415	4.413	4.411	4.405
μ (µPa-s)	18.46	18.44	18.45	18.46	18.47
k (mW/m-K)	25.94	25.92	25.93	25.95	25.96
C_p (kJ/kg-K)	1.012	1.012	1.012	1.012	1.012

Measurements for the heated cases were taken at cold fractions of $\mu_c = 0.3, 0.4,$ 0.5, and 0.7. The heat loss correction function, described in Eqs (51) and (52), was not applied to this analysis since its purpose—to correct the curves to approximately adiabatic conditions—is not relevant here. However, the techniques developed for that function are still applicable. Using Eq (50), shown again here, it is possible to calculate the heat added to the flow.

$$q = \dot{m}_{hot} h_{t,hot} + \dot{m}_{cold} h_{t,cold} - \dot{m}_{inlet} h_{t,inlet} \tag{50}$$

Another property of interest is the fraction of the heat added to the flow which remains in the flow leaving via the hot exit. This can be estimated by referencing an adiabatic condition, if such an uncorrected condition can be found to exist. The process begins by recognizing that the heat added to an adiabatic vortex tube is zero; this is seen in Eq (101). Eq (101) can be subtracted from Eq (50), as seen in Eq (102). Assuming for the experiments of interest that the energy advected in with subsequent heat addition,

$\dot{m}_{inlet}h_{t,inlet}$, is identical to its adiabatic equivalent, $\dot{m}_{inlet,ad}h_{t,inlet,ad}$, and the mass

flow rates exiting both sides are also equal for both conditions, Eq (102) can be reduced

to Eq (103). The fractions of the total heat added to the hot and cold flows, respectively,

then sum to unity as seen by further rearranging to Eq (104).

$$q_{ad} = \dot{m}_{hot,ad}h_{t,hot,ad} + \dot{m}_{cold,\,ad}h_{t,cold,ad} - \dot{m}_{inlet,ad}h_{t,inlet,ad} = 0 \tag{101}$$

$$
\begin{aligned}
q - q_{ad} &= \left(\dot{m}_{hot}h_{t,hot} + \dot{m}_{cold}h_{t,cold} - \dot{m}_{inlet}h_{t,inlet}\right) \\
&- \left(\dot{m}_{hot,ad}h_{t,hot,ad} + \dot{m}_{cold,\,ad}h_{t,cold,ad} - \dot{m}_{inlet,ad}h_{t,inlet,ad}\right)
\end{aligned}
\tag{102}
$$

$$q - q_{ad} = \dot{m}_{hot}\left(h_{t,hot} - h_{t,hot,ad}\right) + \dot{m}_{cold}\left(h_{t,cold} - h_{t,cold,ad}\right) \tag{103}$$

$$1 = \frac{\dot{m}_{hot}\left(h_{t,hot} - h_{t,hot,ad}\right)}{q - q_{ad}} + \frac{\dot{m}_{cold}\left(h_{t,cold} - h_{t,cold,ad}\right)}{q - q_{ad}} \tag{104}$$

In practice, Eq (104) only yields an approximation. In theory, $q_{ad} = 0$ but if a

near-adiabatic case is used as a basis for comparison, then a small but non-zero value

should be used for q_{ad}. Moreover, the advection through the inlet may not be *exactly*

matched between the adiabatic and non-adiabatic cases if the mass flow rates and inlet

temperatures are not exactly identical, i.e. $\dot{m}_{inlet}h_{t,inlet} \neq \dot{m}_{inlet,ad}h_{t,inlet,ad}$.

Nevertheless, the approximation can offer some insight into quantifying the fraction of

the added heat that is found to be retained in the hot and cold flows of the vortex tube.

4.2.1.2 Results and Discussion

The temperature separation curves corresponding to the heat addition cases are presented in Figure 136. Most notably, the addition of heat to the vortex tube causes a dramatic increase to the temperature of the flow exiting via the hot exit, while only slightly increasing the temperature at the cold exit. For example, at a cold fraction of $\mu_C = 0.50$, the temperature change at the cold exit decreases in magnitude by 2.1 K from the 0% rating case (heater off) to the 80% case, while that of the hot exit increases by 23.2 K.
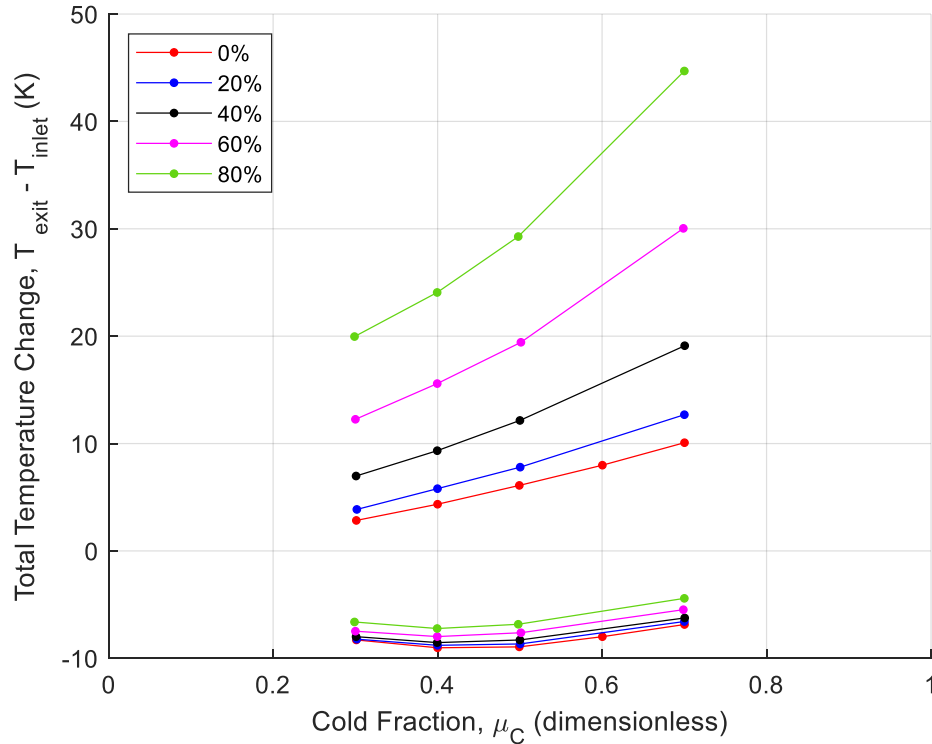

Figure 136. Temperature separation curves with heat addition

It is not surprising that the hot exit flow is more sensitive to external heat addition than the cold exit flow; the hot exit flow is, after all, immediately adjacent to the tube wall and any heat added to the gas must first be conducted through the hot exit flow

246

before it can be transferred to the cold exit flow. However, the temperature difference between the hot and cold exit flows across a 3.1 mm inside radius tube is nevertheless striking.

By now, it is understood that the flow inside a vortex tube can be divided into hot and cold flows separated by a notional interface, across which energy is transferred and the phenomenon of temperature separation emerges. The trend in Figure 136 appears to be consistent with the explanation for the mechanism of temperature separation: that viscous work is responsible for the vast majority of the energy transfer across the hot/cold interface and that heat conduction plays only a minor role. If contribution of heat transfer were strong enough to dominate the phenomenon, then one might expect under the present circumstances that trend could be reversed when a large heat flux is applied to the vortex tube, and that the cold exit temperature would experience a significant temperature rise. As it stands, the temperature increase at the cold exit is less than one tenth that at the hot exit for $\mu_C = 0.50$ between the 0% and 80% cases and, indeed, internal heat conduction appears to be quite limited in magnitude even when the direction is from the periphery to the core.

The total heat added to the flow was computed using Eq (50). The findings, shown in Figure 137, indicate that heat addition is a function of cold fraction, where less heat is added at higher cold fractions. This is because the hot exit flow sees a steep rise in temperature with increasing cold fraction—a classic vortex tube characteristic—and the tube wall likewise gets hotter at high cold fractions. The resulting temperature gradient is then lower, which serves to reduce the heat flux at the tube wall; the remainder of the

heat from the cord heater is conducted through the insulation and is passed to the environment.
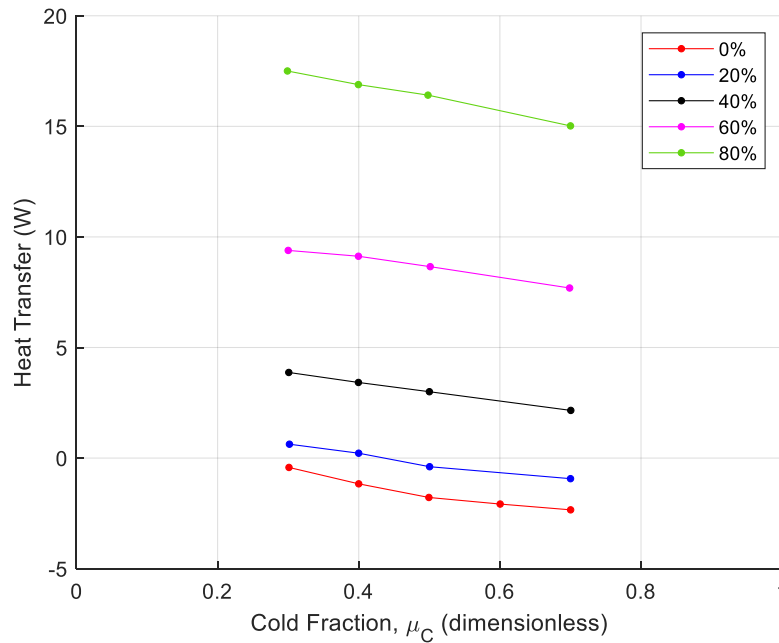
Figure 137. Heat transferred to vortex tube for each case

The heater off case only experiences heat *loss* from the tube wall; this, of course, was part of the motivation behind the heat loss correction function applied during the initial experimental characterization of vortex tubes. Interestingly, the 20% rating case is actually nearest to an uncorrected adiabatic condition: the elevated temperature of the vortex tube due to the hot flow and the warm temperature of the heater very nearly offset each other, apparently minimizing the temperature gradients—at a cold fraction of 0.40, the heat transfer for the 20% case is calculated to be 0.22 W. The tube has an inside diameter of 6.2 mm and a length of approximately 58 mm, so the surface area of the tube wall is 1.13×10^{-3} m^2, so the quasi-adiabatic case still corresponds to a mean surface heat flux of 195.0 W/m^2, which is small in comparison to the other cases but clearly not zero.

It should be noted that the heat transfer into the vortex tube is computed from bulk transport properties, so it is possible that the local heat flux is positive in one part of the tube and negative in another and, in aggregate, the heat transfer sums to the specified amount. The heat added for each heater-on case, as well as the corresponding mean heat flux, is compiled in Table 24. Using the 20% case as the near-adiabatic baseline, the fractions of heat remaining in the hot flow and cold flow, $\frac{\dot{m}_{hot}(h_{t,hot}-h_{t,hot,ad})}{q-q_{ad}}$ and

$\frac{\dot{m}_{cold}(h_{t,cold}-h_{t,cold,ad})}{q-q_{ad}}$, respectively, are shown for the 40%, 60%, and 80% cases. If the baseline case were truly adiabatic and the inlet conditions truly identical between cases, the fractions of heat retained in the hot and cold flows would sum to unity; as it stands, they do not—but they are close. The errors associated with this estimation method, defined as the difference between the sum of the fractions of heat retained in the hot and cold flows and unity, remain within 5%.

Table 24. Heat added to each case with fraction retained in hot and cold flows ($\mu_C = 0.40$)

Case	q (W)	q''_{mean} (W/m^2)	$\dfrac{\dot{m}_{hot}(h_{t,hot} - h_{t,hot,ad})}{q - q_{ad}}$	$\dfrac{\dot{m}_{cold}(h_{t,cold} - h_{t,cold,ad})}{q - q_{ad}}$	Error
20%	0.22	195.0	—	—	—
40%	3.42	3026.8	0.980	0.064	4.4%
60%	9.13	8078.2	0.962	0.077	3.9%
80%	16.89	14947.9	0.969	0.077	4.6%

Table 24 reveals that more than 90% of the heat added to the vortex tube is estimated to remain in the hot flow for each of the cases. From Figure 137, it was seen that the cold fractions other than $\mu_C = 0.40$ do not have as suitable an adiabatic baseline point, so quantitative estimates of the fraction of added heat remaining in the hot flow

will be of poorer quality. Nevertheless, the temperature separation curves in Figure 136 qualitatively imply a similar trend for all cases. This is remarkable. Consider the case where $\mu_C = 0.70$: it is possible that a large, though thus far uncalculated, majority of the added heat is contained in 30% of the total mass flow rate through the tube—a fraction that is easily separated upon exiting the vortex tube.

The pressure loss accompanying the heat transfer cases is slightly higher than when no heat is added, as can be seen in Figure 138, which depicts the dimensional pressure drop across the vortex tube; this is possibly due to Rayleigh losses. For these cases, the change is small: the highest heat gain case corresponds to a 2% increase in pressure drop over the unheated case at $\mu_C = 0.30$, and increasing by 4% at $\mu_C = 0.70$.
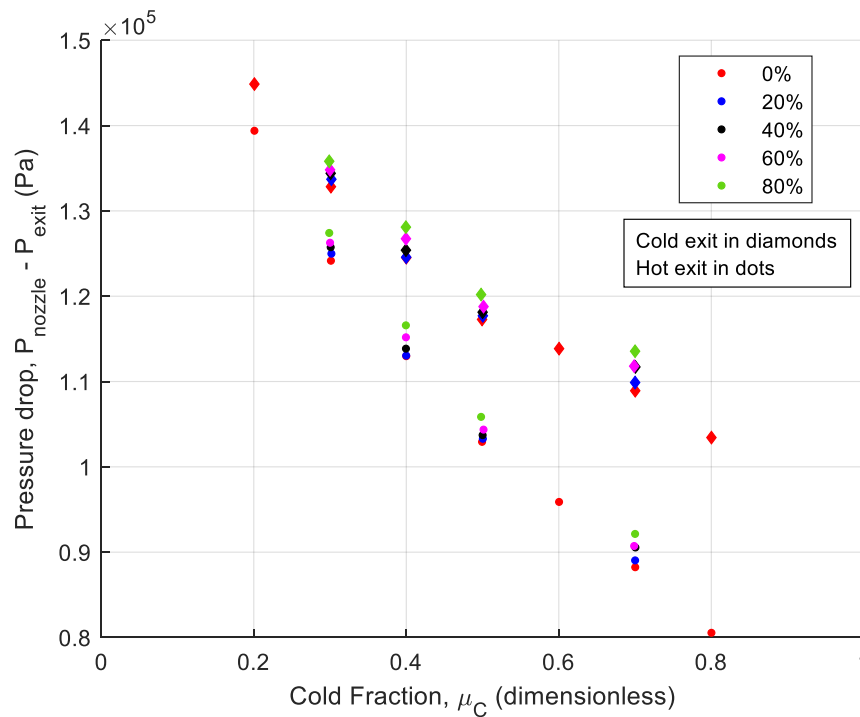

Figure 138. Pressure drop variations for a vortex tube with heat addition

The discovery that heat added externally to a vortex tube remains overwhelmingly in the flow exiting the hot end is quite interesting from a heat transfer perspective, and it adds another dimension—figuratively speaking—to the concept of temperature separation. Up to this point, temperature separation in a vortex tube has been considered exclusively as a phenomenon in which a single stream of gas is separated into two streams, one hotter and the other colder. The present findings add to this by revealing that the temperature of the hot stream in a vortex tube can be dramatically increased, while still remaining, for the most part, thermally separated from the adjacent cold stream. One might even consider this phenomenon an adjunct to temperature separation whereby a difference in temperatures induced by heat addition is sustained by fluidic means. The most extreme example demonstrated here is that for $\mu_C = 0.70$, in which the hot stream was increased by nearly 35 K compared to the unheated case, while the cold stream increased by only 2.5 K. The exact manner in which this phenomenon might be exploited deserves careful consideration.

4.2.2   Computational characterization of temperature separation with heat addition

4.2.2.1   Methodology

To gain further insight into the operating characteristics of a vortex tube experiencing heat addition, a similar scenario was investigated computationally. The CFD methodology for the heat addition scenario was identical to that initially established in Section 3.2.8 (see page 182), with an identical mesh and solver method. The baseline CFD case, with an adiabatic wall boundary condition, is that first introduced during the experimental validation in Section 3.2.8.3 featuring a nozzle static pressure matched to

experimental conditions; it was reused as the 1x scale case in Section 3.2.10 during the investigation of geometric scaling. The present study compares the adiabatic baseline case to one with identical nozzle conditions in which a uniform heat flux of 2500 W/m^2 is applied to the walls.

There are some important differences between the CFD and experimental heat-addition scenarios. The results of the two approaches cannot be directly compared, since the experimental investigation used the unmodified commercial vortex tube geometry and the CFD geometry was the simplified form for computational investigation. Furthermore, in the experimental case, the cord heater was only wrapped around the length of the tube. While there was certainly some degree of three-dimensional internal conduction within the metal of the vortex tube, it was expected that the vast majority of heat addition likely occurred through the tube wall, as opposed to other metal features in the vortex tube. No information was available regarding the uniformity of the experimental heat flux.

By contrast, the heat flux in the CFD scenario was uniform and was applied to the entirety of the interior wall boundary of the mesh, which includes the tube wall as well as the surface area near the cold exit. The overall heat added was still dominated by the flux at the tube wall. Figure 139 depicts the geometry of the vortex tube near the cold exit—the uniform heat flux was applied at the tube wall, the side wall, and the perimeter surfaces surrounding the nozzles and cold exit. The cold exit face and nozzle faces remained as a pressure exit and mass flow inlets, respectively.
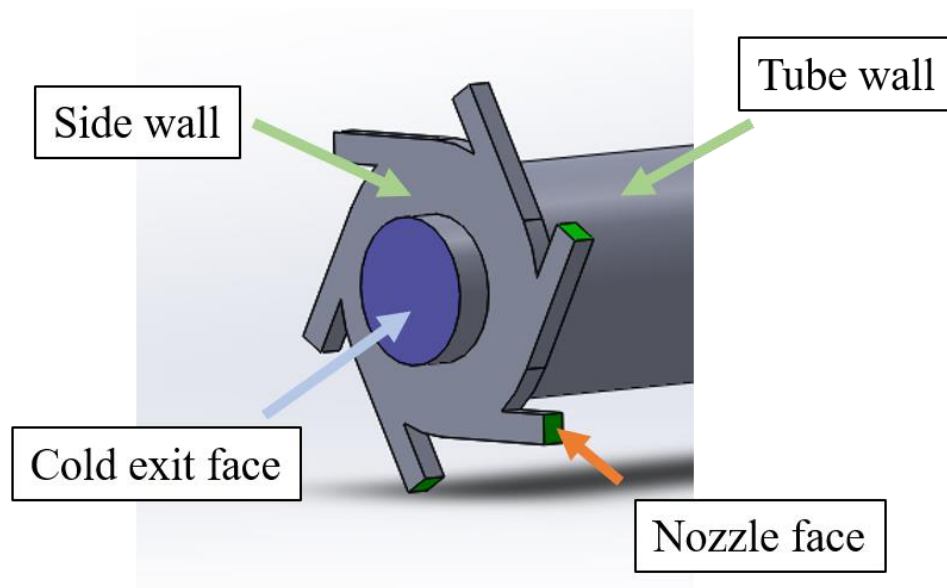
Figure 139. CFD vortex tube geometry near the cold exit

4.2.2.2 Results and Discussion

The nozzle conditions were carefully controlled to be nearly identical to those of

the adiabatic case, and exact values are listed in Table 25. When the temperature

separation curves of the case with uniform heat flux and the adiabatic case are plotted

side-by-side, as shown in Figure 140, it is evident that the temperature of the gas exiting

via the hot exit increased dramatically while the gas exiting via the cold exit increased

only marginally—a trend distinctly reminiscent of the experimental cases. Even for equal

hot and cold mass flow rates, i.e. $\mu_C = 0.50$, the hot flow increased in temperature by 3.9

K, while the cold exit increased by 0.46 K—nearly the order of magnitude increase on

the hot exit observed in the experimental investigation.

Table 25. Nozzle conditions for CFD heat addition and adiabatic cases

	Heat addition	Adiabatic
Hydraulic diameter, D_h (m)	7.21×10^{-4}	7.21×10^{-4}
Mass flow rate (kg/s)	1.420×10^{-3}	1.420×10^{-3}
Inlet T_{total} (K)	293.40	293.40
Re_{D_h}	18024	18027
Pr	0.7206	0.7206
$\rho C_p \mu_{JT}$	0.01124	0.01123
Velocity (m/s)	98.41	98.58
Mach number	0.289	0.289
ρ (kg/m^3)	4.589	4.582
C_p (J/kg-K)	1010.8	1010.8
μ (μPa-s)	18.07	18.06
k (mW/m-K)	0.025	0.025
μ_{JT} (K/bar)	0.2424	0.2424
Nozzle T_{static} (K)	288.56	288.54
Nozzle P_{static} (Pa, absolute)	379537	378890

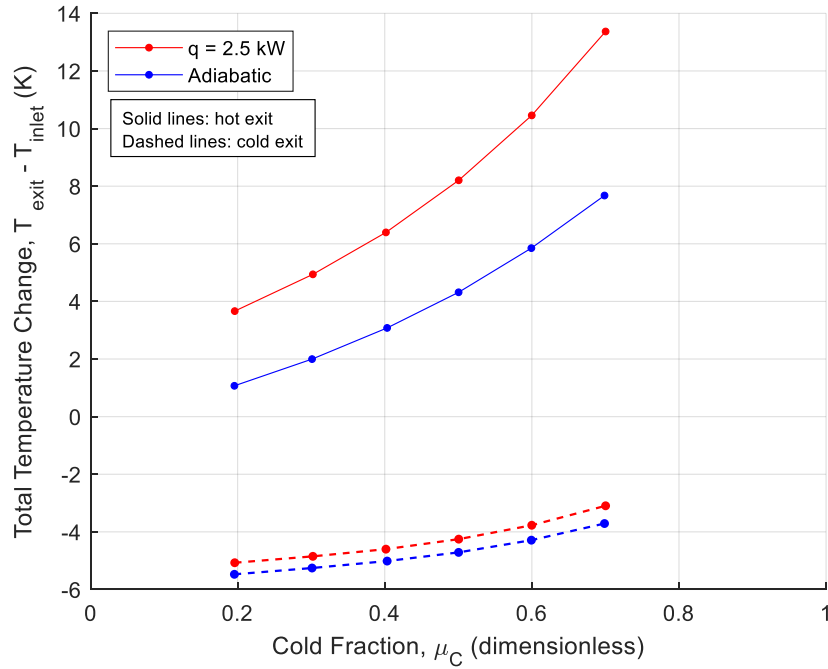**Figure 140. Temperature separation of adiabatic and uniform heat flux CFD cases**

The technique developed through Eqs (101) – (104) to identify the fraction of added heat which exits via the hot and cold exits was applied to assess the behavior with respect to cold fraction, with q_{ad} truly equaling zero for the adiabatic case. The CFD results are shown in Table 26. The errors in this technique—i.e. the difference between the sum $\frac{q_{hot}}{q} + \frac{q_{cold}}{q}$ and unity—are small, ranging from 0.1% to 1.5%. The fraction of heat retained in the hot flow is greatest for lower cold fractions and decreases monotonically with increasing cold fraction, from 95.7% at $\mu_C = 0.20$ to 78.5% at $\mu_C = 0.70$. The CFD compares more favorably with experimental estimates for fraction of heat retained in the cold flow than that retained in the hot flow. For example, for $\mu_C = 0.40$, CFD with a uniform heat flux of 2.5 kW/m² estimated $\frac{q_{cold}}{q} = 0.077$ and $\frac{q_{hot}}{q} = 0.912$, while the experiment with a mean heat flux of 3.0 kW/m², estimated

$$\frac{\dot{m}_{cold}(h_{t,cold} - h_{t,cold,ad})}{q - q_{ad}} = 0.064 \text{ and } \frac{\dot{m}_{hot}(h_{t,hot} - h_{t,hot,ad})}{q - q_{ad}} = 0.980.$$

Table 26. Fractions of heat retained in the hot and cold flows ($q'' = 2.5$ kW/m²)

Cold fraction	q (W)	$\frac{q_{hot}}{q}$	$\frac{q_{cold}}{q}$	Error
0.20	3.101	0.957	0.036	0.6%
0.30	3.101	0.943	0.057	0.1%
0.40	3.101	0.912	0.077	1.2%
0.50	3.101	0.893	0.107	0.1%
0.60	3.101	0.848	0.144	0.8%
0.70	3.101	0.785	0.200	1.5%

In any analysis involving convective heat transfer, it is usually of practical interest to quantify the heat transfer coefficient, h (not to be confused with enthalpy). The manner in which this might be accomplished is not entirely straightforward, and multiple

approaches exist. In general, the heat transfer coefficient defines the relationship between the local heat flux and a driving temperature difference, normally the difference between the wall temperature, T_w, and some appropriate reference temperature, T_{ref}, such as in Eq (105).

$$q'' = h \left(T_{ref} - T_w \right) \qquad (105)$$

The appropriate reference temperature varies by scenario. For example, internal flows with uniform heat flux might make use of the bulk (mass-averaged) temperature at a given axial position, T_{mean}, in a process outlined by Kays et al. [7]. As the flow in the vortex tube is indeed an internal flow and the present analysis does involve a uniform heat flux, it might at first seem that T_{mean} is an appropriate reference. This approach quickly breaks down, however, on practical grounds. If one were indeed to use T_{mean} as a reference, across which flow should the temperature be mass-averaged? Across the entire tube cross section? Or perhaps only the flow exiting via the hot exit? The latter carries stronger physical reasoning, but the analysis then requires repeating much of the effort included earlier in the explanation for the mechanism of temperature separation—particularly the definition of the notional hot/cold interface.

Instead, it seems more appropriate—and straightforward—to employ the approach espoused by Bogard and Thole [14], in which the reference temperature is the adiabatic wall temperature, T_{aw}, and hence the driving potential for local heat flux is the difference between the wall temperatures under adiabatic conditions and under nonzero heat flux. This is expressed with Eq (1), repeated here without film cooling notation.

$$q'' = h \left(T_{aw} - T_w \right) \qquad (1)$$

Eq (1) is straightforward to implement, and enough data has already been taken for a complete characterization. The temperature along the tube wall is extracted for both the adiabatic and uniform heat flux cases, and it is easy to compute h at any location. This is shown in Figure 141, which includes the main part of the tube wall from 1.0 mm to 54.8 mm (94.3% of the length of the 58.1 mm tube) as well as the surface surrounding the cold exit face, which extends from a zero axial location back to -1.0 mm. A gap is seen in the axial region of the nozzles.
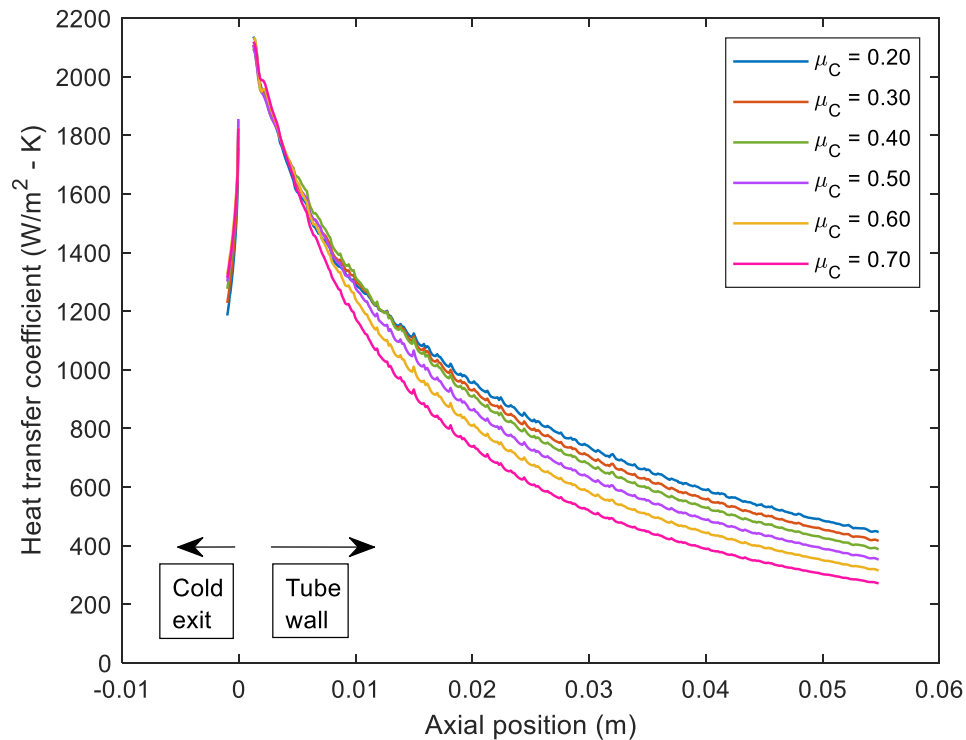
Figure 141. Local heat transfer coefficient inside vortex tube walls

for uniform heat flux of 2500 W/m^2

The local heat transfer coefficient is greatest near the nozzles—where the tangential velocity is also greatest—and decreases rapidly down the axial length of the tube. The maximum value of h is 2132 W/m^2-K and its value is not sensitive to cold

257

fraction in the region closest to the nozzles, but from an axial location of 4.5 mm it becomes clear that h decreases with increasing cold fraction. The minimum observed h value for $\mu_C = 0.20$ is 446 W/m²-K and the minimum for $\mu_C = 0.70$ is 271 W/m²-K. The behavior on the surface surrounding the cold exit orifice is similar but operates somewhat in reverse. The range of magnitudes is within those seen on the tube walls—the maximum is 1824 W/m²-K and the minimum is 1185 W/m²-K —but the magnitudes of h increase with cold fraction on this surface.

The heat transfer coefficient in the tube is much higher than would be seen in other relevant scenarios using a similar geometry. For example, consider a 6.2 mm diameter tube with a mass flow rate of 1.42 g/s—both identical to those of the vortex tube—and the same entering total temperature and total pressure as the vortex tube nozzles. The flow is fully developed and the tube walls are subjected to a uniform heat flux. For such a scenario, the entering static temperature is 293.35 K, the bulk velocity is 9.67 m/s, $Re_{D_h} = 15564$, and $Pr = 0.721$. Eq (106), an empirical correlation introduced by Kays et al. [7], may be used to estimate the Nusselt number for a circular tube with a fully-developed flow of gases with a Prandtl number between 0.5 – 1.0 and a uniform heat flux. The correlation finds a uniform $Nu = 42.17$ on the tube walls; using the definition $Nu \equiv hD/k$, the heat transfer coefficient is $h = 174.8$. The flow in the vortex tube is obviously not fully developed, so the comparison to fully developed flow is not ideal.

$$Nu = 0.022 Pr^{0.5} Re^{0.8} \tag{106}$$

It is known that Nu is greater in the entry region than for fully developed flow, and therefore it may be more appropriate to compare the vortex tube to the pipe flow

entry region. This can be accomplished by first by quantifying the increase in local

Nusselt number of the vortex tube over fully developed pipe flow, i.e. $\frac{Nu_{vortex}}{Nu_{\infty,pipe}}$; next, by

determining the increase in Nusselt number in the thermal entry region compared to fully

developed pipe flow, i.e. $\frac{Nu_{pipe}}{Nu_{\infty,pipe}}$; and then comparing the two at a point along the axial

length of the tube since the ratio of the two is $\frac{Nu_{vortex}}{Nu_{pipe}}$. A value of $Nu_{\infty,pipe} = 42.17$ is

used for the fully developed pipe flow. For consistency, the vortex tube heat transfer

coefficient is nondimensionalized using $k = 25.7$ mW/m-K, the same value for thermal

conductivity used for the pipe flow and the pipe diameter of 6.1 mm.

It is known that in the entry region for pipe flow, local $Nu \to \infty$ as $x \to 0$, and

Figure 142 suggests the same trend for Nu_{vortex} near the nozzles. The dashed red line

indicates $\frac{Nu_{vortex}}{Nu_{\infty,pipe}} = 1$. Solutions for uniform heat flux along the entry length of a circular

tube are drawn from the data of Notter and Sleicher [100]; the same are plotted in terms

of $\frac{Nu_{pipe}}{Nu_{\infty,pipe}}$ along the entry length for Reynolds number of 50,000 – 200,000 in Figure

143, which is drawn from Kays et al. [7] for $Pr = 0.7$. Although $Re_{D_h} = 15564$ in the

pipe flow analogy and is thus outside the range in Figure 143, it can also be seen that

$\frac{Nu_{pipe}}{Nu_{\infty,pipe}}$ is not a strong function of Re.
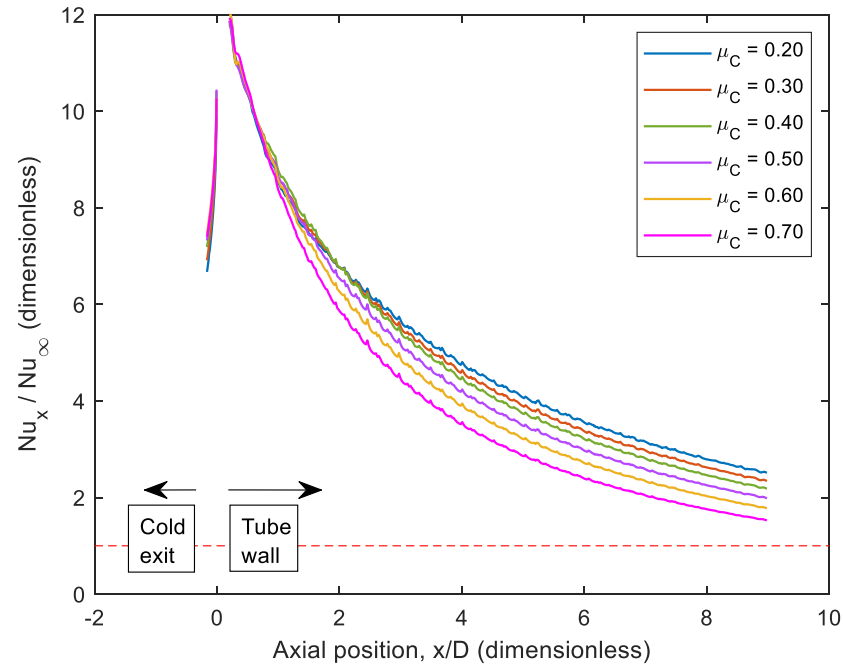
Figure 142. $\frac{Nu_{vortex}}{Nu_{\infty,pipe}}$ **development along vortex tube wall, uniform** q''
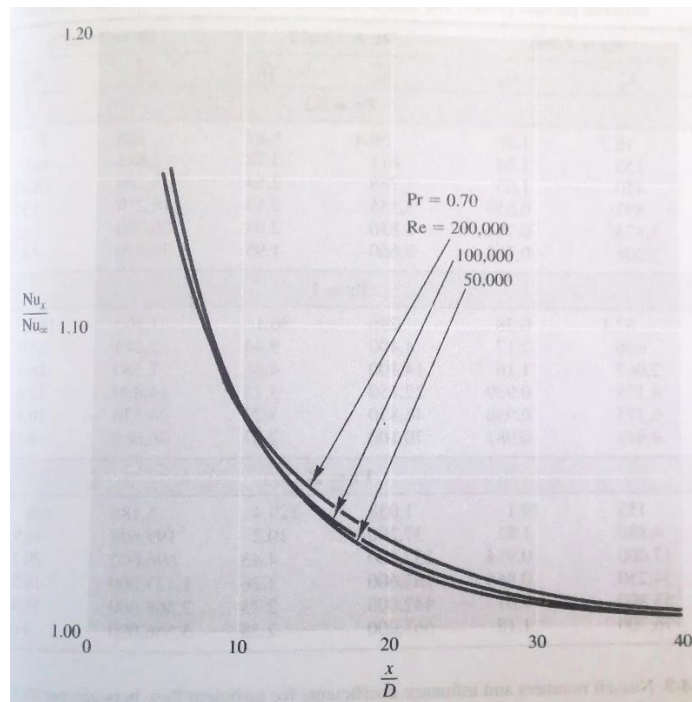

Figure 143. $\frac{Nu_{pipe}}{Nu_{\infty}}$ **along circular pipe thermal entry length, uniform heat flux** $(Pr = 0.7)$ **[7]**

A comparison between Figure 142 and Figure 143 reveals that the vortex tube

offers increased local heat transfer compared to a pipe flow entry region. At $\frac{x}{D} = 5$, the

pipe flow finds $\frac{Nu_{pipe}}{Nu_{\infty,pipe}} = 1.15$, while the vortex tube finds $2.86 \leq \frac{Nu_{vortex}}{Nu_{\infty,pipe}} \leq 4.07$ and

$2.49 \leq \frac{Nu_{vortex}}{Nu_{x,pipe}} \leq 3.54$, depending on cold fraction. Figure 144, drawn from Notter and

Sleicher [100], depicts the Nusselt number progression along the thermal entry length for

a uniform surface temperature circular pipe and is included for reference. While clearly

distinct, the uniform surface temperature and uniform heat flux results are quite similar,

which is expected for turbulent flows.
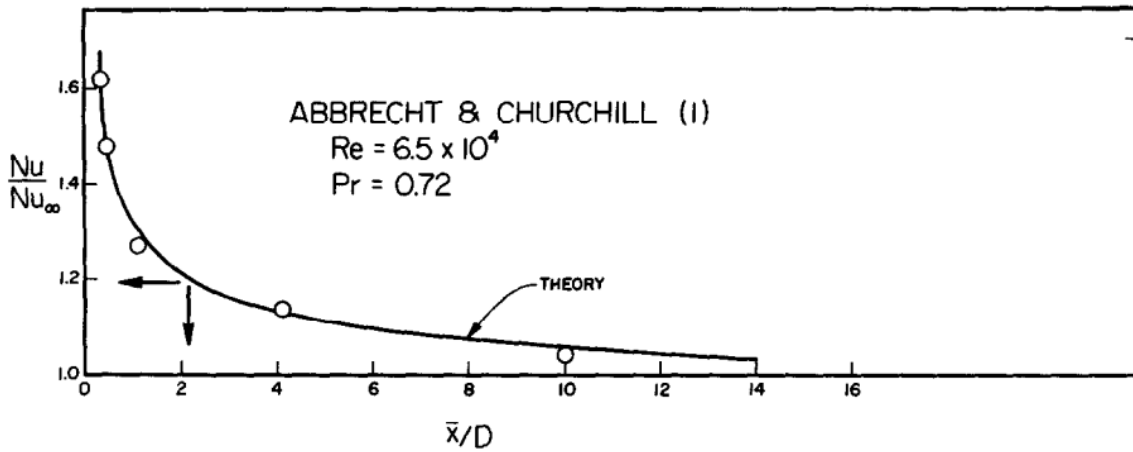
Figure 144. $\frac{Nu_x}{Nu_\infty}$ along circular pipe thermal entry length,

uniform surface temperature ($Pr = 0.72$) [100]

At $\frac{x}{D} = 1$, $\frac{Nu_{x,pipe}}{Nu_{\infty,pipe}} \approx 1.5$ and $8.37 \leq \frac{Nu_{x,vortex\ tube}}{Nu_{\infty,pipe}} \leq 8.77$, or $5.58 \leq \frac{Nu_{x,vortex\ tube}}{Nu_{x,pipe}} \leq 5.85$. At

$\frac{x}{D} = 4$, $\frac{Nu_{x,pipe}}{Nu_{\infty,pipe}} \approx 1.15$ and $8.37 \leq \frac{Nu_{x,vortex\ tube}}{Nu_{\infty,pipe}} \leq 8.77$, or $3.56 \leq \frac{Nu_{x,vortex\ tube}}{Nu_{x,pipe}} \leq 4.18$. The

vortex tube thus offers heat transfer performance several times that of regular pipe flow.

With respect to the integration of vortex tubes into the cooling architecture of a gas turbine engine, the finding that a vortex tube yields a considerable increase in Nusselt number over comparable tube geometries is potentially significant. Generally speaking, the concept of *adding* heat to a vortex tube is novel and its properties as a heat exchanger with its surroundings—as opposed to the internal temperature separation—have not thus far been exploited. The installation of a vortex tube could be used in areas of interest to increase the local heat flux and potentially improve internal cooling performance— provided a sufficient pressure difference is available to motivate the vortex.

4.2.3 *Experimental characterization of temperature separation at elevated inlet temperatures*

The experimental investigation of vortex tube temperature separation has thus far only witnessed the performance at relatively low inlet temperatures of 293 K – 333 K. In anticipation of applying vortex tubes in a gas turbine engine, it was highly desired to characterize the performance at temperatures closer to those of the coolant flow taken from a compressor section. The desired temperature range for high-temperature investigations was 600 K – 750 K; temperatures up to 500 K were achieved due to equipment limitations.

The original, low-temperature vortex tube laboratory configuration adjusted the gas temperature with a brazed-plate heat exchanger connected to a temperature bath, which used a mixture of water and ethylene glycol as the working fluid. The choice of working fluid placed a theoretical upper limit on achievable temperatures near 100°C (373 K)—the boiling point of water—although equipment limitations drove this limit even lower. The net effect was that the original laboratory configuration could not be

used for the high-temperature investigations and, due to its tight integration with other sensitive laboratory elements, could not be modified for this purpose either.

4.2.3.1 Experimental Methodology

A new vortex tube laboratory was assembled to investigate performance at higher temperatures. The high-temperature lab still required the capability to independently control the inlet temperature, pressure, and mass flow rate and therefore mirrored the low-temperature configuration in many respects. The high-temperature lab configuration is shown in Figure 145.
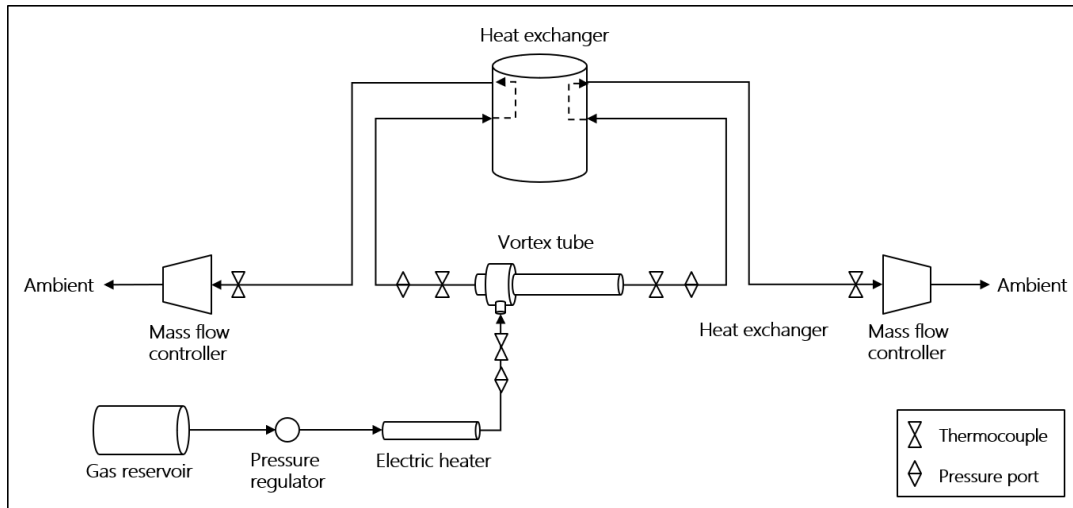
Figure 145. High-temperature vortex tube experimental configuration

An Exair^{TM} model 3208 vortex tube was used; an 8R vortex generator machined from brass was installed in place of the standard plastic component. The identical Omega 2612A digital mass flow controllers were installed downstream of the vortex tube exits, thus again decoupling the inlet pressure and mass flow rate. To achieve the desired inlet temperatures, a Tutco^{TM} 4 kW in-line electric heater was installed upstream of the vortex tube inlet. The heater was installed with its own feedback and control apparatus

263

consisting of a K-type thermocouple, a proportional-integral-derivative (PID) temperature controller and silicon-controlled rectifier (SCR) power controller to maintain the desired inlet temperature.

In practical terms, the upper limit of achievable temperatures was governed by the material limits of the seals installed in the hottest parts of the laboratory: from the heater through the vortex tube exits. Ultimately, the capability of the two O-rings in the vortex tube—one near the cold exit and one near the hot exit—became the limiting factor. The silicone O-rings used in testing had a limit of 505 K (450°F), and thus the upper limit of mean inlet temperatures was decided to be 500 K. As an aside, it became evident during assembly of the lab that the use of O-rings with a commercial vortex tube placed a firm limit on achievable temperatures. Specialty O-rings with a temperature limit of 600 K—the most capable identified during design—did not become available while the lab capability was active.

The method of instrumentation was essentially identical to the low-temperature lab as well. The total temperature and static pressure were measured at an instrumented inlet immediately upstream of the vortex tube, and at the respective exits, also using Omega grounded K-type thermocouples and the same NetScanner pressure transducer. To minimize heat losses, the hot section—all the way from the heater to the vortex tube exit instrumentation—was wrapped in alkaline earth silicate ceramic fiber insulation.

An early design consideration for the high-temperature lab was the desire to achieve greater mass flow rates than could be achieved on the low-temperature lab. To that end, ½-inch diameter tube was used for the flow paths—in contrast to many runs of ¼-inch tubing used in the low-temperature rig—and this had the desired effect. However,

it also had unintended consequences: the larger tubing significantly increased the size and thermal mass of the fittings attached to the vortex tube, and this contributed to greatly protracted times to achieve steady state in the experiments—10 to 20 minutes per data point, depending on the degree of the change between points. Fortunately, the heat loss correction function developed for the low-temperature lab was found to be valid for the high-temperature lab as well.

A prominent feature of the high-temperature lab was the heat exchanger downstream of the vortex tube exits. In the low-temperature lab, brazed-plate heat exchangers were used to protect the mass flow controllers from the elevated temperatures of the vortex tube, but due to the possibility of exceeding the temperature limit of the heat exchangers or insufficiently protecting the mass flow controllers, this approach was not adopted for the high-temperature rig.

To protect the mass flow controllers, a new heat exchanger was designed and built featuring a 55-gallon drum filled with water. The water in the drum functioned as an intermediate heat transfer medium, and immersed in the drum were three stainless steel coils. The first was a cooling line passing 278 K (40°F) water, the other two contained the exit flows from the vortex tube enroute to the mass flow controllers. The heat exchanger was found to sufficiently reduce the exiting gas temperature to an acceptable range and likely had considerable excess capacity.

The experiments required detailed estimates of the flow properties at the nozzle, and the same compressible flow relations—Eqs (45) – (49) (see page 122)—were applied. However, the cross-sectional area of the inlet was 8.52×10^{-5} m^2 and the ratio of the area between all of the nozzles and the instrumented inlet was $\frac{A_{nozzles}}{A_{inlet}} = 0.0369$.

Mass flow rates were varied from 1.18 – 2.96 g/s (60 – 150 SLPM), inlet total temperatures ranged from 350 K to 500 K, and inlet static gauge pressures varied 3.41 – 5.10 bar (49.41 – 74.01 psig). Combinations of these parameters were carefully set to achieve nozzle velocities ranging from 48.4 – 246.5 m/s, Reynolds numbers from 6,692 to 33,443, and Mach numbers ranging from 0.121 to 0.572.

During the initial operational evaluation of the lab, a peculiar characteristic of the configuration was observed. Temperature oscillations were observed at the inlet with a period of approximately 5 sec and an amplitude that increased as a function of inlet temperature; the greatest observed were ±9 K at 500 K. Oscillations were also observed at the vortex tube exits which were of smaller amplitudes than at the inlet but a similar period.

Three factors were identified as potentially contributing to the oscillations. First, the PID temperature controller was said by the supplier to have overshoot characteristics which generate periodic fluctuations, though the amplitude of these fluctuations was thought to be on the order of 1 K (2°F). Temperature oscillations were observed in the temperature controller with the same period and amplitude as seen in the data acquisition equipment, but it is not known if the temperature controller was driving these oscillations or merely observing them. Second, the plumbing surrounding the vortex tube installation was believed to have some resonant characteristics based on distinctive short-period pressure fluctuations at certain mass flow rates. Finally, oscillations were also seen in the flow rate recorded by the mass flow controllers. The period of the mass flow rate fluctuations was about five seconds and, interestingly, the hot and cold mass flow rates were essentially in phase with each other, but approximately 180° out of phase with the

temperature oscillations. In other words, the oscillations in the two mass flow controllers were constructive, leading to higher amplitude overall mass flow rate oscillations, and the trough of the overall mass flow rate corresponded to a peak in inlet temperature.

A likely explanation for the inlet temperature oscillations, then, seems to be that the mass flow controllers—acting under the influence of system dynamics—caused mass flow rate oscillations through the in-line heater which, in turn, drove the temperature oscillations. However, the oscillations were not observed when the in-line heater was turned off, suggesting that the heater itself may have been part of the system dynamics affecting the mass flow controllers. Regardless of the cause, the practical effect was to significantly increase the sampling window for each measurement. Sampling was still conducted at a frequency of 1 Hz, but the number of collected samples was increased to 30 for each data point to ensure a representative mean value. This approach yielded increased standard errors of temperature measurements compared to those seen in the low-temperature lab (which were typically 0.05 K for all thermocouples), but this effect was greater at the inlet than the exits. The high temperature rig saw inlet standard errors ranging from 0.3 – 1.0 K, depending on inlet temperature, mass flow rate and cold fraction; standard errors at the exits ranged from 0.07 – 0.25 K and typically from 0.04 – 0.15 K for a cold fraction of $\mu_C = 0.40$.

4.2.3.2   Results and Discussion

The high-temperature experimental investigation consisted of three parts: first, a demonstration of the effect of inlet temperature on temperature separation; second, an examination of whether the dimensional scaling principles first identified on the low-temperature rig are extensible to higher temperatures; and lastly, a more direct study of

the effect of nozzle velocity on temperature separation. A review of dimensionless characteristics follows the dimensional effort.

The investigation of the effect of inlet temperature on temperature separation was conducted through the use of three cases, labeled H1, H2, and H3, with target inlet temperatures of 350 K, 400 K, and 450 K, respectively. Exact values of nozzle properties are listed in Table 27. It was not possible to achieve the target mass flow rate of 2.960×10^{-3} kg/s (150 SLPM) for most cold fractions at an inlet temperature of 450 K, and the achievable mass flow rate decreased with increasing cold fraction, as can be seen in Figure 146. The mass flow rate was not a limiting factor for the cases with inlet temperatures of 350 K and 400 K.

As a result, the velocity, Reynolds number, and Mach number at the nozzle each decreased with increasing cold fraction for the case with an inlet temperature of 450 K, as can be seen in Figure 147; volumetric heat capacity, ρC_p, increased with cold fraction. It bears some emphasis that the mass flow rate and nozzle values listed in Table 27 are *mean* values across all cold fractions.

Table 27. Nozzle conditions for cases evaluating effect of increased inlet temperature

Case:	H1	H2	H3
Mass flow rate (kg/s)	2.960×10^{-3}	2.959×10^{-3}	2.900×10^{-3}
Inlet T_{total} (K)	**350.7**	**401.2**	**451.4**
Inlet P_{static} (bar, gauge)	5.001	5.000	5.000
Re	33451	30444	27508
Pr	0.739	0.733	0.730
$\rho_0 C_{p,0} \mu_{JT,0}$	0.0087	0.0052	0.0031
Velocity (m/s)	177.14	207.35	232.55
ρC_p (kJ/m³-K)	5.563	4.753	4.164
Mach number	0.482	0.530	0.563
ρ (kg/m³)	5.313	4.538	3.967

μ (µPa-s)	20.29	22.28	24.18
k (mW/m-K)	28.74	31.82	34.77
C_p (kJ/kg-K)	1.047	1.047	1.050
μ_{JT} (K/bar)	0.1557	0.1086	0.0737
Nozzle T_{static} (K)	335.0	379.8	424.4
Nozzle P_{static} (Pa, absolute)	510980	494688	483202
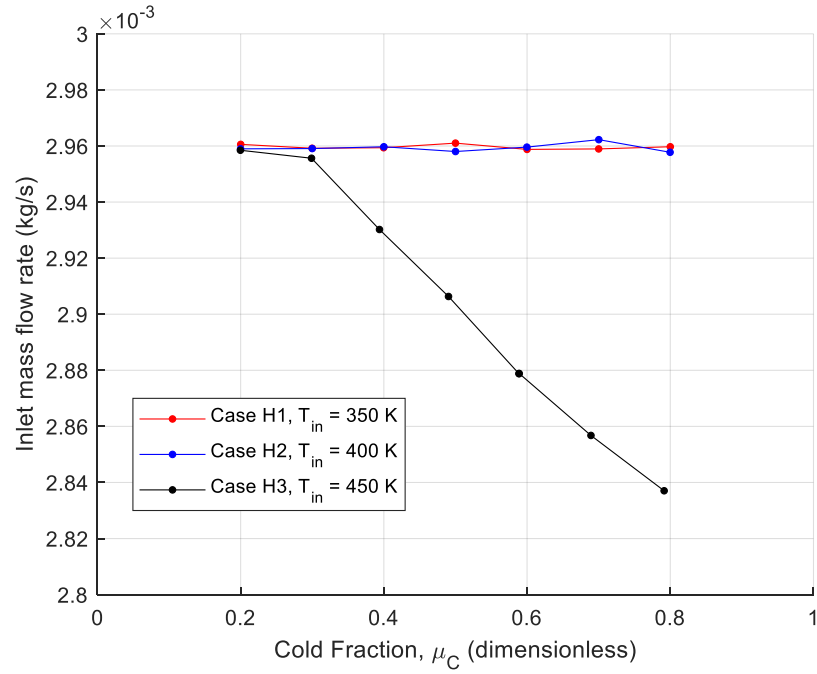
Figure 146. Mass flow rate for cases evaluating effect of inlet temperature
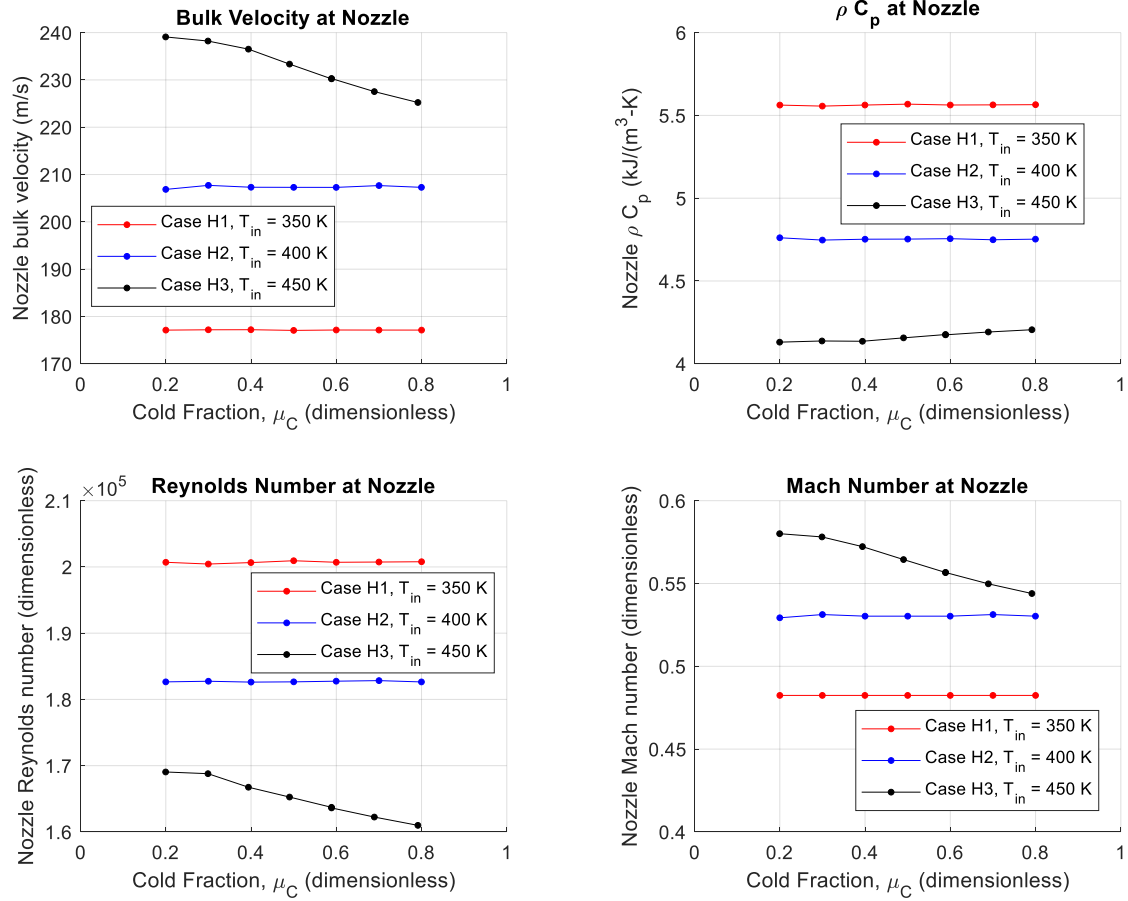
Figure 147. Nozzle conditions for cases evaluating effect of inlet temperature, as a function of cold fraction

In spite of the decrease in nozzle velocity as a function of cold fraction for Case H3 ($T_{in} = 450$ K), the resulting dimensional temperature separation curves, shown in Figure 148, still display a distinct increase with inlet total temperature. At the cold exit for a cold fraction of $\mu_C = 0.50$, the change in total temperature compared to the inlet more than doubles—from -23.9 K to -53.5 K—with an increase in inlet temperature of 100 K. The increasing temperature separation associated with increased inlet temperature was previously identified as a consequence of the greater nozzle velocities. In an indirect

sense, the curves of Case H3 reinforce the role of nozzle velocity as a scaling factor for dimensional temperature separation: the apparent inflection point in the hot exit curve and the observation that it bows toward the curve of H2 at high cold fractions are clear manifestations of the relationship.
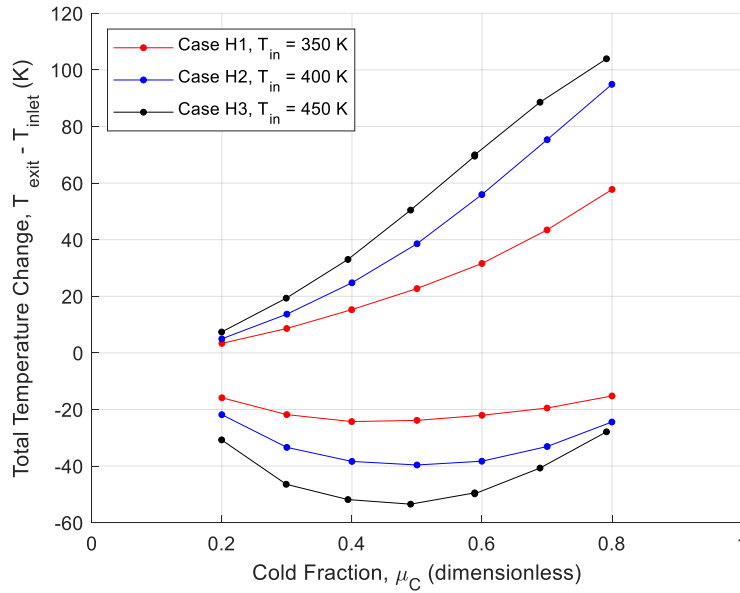
Figure 148. Temperature separation curves for cases evaluating effect of inlet temperature

Next, the investigation regarding the ability to match dimensional temperature separation despite differing inlet temperatures and pressures included three cases, dubbed H4, H5, and H6 with inlet temperatures of 350 K, 400 K, and 500 K, respectively. Data were collected for $\mu_C = 0.3$, 0.4, 0.5, and 0.7. Based on the results of cases H1 – H3, it was clear that matching the nozzle velocity for cases H4 – H6 across such a wide temperature range for all cold fractions required the use of a smaller mass flow rate, and all three used a nominal mass flow rate of 1.89×10^{-3} kg/s (95.9 SLPM). Actual nozzle properties for Cases H4 – H6 are shown in Table 28, which confirms closely matched

nozzle velocities and ρC_p between cases. The mass flow rate was held constant with respect to cold fraction for all three cases, as is evident in Figure 149.

Table 28. Nozzle conditions for cases evaluating matched nozzle velocity and ρC_p

| Case:	H4	H5	H6
Mass flow rate (kg/s)	1.892×10^{-3}	1.890×10^{-3}	1.874×10^{-3}
Inlet T_{total} (K)	350.3	400.7	501.0
Inlet P_{static} (bar, gauge)	3.407	3.997	5.103
Re	21197	19080	16028
Pr	0.738	0.732	0.728
$\rho_0 C_{p,0}\mu_{JT,0}$	0.0066	0.0046	0.0020
Velocity (m/s)	**148.93**	**148.55**	**148.68**
ρC_p (kJ/m³-K)	**4.222**	**4.237**	**4.238**
Mach number	0.403	0.375	0.335
ρ (kg/m³)	4.039	4.045	4.008
μ (µPa-s)	20.46	22.71	26.81
k (mW/m-K)	29.00	32.47	38.94
C_p (kJ/kg-K)	1.045	1.047	1.057
μ_{JT} (K/bar)	0.1567	0.1091	0.0471
Nozzle T_{static} (K)	339.3	389.7	490.0
Nozzle P_{static} (Pa, absolute)	393269	452474	563711
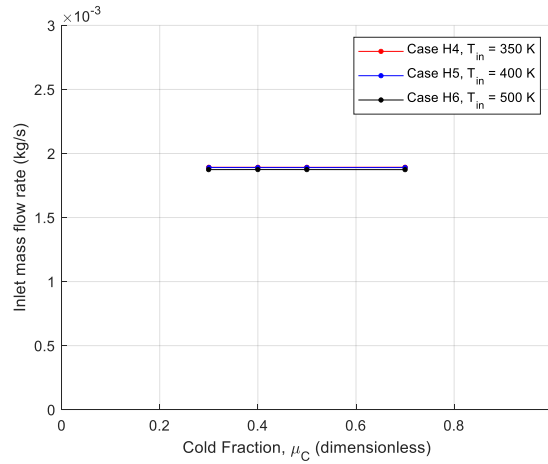
Figure 149. Mass flow rates for cases evaluating effect of matched nozzle velocity and ρC_p

272

The resulting temperature separation curves, shown in Figure 150, indicate that it is indeed possible to dimensionally match temperature separation characteristics with dissimilar inlet temperatures and pressures, as long as the nozzle bulk velocity and volumetric heat capacity are matched. The matched curves are quite close: the interval containing the points of 350 K and 400 K is ±0.3 K, and much less for many cold fractions; the interval containing 350 K, 400 K, and 500 K is ±0.6 K. The principle of dimensionally matching temperature separation was first introduced across a range of 40 K, but this demonstrates that the principle still works for a different configuration across a much wider range of 150 K. Moreover, the favorable comparison between the curves at higher nozzle Mach numbers than previously achieved—here, ranging between 0.335 and 0.403—implies that the technique of employing compressible flow relations to estimate nozzle velocity while approximating the flow constriction as an isentropic converging nozzle is fundamentally sound.
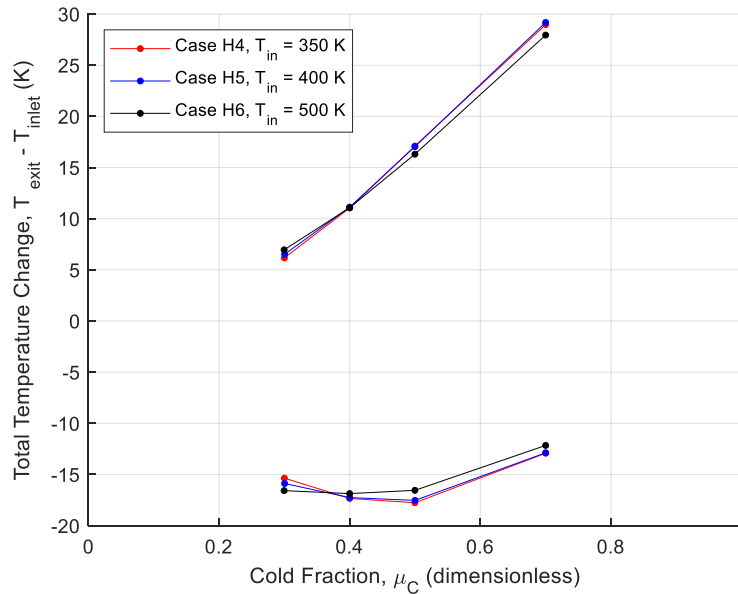
Figure 150. Temperature separation curves for cases with matched nozzle velocity and ρC_p

To characterize the relationship between nozzle velocity and temperature separation, a set of higher-resolution data was collected for a cold fraction of $\mu_C = 0.40$. For a thorough investigation, a variety of cases was tested using combinations of inlet temperatures of 350 K, 400 K, and 500 K, an inlet gauge pressure of 5 bar (72.52 psi), and mass flow rates of 0.00118 – 0.00296 kg/s (60 – 150 SLPM). This also afforded the opportunity to gather repeatability points to compare with those from cases H1 and H2 at $\mu_C = 0.40$. Figure 151 depicts the curves of dimensional temperature separation as a function of nozzle velocity.
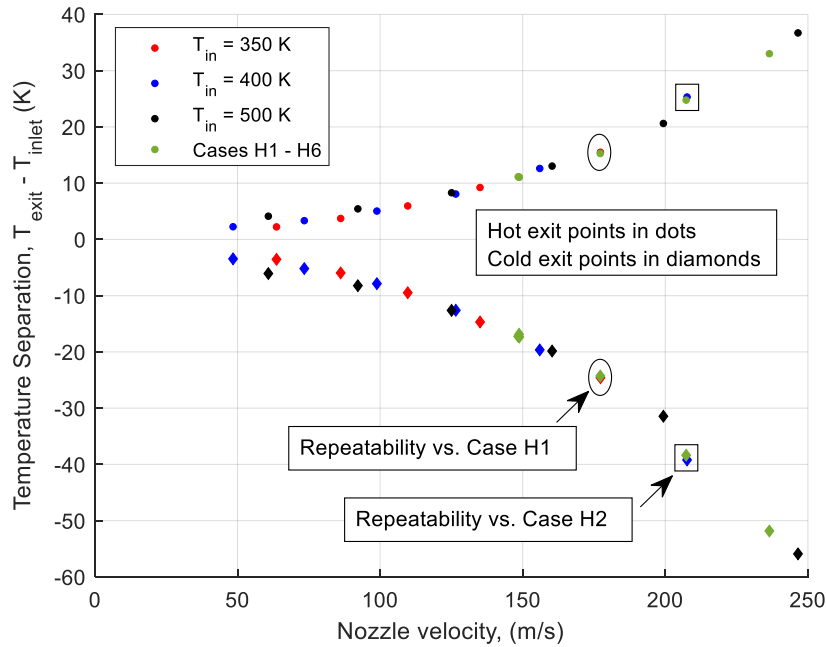
Figure 151. Temperature separation as a function of nozzle velocity for all cases ($\mu_C = 0.4$)

The points generally collapse into curves of hot and cold exit temperature separation, indicating consistent behavior between the cases across inlet temperatures and mass flow rates. Moreover, the comparison points for cases H1 and H2—indicated on the plot with ellipses and rectangles, respectively—indicate strong repeatability of the data.

The prominent curvature of the data indicates that temperature separation scales as a higher order function of nozzle velocity, which is consistent with the trend observed experimentally on the low-temperature rig. This is also broadly in line with the analytical finding from the nondimensionalization of the energy equation that the appropriate temperature scale includes the square of velocity.

The dimensionless characteristics of the high-temperature rig are also of interest. When the temperature separation of Cases H1 – H3 is nondimensionalized to $\rho^* C_p^* T_t^*$ at the exits, as shown in Figure 152, it is seen that the curves do not collapse into a single curve; this unexpected result stands in contrast to the results from the low-temperature rig in which the curves of $\rho^* C_p^* T_t^*$ do collapse to nearly a single curve. A reduction of Cases H4 – H6 to $\rho^* C_p^* T_t^*$, in Figure 153, reveals similar behavior. When curves of $\rho^* C_p^* T_t^*$ for Cases H1 – H6 are all plotted together in Figure 154, the surprising diversity of the performance curves is fully in view.

Figure 152. Dimensionless temperature separation, $\rho^* C_p^* T_t^*$, for cases evaluating effect of increasing inlet temperature
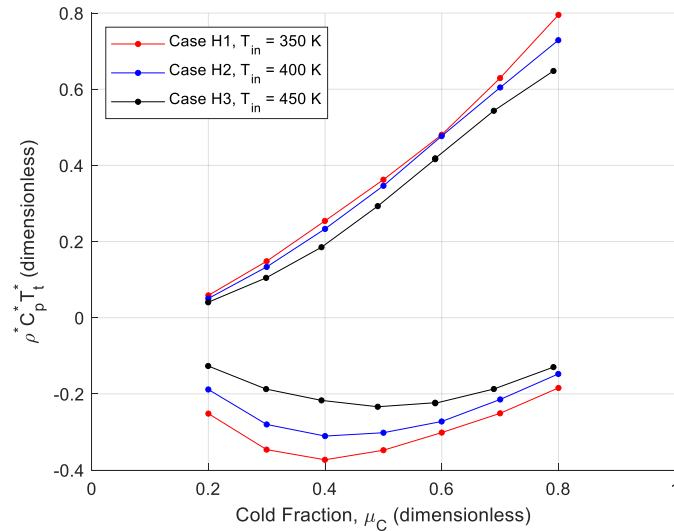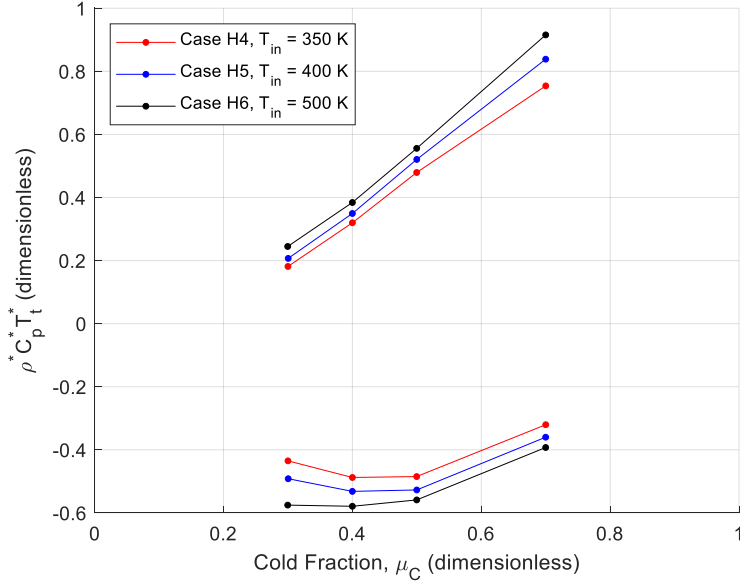
Figure 153. Dimensionless temperature separation, $\rho^* C_p^* T_t^*$, for cases evaluating effect of increasing inlet temperature
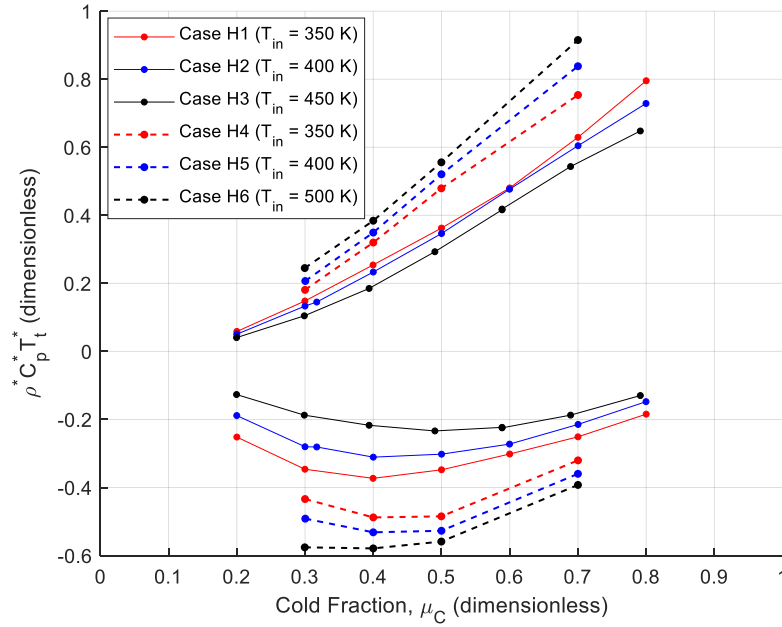
Figure 154. Dimensionless temperature separation, $\rho^* C_p^* T_t^*$, for cases evaluating effect of increasing inlet temperature, and matched nozzle velocity and ρC_p

276

To better understand this behavior, it is necessary to examine the relationships between the dimensionless temperature separation parameter, $\rho^* C_p^* T_t^*$, at the hot and cold exits and the governing parameters. The role of Reynolds number is first investigated, and Figure 155 indeed reveals an apparent influence between on $\rho^* C_p^* T_t^*$ at the exits such that $\rho^* C_p^* T_t^*$ generally seems to decrease with Re.
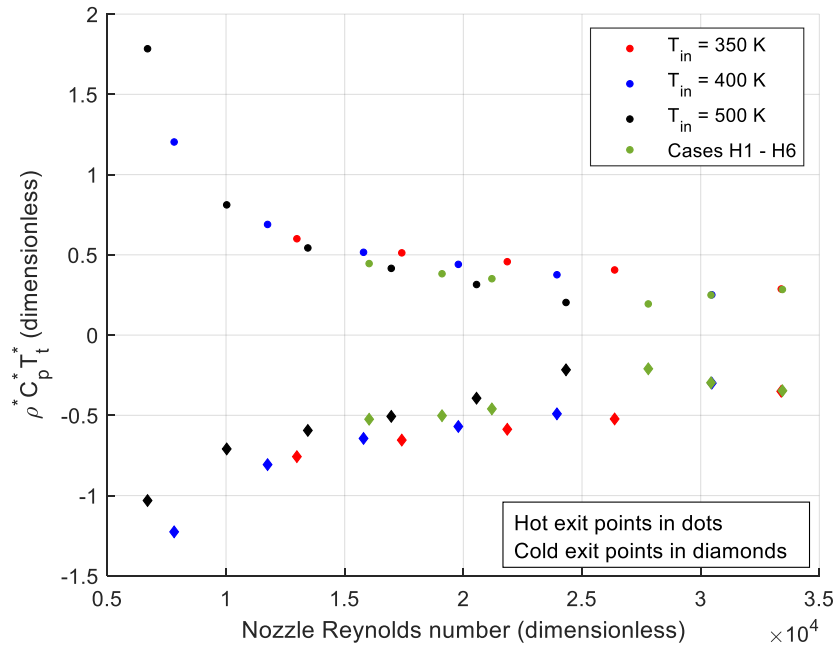
Figure 155. Dimensionless temperature separation, $\boldsymbol{\rho^* C_p^* T_t^*}$,

as a function of nozzle Reynolds number for all cases ($\boldsymbol{\mu_C = 0.4}$)

Next, adopting the same analysis methodology as for the low-temperature rig, the effect of $\rho_0 C_{p,0} \mu_{JT,0}$ on $\rho^* C_p^* T_t^*$ is investigated, as shown in Figure 156. Although there are certainly wide variations $\rho^* C_p^* T_t^*$ in Figure 156, it does not appear that they are a systematic function of $\rho_0 C_{p,0} \mu_{JT,0}$; moreover, the wide variation of $\rho_0 C_{p,0} \mu_{JT,0}$ associated with Cases H1 – H6 does not seem to yield a correspondingly large or systematic

variation of $\rho^* C_p^* T_t^*$. Overall, it does not appear that $\rho_0 C_{p,0} \mu_{JT,0}$ has a prominent nor

consistent role in determining $\rho^* C_p^* T_t^*$ for the high-temperature configuration. It should

also be noted that the values of $\rho_0 C_{p,0} \mu_{JT,0}$ achieved here span 1.17×10^{-3} to 9.36×10^{-3} for

an overall range of 8.18×10^{-3}; this is smaller than the range of 11.4×10^{-3} achieved on the

low-temperature configuration and therefore the negligible influence of $\rho_0 C_{p,0} \mu_{JT,0}$ on

$\rho^* C_p^* T_t^*$ for the high-temperature rig is not surprising.
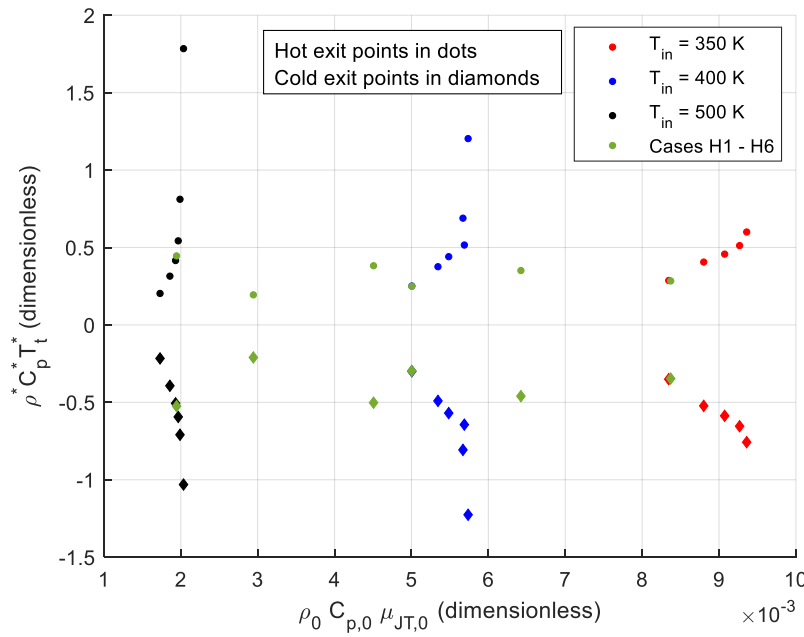
Figure 156. Dimensionless temperature separation, $\rho^* C_p^* T_t^*$,

as a function of nozzle Reynolds number for all cases ($\mu_C = 0.4$)

Finally, the variation of $\rho^* C_p^* T_t^*$ with nozzle Mach number is considered, though

this relationship was examined during the analysis of the low-temperature rig and found

not to be significant. Mach number was not present in the nondimensionalization of the

energy equation as originally cast in Table 11 and Eq (73) (see pages 148 and 150) and

was therefore not considered a governing parameter. However, the Mach number can be

introduced into the nondimensionalization by way of a reduction of thermodynamic

derivatives, a key result of which is drawn from Panton [91] and shown in Eq (107).

$$\frac{V_0^2}{C_{p,}T_0} = \frac{M_0^2 \gamma_0}{\alpha_0 \rho_0 C_{p,0} T_0} \tag{107}$$

The original nondimensionalization used a temperature scale of $\frac{V_0^2}{C_{p,0}}$, which is

clearly equivalent to the term $\frac{M_0^2 \gamma_0}{\alpha_0 \rho_0 C_{p,0}}$, where α_0 is the isothermal compressibility

coefficient. By extension, the static temperature can be nondimensionalized according to

Eq (108), which is valid for real gases. Similarly, it is possible to accomplish an alternate

nondimensionalization of the energy equation in terms of a temperature scale based on

the Mach number, although that will not be done here.

$$T^* = \frac{T - T_0}{\dfrac{M_0^2 \gamma_0}{\alpha_0 \rho_0 C_{p,0}}} \tag{108}$$

When $\rho^* C_p^* T_t^*$ at the exits is plotted as a function of Mach number, as shown in

Figure 157, the data points from the high-temperature rig collapse to nearly a single curve

and reveal that, for the high-temperature vortex tube configuration, $\rho^* C_p^* T_t^*$ is a strong,

continuous function of Mach number, decreasing with increasing Mach number. The

dispersion at very low Mach numbers is likely attributable to experimental uncertainty at

low flow rates and possibly also to difficulty in achieving steady state operation. Figure

157 indicates that the disparity among the curves of $\rho^* C_p^* T_t^*$ at the exits among Cases H1

– H6, seen in Figure 154, is due to differing Mach numbers. However, recall from Figure

74 that the $\rho^* C_p^* T_t^*$ points from the low-temperature rig were seen to be independent of

Mach number; those points are now plotted in yellow in Figure 157. Although the range

of Mach numbers involved in the high-temperature lab is considerably wider than in the

low-temperature lab, which achieved Mach $0.13 - 0.35$, the relationship between $\rho^* C_p^* T_t^*$

and Mach number is clearly different between the two. This behavior is likely a feature of

the hardware configuration in the high-temperature rig. The exact reason is not known;

however, the tubing runs at the exits were considerably longer in the high-temperature rig

than the low-temperature rig—more than six meters compared to less than three meters—

and this may have been a contributing factor.
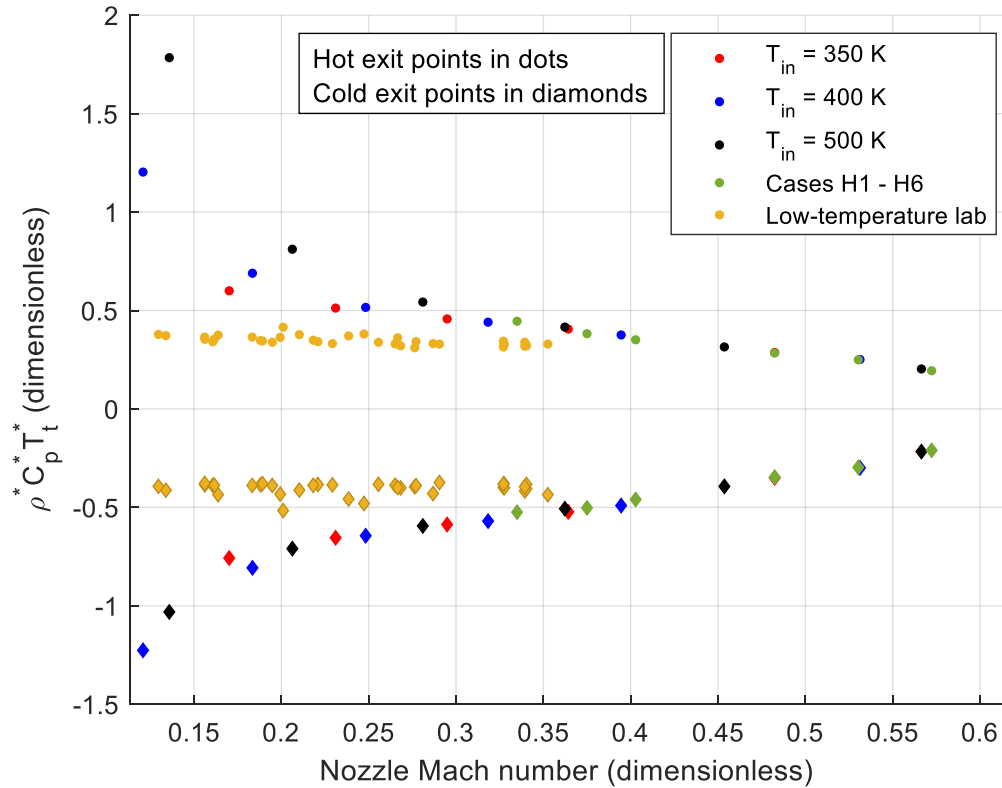
Figure 157. Dimensionless temperature separation, $\rho^* C_p^* T_t^*$,

as a function of nozzle Mach number for all cases ($\mu_C = 0.4$)

The high-temperature and low-temperature configurations also feature qualitatively different pressure drop characteristics. In Figure 158, the static pressure drop between the nozzle and both exits is plotted as a function of the cold fraction. Because Cases H4 and L feature different nozzle velocities and the pressure drop is a function of the square of nozzle velocity, it is not entirely appropriate to directly compare the magnitude of pressure drop. Instead, the difference in *trends* between the two cases should be considered. Some similarities are present, such as the fact that the pressure drop between the nozzle and cold exit is larger than that between the nozzle and the hot exit. Also, the difference between the two pressure drops increases with cold fraction.
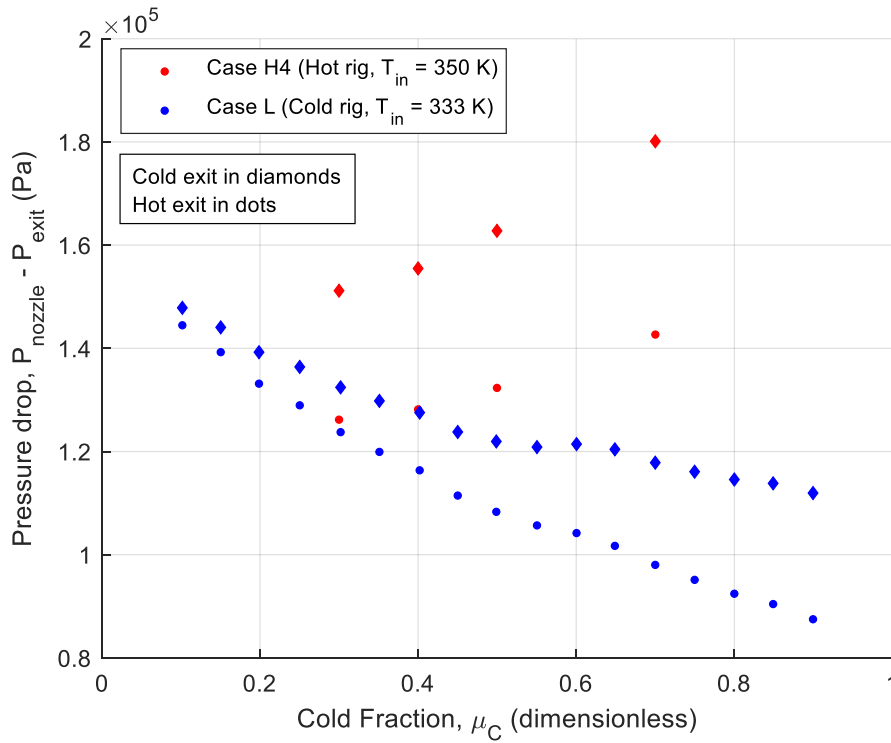
Figure 158. Comparison of pressure drop characteristics between comparable cases on high- and low-temperature laboratory configurations

However, the glaring difference between the two cases is the observation that the pressure drop between the nozzle and both exits *increases* with cold fraction for the high-temperature rig but decreases with cold fraction for the low-temperature rig. A practical consequence of this behavior has already been seen in Figure 146 in the comparison of the mass flow rates of Cases H1 – H3, where Case H3 saw that smaller mass flow rate could be achieved at increasing cold fractions for a given inlet pressure. At the time, this was considered an unexpected result since experience with the low-temperature configuration had suggested that if a particular mass flow rate could be achieved at $\mu_c = 0.20$, it could be achieved for greater cold fractions as well.

The investigation of the high-temperature configuration will be concluded with an analysis of the pressure drop characteristics. Recall that the pressure drop across any device or fitting can be described in terms of a pressure loss coefficient and the dynamic pressure, as in Eq (75) repeated here.

$$\Delta P = \xi \left(\frac{1}{2}\rho V^2\right) \tag{75}$$

It should be reiterated that the flow physics surrounding the pressure drop are complicated even for a relatively simple device such as an asymmetric T-junction and therefore it is unsurprising that they are quite nuanced for a more complex device like a vortex tube. However, the data sets gathered can be used to illustrate some broad trends regarding the pressure loss coefficient for $\mu_c = 0.4$. First, the loss coefficient is plotted as a function of Mach number, as shown in Figure 159. This yields an unusual "notch" at Mach 0.48, and the discontinuous nature of the data—in the absence of a more detailed

physics-based explanation—implies that the phenomenon may not actually be due to a
Mach number effect.
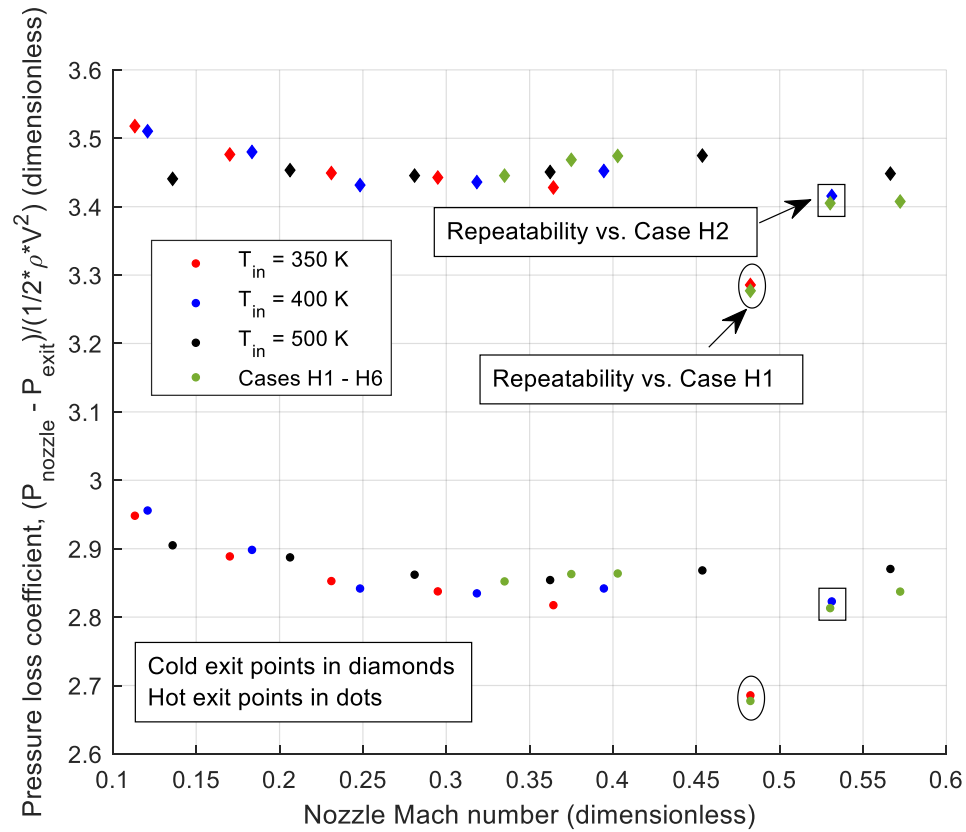
Figure 159. Pressure loss coefficient as a function of Mach number ($\mu_C = 0.4$)

The pressure loss coefficient is plotted as a function of *Re* in Figure 160, and it
appears that the loss coefficient is more appropriately characterized as a function of the
nozzle Reynolds number. At the cold exit, it is fairly constant between 3.4 and 3.5 for
Reynolds numbers in the range of 10,000 to 25,000 and decreases somewhat beyond that
range. However, the fact that the rapid decrease in ξ with respect to *Re* occurs for the
single greatest value makes a conclusive determination of this trend impossible.
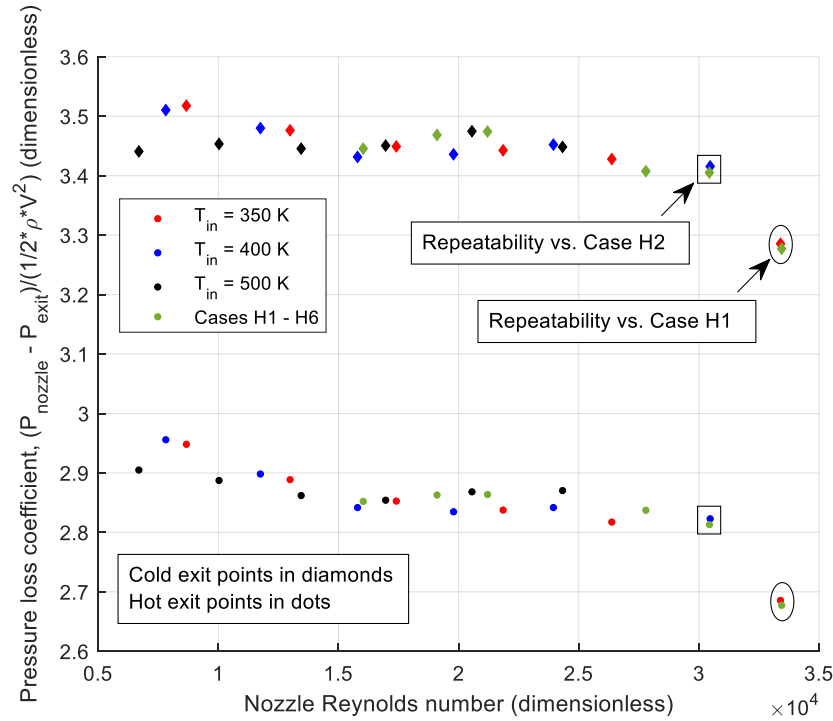
Figure 160. Pressure loss coefficient as a function of Reynolds number ($\mu_C = 0.4$)

A few salient points regarding vortex tube operation have been revealed with the investigation of high-temperature vortex tube operation. First, it has been demonstrated that the practice of dimensionally matching vortex tube temperature separation curves is possible at temperatures up to 500 K—higher than any known, published, experimental work—and across a range of 150 K. Additionally, the result that dimensional temperature separation scales as a higher order function of nozzle velocity is broadly consistent with the theoretical finding that the temperature scale includes velocity squared.

However, some important lessons regarding the integration of vortex tubes into a complex, high-temperature apparatus have also been observed. It is possible that some of the findings from the low-temperature rig are perhaps not as universal as previously thought. Different hardware configurations may feature qualitatively different trends

284

regarding performance, such as trends of pressure drop with respect to cold fraction, which were exactly opposite between the high-temperature and low-temperature lab configurations. While the pressure loss coefficient in the low-temperature rig could be empirically correlated with temperature and pressure, though not very well with Reynolds number, the high-temperature rig saw the pressure loss coefficient as a reasonable function of Reynolds number. Additionally, the dimensionless temperature separation, $\rho^* C_p^* T_t^*$, of the high-temperature rig was a strong and continuous function of Mach number—an unexpected result, given the insensitivity of $\rho^* C_p^* T_t^*$ on the low-temperature results to Mach number or any other governing parameters. The dependence of $\rho^* C_p^* T_t^*$ on Mach number in the high temperature rig does appear amenable to the derivation of an engineering correlation between the two, which would serve as an intermediate step in estimating dimensional temperature separation across a wide range of nozzle conditions.

The reasons for the differing qualitative trends between high- and low-temperature configurations were not precisely determined. However, a key takeaway from this research is that important, practical characteristics of a vortex tube are significantly affected by its installation. The identical commercial vortex tube, when installed in two different lab configurations, produced qualitatively different behaviors despite several commonalities between the two setups. Ultimately, it is essential that some initial investigation of performance characteristics for a particular embodiment—the vortex tube *and* its installation—should be undertaken to understand the qualitative trends and how they might affect a desired application.

4.2.4 *Computational investigation vortex tube performance at engine-representative pressures and temperatures*

Finally, it is essential to estimate the performance of vortex tubes in an actual turbine engine. As has become amply clear, the performance of a vortex tube varies considerably with nozzle conditions and thus the nozzle conditions must be appropriately defined. In this section, it is expected that the intended application is for a gas turbine engine installed on an aircraft and the nozzle conditions are derived from this assumption.

4.2.4.1 Methodology

The process of determining nozzle conditions begins with defining flight conditions, then applying assumptions regarding the performance of the engine, and finally joining these findings with a specified vortex tube geometry to compute the nozzle conditions. The notional flight conditions correspond approximately to those of an airliner in a cruise leg at an altitude of 30,000 ft and a flight Mach number of 0.80. Static pressure and temperature were drawn from the 1976 U.S. Standard Atmosphere [101] at geometric altitudes. The engine inlet was assumed to be lossless, and therefore the total temperature and pressure entering the compressor, T_{t2} and P_{t2}, respectively, were computed using the compressible flow relations in Eq (45), repeated below, and Eq (109), using $\gamma = 1.402$, drawn from the data of NIST REFPROP 9.1 [93] corresponding to flight level conditions.

$$T_{t2} = T\left(1 + \frac{\gamma - 1}{2}M^2\right) \tag{45}$$

$$P_{t2} = P\left(1 + \frac{\gamma - 1}{2}M^2\right)^{\frac{\gamma}{\gamma-1}} \tag{109}$$

The compressor section was modeled after an ideal, isentropic compressor. Total properties exiting the compressor were determined using a specified pressure ratio, π_c, defined as the ratio of the total pressure exiting the compressor, P_{t3}, to the total pressure entering the compressor, P_{t2}, and a total temperature ratio, τ_c, defined as the ratio of the total temperature exiting the compressor, T_{t3}, to the total temperature entering the compressor, T_{t2}. The value of τ_c was computed from the compressor pressure ratio using Eq (110) [1] and the same value of γ.

$$\tau_c = \pi_c^{\frac{\gamma-1}{\gamma}} \tag{110}$$

Pressures and temperatures at sea level static, altitude static, altitude at Mach 0.8, and exiting compressor sections with pressure ratios of 20 and 30 are listed in Table 29.

Table 29. Pressures and temperatures for modeling vortex tubes at engine conditions

Property	Condition				
	Sea level static	Altitude 30 kft, static	Altitude 30 kft, Mach 0.8	Post-compressor, $\pi_c = 20$ 30 kft, Mach 0.8	Post-compressor, $\pi_c = 30$ 30 kft, Mach 0.8
Static pressure (Pa)	101325	30148	30148		
Total pressure (Pa)			45956	919120	1378680
Static temp (K)	288.15	228.80	228.80		
Total temp (K)			258.23	609.62	684.78

It should be noted that the total temperatures exiting the compressors are considerably lower than the notional range of coolant temperatures of 800 K to 1000 K [1]. This discrepancy is due to additional factors such as non-isentropic compression and heat addition. Furthermore, the present analysis does not account for pressure losses nor

heat addition between the compressor bleed and the entrance to the turbine section or wherever a vortex tube might be installed. Nevertheless, this method does provide a sufficiently detailed characterization to proceed with the next step of the analysis and the flexibility to accommodate additional engine data, should it become available.

The total properties exiting the compressor stage were then used to set boundary conditions for the CFD solution. Due to the nature of the CFD code, this was accomplished through a combination of direct and indirect methods. Recall that the total temperature at the inlet—which, in the CFD mesh, is equivalent to the nozzle—is explicitly specified as a boundary condition and therefore can be easily matched to the corresponding value in Table 29. However, the total pressure at the inlet is not an explicit boundary condition and must be indirectly matched. Here, the specific vortex tube geometry becomes important.

The vortex tube geometry is based on a simplified form of the Exair™ model 3208 vortex tube, with a hydraulic diameter of 0.721 mm; see Section 3.2.1 on page 114 for additional details. The CFD mesh and solution method are identical to those described in Section 3.2.8 on page 182. The only explicit inlet boundary conditions are the mass flow rate and total temperature—the total pressure at the inlet is derived from the resulting solution, which is also defined by the static pressure boundary conditions at the exits. To fully define the boundary conditions, it is necessary to specify a mass flow rate.

Using the compressible flow relations described in Section 3.2.1, a mass flow rate was predicted which would correspond to the target total pressure. Estimates of nozzle static pressure, static temperature, and velocity were also produced and were used to adjust the hot exit static pressure boundary condition such that the desired nozzle

288

conditions could be achieved indirectly in CFD. The compressible flow relations used to identify a target mass flow rate employed a constant $\gamma = 1.402$ but the CFD used a real gas model and therefore there was not a perfect match between predicted nozzle properties and those actually manifested in the CFD solution. However, using this method, it was possible to match the CFD solution to an anticipated nozzle velocity within $0.2\% - 0.3\%$, static pressure within $0.1\% - 0.5\%$, and total pressure within $2.7\% - 5.5\%$. A final criterion was that the boundary conditions should yield a total pressure drop across the vortex tube that is relevant to a pressure drop between the compressor and turbine sections in an engine. For the given geometry, a mass flow rate of 1.84 g/s was considered reasonable for this purpose.

CFD solutions were sought for cold fractions of $0.20 \leq \mu_C \leq 0.80$, but the demanding conditions and real gas model prevented the solution from reaching convergence for some of these cold fractions for each scenario. For both scenarios, the walls of the vortex tube were modeled as adiabatic. This permitted the analysis to determine the degree of temperature separation achieved solely by virtue of the nozzle conditions and without the need to estimate nor model a more realistic distribution of local heat flux across the vortex tube.

4.2.4.2 Results and Discussion

The nozzle properties corresponding to the cases at engine conditions and to a baseline case at laboratory conditions are shown in Table 30, each for $\mu_C = 0.40$. The total pressure ratio between the hot exit and nozzle is a rough approximation of the maximum combustor pressure ratio, π_b, which would drive the flow; if π_b exceeds this value in an engine, the required pressure difference to drive the flow is no longer

available and a lower mass flow rate and nozzle velocity results. Generally speaking,

high π_b values are desired in an engine and this goal presents a fundamental constraint on

vortex tube performance in a turbine engine. From Table 30, it can be seen that

$\pi_b = 0.893$ and 0.944 for the compressors with $\pi_c = 20$ and 30, respectively. While

$\pi_b = 0.944$ is reasonable for a modern compressor, $\pi_b = 0.893$ would be considered

low—implying that the mass flow rate and nozzle velocity corresponding to the $\pi_c = 20$

case are probably higher than could be achieved in practice.

Table 30. CFD nozzle properties for engine conditions and lab baseline ($\mu_C = 0.40$)

Property at nozzle (or specified site)	Engine, $\pi_c = 20$ 30 kft / M0.8	Engine, $\pi_c = 30$ 30 kft / M0.8	Lab baseline
Mass flow rate (kg/s)	0.00184	0.00184	0.00142
Total temperature (K)	609.62	684.78	293.40
Total pressure (Pa)	970451	1416238	401617
Total pressure, *hot exit* (Pa)	866243	1337094	328421
Total pressure ratio, π_b	0.893	0.944	0.818
Static pressure (Pa)	863140	1391907	378890
Static temperature (K)	604.04	681.60	288.54
ρ (kg/m^3)	5.393	7.078	4.582
C_p (J/kg-K)	1054.7	1073.5	1010.8
μ (μPa-s)	31.05	33.73	18.06
k (mW/m-K)	45.80	50.24	25.34
μ_{JT} (K/bar)	0.0081	-0.0118	0.2424
Velocity (m/s)	108.51	82.68	98.58
Reynolds number	13589	12508	18027
Prandtl number	0.715	0.721	0.721
$\rho C_p \mu_{JT}$	0.00046	-0.00090	0.01123
Mach number	0.221	0.159	0.289

The dimensional temperature separation curves for the engine condition cases are

compared to the baseline case in Figure 161. As expected, the case with $\pi_c = 30$ yields a

lesser degree of temperature separation owing to its lower nozzle velocity and slightly

greater C_p. The dimensional temperature separation achieved at engine conditions is

small: at $\mu_C = 0.40$, the case with $\pi_c = 20$ yielded a cold exit ΔT_c of -5.3 K while the case with $\pi_c = 30$ yielded ΔT_c = -2.8 K. At the hot exit, the case with $\pi_c = 20$ yielded ΔT_h = +8.6 K for $\mu_C = 0.70$ and although the $\pi_c = 30$ case could not be solved for $\mu_C = 0.70$, it otherwise is estimated to yield half that of the $\pi_c = 20$ case.
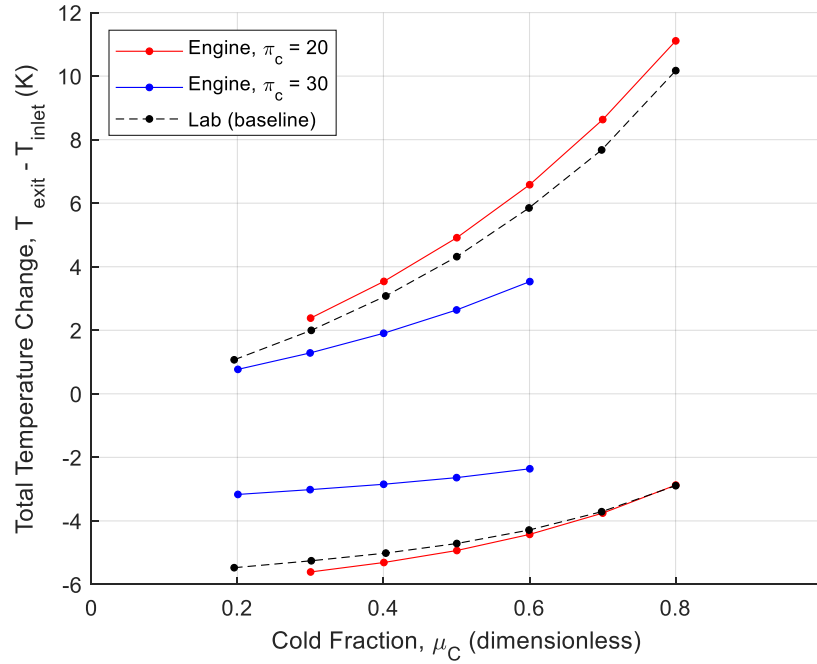
Figure 161. Dimensional temperature separation at engine conditions (and lab baseline)

When the temperature separation is nondimensionalized to $\rho^* C_p^* T_t^*$, as shown in Figure 162, the lines collapse to nearly a single curve—including the baseline case. This result suggests that the CFD cases all bear a fundamental similarity and therefore additional CFD may not be necessary to estimate dimensional temperature separation for new cases of interest. Instead, it may be possible to estimate results for any nozzle condition using two curves of $\rho^* C_p^* T_t^*$ generated from a CFD solution—one evaluated at the hot exit and the other at the cold exit, each for a range of cold fractions—and the method prescribed in Section 3.2.6 on page 172 based on experimental results. Of course,

291

the prescribed method also requires a model of the pressure drop and this could be established using data from experimental or computational methods.

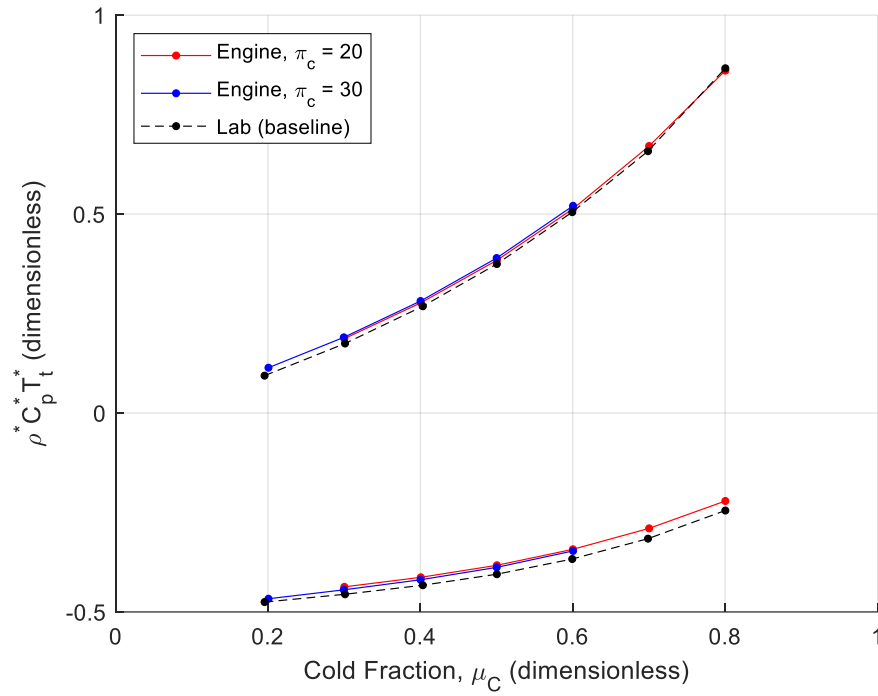**Figure 162. Dimensionless temperature separation, $\rho^* C_p^* T_t^*$, at engine conditions (and lab baseline)**

This page is intentionally left blank

5 Research Objective 4: Apply vortex tube and film cooling findings to inform turbine engine design

Research Objective 4 considers the potential effects of vortex tube temperature separation on film cooling performance and, to that end, represents a synthesis of the findings from the respective investigations. No new computational or experimental investigations were conducted in pursuit of this research objective; rather, the models developed in the research thus far were applied. The analytical frameworks developed as a part of Research Objective 1 form the basis for the film cooling evaluation and the computational results of Research Objective 3 are used as a starting point in estimating the coolant temperatures involved. Gas turbine film cooling scenarios present notoriously difficult conjugate heat transfer problems, and some simplifying assumptions were applied in order to lay the foundation for a tractable first-order analysis.

5.1 Methodology

Analyses of the effect of temperature separation on the adiabatic wall temperature, T_{aw}, and on the metal surface temperature, T_s, were conducted for the CFD results corresponding to engine conditions with $\pi_c = 20$ and $\pi_c = 30$. In those cases, the inlet temperature was 609.62 K for $\pi_c = 20$ and 684.78 K for $\pi_c = 30$. A notional two-row cooling scenario is presented, shown in Figure 7 (repeated from page 19). The general configuration was assumed for assessments of T_{aw} and T_s though only T_{aw} is shown in Figure 7. In the scenario, the upstream row issued the colder coolant at temperature T_{c1} while the downstream row issued the warmer coolant at temperature T_{c2}. The freestream temperature was $T_\infty = 2000$ K.
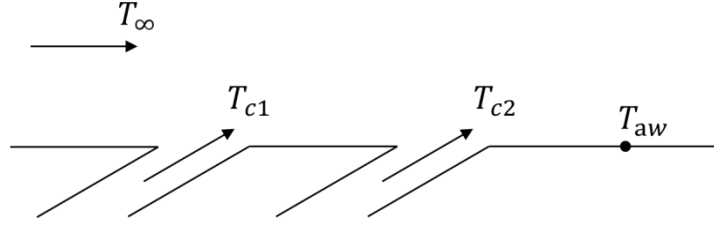
Figure 7. Double row cooling configuration with two coolant temperatures

5.1.1 Determining coolant temperatures

The coolant temperatures T_{c1} and T_{c2} depended on whether the temperature separation was adiabatic or nonadiabatic; in other words, whether they were induced solely by the action of the vortex tube or also in combination with external heat added via the tube walls. Without any heat addition, the coolant temperatures drawn from the adiabatic vortex tube were the coldest that could be expected, since they were derived from an ideal, isentropic compressor with no heat added between the compressor and the turbine blade. A vortex tube with heat addition, therefore, likely yields a more realistic scenario for modelling cooling effectiveness in engine conditions, so both adiabatic and nonadiabatic cases were included in the analysis.

In Sections 4.2.1.1 and 4.2.2, it was discovered via experimental and computational investigations that when the exterior of a vortex tube is heated, causing net heat transfer to the flow within, the flow exiting the hot exit sees a disproportionately large increase in temperature compared to the flow exiting the cold exit. The fraction of the heat added via the tube walls that is retained in the cold flow will be defined as α, and Eqs (111) and (112) define the relationships between the total heat added, that retained in the cold flow, and that retained in the hot flow. The computational findings of Section

294

4.2.2 produced a set of $\alpha = f(\mu_C)$ for one uniform heat flux case, and those values will be applied in this analysis as presented in Table 31 (extracted from Table 26, page 255).

$$\alpha = \frac{q_{cold}}{q_{total}} \tag{111}$$

$$(1 - \alpha) = \frac{q_{hot}}{q_{total}} \tag{112}$$

Table 31. Cold flow heat retention as a function of cold fraction

Cold fraction, μ_C	Cold flow heat retention fraction, α
0.20	0.036
0.30	0.057
0.40	0.077
0.50	0.107
0.60	0.144
0.70	0.200

In the absence of more detailed information, it will be assumed that α is not a function of the total heat added. There is reason to doubt this assumption: the experimental findings presented in Table 24 suggest that, for $\mu_C = 0.40$, values of α are not constant with increasing q_{total}; however, the 5% error associated with the analysis of experimental results is large enough that the relationship between α and q_{total} is not conclusive. In any event, the present study will assume that α is only a function of μ_C.

For cases where the temperature increase resulting from heat addition is small, the change in temperature can be modeled with a constant C_p, as in Eqs (113) and (114). By substituting in the cold fraction and rearranging, the temperature changes can be represented using Eqs (115) and (116). However, it has been seen that increases in the

temperature of the hot flow are much greater than those of the cold flow, and it may be possible that $C_{p,hot}$ is appreciably greater than $C_{p,cold}$. In such a case, it is more appropriate to determine the exiting temperature from exit enthalpies, as in Eqs (117) and (118). All nonadiabatic data in this study was generated from the enthalpy method. In practice, it was assumed that the exit pressures were identical for the adiabatic and nonadiabatic cases; this is reasonable in view of the experimental finding that the changes in the exit pressures as a result of heat addition are small and the empirical understanding that the enthalpy of air is a very weak function of pressure.

$$\dot{m}_{cold} C_{p,cold} \Delta T_{cold} = \alpha q_{total} \tag{113}$$

$$\dot{m}_{hot} C_{p,hot} \Delta T_{hot} = (1 - \alpha) q_{total} \tag{114}$$

$$C_{p,cold} \Delta T_{cold} = \left(\frac{\alpha}{\mu_C}\right) \left(\frac{q_{total}}{\dot{m}_{total}}\right) \tag{115}$$

$$C_{p,hot} \Delta T_{hot} = \left(\frac{1 - \alpha}{1 - \mu_C}\right) \left(\frac{q_{total}}{\dot{m}_{total}}\right) \tag{116}$$

$$h_{cold,nonadiabatic} - h_{cold,adiabatic} = \left(\frac{\alpha}{\mu_C}\right) \left(\frac{q_{total}}{\dot{m}_{total}}\right) \tag{117}$$

$$h_{hot,nonadiabatic} - h_{hot,adiabatic} = \left(\frac{1 - \alpha}{1 - \mu_C}\right) \left(\frac{q_{total}}{\dot{m}_{total}}\right) \tag{118}$$

A reference temperature $T_{exit,nonadiabatic}$ was also determined for a notional case with identical heat addition but no temperature separation—such as for flow in a tube with the same exposed surface area and mean heat flux; nuances of this equivalency will

be discussed later. This was accomplished starting with Eq (119) and using the value of h_{inlet} entering the vortex tube, where h_{inlet} refers to enthalpy. The total heat added, q_{total}, was the product of the mean heat flux, q'', and the total exposed surface area. For the CFD solution, from which the adiabatic temperature separation curves were derived, the surface area was 1.241×10^{-3} m^2 and this was used for the analysis. Five cases of heat addition were incorporated into the analysis: an adiabatic case where $q'' = 0$ kW/m^2 and cases with $q'' = 10, 20, 30,$ and 40 kW/m^2. These five heat flux cases equated to q_{total} values of 0, 12.41, 24.82, 37.23, and 49.64 W, respectively.

$$h_{exit} - h_{inlet} = \frac{q_{total}}{\dot{m}_{total}} \tag{119}$$

5.1.2 *Assessing adiabatic wall temperature in the presence of two coolant temperatures generated by a vortex tube*

To determine the effect of two coolant temperatures on adiabatic wall temperature, it was necessary to first determine the temperature ratio parameter, ξ, using Eq (19), repeated below, where T_{c1} is the temperature of the coolant issuing from the upstream row and T_{c2} is that from the downstream row; recall that here $T_{c1} < T_{c2}$. Next, the effect of the two coolant temperatures on adiabatic effectiveness was evaluated using Eq (21)—the form corresponding to the scenario where $\xi < 1$, repeated below—where η_1 and η_2 represent the adiabatic effectiveness at a point resulting from only the upstream or downstream row issuing coolant, respectively.

$$\xi \equiv \frac{T_\infty - T_{c2}}{T_\infty - T_{c1}} \tag{19}$$

297

$$\hat{\eta} = \eta_1 + \xi\eta_2 - \eta_1\eta_2 \tag{21}$$

The value of the overall effectiveness in the presence of two coolant temperatures, $\hat{\eta}$, depends on the values of η_1 and η_2; that is, the adiabatic effectiveness resulting from only the upstream row issuing coolant and only the downstream row issuing coolant, respectively. Plausible values of η_1 and η_2 may be drawn from experimental results; consider, for instance, the results of the adiabatic effectiveness study presented in Section 2.2.3. Reading from Figure 13, reproduced below, it can be seen that at a location of x/D = 10, y/D = 0, $\eta_1 \approx 0.45$ and $\eta_2 \approx 0.30$.
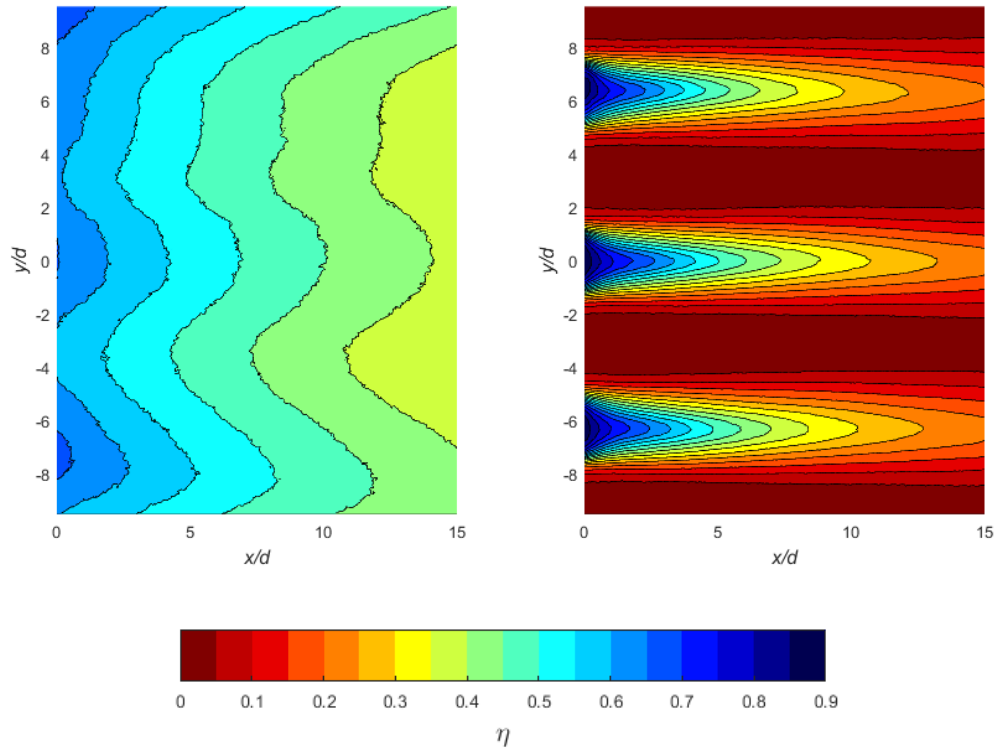

Figure 13. η_1 (left), η_2 (right)

This is a special situation in that the effectiveness of the upstream row is greater than that of the downstream row, due to the outsized effectiveness of the upstream slot compared to the downstream 7-7-7 holes. Alternatively, one might be interested in a scenario in which the effectiveness of the downstream row at a location of interest is greater than that of the upstream row. Two cases will be included in the analysis: one with $\eta_1 = 0.45$ and $\eta_2 = 0.30$, based on the experimental configuration, and a second with arbitrary values of $\eta_1 = 0.15$ and $\eta_2 = 0.30$.

However, recall that the reference temperatures are not the same for the single- and dual-temperature and cases, as indicated by Eqs (7) and (14) for the single-temperature and dual-temperature cases, respectively, repeated below. Please note that subscripts of $2T$ and $1T$ have been added to refer to dual- and single-temperature cases, respectively, but that both the upstream and downstream rows are issuing coolant for both cases.

$$\eta = \frac{T_\infty - T_{aw,1T}}{T_\infty - T_{c,exit}} \tag{7}$$

$$\hat{\eta} = \frac{T_\infty - T_{aw,2T}}{T_\infty - T_{ref}} \tag{14}$$

For Eq (7), $T_{c,exit}$ is equal to the vortex tube inlet temperature for adiabatic temperature separation, but $T_{exit,nonadiabatic}$ for the case with heat addition. For Eq (14), T_{ref} is always equal to T_{c1} since the cold row is upstream in the present analysis. The value of T_{aw} was computed for the dual-temperature scenario and the corresponding single-temperature scenario for each heating case, though the difference, $(T_{aw,2T} - T_{aw,1T})$, was generally considered of greater interest. It should be reiterated

that this method of determining adiabatic effectiveness in the presence of two coolant temperatures is only valid where the principle of superposition applies and therefore presupposes relatively low ACRs.

5.1.3   *Assessing metal surface temperature in the presence of two coolant temperatures generated by a vortex tube*

Determining the effect on the surface temperature of a conductive metal blade is a more straightforward process in some respects, and a more convoluted process in others. The temperature difference parameter is ζ, defined in Eq (34) and repeated here. For adiabatic temperature separation, the differences in coolant temperature relative to the mean temperature, $\Delta T_{c,1}$ and $\Delta T_{c,2}$, can be read directly from the dimensional temperature separation plot. Recall also that a weighting parameter, μ, defined by Eq (32), is used to determine mean temperature, defined by Eq (27).

$$\zeta = \frac{(1-\mu)\Delta T_{c,2} - \mu\Delta T_{c,1}}{T_\infty - T_{mean}} \tag{34}$$

$$\mu \equiv \frac{\dot{m}_{c,1}C_{p,c,1}}{\dot{m}_{c,1}C_{p,c,1} + \dot{m}_{c,2}C_{p,c,2}} \tag{32}$$

$$T_{mean} = \mu T_{c,1} + (1-\mu)T_{c,2} \tag{27}$$

An important clarification must be made here, since experimental data on overall effectiveness are only available for $\mu = 0.50$, but it was desired to investigate the effects of temperature curves corresponding to a wider range than just $\mu_C = 0.50$. Two analytical approaches were identified to accommodate $\mu \neq \mu_C$. The first approach is to use a fixed $\mu = 0.50$ with the variety of μ_C values and their corresponding coolant

temperatures. A physical realization of this might involve two plenums supplied by the

exits of one or more vortex tubes such that the mass flow rates are identical—as are the

*ACR*s, assuming the rows are identical—with the assumption that any "excess" mass flow

from the vortex tubes is exhausted outside the region of interest. A benefit of this

approach is that realistic values of $\hat{\phi}$ and $\frac{\partial \hat{\phi}}{\partial \zeta}$ can be chosen which have been found to

exist on an experimental configuration. However, as a result of forcing $\mu = 0.50$ when

$\mu \neq \mu_C$, T_{mean} is always the arithmetic mean of T_{c1} and T_{c2} and thus varies with μ_C.

The second approach is to model the coolant temperatures using $\mu \approx \mu_C$ with

some assumptions regarding the applicability of the results. For this approach to be

physically realized, one might imagine two identical rows or cooling holes fed from the

exits of the same vortex tube according to the cold fraction; when the upstream row

issues the colder coolant, then $\mu \approx \mu_C$. Recall that when $\mu = 0.50$ for identical rows or

holes, the *ACR*s are identical. Assuming *ACR₁* = 2.0 for two identical rows, *ACR₂* ranges

from 4.67 – 0.86 while μ_C varies from 0.3 to 0.7. Alternatively, one might recall Eq (31),

repeated below, which involves the ratios of the cross-sectional areas of the two rows.

$$\mu = \frac{1}{\dfrac{A_{c,2}ACR_2}{A_{c,1}ACR_1} + 1} \tag{31}$$

One might assume various ratios between the cross-sectional areas of the two

rows, $\frac{A_{c,2}}{A_{c,1}}$, such that *ACR₁* = *ACR₂* for any μ without any assumptions about excess

coolant being vented to another region of interest. Moreover, T_{mean} is constant with

respect to μ_C. The primary drawback of this approach is that the ranges of realistic $\hat{\phi}$ and

$\frac{\partial \widehat{\phi}}{\partial \zeta}$ have not been determined experimentally; however, given the theoretical flexibility of

its implementation, it is not hard to imagine that *some* location might be found in a region

of interest with $\mu_C \neq 0.50$ in which $\widehat{\phi}$ and $\frac{\partial \widehat{\phi}}{\partial \zeta}$ can found that are comparable to those

found experimentally for $\mu_C = 0.50$. In other words, the risk of using unrealistic values

appears low; moreover, achievable values of $\widehat{\phi}$ and $\frac{\partial \widehat{\phi}}{\partial \zeta}$ still vary considerably from model

to model. For these reasons, the second approach was adopted in the analysis.

The adopted approach uses $\mu \approx \mu_C$, but the exactness of this near equality

depends on the variation of the specific heat. Since the cold fraction is defined as

$\mu_C \equiv \frac{\dot{m}_{c,1}}{\dot{m}_{c,1}+\dot{m}_{c,2}}$, the equivalency in Eq (120) can be found through algebraic manipulation.

When it is reasonable to expect that the temperature differences across a vortex tube are

not sufficient to appreciably change C_p, i.e. $C_{p,c,1} \approx C_{p,c,2}$, then $\mu = \mu_C$ almost exactly.

When $C_{p,c,2} > C_{p,c,1}$, it can be shown that $\mu < \mu_C$. The extent of the difference depends

on μ_C: for example, using $C_{p,c,2} = 1.05 C_{p,c,1}$, it can be found that $\mu = 0.96\mu_C$ for

$\mu_C = 0.20$, but $\mu = 0.99\mu_C$ when $\mu_C = 0.80$.

$$\mu = \mu_C \left[\frac{C_{p,c,1}}{C_{p,c,2} + \mu_C\left(C_{p,c,1} - C_{p,c,2}\right)} \right] \tag{120}$$

The mean temperature, T_{mean}, is equal to the single-coolant reference

temperature, i.e. $T_{mean} = T_{c,i}$ (although this is actually a feature of *both* analytical

approaches). For the case of adiabatic temperature separation, this is simply the inlet

temperature to the vortex tube. This convenient identity means that the *change* in surface

temperature at any location in a region of interest can be determined by subtracting the

overall effectiveness with a single coolant temperature from that with two coolant

temperatures, i.e. $\hat{\phi} - \phi$. By subtracting Eq (121) from Eq (33), both repeated below,

Eq (123) follows; note the subscripts of "1T" and "2T" to indicate single- and dual-

temperature cases, respectively.

$$\phi = \frac{T_\infty - T_{s,1T}}{T_\infty - T_{c,i}} \tag{122}$$

$$\hat{\phi} = \frac{T_\infty - T_{s,2T}}{T_\infty - T_{mean}} \tag{33}$$

$$\hat{\phi} - \phi = \frac{T_{s,1T} - T_{s,2T}}{T_\infty - T_{mean}} \tag{123}$$

The same principle applies to determining the laterally averaged surface

temperature, $\bar{T}_s$, from a laterally averaged overall effectiveness, $\bar{\phi}$ or $\bar{\hat{\phi}}$. Additionally, it

can also be seen that the relationship between $\bar{\phi}$ and $\bar{\hat{\phi}}$ at any streamwise position can be

expressed in terms of ζ and the sensitivity of $\bar{\hat{\phi}}$ to ζ at that location, i.e. $\frac{\partial \bar{\hat{\phi}}}{\partial \zeta}(x/D)$, as seen

in Eq (40), repeated below. By combining Eq (123)—when considered with respect to a

lateral average—and Eq (40) and applying some manipulation, the resulting equation, Eq

(124), shows exactly how the difference in laterally averaged surface temperatures

between scenarios, $\left(\bar{T}_{s,2T} - \bar{T}_{s,1T}\right)$, can be computed at any x/D location. Significantly, it

was found that $\frac{\partial \bar{\hat{\phi}}}{\partial \zeta}$ appeared to be constant with respect to ζ. Some information is

required, of course, regarding the distribution of $\frac{\partial \bar{\hat{\phi}}}{\partial \zeta}$ across a region of interest and this

can be drawn from experimental data.

$$\bar{\bar{\phi}}(x/D) = \bar{\phi}(x/D) + \zeta \left[\frac{\partial \bar{\bar{\phi}}}{\partial \zeta} (x/D) \right] \tag{40}$$

$$\bar{T}_{s,2T} - \bar{T}_{s,1T} = -(T_\infty - T_{mean}) \left\{ \zeta \left[\frac{\partial \bar{\bar{\phi}}}{\partial \zeta} (x/D) \right] \right\} \tag{124}$$

The mean temperature with heat addition is not the same as the inlet temperature for adiabatic temperature separation and therefore must be computed separately. The single-coolant reference temperature and T_{mean} should be extremely close, if not identical; in practice, they differed by between 0.9×10^{-4} K and 0.40 K across all cases. The two temperatures were still assumed to be equal, permitting Eq (124) to be used for nonadiabatic temperature separation with the values of T_{mean} actually used in the calculations.

5.2 Results and Discussion

5.2.1 Coolant temperatures from a vortex tube

Ten cases were considered, based on the adiabatic temperature separation curves produced from the computational effort that used compressor pressure ratios of $\pi_c = 20$ and $\pi_c = 30$, first seen in Figure 161 (see page 291). By applying the heat addition model derived from the computational investigation of a nonadiabatic vortex tube, temperature separation curves were produced for each engine condition; these are seen in Figure 163 for $\pi_c = 20$ and Figure 164 for $\pi_c = 30$.
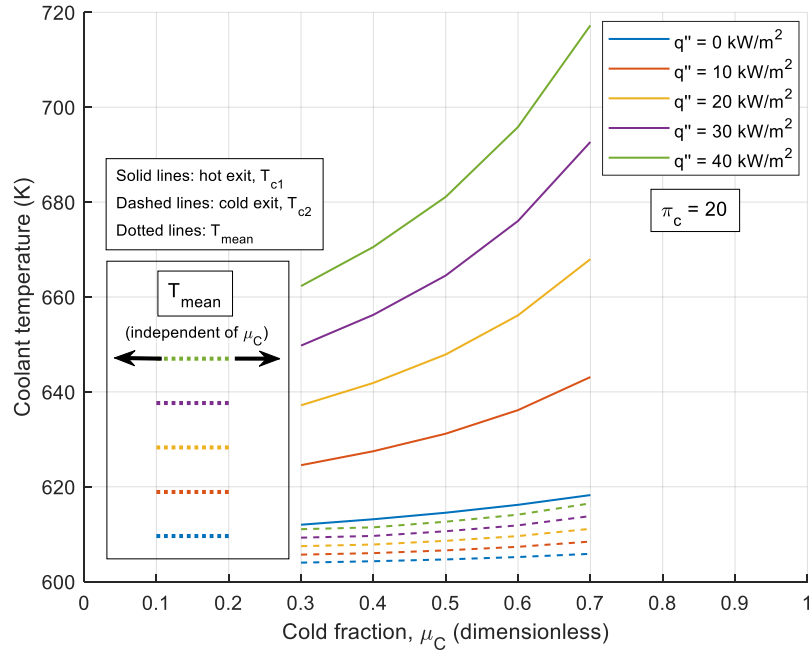
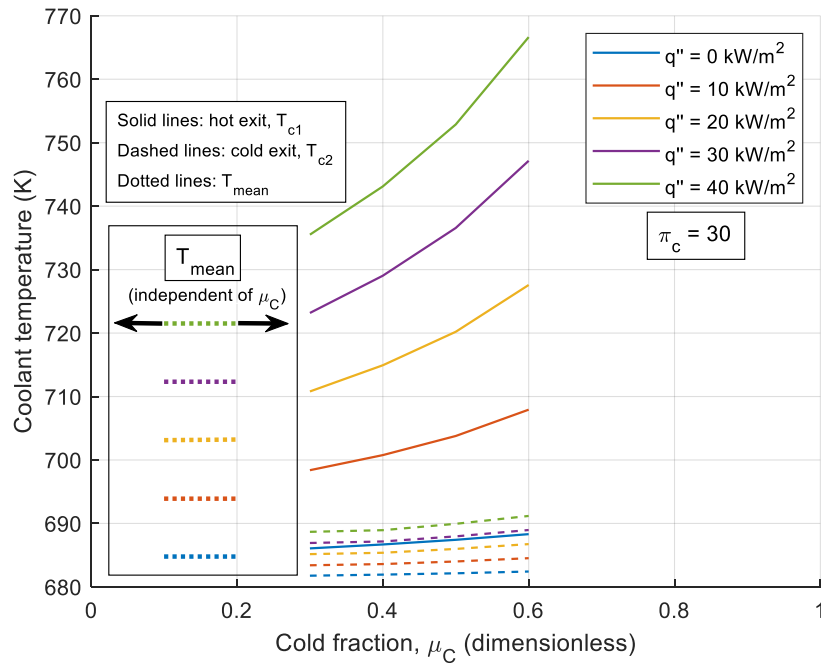**Figure 163. Temperature separation curves for $\pi_c = 20$**

Figure 164. Temperature separation curves for $\pi_c = 30$

Also seen in Figure 163 and Figure 164 are the mean temperatures, shown on the left side; these range from 609.62 K for the unheated case with $\pi_c = 20$ up to 721.51 K for the $q'' = 40$ kW/m^2 case with $\pi_c = 30$. The differences in coolant temperatures are quite pronounced: at $\mu_c = 0.60$ and $q'' = 40$ kW/m^2, $T_{c2} - T_{c1} = 81.7$ K for $\pi_c = 20$ and $T_{c2} - T_{c1} = 75.5$ K for $\pi_c = 30$. These temperature profiles were then used to determine the effects on adiabatic wall temperature and metal surface temperature.

5.2.2 Effect of vortex tube temperature separation on adiabatic wall temperature

Values of ξ as a function of cold fraction and q'' are plotted for both $\pi_c = 20$ and $\pi_c = 30$ in Figure 165. As might be expected, the coolant temperature ratio parameter, ξ, is a strong function of the amount of heat added to the flow and the cold fraction, which dictates the fraction of heat retained in the hot and cold streams. Both the hot and cold streams increase in temperature with increasing heat flux, but the fact that a large majority is retained in the hot stream means that T_{c1} increases by a comparatively small amount while T_{c2} increases by a comparatively large amount—and this tends to decrease ξ with increasing q''. This effect is also intensified with increasing cold fraction.
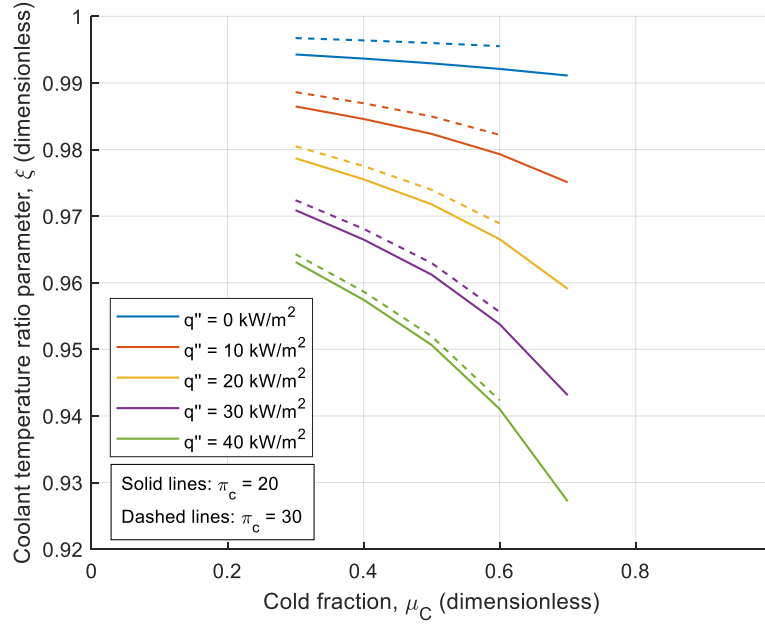
Figure 165. Variation of ξ with heat addition as a function of cold fraction

The effect of the two temperatures on adiabatic wall temperature depends greatly on the details of the cooling scenario, i.e. the values of η_1 and η_2 in a region of interest. Figure 166 contains four plots: on the upper left side, curves of $\hat{\eta}$ are shown for a point in a notional region of interest dominated by downstream row effects at which $(\eta_1, \eta_2) = (0.15, 0.30)$; on the upper right side, curves of $\hat{\eta}$ are shown for a point dominated by upstream row effects at which $(\eta_1, \eta_2) = (0.45, 0.30)$. The trends between the two are identical and they differ only in magnitude; this is intuitive based on the mechanics of Eq (21). The variations of $\hat{\eta}$ do not appear large: the entire span of values is less than 0.03; however, even small differences can have a pronounced effect at elevated temperatures.
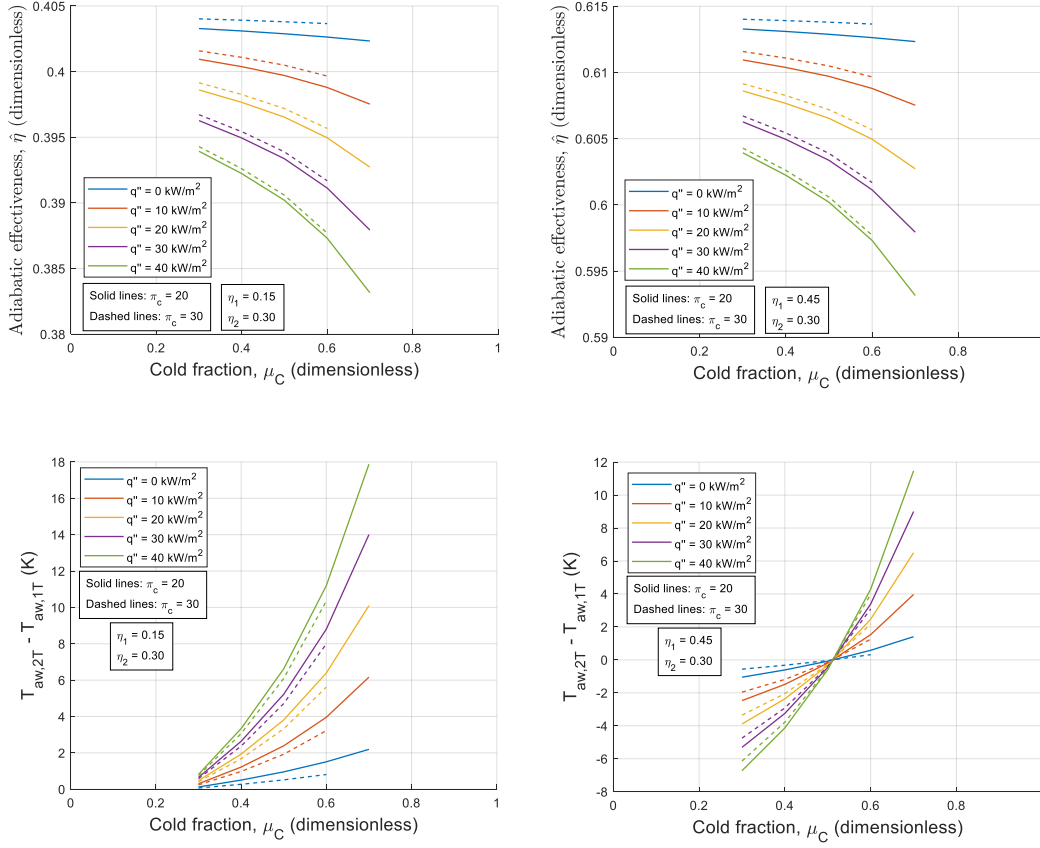
Figure 166. Variations of $\hat{\eta}$ and changes in T_{aw} with q'' and μ_C

Below the respective plots of $\hat{\eta}$ are the corresponding changes in adiabatic wall temperature, $\left(T_{aw,2T} - T_{aw,1T}\right)$, reflecting the difference in T_{aw} observed with the rows issuing coolant at two different temperatures versus the T_{aw} observed with the rows issuing coolant at T_{mean}. On the left, the curves of $\left(T_{aw,2T} - T_{aw,1T}\right)$ indicate that as the downstream row increases in temperature relative to the upstream row, the value of T_{aw} at that point also increases; this makes sense because the point is much more strongly affected by the downstream row than the upstream row. The downstream-dominated point on the left sees the adiabatic wall temperature increase by up to 18 K with $\mu_C = 0.70$, $q'' = 40$ kW/m², and $\pi_c = 20$.

On the bottom right, the situation is more complicated. The point in question is dominated by the upstream row, i.e. the cold exit, and the temperatures associated with smaller cold fractions are colder—hence, the reduced adiabatic wall temperature. At very high cold fractions, the greatly elevated coolant temperatures issuing from the downstream row serve to increase the adiabatic wall temperature in spite of the fact that $\eta_2 < \eta_1$. However, the bottom right plot contains a distinctive feature where the differences in temperature apparently have no effect on the adiabatic wall temperature. These notional temperature differences are associated with a cold fraction of $\mu_C = 0.512$ and reflect a balance between the low temperatures and high influence of the upstream row with the high temperatures and low influence of the downstream row. The range of $\left(T_{aw,2T} - T_{aw,1T}\right)$ observed for the upstream-dominated point is comparable to the other scenario, but the existence of this balance point tempers the maximum difference, which is 11.5 K with $\mu_C = 0.70$, $q'' = 40$ kW/m², and $\pi_c = 20$.

On a final note, it is worth pointing out that the unusual phenomenon first observed in Section 2.2.3.2, in which it is better not to have a second row at all, did not come into play here—nor was it even close. That phenomenon becomes important in scenarios where the downstream row is issuing the warmer coolant—which was the case here—but a film cooling scenario is only vulnerable to that issue when the value of ξ drops below that of η_1. The minimum ξ value here was 0.93—much more temperature separation would be required before that phenomenon became practically significant.

5.2.3 *Effect of vortex tube temperature separation on metal surface temperature*

The trends of the coolant difference parameter, ζ, are plotted Figure 167. Intuitively, the temperature curves associated with increased cold fractions correlate with

increasing ζ values. The ζ values in Figure 167 appear fairly small in comparison to the range explored in the development of the analytical framework: the maximum value seen here is $\zeta = 0.031$ with $\mu_C = 0.70$, $q'' = 40$ kW/m², and $\pi_c = 20$. However, the contribution of these values to surface temperature must be assessed in the context of the assumed film cooling scenario.
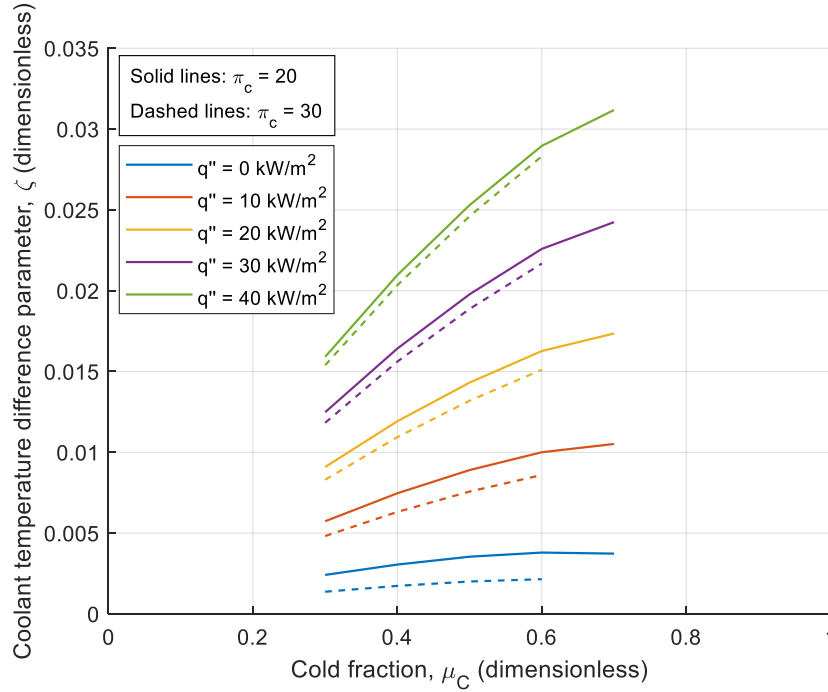
Figure 167. Variation of coolant temperature variation parameter, ζ, with q'' and μ_C

One might be interested in variations of $\bar{\bar{\phi}}$, the laterally averaged overall effectiveness in the presence of two coolant temperatures. However, this requires some assumptions regarding overall effectiveness with a single coolant temperature, $\bar{\phi}$, and the sensitivity of $\bar{\bar{\phi}}$ to changes in ζ, i.e. the partial derivative $\frac{\partial \bar{\bar{\phi}}}{\partial \zeta}$. Some information is required, of course, regarding the distribution of $\frac{\partial \bar{\bar{\phi}}}{\partial \zeta}$ across a region of interest and this

can be drawn from experimental data. Moreover, since the overall effectiveness experiments in Section 2.3 were conducted using Inconel 718, a material with a Biot number matched between lab and engine conditions, it is reasonable that the cooling characteristics can be scaled up to engine conditions. The ranges of $\frac{\partial \bar{\bar{\phi}}}{\partial \zeta}$ were found to be approximately $-0.30 \leq \frac{\partial \bar{\bar{\phi}}}{\partial \zeta} \leq 0.5$ and $-0.45 \leq \frac{\partial \bar{\bar{\phi}}}{\partial \zeta} \leq 0.4$ for the 15 D and 7 D models, respectively. Near the regions of maximum sensitivity, it was found that $\bar{\phi} \approx 0.50$. For a notional cooling scenario, it was assumed that $\bar{\phi} = 0.50$ and $\frac{\partial \bar{\bar{\phi}}}{\partial \zeta} = 0.40$ at some location for each cold fraction. Figure 168 shows the trends of $\bar{\bar{\phi}}$ with the coolant temperatures associated with the cold fractions; the range of $\bar{\bar{\phi}}$ values is less than 0.02.

It must be emphasized that different experimental configurations were used to determine parameters related to adiabatic effectiveness and overall effectiveness; therefore, the influence of the temperature separation profiles on overall effectiveness and surface temperature must be interpreted separately from the analysis of adiabatic effectiveness and adiabatic wall temperature. Obviously, for a *single* experimental configuration, η and ϕ would be related.
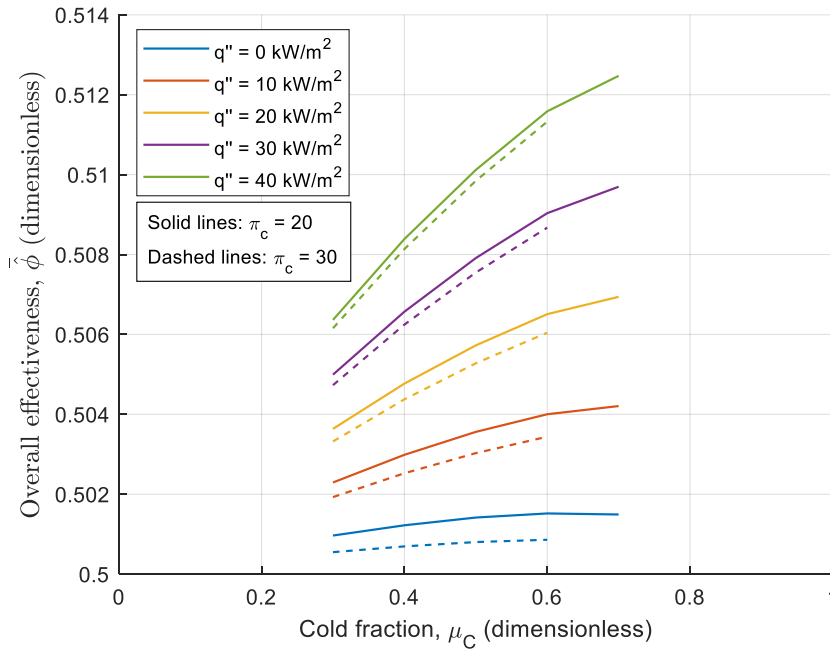
Figure 168. Variation of overall effectiveness with film cooling from a vortex tube,

at a location where $\overline{\phi} = 0.50, \frac{\partial \overline{\overline{\phi}}}{\partial \zeta} = 0.40$

The resulting changes in surface temperature are more pronounced, however, with differences of up to -17 K, as seen in Figure 169. The differences in Figure 169 are, of course, somewhat optimistic in that they are all cast as *reductions* in surface temperature. However, it was seen for both experimental models used in the original experimental study that there are locations where $\frac{\partial \overline{\overline{\phi}}}{\partial \zeta} > 0$ and thus $\zeta > 0$ leads to a reduction in surface temperature, as well as locations where $\frac{\partial \overline{\overline{\phi}}}{\partial \zeta} < 0$, and then $\zeta > 0$ leads to *increased* surface temperatures. Therefore, while Figure 169 does reveal some of the promise of temperature separation with respect to film cooling, one must more roundly consider its potency and the need for deliberation in where best to apply it.
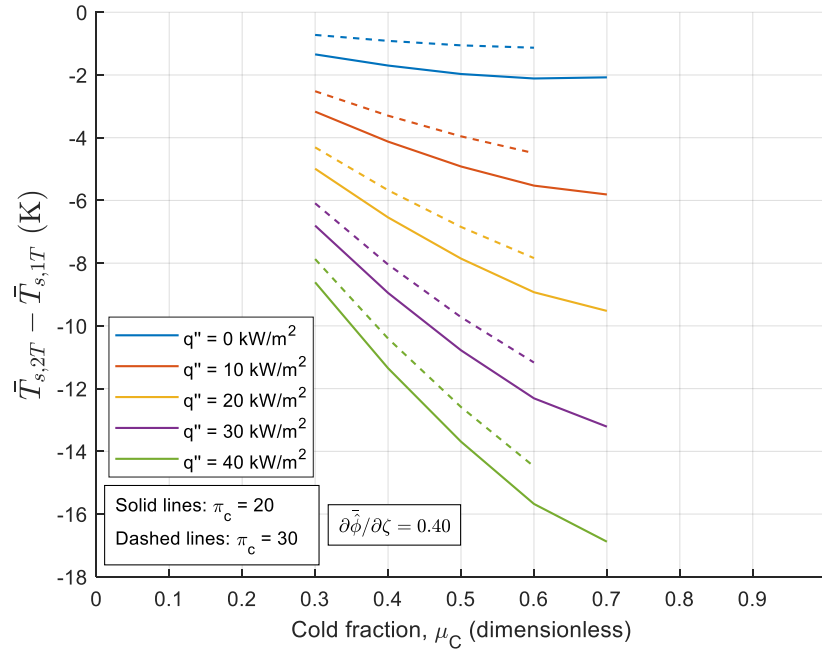
Figure 169. Changes in laterally averaged surface temperature with film cooling from a vortex tube, at a location where $\bar{\phi} = 0.50, \frac{\partial \bar{\bar{\phi}}}{\partial \zeta} = 0.40$

5.2.4 *General trends and practical applications*

Some general conclusions can be drawn regarding the performance of vortex tubes in a film cooling scenario. First, the temperature separation induced by an adiabatic vortex tube seem unlikely to have an appreciable effect on a film cooling scenario: values of T_{aw} and $\bar{T}_s$ changed by 2 K or less for temperatures corresponding to a relatively low value of $\pi_b = 0.89$ for the $\pi_c = 20$ cases, and about half that for a more realistic $\pi_b = 0.94$ for the $\pi_c = 30$ cases. On the other hand, the differences between the hot and cold coolant temperatures become quite significant with increasing levels of heat flux.

This generally suggests that if vortex tubes are to be introduced to a gas turbine engine, that they should be installed in regions of high heat flux.

The coolant differences associated with nonadiabatic temperature separation are quite pronounced, and this is a potentially fruitful avenue of further investigation. To be sure, assessing the practical significance of the temperature changes seen in this analysis is out of scope of this study since it requires detailed knowledge of the metallurgy and stresses involved. That said, reducing the metal temperature of turbine blades in terrestrial power generation equipment by 25 K can double the life of the part [14]. Given that degree of sensitivity to metal temperatures, perhaps scenarios can be identified in which even the temperature curves resulting from adiabatic temperature separation can be of practical interest.

However, the temperature separation resulting from a vortex tube with heat addition can, for the same scenario, contribute potentially significant changes to T_{aw} and T_s. For the cases herein, it may be possible to modify the values of T_{aw} and $\bar{T}_s$ by up to 18 K. The heated cases studied here had mean temperatures of up to 721.5 K, which is on the low side of the practical range of coolant temperatures; with more heat added, it is easy to see that the changes to T_{aw} and $\bar{T}_s$ may become even more substantial.

Naturally, there are caveats to the results—these are for a given flight condition and engine performance parameters and a specific hypothetical cooling scenario with assumed values for $\eta_1, \eta_2, \bar{\phi}, \frac{\partial \bar{\bar{\phi}}}{\partial \zeta}$, and T_∞. Still, some care should be taken in interpreting these findings. For the analysis of the effects on adiabatic wall temperature, the streams exhausted from the vortex tube exits were assumed to exit immediately from the film

314

cooling holes and thus were surrogates for $T_{c,exit}$. In such a scenario, the relative ACRs issuing from the two coolant holes is linked to the cold fraction. The cold fraction, of course, is further linked to the relative temperatures of the coolant streams. Moreover, the magnitude of adiabatic and nonadiabatic temperature separation is directly linked to the mass flow rate entering the vortex tube and increasing this flow rate will increase the magnitude of the ACR at each cooling hole even if μ_C is held constant.

Even more complex scenarios are possible, such as feeding a single plenum with the cold exhaust from multiple vortex tubes while diverting the hot exit coolant to other regions; this probably would have been necessary to drive the slot in the $\hat{\eta}$ scenario, for example, since the coolant flow rate weighting parameter stemming from its large mass flow rate was $\mu = 0.85$. The findings of the present study are encouraging and may inspire some system-level configuration studies to more exhaustively investigate the combined relationships between μ_C, ACR, temperature separation curves, and T_{aw}.

Caveats also apply to the analysis of the effects on metal surface temperature. The exact arrangement of vortex tubes in a cooling scheme would be expected to significantly affect the result, and the manner in which various aspects of the design are coupled would be manifested in different ways. It must be stressed that this analysis modeled the integration of a vortex tube into the cooling scenario as simply filling two plenums with different temperature coolants without changing the underlying heat transfer characteristics; this was essential to assuming the vortex tube exit temperatures were equivalent to $T_{c,1}$ and $T_{c,2}$. The location at which the heat was added was not specified but it was not located in the region of interest.

It may be a slight logical artifice to assume $T_{mean} = T_{c,i}$, where $T_{c,i}$ was the single

coolant temperature *resulting from the same heat addition as the vortex tube*, because it

has already been seen that the heat transfer coefficient in a vortex tube is much greater

than that seen in circular pipe flow. However, cooling channels are constantly being

devised to increase heat transfer and one can simply imagine an internal passage with

sufficient length and heat flux such that the overall heat addition is the same as that

induced by the vortex tube. Additionally, it was assumed that the fraction of heat retained

in the cold fraction, α, was independent of the amount of heat added, q. While that was

necessary to begin this analysis, the maximum heat flux used in the foregoing

calculations was 16 times that of the heat flux used in determining the values of α. If

subsequent study reveals that α is indeed a function of q, then the results may be affected

considerably.

It is not a great leap to consider the effect of installing a vortex tube to provide

backside internal cooling in the same region covered by the film cooling holes. Although

such a study is outside the scope of the present effort, it seems likely that regions of high

local heat transfer coefficient, h, would be more sensitive to the effects of different

coolant temperatures, i.e. the local values of $\frac{\partial \hat{\phi}}{\partial \zeta}$ would potentially be of greater

magnitudes. Moreover, because the elevated h values—compared to pipe flow—are

almost certainly due to the high-velocity swirl, it is expected that there is a strong

relationship between h and nozzle velocity; by extension, this implies a relationship

between h and ACR. However, the tightly coupled nature of vortex tube temperature

separation, ACR, μ_C, h, $\frac{\partial \hat{\phi}}{\partial \zeta}$, ζ, and $\hat{\phi}$ suggest that fully investigating the relationships in

the context of overall effectiveness would be quite a complex endeavor. The present study cannot investigate all of these practical interdependencies but perhaps will inspire a design study to do just that.

Three embodiments of vortex tubes have been considered for integration into gas turbine engines. First is a "master" vortex tube, likely the only one in an engine, and which separates a large amount of coolant into warmer and cooler streams which could be made available to cool a large number of components, such as all or part of a turbine stage, routing the warmer and cooler streams according to known requirements. Second is a smaller, intermediate vortex tube, which would separate a supply of coolant on the order of that required for a single turbine blade, making two temperature coolants available only for the one component. Third is a micro vortex tube, on the scale of a single film cooling hole. Several might exist in a turbine blade and generate two coolant temperatures in a very localized cooling scenario.

Based on the findings here, the first embodiment seems especially impractical. By its nature, the more centralized design concept would prevent it from being installed near the regions where the greatest heat flux is desired. It would also require a large mass flow rate and create a large pressure drop, but would likely offer comparably little temperature separation in return.

Nonadiabatic temperature separation is apparently the most effective means of inducing large differences between coolant temperatures, but achieving this is best accomplished by placing vortex tubes in regions where high local heat fluxes are desired. Thus, to make best use of the coolant, it appears that the second or third embodiments are more worthwhile. Due to the scales involved and limitations on manufacturing

techniques, the second embodiment seems more readily realizable than the third. While the third embodiment obviously faces fabrication challenges, it also has the potential for installation in regions where the highest heat fluxes are desired. However, it remains to be seen whether the associated small-channel mass flow rates are sufficient to sustain the nonadiabatic temperature separation.

It is important not to be naïve regarding the exceptional value of the pressure difference available in an engine; it is, after all, the potential that makes film cooling—and thus modern turbine engines—possible. It also is amply clear by now that conventional vortex tubes are no ordinary pressure-driven flow: they require very large pressure drops to deliver the degree of temperature separation for which they became so well known. A means of reconciling the two applications, that is, the narrow pressure margins of turbine engines with the pressure-hungry vortex tubes, is not entirely straightforward. However, two novel approaches may yield some common ground here.

First, recall that the simplified vortex tube used as a basis for comparison with CFD was tested with two hot exit geometries: one was an annular exit further used in the CFD comparison; the other was an orifice exit. The orifice is a novel configuration for a vortex tube hot exit and is the most basic possible implementation—which is also of benefit from a manufacturing standpoint. Interestingly, it did yield noticeable temperature separation, though it was considerably less than either the commercial or annular exits. However, the orifice also featured the lowest pressure drop of the configurations, lower than that of the simplified annular exit by $25 - 33\%$, depending on cold fraction (see Figure 86 on page 179 and Figure 88 on page 181 for dimensional plots of temperature separation and pressure drops, respectively). It may be possible to leverage that simple

318

design to induce nonadiabatic temperature separation for comparatively low pressure losses, perhaps even acceptable to turbine engines.

Broadly speaking, the use of compressor bleed air as turbine section coolant represents merely a tolerable penalty in the pursuit of greater turbine inlet temperatures and overall engine performance. However, nonadiabatic temperature separation may be of use in another way. If the hot stream can be heated enough, it may be usable as a source of oxygen for combusting excess hydrocarbons in the turbine section by venting the "coolant" normal to the surface. Meanwhile, a relatively cold coolant stream would also be available locally, due to the temperature separation, to prevent overheating from the combustion. If successful, this would accomplish two objectives simultaneously: cool the hot turbine parts and add energy to the freestream; perhaps such a concept would be worth the corresponding pressure loss. A similar principle could be applied to the design of a combustor liner. Additional information would be required to fully inform such a design, such as a more complete characterization of heat transfer into the hot flow as a function of the total heat added, a fuller understanding of the operating characteristics of a vortex tube with an orifice hot exit, and detailed knowledge of the minimum flow rates required to sustain nonadiabatic temperature separation.

This page is intentionally left blank

6 Conclusions and Recommendations

6.1 Conclusions of Research

In the most overarching sense, the present research aspired to explain how vortex tubes work and to use that understanding to adjust gas turbine coolant temperatures. As has been demonstrated in the present research—conducted with a computational investigation and validated with experiments—the explanation for the temperature separation in a vortex tube is simple. At any radial position in the vortex where the velocity profile does not follow solid body like rotation, the part of the flow with a higher angular velocity performs viscous work on an adjacent part at a lower angular velocity and this represents a transfer of energy among the radial "layers" of fluid. This energy transfer passes from the inner part of the flow eventually exhausted as the cold stream to that which becomes the hot stream due to the relative positions of the angular velocity gradients and the notional internal boundary between the two streams. This behavior is manifested through a difference in total temperature at the exits. Conductive heat transfer is present due to the static temperature gradients, but its magnitude is insignificant compared to that of viscous work. The present work is the first to demonstrate this with an unconstrained three-dimensional flow solution using a real gas model, and with the most robust experimental validation of any previous study.

Research investigating "how vortex tubes work" has favored explanations of the mechanics of vortex tubes, but have not generally appreciated the importance of scaling as a contributing factor. As was shown, speculation in the literature regarding the role of gas properties—which is certainly part of the scaling problem—was inconclusive.

321

Particularly distinctive to the present work are the investigations regarding governing parameters and scaling. A novel nondimensionalization of the energy equation was completed, which identified the governing parameters and appropriate reference scales for temperature separation. Most significantly, it was found that dimensional temperature separation scales primarily with the square of the bulk velocity of the gas passing through the vortex tube nozzles. This was verified by experiment with a novel laboratory configuration, which confirmed the appropriate nondimensionalization and, in a notable first, demonstrated that dimensional temperature separation characteristics could be matched even when inlet pressures and temperatures were not matched.

Three governing dimensionless parameters were identified: Reynolds number, Prandtl number, and a new parameter introduced in this dissertation, $\rho C_p \mu_{JT}$, which indicates the contribution of real gas effects. It was found that temperature separation is not a strong function of Reynolds number nor of $\rho C_p \mu_{JT}$ for air, but that real gas effects likely drive performance differences between different gases such as air and CO_2. A proper understanding of the scaling of vortex tube temperature separation permits a researcher, using a small initial data set, to quickly and easily estimate dimensional performance under a wide variety of conditions without the need for additional experiments or CFD.

Experiments conducted under conditions increasingly representative of those found in a gas turbine engine identified some important additional trends. First, experiments at high temperatures revealed that most of the findings from the low temperature experiments continued to be applicable: dimensional temperature separation scaled as a higher order function of nozzle velocity, and dimensional temperature

322

separation was matched between dissimilar inlet temperatures and pressures when nozzle velocity and volumetric heat capacity were also matched. However, it was also found that nondimensionalized temperature separation can follow slightly different trends for the same vortex tube when installed in different configurations. Because historical vortex tube experiments featured fairly similar configurations but with different vortex tubes, the role of the surrounding installation was not generally appreciated; this should be considered in performance estimates and prototyping activities for novel applications.

Experiments with a vortex tube to which an external heat flux was applied revealed a surprising trend: the vast majority of the heat added to the flow—in excess of 90% for $\mu_C = 0.40$—remained in the hot stream, and the temperature of the stream leaving the cold exit increased little. A subsequent computational study was in agreement with these findings and additionally quantified the fraction of the heat retained in the hot and cold streams as a function of cold fraction. Even when the hot stream accounted for only 30% of the overall mass flow rate, 80% of the heat added remained in that stream and its temperature increased dramatically compared to the cold stream. It was also discovered that the Nusselt number along the tube wall was several times greater than that in the thermal entry region for circular pipe flow. In a novel twist, this suggests the possibility that a vortex tube could be a very effective means of facilitating external heat transfer *into* the hot flow. Moreover, this observation represents an interesting extension to the principle of temperature separation: by virtue of its flow structure, a vortex tube can also *sustain* a separation of temperatures which was induced by external heat addition rather than solely by internal fluidic means.

CFD investigations were also conducted at inlet temperatures and pressures corresponding to the compressor exit in a gas turbine engine installed in an aircraft at a notional altitude of 30,000 ft and a flight Mach number of 0.80. The scenarios were computationally demanding and converged solutions could not be generated for as many cold fractions as desired, but temperature separation curves were nevertheless produced. The temperature differences were relatively small: no more than +12 K at the hot exit and less than -6 K at the cold exit.

However, the temperature differences introduced by a vortex tube are only entering arguments in determining the effect on a turbine blade. Two new analytical models were devised to assist with this task. The first is a generalization of superposition theory, with respect to adiabatic effectiveness, for an arbitrary number of rows issuing coolant at different temperatures. With knowledge of the performance of separate film cooling holes or slots, the model allows a designer to synthesize the experimental data to estimate the adiabatic effectiveness and, by extension, adiabatic wall temperature at any point of interest for a film cooling scenario; this is accomplished by using a new dimensionless parameter, ξ, known as the coolant temperature ratio parameter. The model works anywhere that superposition theory is valid, though this generally corresponds to lower ACRs. The second analytical model is valid for a double row and is not limited to superposition scenarios: it extends the determination of overall effectiveness to cooling scenarios with two coolant temperatures. The model introduces two new parameters, a coolant enthalpy weighting parameter, μ, and a coolant temperature variation parameter, ζ. This model permits a designer to completely characterize surface temperatures and temperature gradients for a particular combination

324

of *ACR*s and *any* combination of coolant temperatures based on only two experimental data points.

By integrating the computational results of temperature separation expected at engine conditions with the trends observed regarding the heat retained in the hot and cold streams, a set of notional coolant temperatures were estimated for various cold fractions and levels of heat flux. For the cases with significant heat addition, the coolant temperature differences were found to induce potentially significant differences in adiabatic wall temperature and metal surface temperature when compared to a similar scenario with only a single coolant temperature.

6.2   Significance of Research

It has long been understood that a vortex tube yields greater temperature separation when a higher pressure is applied to the inlet, assuming it is vented to the same ambient conditions. This large pressure drop—another of its defining features—also presents a challenge to its application in new domains. This challenge is acute for gas turbine engines, in which the pressure difference between compressor and turbine is low by design, and thus offers a fraction of the pressure drop available in more conventional applications. It was also understood that temperature separation increases with inlet temperature, though the reason for this was not initially known. At the outset of this research, without fully understanding the mechanism of temperature separation nor its scaling parameters, it was hoped that operating at elevated temperatures in an engine would compensate for the decreased performance associated with the lower pressure drop.

Some key findings now temper this expectation. First, it was discovered that increases in temperature served to increase the nozzle velocity, and that temperature separation scales with the square of nozzle velocity; this is the entire contribution of inlet temperature. Next, in a fashion similar to that of other pressure-driven flows, it was confirmed that the pressure drop across the vortex tube also scales with the square of nozzle velocity. It is therefore effectively impossible to overcome the drawbacks of a small pressure difference by operating at an increased inlet temperature; this obviously limits the temperature separation achievable in the absence of heat addition.

It was a surprise that heat conduction is evidently a weak mechanism in the vortex tube, and this discovery appears consistent with the very high degree of heat retention in the hot flow. It is also this feature that may feasibly permit the application of vortex tubes in high temperature environments such as turbines or combustors. It is well known that heat transfer rates and pressure losses are correlated; however, if the hot stream can be preferentially heated and then directed to release further energy in the flow—such as through combustion of unburned hydrocarbons—then perhaps the use of vortex tubes may be worthwhile.

The principal objectives—explain how vortex tubes work and use that understanding to adjust gas turbine coolant temperatures—have been met. A theory of operation, derived from the energy equation, based on computational investigation, and consistent with experiment, has been established. A means of inducing significant coolant temperature differences despite poor adiabatic temperature separation has also been proposed, including the embodiments most likely to achieve this. However, the question

of whether to pursue application is less clear and the answer must come from practitioners.

6.3   Recommendations for Future Research

Several avenues of potential future research remain, with varying degrees of complexity. The ultimate goal, if the present path is to be continued, is a working model incorporating at least one embodiment of a vortex tube into a film cooling scenario—either for experimental or computational investigation. This might include, for example, gathering data points sufficient to expand or apply the two-temperature overall effectiveness model for use in such a scenario. Although a computational model would allow greater flexibility in terms of achievable temperatures, this would be no small feat if different turbulence models are desired for modeling film cooling or vortex tubes.

Short of modeling the entire film cooling scenario, several discrete research efforts could improve the fidelity of the applied analysis in Section 5.2 and lend additional insight into the feasible use of vortex tubes. First, experimental data could be gathered for coolant enthalpy weighting parameters other than $\mu = 0.50$. This would permit a characterization of surface temperatures across an entire region of interest as a function of cold fraction, assuming $\mu \approx \mu_C$.

Also, more must be known about heat transfer into the vortex tube. A computational investigation of the fraction of added heat retained in the cold flow, α, as a function of heat added, q, would be especially valuable; with a definitive function, it may be possible to extrapolate coolant temperatures significantly beyond the current values. Such research likely has two potential branches. First, it would be desirable to know, for a given vortex tube inlet condition, how α varies with increasing q. Equally interesting

would be a study of how α varies, for a given q, with decreasing nozzle velocities—this would provide some idea of the minimum nozzle conditions required to adequately sustain nonadiabatic temperature separation. Alternate boundary conditions should also be investigated: the computational effort thus far has only used a uniform heat flux condition, but further efforts should also apply a uniform surface temperature boundary condition to determine corresponding local Nu values.

The hot exit orifice geometry was included in the present research essentially as a target of opportunity and was not central to the research objectives. That said, its potential for use, in view of its simplicity and low pressure drop, may pair well with nonadiabatic temperature separation. Further study should include this configuration.

While the understanding of vortex tube performance has progressed considerably as a result of this research, additional questions remain. First, the Mach numbers used in the low temperature rig were generally low—at or below Mach 0.35. Mass flow rate restrictions imposed by the installation prevented Mach numbers higher than 0.40 from being used in air. Orientation tests on the low temperature rig using He found that sonic flow could be achieved at the nozzles; however, the data collected were very anecdotal and unsuitable for evaluating any trends. Investigations could be conducted on the nondimensionalization of temperature separation at higher Mach numbers using He. A variety of gases could also be used to investigate real gas effects across a much wider range of the new dimensionless parameter, $\rho C_p \mu_{JT}$.

During the initial installation of the Exair^{TM} 3208 vortex tube, prior to the integration of the mass flow controllers, the temperature separation effect was investigated by manually setting the hot exit valve to adjust the cold fraction. It was

found that at very high—but unquantified—cold fractions, the temperature separation reversed and the colder air was exhausted from the end that had previously exhausted the hotter air and vice versa. The temperature of the air exhausted from "hot" end was then approximately 2 K colder than the inlet, while that from the "cold" end was 10 K warmer than the inlet. The reason for this is not known, nor was it ever observed computationally. A similar finding was encountered by Martynovskii and Alekseev [53]. It is possible that the internal interface between hot and cold streams was so displaced from its usual location that different components of work and heat transfer became dominant; for example, it has been shown that the axial viscous work component, $\int n_r \tau_{rz} v_z dS$, acts such that work is performed by the hot stream on the cold stream. This unusual mode of temperature separation has not been conclusively investigated.

A final avenue of future research involves the specific vortex tube installations in the laboratory. During the investigations of the high-temperature configuration, a peculiar phenomenon that could be best described as an alternate vortex "mode" was anecdotally encountered. In the alternate mode, temperature separation was found to increase substantially for a given mass flow rate. However, this mode was periodically encountered by accident, normally during abrupt changes in experimental conditions, and it was thought not to be stable—small changes in commanded mass flow rate, for example, could cause the operation to revert to the normal mode. A detailed investigation of this behavior could not be undertaken in the time available for the present research, so it was never determined how one might deliberately induce, characterize, or control the alternate mode. None of the data presented herein was knowingly taken in that mode. If it is indeed a valid flow solution, it is possible that it is a driven by Reynolds number

329

effects—which are known to contribute to flow stability. This mode was also believed to have been encountered on the low-temperature rig as well, so the possibility also exists that the local hardware, such as the mass flow controllers, may also have been a factor.

References

[1]   Mattingly, J. D., and Boyer, K. M., 2016, *Elements of Propulsion: Gas Turbines and Rockets, Second Edition*, American Institute of Aeronautics and Astronautics, Inc., Washington, DC.

[2]   Halford, G. R., 1986, *Low-Cycle Thermal Fatigue.*, NASA Technical Memorandum 87225.

[3]   Eckert, E. R. G., 1987, "Cross Transport of Energy in Fluid Streams," Wärme- und Stoffübertragung, **21**(2–3), pp. 73–81.

[4]   Rakowski, W., Ellis, D., and Bankhead, H., 1978, "A Research Program for the Experimental Analysis of Blade Instability," *14th Joint Propulsion Conference*, American Institute of Aeronautics and Astronautics, Reston, Virigina.

[5]   Kurosaka, M., 1982, "Acoustic Streaming in Swirling Flow and the Ranque-Hilsch (Vortex-Tube) Effect," J. Fluid Mech., **124**, pp. 139–172.

[6]   Seol, W. S., and Goldstein, R. J., 1997, "Energy Separation in a Jet Flow," J. Fluids Eng., **119**(1), pp. 74–82.

[7]   Kays, W. M. ., Crawford, M. E., and Weigand, B., 2005, *Convective Heat and Mass Transfer*, McGraw Hill, New York City, NY.

[8]   Hollinger, S., and Lücke, M., 1995, "Influence of the Dufour Effect on Convection in Binary Gas Mixtures," Phys. Rev. E, **52**(1), pp. 642–657.

[9]   Exair, "Vortex Tubes" [Online]. Available: http://www.exair.com/index.php/products/vortex-tubes-and-spot-cooling-products/vortex-tubes/vt.html. [Accessed: 04-Feb-2019].

[10]   Tin, S., and Pollock, T. M., 2014, "Nickel-Based Superalloys," *Turbine Aerodynamics, Heat Transfer, Materials, and Mechanics*, American Institute of Aeronautics and Astronautics, Inc., Reston, VA, pp. 423–466.

[11]   Bunker, R. S., 2014, "Turbine Cooling Design," *Turbine Aerodynamics, Heat Transfer, Materials, and Mechanics*, American Institute of Aeronautics and Astronautics, Inc., Reston, VA, pp. 39–60.

[12]   Magge, S. S., Sharma, O. P., Stetson, G. M., and Wagner, J., 2014, "Overview of Turbine Design," *Turbine Aerodynamics, Heat Transfer, Materials, and*

Mechanics, American Institute of Aeronautics and Astronautics, Inc., Reston, VA, pp. 1–37.

[13]   Ekkad, S. V., 2014, "Internal Cooling," *Turbine Aerodynamics, Heat Transfer, Materials, and Mechanics*, American Institute of Aeronautics and Astronautics, Inc., Reston, VA, pp. 189–222.

[14]   Bogard, D. G., and Thole, K. A., 2006, "Gas Turbine Film Cooling," J. Propuls. Power, **22**(2), pp. 249–270.

[15]   Schroeder, R. P., and Thole, K. A., 2014, "Adiabatic Effectiveness Measurements for a Baseline Shaped Film Cooling Hole," *ASME Turbo Expo 2014*, Paper No. GT2014-25992, pp. 1–13.

[16]   Saumweber, C., Schulz, A., and Wittig, S., 2003, "Free-Stream Turbulence Effects on Film Cooling with Shaped Holes," J. Turbomach., **125**(1), pp. 65–73.

[17]   Rutledge, J. L., and Polanka, M. D., 2014, "Computational Fluid Dynamics Evaluations of Unconventional Film Cooling Scaling Parameters on a Simulated Turbine Blade Leading Edge," J. Turbomach., **136**(10), pp. 1–11.

[18]   Bogard, D. G., and Thole, K. A., 2014, "Film Cooling," *Turbine Aerodynamics, Heat Transfer, Materials, and Mechanics*, American Institute of Aeronautics and Astronautics, Inc., Reston, VA, pp. 223–273.

[19]   Sellers, J. P., 1963, "Gaseous Film Cooling with Multiple Injection Stations," AIAA J., **1**(9), pp. 2154–2156.

[20]   Muska, J. F., Fish, R. W., and Suo, M., 1976, "The Additive Nature of Film Cooling From Rows of Holes," J. Eng. Power, **98**(4), pp. 457–463.

[21]   Sasaki, M., Takahara, K., Kumagai, T., and Hamano, M., 1979, "Film Cooling Effectiveness for Injection from Multirow Holes," J. Eng. Power, **101**(1), pp. 101–108.

[22]   Saumweber, C., 2004, "Interaction of Film Cooling Rows: Effects of Hole Geometry and Row Spacing on the Cooling Performance Downstream of the Second Row of Holes," J. Turbomach., **126**(2), pp. 237–246.

[23]   Metzger, D. E., Kuenstler, P. A., Hale, P. L., and Anderson, J., 1978, "Influences of Upstream Injection and Intermediate Panel Temperature on Multiple Slot Film Cooling," *Proceeding of International Heat Transfer Conference 6*, Begellhouse,

Connecticut, pp. 261–266.

[24] Harrington, M. K., McWaters, M. A., Bogard, D. G., Lemmon, C. A., and Thole, K. A., 2001, "Full-Coverage Film Cooling With Short Normal Injection Holes," J. Turbomach., **123**(4), pp. 798–805.

[25] Albert, J. E., Bogard, D. G., and Cunha, F., 2004, "Adiabatic and Overall Effectiveness for a Film Cooled Blade," *ASME Turbo Expo 2004*, Paper No. GT2004-53998.

[26] Martiny, M., Schulz, A., and Wittig, S., 1997, "Mathematical Model Describing the Coupled Heat Transfer in Effusion Cooled Combustor Walls," *ASME 1997 International Gas Turbine and Aeroengine Congress and Exhibition*, Paper No. 97-GT-329.

[27] Williams, R. P., Dyson, T. E., Bogard, D. G., and Bradshaw, S. D., 2014, "Sensitivity of the Overall Effectiveness to Film Cooling and Internal Cooling on a Turbine Vane Suction Side," J. Turbomach., **136**(3), pp. 031006-1–7.

[28] Sweeney, P. C., and Rhodes, J. F., 2000, "An Infrared Technique for Evaluating Turbine Airfoil Cooling Designs," J. Turbomach., **122**(1), pp. 170–177.

[29] Stewart, W. R., and Dyson, T. E., 2017, "Conjugate Heat Transfer Scaling for Inconel 718," *ASME Turbo Expo 2017*, Paper No. GT2017-64873.

[30] Wiese, C. J., Bryant, C. E., Rutledge, J. L., and Polanka, M. D., 2018, "Influence of Scaling Parameters and Gas Properties on Overall Effectiveness on a Leading Edge Showerhead," J. Turbomach., **140**(11), pp. 111007-1–12.

[31] Bryant, C. E., Wiese, C. J., Rutledge, J. L., and Polanka, M. D., 2019, "Experimental Evaluations of the Relative Contributions to Overall Effectiveness in Turbine Blade Leading Edge Cooling," J. Turbomach., **141**(4), pp. 041007-1–12.

[32] Polanka, M., Gillaugh, T., Anthony, R., Umholtz, M., and Reeder, M., 2007, "Comparisons of Three Cooling Techniques in a High Speed, True Scale, Fully Cooled Turbine Vane Ring," *43rd AIAA/ASME/SAE/ASEE Joint Propulsion Conference & Exhibit*, Paper No. AIAA 2007-5097.

[33] Rolls Royce, 2015, *The Jet Engine*, Wiley, Hoboken, NJ.

[34] Alqefl, M. H., Nawathe, K., Chen, P., Zhu, R., and Simon, T. W., 2019, "A Multi-

Plenum Superposition Method for Scalar Transport with Application to Endwall Film Cooling," Paper No. IGTC 2019-51.

[35]   Fischer, J. P., McNamara, L. J., Rutledge, J. L., and Polanka, M. D., 2020, "Scaling Flat-Plate, Low-Temperature Adiabatic Effectiveness Results Using the Advective Capacity Ratio," J. Turbomach., **142**(8), pp. 081010-1–12.

[36]   Wiese, C. J., Rutledge, J. L., and Polanka, M. D., 2018, "Experimental Evaluation of Thermal and Mass Transfer Techniques to Measure Adiabatic Effectiveness With Various Coolant to Freestream Property Ratios," J. Turbomach., **140**(2), pp. 021001-1–9.

[37]   Kline, S. J., and McClintock, F. A., 1953, "Describing Uncertainties in Single-Sample Experiments," Mech. Eng., **75**(1), pp. 3–8.

[38]   Ranque, G. J., 1933, "French Patent: 743,111. Procédé et Appareil Permettant d'obtenir, à Partir d'un Fluide Sous Pression, Deux Courants de Fluide de Températures Différentes."

[39]   Ranque, G. J., 1934, "United States Patent: 1,952,281. Method and Apparatus for Obtaining from a Fluid under Pressure Two Outputs of Fluid at Different Temperatures," US Pat.

[40]   Westley, R., 1954, "A Bibliography and Survey of the Vortex Tube."

[41]   Hilsch, R., 1947, "The Use of the Expansion of Gases in a Centrifugal Field as Cooling Process," Rev. Sci. Instrum., **18**(2), pp. 108–113.

[42]   Fulton, C., 1965, "United States Patent: 3,173,273. Vortex Tube."

[43]   Fulton, C., 1965, "United States Patent: 3,208,229. Vortex Tube."

[44]   Fulton, C. D., 1950, "Ranque's Tube," Refrig. Eng., **58**(5), pp. 473–479.

[45]   Stephan, K., Lin, S., Durst, M., Huang, F., and Seher, D., 1983, "An Investigation of Energy Separation in a Vortex Tube," Int. J. Heat Mass Transf., **26**(3), pp. 341–348.

[46]   Schultz-Grunow, F., 1951, "Turbulenter Wärmedurchgang Im Zentrifugalfeld," Forsch. auf dem Gebiet des Ingenieurwesens A, **17**(3), pp. 65–76.

[47]   Elser, V. K., and Hoch, M., 1951, "Das Verhalten Verschiedener Gase Und Die Trennung von Gasgemischen in Einem Wirbelrohr," Zeitschrift fur Naturforsch. - Sect. A J. Phys. Sci., **6**(1), pp. 25–31.

[48]   Kassner, R., and Knoernschild, E., 1948, *Friction Laws and Energy Transfer in Circular Flow*, Dayton, Ohio.

[49]   Scheper, G. W., 1951, "The Vortex Tube-Internal Flow Data and a Heat Transfer Theory," J. ASRE, Refrig. Eng., **59**, pp. 985–989.

[50]   Scheller, W. A., 1957, "The Ranque-Hilsch Vortex Tube," Fluid Mech. Chem. Eng., **49**(6), pp. 1013–1016.

[51]   Takahama, H., 1965, "Studies on Vortex Tubes," Bull. JSME, **8**(31), pp. 433–440.

[52]   Bruun, H. H., 1969, "Experimental Investigation of the Energy Separation in Vortex Tubes," J. Mech. Eng. Sci., **11**(6), p. 567.

[53]   Martynovskii, V.S., Alekseev, V. P., 1957, "Investigation of the Vortex Thermal Separation Effect for Gases and Vapour," Sov. Physics. Tech. Phys., **1**(10), pp. 2233–2243.

[54]   Lay, J. E., 1959, "An Experimental and Analytical Study of Vortex-Flow Temperature Separation by Superposition of Spiral and Axial Flow: Part 2," J. Heat Transfer, **81**(3), pp. 213–221.

[55]   Hartnett, J. P., and Eckert, E. R. G., 1957, "Experimental Study of the Velocity and Temperature Distribution in a High Velocity Vortex Type Flow," Trans. ASME, **79**(4), pp. 751–758.

[56]   Smith, J. L., 1962, "An Analysis of the Vortex Flow in the Cyclone Separator," J. Fluids Eng. Trans. ASME, **84**(4), pp. 609–616.

[57]   Chiné, B., and Ferrara, G., 1997, "Comparison between Flow Velocity Profiles in Conical and Cylindrical Hydrocyclones," KONA Powder Part. J., **15**(May), pp. 170–179.

[58]   Reynolds, A. J., 1960, "Studies of Rotating Fluids: The Ranque-Hilsch Vortex Tube," University of London.

[59]   Fulton, C. D., 1951, "Comments on the Vortex Tube," J. ASRE, Refrig. Eng., **59**, p. 984.

[60]   Rott, N., 1959, "On the Viscous Core of a Line Vortex II," Zeitschrift für Angew. Math. und Phys. ZAMP, **10**(1), pp. 73–81.

[61]   Van Deemter, J. J., 1952, "On the Theory of the Ranque-Hilsch Cooling Effect," Appl. Sci. Res. Sect. A, **3**(3), pp. 174–196.

[62]   Deissler, R. G., and Perlmutter, M., 1960, "Analysis of the Flow and Energy Separation in a Turbulent Vortex," Int. J. Heat Mass Transf., **1**(2–3), pp. 173–191.

[63]   Sibulkin, M., 1962, "Unsteady, Viscous, Circular Flow Part 3. Application to the Ranque-Hilsch Vortex Tube," J. Fluid Mech., **12**(02), p. 269.

[64]   Dutta, T., Sinhamahapatra, K. P., and Bandyopadhyay, S. S., 2013, "CFD Analysis of Energy Separation in Ranque-Hilsch Vortex Tube at Cryogenic Temperature," J. Fluids, **2013**, pp. 1–14.

[65]   Xue, Y., Arjomandi, M., and Kelso, R., 2013, "The Working Principle of a Vortex Tube," Int. J. Refrig., **36**(6), pp. 1730–1740.

[66]   Behera, U., Paul, P. J., Dinesh, K., and Jacob, S., 2008, "Numerical Investigations on Flow Behaviour and Energy Separation in Ranque-Hilsch Vortex Tube," Int. J. Heat Mass Transf., **51**(25–26), pp. 6077–6089.

[67]   Ahlborn, B., and Groves, S., 1997, "Secondary Flow in a Vortex Tube," Fluid Dyn. Res., **21**(2), pp. 73–86.

[68]   Fröhlingsdorf, W., and Unger, H., 1998, "Numerical Investigations of the Compressible Flow and the Energy Separation in the Ranque-Hilsch Vortex Tube," Int. J. Heat Mass Transf., **42**(3), pp. 415–422.

[69]   Skye, H. M., Nellis, G. F., and Klein, S. A., 2006, "Comparison of CFD Analysis to Empirical Data in a Commercial Vortex Tube," Int. J. Refrig., **29**(1), pp. 71–80.

[70]   Behera, U., Paul, P. J., Kasthurirengan, S., Karunanithi, R., Ram, S. N., Dinesh, K., and Jacob, S., 2005, "CFD Analysis and Experimental Investigations towards Optimizing the Parameters of Ranque-Hilsch Vortex Tube," Int. J. Heat Mass Transf., **48**(10), pp. 1961–1973.

[71]   Oliver, R., Boyle, F., and Reynolds, A., 2006, "Computer Aided Study of the Ranque–Hilsch Vortex Tube Using Advanced Three-Dimensional Computational Fluid Dynamics Software," *Proceedings of the 6th WSEAS International Conference on Applied Computer Science*, Tenerife, Canary Islands, pp. 478–483.

[72] Eiamsa-ard, S., and Promvonge, P., 2007, "Numerical Investigation of the Thermal Separation in a Ranque-Hilsch Vortex Tube," Int. J. Heat Mass Transf., **50**(5–6), pp. 821–832.

[73] Thakare, H. R., and Parekh, A. D., 2014, "CFD Analysis of Energy Separation of Vortex Tube Employing Different Gases, Turbulence Models and Discretisation Schemes," Int. J. Heat Mass Transf., **78**, pp. 360–370.

[74] Dutta, T., Sinhamahapatra, K. P., and Bandyopdhyay, S. S., 2010, "Comparison of Different Turbulence Models in Predicting the Temperature Separation in a Ranque-Hilsch Vortex Tube," Int. J. Refrig., **33**(4), pp. 783–792.

[75] Farouk, T., and Farouk, B., 2007, "Large Eddy Simulations of the Flow Field and Temperature Separation in the Ranque-Hilsch Vortex Tube," Int. J. Heat Mass Transf., **50**(23–24), pp. 4724–4735.

[76] Secchiaroli, A., Ricci, R., Montelpare, S., and D'Alessandro, V., 2009, "Numerical Simulation of Turbulent Flow in a Ranque-Hilsch Vortex Tube," Int. J. Heat Mass Transf., **52**(23–24), pp. 5496–5511.

[77] Aljuwayhel, N. F., Nellis, G. F., and Klein, S. A., 2005, "Parametric and Internal Study of the Vortex Tube Using a CFD Model," Int. J. Refrig., **28**(3), pp. 442–450.

[78] Stephan, K., Lin, S., Durst, M., Huang, F., and Seher, D., 1984, "A Similarity Relation for Energy Separation in a Vortex Tube," Int. J. Heat Mass Transf., **27**(6), pp. 911–920.

[79] Entov, V. M., Kalashnikov, V. N., and Raiskii, Y. D., 1971, "Parameters Which Determine the Vortex Effect," Fluid Dyn., **2**(3), pp. 18–22.

[80] Pope, S. B., 2000, *Turbulent Flows*, Cambridge University Press, Cambridge.

[81] Pourmahmoud, N., Rafiee, S. E., Rahimi, M., and Hassanzadeh, A., 2013, "Numerical Energy Separation Analysis on the Commercial Ranque-Hilsch Vortex Tube on Basis of Application of Different Gases," Sci. Iran., **20**(5), pp. 1528–1537.

[82] Rafiee, S. E., and Sadeghiazad, M. M., 2016, "Three-Dimensional Numerical Investigation of the Separation Process in a Vortex Tube at Different Operating Conditions," J. Mar. Sci. Appl., **15**(2), pp. 157–165.

[83] Torrella, E., 2013, "Experimental Evaluation of the Energy Performance of an Air

Vortex Tube When the Inlet Parameters Are Varied," Open Mech. Eng. J., **7**(1), pp. 98–107.

[84] Pourmahmoud, N., Rahimi, M., Rafiee, S., and Hassanzadeh, A., 2014, "A Numerical Simulation of the Effect of Inlet Gas Temperature on the Energy Separation in a Vortex Tube," J. Eng. Sci. Technol., **9**(1), pp. 81–96.

[85] Soni, Y., and Thomson, W. J., 1975, "Optimal Design of the Ranque-Hilsch Vortex Tube," J. Heat Transfer, **97**(2), pp. 316–317.

[86] Saidi, M. H., and Valipour, M. S., 2003, "Experimental Modeling of Vortex Tube Refrigerator," Appl. Therm. Eng., **23**(15), pp. 1971–1980.

[87] Dyskin, L. M., and Kramarenko, P. T., 1984, "Energy Characteristics of Vortex Microtubes," J. Eng. Phys., **47**(6), pp. 1394–1395.

[88] Hamoudi, Amar, F., Fartaj, A., and Rankin, G. W., 2006, "An Investigation of a Micro-Scale Ranque-Hilsch Vortex Tube," *2006 ASME International Mechanical Engineering Congress and Exposition*, Paper No. IMECE2006-14711, pp. 1–8.

[89] Hamoudi, A. F., Fartaj, A., and Rankin, G. W., 2008, "Performance Characteristics of a Microscale Ranque–Hilsch Vortex Tube," J. Fluids Eng., **130**(10), pp. 101206-1–8.

[90] Polihronov, J. G., and Straatman, A. G., 2012, "Thermodynamics of Angular Propulsion in Fluids," Phys. Rev. Lett., **109**(5), pp. 1–4.

[91] Panton, R. L., 2013, *Incompressible Flow*, Wiley, Hoboken, NJ.

[92] John, J. E. A., 1984, *Gas Dynamics*, Allyn & Bacon, Boston, MA.

[93] Lemmon, E. W., Huber, M. L., and McLinden, M. O., 2013, *NIST Standard Reference Database 23: Reference Fluid Thermodynamic and Transport Properties-REFPROP, Version 9.1*, Gaithersburg, MD.

[94] Lemmon, E., McLinden, M., and Friend, D., "Thermophysical Properties of Fluid Systems," *NIST Chemistry WebBook, NIST Standard Reference Database Number 69*, P. Linstrom, and W.G. Mallard, eds., National Institute of Standards and Technology, Gaithersburg.

[95] Ahlborn, B., Keller, J. U., Staudt, R., Treitz, G., and Rebhan, E., 1994, "Limits of Temperature Separation in a Vortex Tube," J. Phys. D. Appl. Phys., **27**(3), pp.

480–488.

[96]   Demirel, Y., and Gerbaud, V., 2018, *Nonequilibrium Thermodynamics*, Elsevier, Amsterdam.

[97]   Weisstein, E. W., 2015, "Conical Frustum," MathWorld--A Wolfram Web Resour., p. 1 [Online]. Available: http://mathworld.wolfram.com/ConicalFrustum.html.

[98]   Incropera, F. P., Dewitt, D. P., Bergman, T. L., and Lavine, A. S., 2003, *Principles of Heat and Mass Transfer*, Wiley, Hoboken, NJ.

[99]   Takahama, H., Kawamura, H., Kato, S., and Yokosawa, H., 1979, "Performance Characteristics of Energy Separation in a Steam-Operated Vortex Tube," Int. J. Eng. Sci., **17**(6), pp. 735–744.

[100]   Notter, R. H., and Sleicher, C. A., 1972, "A Solution to the Turbulent Graetz Problem--III Fully Developed and Entry Region Heat Transfer Rates," Chem. Eng. Sci., **27**(11), pp. 2073–2093.

[101]   U.S. Committee on Extension of the Standard Atmosphere, 1976, *U.S. Standard Atmosphere*, U.S. Government Printing Office, Washington, DC.

REPORT DOCUMENTATION PAGE

Form Approved
OMB No. 0704-0188

1. REPORT DATE *(DD-MM-YYYY)*	2. REPORT TYPE	3. DATES COVERED *(From - To)*
16-09-2021	Doctoral Dissertation	Sep 2018 – Sep 2021

4. TITLE AND SUBTITLE	5a. CONTRACT NUMBER
The Application of Vortex Tubes to Gas Turbine Film Cooling	5b. GRANT NUMBER
	5c. PROGRAM ELEMENT NUMBER

6. AUTHOR(S)	5d. PROJECT NUMBER
Fuqua, Matthew N., Lieutenant Colonel, USAF	5e. TASK NUMBER
	5f. WORK UNIT NUMBER

7. PERFORMING ORGANIZATION NAME(S) AND ADDRESS(ES)	8. PERFORMING ORGANIZATION REPORT NUMBER
Air Force Institute of Technology Graduate School of Engineering and Management (AFIT/EN) 2950 Hobson Way Wright-Patterson AFB, OH 45433-7765	AFIT-ENY-DS-21-S-093

9. SPONSORING / MONITORING AGENCY NAME(S) AND ADDRESS(ES)	10. SPONSOR/MONITOR'S ACRONYM(S)
Air Force Research Lab, Turbine Engine Division, Turbomachinery Branch Dr. Andrew T. Lethander 1950 5th St Wright-Patterson AFB, OH 45433 Andrew.Lethander@us.af.mil	AFRL/RQTT
	11. SPONSOR/MONITOR'S REPORT NUMBER(S)

12. DISTRIBUTION / AVAILABILITY STATEMENT

DISTRIBUTION STATEMENT A. APPROVED FOR PUBLIC RELEASE; DISTRIBUTION UNLIMITED

13. SUPPLEMENTARY NOTES
This material is declared a work of the U.S. Government and is not subject to copyright protection in the United States.

14. ABSTRACT

To improve thermal efficiency and reduce fuel consumption, gas turbine engines typically operate at increasingly higher turbine inlet temperatures—well in excess of turbine blade material limits—and film cooling schemes are normally employed to reduce metal temperatures within acceptable limits and prevent structural failure. Cooling requirements vary across a blade surface, but there currently exists no means by which coolant temperatures can be locally adjusted to facilitate optimized usage across a blade. Ranque-Hilsch vortex tubes were investigated as a means of adjusting coolant temperatures solely by fluidic means, induced by the phenomenon of temperature separation. Analytical frameworks were developed to determine adiabatic and overall effectiveness in the presence of multiple coolant temperatures and validated via experiment. Through the integrated application of experimental, analytical, and computational investigations, the parameters which govern temperature separation were identified as well as the proper means of scaling temperature separation and the underlying physics behind the mechanism of temperature separation. Heat transfer characteristics of vortex tubes were determined and vortex tube performance near engine conditions was modeled. Findings were synthesized to estimate the net effect of multiple local coolant temperatures on turbine blades, including adiabatic wall temperatures and thermally conductive metal surface temperatures, and the effect was found under some circumstances to be operationally significant.

15. SUBJECT TERMS
Film Cooling, Vortex Tubes, Gas Turbine Engines

16. SECURITY CLASSIFICATION OF:			17. LIMITATION OF ABSTRACT	18. NUMBER OF PAGES	19a. NAME OF RESPONSIBLE PERSON James L. Rutledge, AFIT/ENY
a. REPORT U	b. ABSTRACT U	c. THIS PAGE U	UU	358	19b. TELEPHONE NUMBER *(include area code)* (937) 255-6565 ext 4734 (James.Rutledge@afit.edu)

Standard Form 298 (Rev. 8-98)
Prescribed by ANSI Std. Z39.18